Doctoral Dissertation
Doctoral Program in Electrical, Electronics and Communications Engineering (36th Cycle)

Online Partial Discharge Detection and Localization of Medium-voltage Overhead Distribution Networks

By

Yuan Yan
******

Supervisor(s):
Prof. Igor Simone Stievano and Prof. Hongjie Li, Supervisor
Prof. Riccardo Trinchero, Co-Supervisor

Doctoral Examination Committee:
Prof. Shengchang Ji, Referee, Xi 'an Jiaotong University (Chairman)
Prof. Yanzhao Xie, Referee, Xi 'an Jiaotong University
Prof. Weidong Ding, Referee, Xi 'an Jiaotong University
Prof. Zheng Qian, Referee, Beihang University
Prof. Jiandong Duan, Referee, Xi 'an University of Technology
Prof. Wanzhao Cui, Referee, China Academy of Space Technology
Prof. Paolo Manfredi, Referee, Politecnico di Torino

Politecnico di Torino
2024

Declaration

I hereby declare that, the contents and organization of this dissertation constitute my own original work and does not compromise in any way the rights of third parties, including those relating to the security of personal data.

Yuan Yan

2024

* This dissertation is presented in partial fulfillment of the requirements for **Ph.D. degree** in the Graduate School of Politecnico di Torino (ScuDo).

I would like to dedicate this dissertation to my loving parents

Acknowledgment

I would like to thank my supervisor, Professor Li Hongjie, for his careful guidance during my doctoral studies. Professor Li Hongjie gave me profound guidance in scientific research ability cultivation, project investigation, research plan formulation, discussion of experimental results, etc., and exercised my independent scientific research, expression, and innovation ability. Professor Li Hongjie's rigorous academic attitude, keen thinking ability, rich practical experience, and pragmatic work style have set a benchmark for my study and life. During my joint training at Politecnico di Torino in Italy, I would like to thank my co-supervisors, Professor Igor Simone Stievano and Professor Riccardo Trinchero. Professor Igor Simone Stievano's patient guidance for more than a year was the biggest source of motivation for my substantial breakthroughs in scientific research. He has given me great help in condensing scientific issues, writing papers, and academic expression. He exercised my ability to solve scientific and technical problems step by step and cultivated my critical scientific thinking. Professor Riccardo Trinchero's profound mathematical skills and rigorous scientific research attitude have helped me overcome critical technical problems and cultivated my mathematical modeling ability. I would like to express my deep gratitude to these two co-supervisors.

I would like to express my heartfelt thanks to Professor Ding Weidong and Associate Professor Guo Jun of the High Voltage Insulation Institute for reviewing the first draft of this article and providing many valuable comments. Thanks to Professor Wang Zhongyi for his careful review of the paper format. Thanks to all the experts and scholars who participated in the review of my paper. Their comments and suggestions played a vital role in improving the dissertation.

During the research process of this dissertation, I received help from the students in the research group. I would like to thank Lu Yuxin, He Weisheng, Zeng Xiaoming, and Yang Saike for their guidance in the beginning of my scientific research; I would like to thank Zhang Hangwei, Xu Xiaolong, Xu Penglai, Lu Zhenyu, Tao Jiaqi, Wang Yanchao, Gao Yincheng, Di Yunpeng, Tang Kun, Yue Xianyu, Zhao Kun, Jin Lei, Zhao Yinsong, and Wang Li, Chen Junbai, Zhu Mengxin, Wang Tiantian, Shi Fangzhou, Wang Zongyao, Xu Zixing, Xia Xin, etc. fought side by side with me and worked hard together, giving me the motivation to move forward; thanks to Chen Shuo, Zeng Xiangfeng, Chen Yufei, Wang Haochen, Li Tian, Li Ruipeng, Hou Zhe, Li Baojie, etc. helped me in scientific research and life. They shared their scientific research experience with me and gave me a lot of inspiration and help. We also formed a deep friendship.

Special thanks go to my wife, Ms. Ma Jiao, who has always supported me firmly and given me endless understanding, encouragement, and advice during my studies and scientific research. At every hard moment, she used her optimistic comfort and correct guidance to push me forward and help me overcome one difficulty after another. During this difficult year in a foreign country, thousands of miles apart, we comforted with each other. Her strength and patience made me feel extremely lucky and happy. I will continue to work hard to create a better life for our future! I would like to thank my father, Mr. Yan Guangyong, and my mother, Ms. Zhang Xiaoqin, for their education and encouragement over the years. They have taught me to treat people sincerely and do things down-to-earthly. Their selfless dedication has strongly backed me.

In addition, there are many classmates, friends, and teachers who silently care about and support the author. It is impossible to list them all here. I would like to express my heartfelt thanks to them.

I would like to thank the China Scholarship Council for funding my study in Italy.

Abstract

Medium-voltage (MV) overhead distribution networks play a vital role in ensuring reliable power supply and minimizing disruptions and inconveniences to consumers; however, insulation faults in these networks can result in power outages, compromising stability, and causing significant economic and social impacts. The solution to this problem is to conduct condition-based maintenance of the networks. Partial discharge (PD), a phenomenon able to reveal or cause incipient failure of electrical apparatus, is a fundamental indicator in condition-based maintenance. Traditionally, technicians patrol along MV overhead lines to identify PDs by vision- and ultrasonic-based methods. However, this technique is insensitive to the PDs inside the electrical equipment and is laborious and time-consuming for sizeable distribution networks. To overcome these limitations, the traveling wave-based PD diagnosis technique has been explored recently, and it has been proven to detect PD more efficiently and allow monitoring of all apparatuses in the networks online. However, uncertain PD signal propagation distortions, electromagnetic noise interferences, synchronization problems in PD localization, etc., significantly reduce the accuracy and reliability of the technique, impeding its further application for distribution networks. The issues in the traveling wave-based PD diagnosis technique motivated our current study, which offers the following contributions:

PD propagation characteristics in MV three-phase overhead distribution networks are thoroughly investigated. Firstly, PD propagation in MV three-phase overhead distribution networks is modeled based on multiple-conductor theory, along with considering the effect of the alongside towers. The formulas for calculating the frequency-dependent transmission line parameters are derived

from the physical parameters of the overhead line. The developed models and formulas allow us to simulate PD signals at any location within an overhead distribution network. Simulations and measurements validate the feasibility and accuracy of the developed models and formulas. Furthermore, PD propagation simulation experiments are conducted in PSCAD to quantitatively evaluate the effects of network parameters and structures on PD signal features. The results reveal several crucial PD propagation characteristics in MV three-phase overhead distribution networks.

A fully automatic tool for extracting PD signals from noises is developed. The proposed solution addresses the challenges of field noise filtering and hardware selection. On one side, field noise has unavoidable detrimental effects on monitoring, thus demanding a clever and robust solution. On the other hand, the implementation of limited resource hardware is a crucial requirement for a practical design, allowing to reduce production costs. This work describes an adaptive and efficient PD de-noising algorithm based on the improved spectral decomposition of the noisy PD signal. PD pulses are accurately extracted from the noisy signal by cleverly selecting the dominant components via a low-rank singular value decomposition of the time-frequency spectrogram of the signal, thus reducing the size of the involved matrices and the computational complexity. The performance of the proposed de-noising algorithm is first demonstrated on a synthetic PD signal and compared with state-of-the-art alternative techniques implemented on three embedded systems commonly used for PD monitoring. Finally, the proposed approach's strength and effectiveness are further validated on experimental data, demonstrating its better de-noising performance in improving the sensitivity and accuracy of on-site PD measurement.

An improved double-sided (or multiple-sided) PD detection and localization method is developed. Firstly, a specialized high-frequency current transformer with a notch is designed for detecting PD signals online, and a digital compensation algorithm is developed to enhance its performance. Then, an innovative PD localization technique is proposed utilizing an improved

double-sided traveling-wave method. This method boasts two key advantages: precise synchronization of double-sided testing units through the combined use of Global Positioning Systems and a pulse-based interaction process, as well as the integration of a windowed phase difference method that robustly estimates time-of-arrival differences even in environments with low signal-to-noise ratios. Moreover, an algorithm for estimating the PD source location based on statistical mapping of multiple location results is proposed to reduce the uncertainty caused by noise. Further, building upon the double-sided localization method, a multiple-sided location algorithm is formulated to identify the source of PD in radial networks. The effectiveness and reliability of the algorithm are verified through Monte Carlo simulations.

Two system prototypes with different PD diagnosis functions are developed based on the proposed methods and techniques. The first is an online PD monitoring system, including a set of compact PD monitors that can achieve low-cost, flexible, and real-time PD monitoring. The in-house design of the PD monitor is presented, including non-invasive sensing, a field energy harvesting function, a low-power working operation, and reliable networking and diagnosis. The other is a portable PD detection and location system, which outputs more detailed information on PDs, i.e., the PD apparent quantity, the PD source location, and the PD-affected apparatuses. The issues of non-invasive pulse injection, safe signal transmission, and clock precise improvement are addressed in this system. The strengths of the two systems are validated via multiple typical application cases. Furthermore, a cost-efficient PD diagnosis strategy for MV overhead distribution networks is developed via the joint application of the two systems.

Contents

List of Figures

List of Tables

1 Preface

1.1 Background

This section first introduces the partial discharge (PD) phenomenon in medium-voltage (MV) overhead distribution networks, a crucial indicator in the condition-based maintenance of electrical apparatuses. Then, PD diagnosis methods for MV overhead distribution networks are reviewed; it turns out that the traveling-based PD detection method shows great potential in achieving high-efficient and accurate PD diagnosis of widely distributed electrical apparatuses. Furthermore, we summarized four crucial technical issues in the traveling wave-based PD diagnosis method that impede its further applications for MV overhead distribution networks. These issues will be addressed one by one in this dissertation.

1.1.1 Partial Discharge in Medium-Voltage Overhead Distribution Networks

1）Medium-voltage overhead Distribution Networks

The power distribution system is designed to deliver electric power to customers from distribution substations. The most common distribution system consists of radial circuits (feeders) operating in an MV range between 2 kV and 35 kV. These feeders can be overhead (in rural areas), underground, or a combination. The overhead distribution networks are currently most widely used in the MV distribution system due to their low cost and ease of installation. For example, more than 80 percent of components in the MV distribution system are overhead in China, and the length of 10-kV distribution overhead lines in China exceeded 4,370,800 km in 2022, according to a report by Nat. Energy Admin. China.

The MV overhead distribution network consists of transmission lines and series or parallel power apparatuses, the latter being feeder breakers, insulators, arresters, transformers, etc., as shown in Figure 1-1. Before the 21st century, utilities worldwide used bare conductor lines to distribute electric power in the MV overhead network. Nowadays, the bare conductor lines have been gradually replaced by covered conductor (CC) lines due to their higher reliability, which is given by a cross-linked polyethylene insulation system [1][2]. The contact of an object (e.g., a leaning tree) on a single or two phases does not lead to a short circuit fault, thus reducing power interruptions [3][4].

2）Insulation Failures

As the service period of the MV overhead distribution network increases, diverse weather conditions, falling trees, and many other environmental stresses can weaken its insulation system and eventually lead to failure, disrupting customers' daily activities and harming the economy [5][6]. Figure 1-2 collects some common insulation failures that occurred in overhead lines and alongside apparatuses. Sometimes, the failure can be

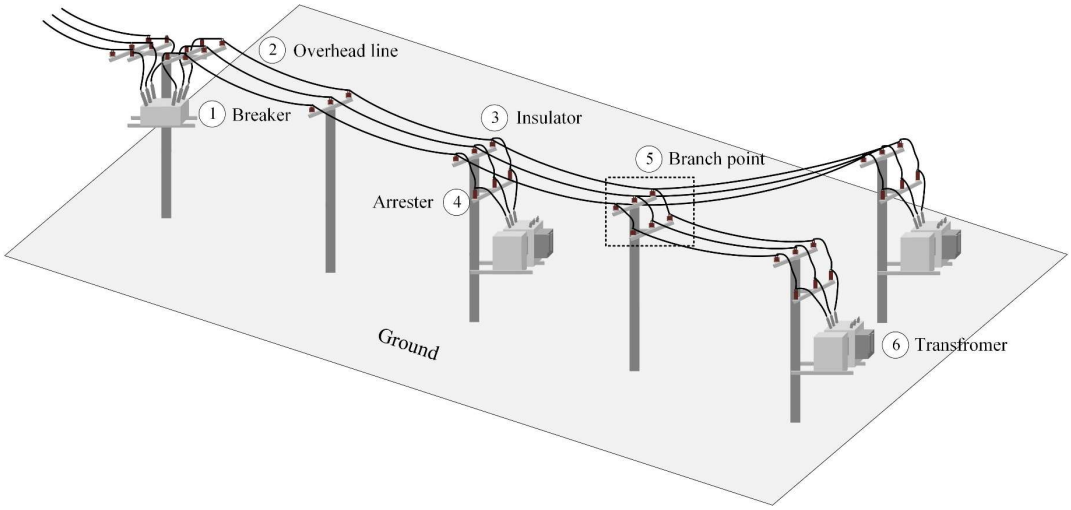

Figure 1-1 Schematic diagram of a feeder in MV overhead distribution networks

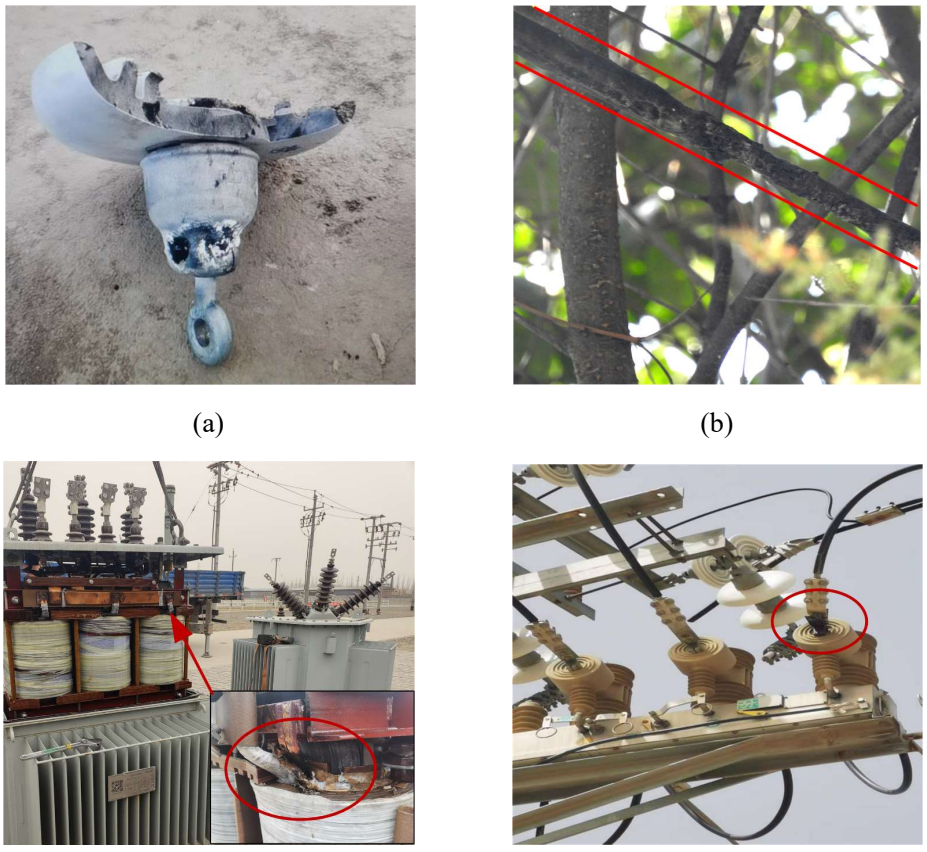

(a) (b)

(c) (d)

Figure 1-2 Insulation failures occurred in (a) an insulator, (b) an overhead covered conductor line, (c) a transformer, and (d) a breaker.

catastrophic, especially in forest areas, as forest fires can inflict significant economic damage much higher than the cost of the power apparatuses [7][8].

To reduce the influence of insulation failures, Chinese power utilities have started to construct a smart grid since 2009 [9][10]. The investment in MV overhead distribution networks is increasing yearly; meanwhile, higher power supply reliability is required. The

stability and reliability of the power distribution system can be quantified by two indices: the System Average Interruption Duration Index (SAIDI) and the Customer Average Interruption Duration Index (CAIDI) [11]. In the modern smart grid, SAIDI and CAIDI are maintained by the distribution automation system, which can quickly isolate the faulty area via smart breakers to minimize the influence of power outages [12][13][14]. However, many application experiences show a bottleneck for further improvement of the distribution automation system to improve SAIDI and CAIDI because it can never prevent failure. According to a 2022 power outage investigation by Shannxi Electric Power Research Institute, insulation failures of MV overhead distribution networks with a distribution automation system were still the main contributors to reducing SAIDI and CAIDI. Therefore, additional techniques for insulation fault diagnosis are required.

Many papers have been published on post-fault diagnosis techniques, including offline time (or frequency) domain reflectometry and online fault (transient) detection and location methods [5][6][15][16][17]. Indeed, the post-fault diagnosis tools can speed up the process of fault identification and isolation and power supply restoration. However, in principle, post-fault diagnosis can never prevent a failure (as the same deficiency of the distribution automation system) since it is essentially a reactive approach after the failure, resulting in its limited capacity to maintain SAIDI and CAIDI at a high level.

3）Condition-based Maintenance

An alternative solution is to perform condition-based maintenance on the MV overhead distribution network. Condition-based maintenance is a strategy to optimize maintenance and operation actions from the asset/grid management side by evaluating the operating condition indicators of electrical apparatuses [18][19], e.g., their insulation integration. The basic idea in condition-based maintenance is to predict possible failures of electrical apparatuses via their present or past condition, thus preventing a fault, as shown in Figure 1-3. It is a proactive approach to electrical apparatus maintenance. Therefore, condition-based maintenance is expected to be another promising "key" further to improve the stability and reliability of the power system.

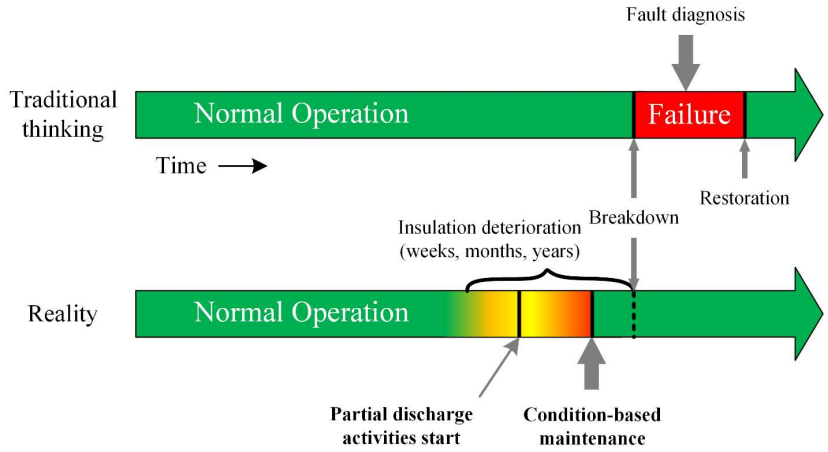

Figure 1-3 Paradigms of reactive (past) and proactive (present) insulation diagnosis strategies for MV overhead distribution networks.

Partial discharge (PD), a phenomenon able to reveal or cause the incipient failure of electrical apparatuses, plays a fundamental role in condition-based maintenance [20][21][22][23]. PD is a localized electrical discharge that only partially bridges the insulation between conductors and can or cannot occur adjacent to a conductor [20]. PD does not immediately cause an insulation breakdown, and there is always a time interval of several days, months, or years between PD and failure. Thus, regular PD diagnosis can predict upcoming insulation failures, enabling electric utilities to promptly repair or remove the defective apparatus [22][23].

4）Partial Discharge Defects

The PD types are diverse in MV overhead distribution networks, which depends on their locations, the surrounding environment, and materials. Figure 1-4 collects some examples of PD defects in insulators, CC lines, and transformers. More details of the PD defects are described as follows.

One common cause of PD in overhead distribution networks is pollution on the surface of insulators, as shown in Figure 1-4(a). When the accumulation of pollution reaches critical levels, it can initiate PD events that can lead to complete insulation failure. Pollution buildup can occur due to various factors such as dust, salt, industrial emissions, and biological growth such as algae and lichens [24]. As a result, maintaining insulators' cleanliness is crucial to prevent pollution-induced PD. Moisture ingress is another factor that can lead to PDs [25]. High humidity conditions increase the likelihood of moisture buildup on insulator surfaces, leading to increased PD activities. Additionally, rain, snow, and ice accumulation on the insulator can result in PD events due to the dielectric breakdown of the insulation material [26]. Another factor that can cause PD is lightning strikes. Lightning strikes produce high-voltage impulses that can lead to partial discharge events of the insulation material [27]. Moreover, some voids, cracks, and punctures can occur in the insulator due to substandard manufacturing, construction, and environmental factors, e.g., windstorms. These events can cause insulation damage and even complete line failures. Insulation aging is another significant factor that can lead to PD in the insulation material [28]. Over time, the insulation material used in overhead lines can degrade due to exposure to ultraviolet radiation, temperature cycling, and chemical aging. As the insulation degrades, voids and other defects can form, leading to increased PD activities.

Another reason for PDs in overhead distribution networks is leaning trees (see Figure 1-4(b)), as tree branches or trunks leaning against or touching the conductors can introduce localized electrical stress and insulation damage [29][30]. This can lead to PD and eventual insulation failure. The presence of leaning trees near overhead lines is a common occurrence, especially in areas with dense vegetation or strong winds. As trees sway and move, they can touch or come too close to the conductors, causing electrical arcing and insulation damage. Tree branches or trunks that lean against the conductors can also cause mechanical stress, leading to insulation failure over time.

PD could also occur in the alongside apparatuses in series or parallel. Taking the MV transformer as an example, insulation aging is a significant cause of PD in MV transformers.

Over time, insulation material can degrade due to high temperatures, humidity, and chemical contamination [31]. The formation of voids, cracks, and other structural degradations within insulating material can cause electrical stress and PD activity, as shown in Figure 1-4(c). Contamination is another common cause of PD in MV transformers [32]. Contaminants such as moisture, dust, or metallic particles can be deposited on the insulation surface, creating a path for PD. These contaminants can also contribute to the degradation of the insulation material, further increasing the risk of insulation failure and PD activity. Bubbles or voids within the insulating oil of transformers are another reason for PDs [33]. Bubbles can form due to improper installation, transformer aging, or insulating materials degradation. These voids create regions where the electric field strength exceeds the breakdown voltage of the surrounding insulation, causing partial discharge events. Regular maintenance and monitoring, along with proper design and insulation materials, are crucial in preventing bubble-induced partial discharge and ensuring the reliable operation of transformers. Other factors, such as mechanical vibration, electrical overloading, and voltage surges, can also contribute to PD activity in MV transformers [34].

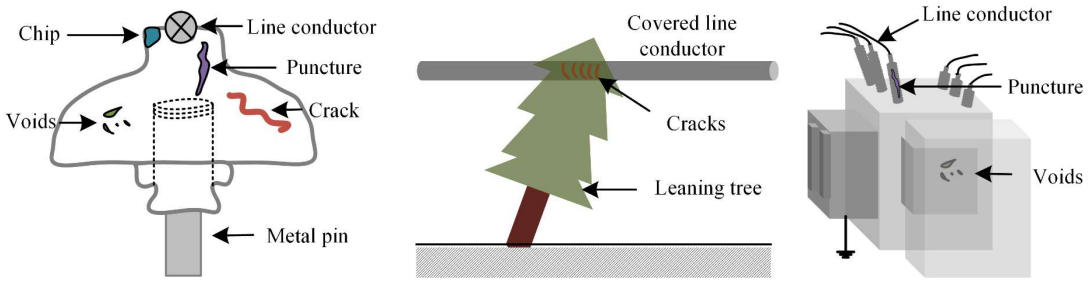

Figure 1-4 Examples of PD defects in MV overhead distribution networks: (a) PDs in insulators; (b) PDs in covered conductors caused by a leaning tree; (c) PDs in alongside apparatuses (e.g., a transformer).

1.1.2 Partial Discharge Diagnosis Methods

Traditionally, utilities use the radiating wave-based detection method to diagnose PD activities of the MV overhead distribution network. This method achieves PD diagnosis by detecting electromagnetic or ultrasonic radiations from the PD source. It mainly includes ultraviolet [35], radio frequency [36][37][38], and ultrasonic detections [39][40]. The ultraviolet-based device can detect external or surface PDs from lines or insulators [35]. However, its price is costly, impeding its further application. The radiofrequency antenna is used to detect the internal or external PDs in insulators, arresters, and transformers [37][38], but its reliability is often affected by field noise interference, causing it to be hardly used by utilities. Unlike the previous two methods, the ultrasonic-based PD inception method is widely used due to its low cost and good anti-interference ability [39]. Currently, utilities termly dispatch technicians to patrol the overhead distribution network with ultrasonic-based devices (e.g., the ultrasonic camera [40]) to seek PDs. Many application cases show that the information obtained via ultrasonic-based devices avoided many failures. However, accumulated field experience and data reveal two fundamental limits of the ultrasonic-based

PD inception. On the one hand, this method is insensitive to the PDs that occur inside the electrical equipment because the energy of the ultrasonic PD signal attenuates sharply when traveling from a solid medium to a gas medium. On the other hand, this method is time-consuming and laborious for the vast distribution network (i.e., with the size of several or tens of kilometers), primarily due to its limited effective detection range, i.e., a few tens of meters.

Since 2008, the traveling wave-based approach has been first explored to overcome these fundamental limitations of the radiating wave-based method to detect PDs in CC lines [41]. The technique achieves PD measurement by detecting the PD traveling wave current or voltage signals coupled to transmission lines from the PD source. The apparent advantages of the traveling wave-based method are summarized and listed as follows:

(1) It can detect internal and external PDs in all power apparatuses within the effective detection range of the traveling wave detector.
(2) Its coverage (e.g., several kilometers) is significantly more extensive than that of the radiating wave-based method (e.g., a few tens of meters), as shown in Figure 1-5. This allows it to detect PD at a remote distance, thus avoiding time-consuming and laborious line patrols.
(3) The data can be continuously registered via online traveling wave detectors, so time-related information, such as variation of PD activity in time and the effects of load fluctuation, are detected. Also, the detectors can capture PDs occurring shortly before failure.
(4) PD localization based on the traveling wave-based method can enable quick identification of the exact defective power apparatuses in the widely distributed MV overhead distribution network.

The last point may be the most crucial argument from both technical and practical perspectives. On the one hand, the PD location is a natural anti-interference information. A PD location map can reveal the statistical characteristics of the location concentration of PD events. Noise interferences hardly have the same features. On the other hand, since the MV overhead distribution network is widely distributed and has lots of series and parallel power apparatuses, it is almost impossible to inspect them individually. This problem is particularly prominent in rural, forest, and farm areas without sidewalks. With the information on PD locations, utilities can know where to perform maintenance and which apparatus is defective. This can significantly improve their efficiency and save many human and financial resources.

Moreover, it is essential to point out that although many traveling wave-based PD diagnosis methods have been successfully applied for underground cables, which have a similar physical structure to the overhead line, these methods are difficult to use for the MV overhead distribution network for the following reasons. The traveling wave-based PD diagnosis of cables includes offline PD testing and online PD monitoring. For offline PD testing, a capacitive coupler connected to the line detects PD signals [43], and the time domain reflectometry method is used to locate the PD source [44]. The offline PD testing

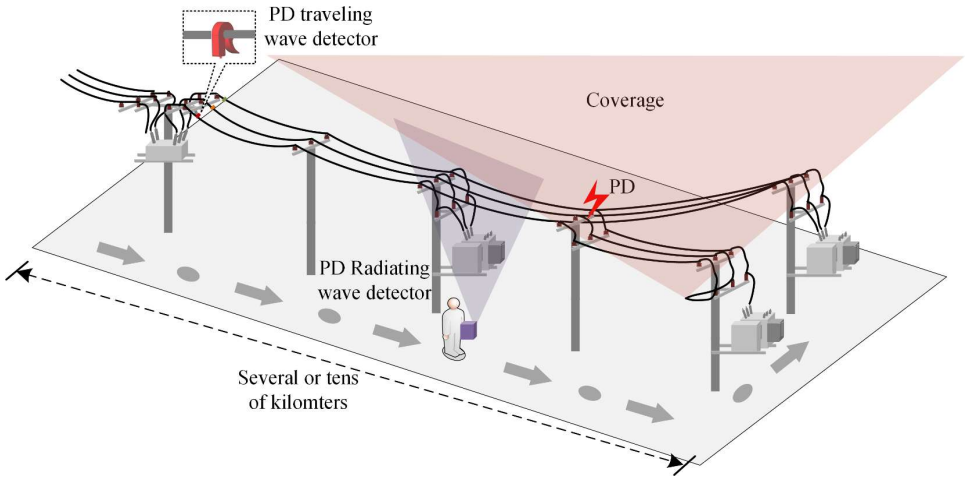

Figure 1-5 Coverage comparison between the traveling wave-based and radiating wave-based PD diagnosis methods

requires an additional power supply, e.g., a damped oscillatory wave system [45], a series resonant system [46], etc. This is feasible for MV cables in cities with lanes for transporting the heavy power supply system. However, it isn't easy to use for the MV overhead distribution network, which is always located in rural or forest areas without lanes. For online PD monitoring, non-invasive PD sensors (e.g., high-frequency current transformers mounted on the earth wires of cables [47]) are used to detect the PD signal; time domain reflectometry or arrival time analysis methods are used to locate a PD [48]. Based on the above techniques, some commercial PD diagnosis devices for MV cables have been presented, such as the Oscillatory Wave PD Detection System [49], Smart Cable Guard [51], PDscope [52], etc. Unlike underground cables, the overhead distribution network has no earth wires, more complex structures, and changeable transmission line parameters. This leads to many issues in applying the existing PD diagnosis techniques of cables to MV overhead distribution networks, e.g., magnetic saturation problem of high-frequency current transformer, safety issues of PD sensor installation, changeable propagation velocity, more severe noise interferences, etc.

1.1.3 Issues in Traveling Wave-based Partial Discharge Diagnosis

The traveling wave-based PD detection of MV overhead distribution networks involves several crucial issues that must be addressed for accurate and reliable monitoring. These issues include PD propagation, noise reduction, PD detection, and PD localization, which is illustrated in Figure 1-6 and explained as follows:

PD propagation issue: PD signals generated in an overhead distribution network may propagate along the conductors and other equipment in series or parallel. However, the propagation characteristics of PD signals may vary due to the complex nature of the overhead line structures, including three-phase conductors, multiple branches, splices, and connections. This makes it challenging to detect the PD, determine the exact location where the PD originated, or distinguish between different PD sources. Therefore, a comprehensive study of the PD propagation characteristics is required.

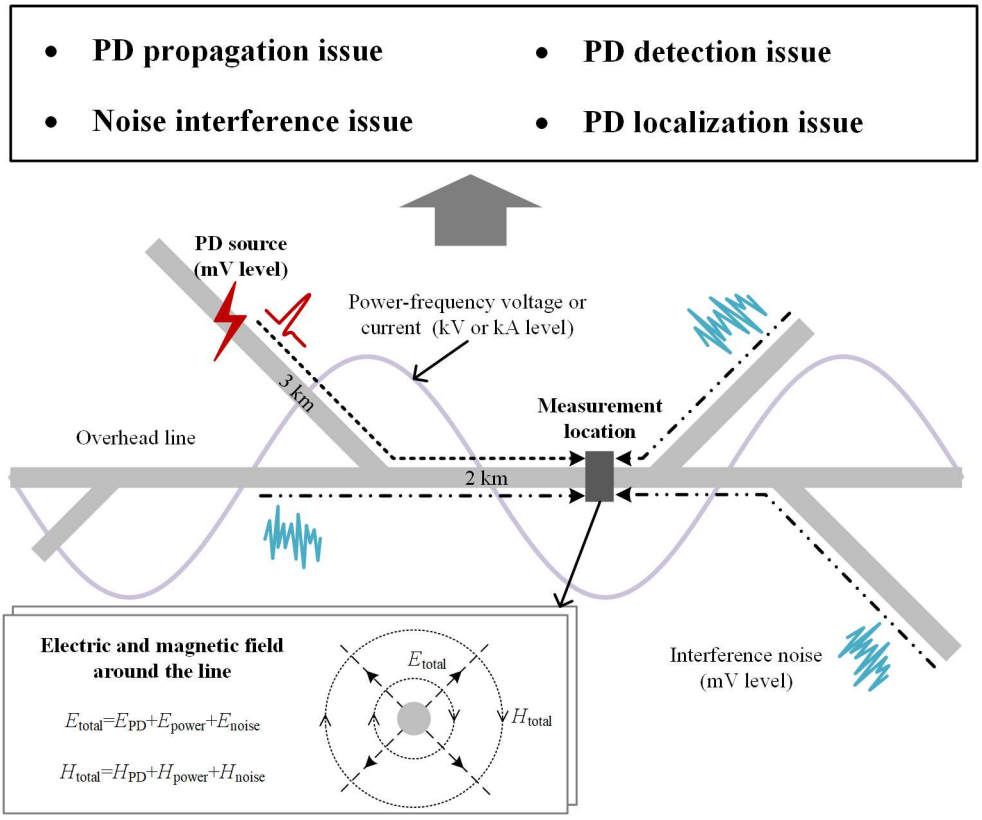

Figure 1-6 Illustration of the issues in traveling wave-based PD diagnosis of MV overhead distribution networks

Noise interference issue: PD detection of overhead distribution networks is subjected to various sources of electromagnetic interference and environmental noise, such as carrier communication, radio communication, high-order harmonic, ground noise, rand noise, etc. These external factors can introduce noise into the PD measurement, making it difficult to differentiate between genuine PD signals and background noise. Effective noise reduction techniques and signal processing algorithms are necessary to minimize the effect of external noise and improve the detection sensitivity.

PD detection issue: Detecting and capturing PD signals in MV overhead distribution networks can be challenging due to the relatively low magnitude of these signals compared to the background noise. PD sensors or detectors should possess high sensitivity to detect weak PD signals accurately. Additionally, the sensors must withstand the influence of the high-amplitude power-frequency voltage or current, such as the magnetic saturation problem caused by power-frequency current or the insulation problem caused by power-frequency voltage.

PD localization issue: Accurately localizing the source of the PD within an overhead distribution network is crucial for effective maintenance and repair. However, achieving precise PD localization can be challenging due to the complexity of the network's distributed nature and the surrounding infrastructure. Location techniques typically rely on analyzing the characteristics of PD signals at different locations to estimate the source location. However, this requires a sufficient number of sensors strategically placed throughout the system and robust algorithms for accurate localization.

In summary, addressing these problems involves advancements in sensor technology, signal processing techniques, data analysis algorithms, and modeling approaches. Ongoing research and development aim to improve detection sensitivity, reduce noise interference, enhance PD localization accuracy, and provide more comprehensive monitoring solutions.

1.2 Related Research Work

This section reviews the state-of-the-art solutions to the four issues of traveling wave-based PD detection raised in the last section. These issues are discussed one by one in the following subsections, along with analyzing the deficiencies of the state-of-the-art solutions and exploring the direction of improvement.

1.2.1 Partial Discharge Propagation

Studying the propagation characteristics of PD in MV overhead lines is crucial. It helps locate PD sources, differentiate PD types, assess defect severity, and validate diagnostic methods. Understanding PD propagation behavior allows for effective PD diagnosis, facilitating proactive maintenance. In 2007, Hashmi *et al*. introduced a model for analyzing overhead CC lines [53]. They calculated the frequency-dependent distributed transmission line parameters, wave propagation characteristics, and characteristic impedance of the CC line. The model was then utilized to simulate PD propagation characteristics in the Electromagnetic Transients Program (EMTP)/Alternative Transients Program (ATP). This simulation helped determine the optimal sensor locations for reliable PD detection results. Then, they compared the difference between overhead CC lines and underground cables via the time-domain reflection technique [54]. The result showed that the high-frequency attenuation coefficient of the overhead CC line is significantly less than that of cable. This means the PD signal can travel farther on overhead lines than cables. In 2022, a simulation study conducted by Lijun Zhou *et al.* focused on the propagation characteristics of PD signals using measured data [55]. Their findings indicated several vital factors that can influence the propagation characteristics of pulse currents. These factors include the pulse current frequency, the covered conductor’s height above the ground, and the conductor’s phase distance and cross-sectional area. However, the above studies only investigate the PD propagation characteristics of single-phase overhead lines, and the commonly used three-phase overhead line is not discussed. In 2021, Fernando *et al.* conducted a mathematical study on the traveling wave propagation phenomena on three-phase power lines under fault conditions [56]. This work uses a multiple transmission line model to study the fault travel waves in three-phase power lines. They demonstrate that the obtained mathematical formulas for fault diagnosis are reliable for aerial travel waves. To simplify the calculation, the effects of alongside apparatuses are ignored in the developed models. However, the models and methods cannot be used for PD signal analysis in MV overhead distribution network since the central frequency of PD signal (i.e., several MHz) is much larger than that of fault signal (i.e., few tens of kHz), leading to the effects of the alongside apparatuses non-negligible.

In summary, no reports or publications addressed a systematic comparative study on PD (i.e., an MHz-level signal) propagation characteristics study on MV three-phase overhead distribution networks, especially considering the effect of the alongside towers.

1.2.2 Partial Discharge De-noising

On-site PD measurements are susceptible to field noise interferences, with unavoidable detrimental effects of white noise and discrete spectrum disturbance [57][58]. Therefore, de-noising is an essential step in on-site PD measurement. However, de-noising PD signals (in resource-limited monitoring devices) is very challenging, and no suitable solution is available, primarily due to the following three critical reasons. The first one is that the magnitude of field noises (i.e., mV level) is often the same as or even higher than that of PD signals [59], causing PD signals to be wholly drowned in noises. The second one is that the PD waveforms are always various, which depends on the size, location, and materials of the PD source and the transfer functions of the PD propagation path and used PD sensors [60][61]. Such uncertainties on PD signal waveforms pose great difficulty setting the algorithms' proper de-noising parameters. The last and most important one is that the hardware resources in the PD monitoring devices are minimal, requiring the embedded PD de-noising algorithms to have high computational efficiency.

In the last two decades, many papers have been published on alternative pulse signal (e.g., PD) de-noising approaches, being wavelet transform (WT), empirical mode decomposition (EMD), local mean decomposition (LMD), variational mode decomposition (VMD), Machine learning (ML), and singular value decomposition (SVD). Table 1-1 lists the deficiencies of the methods and detailed discussions of these methods are described as follows.

Table 1-1 Comparison of the state-of-the-art PD de-noising methods

Methods	Challenges		
	Uncertain PD waveforms	High-level noise	Limited computing resources
WT [57]	×	√	√
AWT [63]	√	√	×
EMD [67]	√	×	√
LMD [68]	√	×	×
VMD [69]	√	×	×
ML [72]	√	×	×
SVD [74]	√	×	×
ASVD [75]	√	×	×
WT+SVD [78]	√	√	×
EMD+SVD [79]	√	√	×
S-SVD [81]	√	√	×

In [62][63][64][65][66][67][68], WT has proven to have an outstanding PD de-noising performance for extremely noisy signals if the mother wavelet and decomposition levels are appropriately selected. Prior knowledge of the PD signal's characteristics is required to determine the mother wavelet and decomposition level, which is always challenging in the field due to the variable waveforms of PD signals. In [69] and [70], iteration-based algorithms are proposed to automatically determine the optimal mother wavelet and decomposition level. Despite these methods' excellent automatic features, a common unfavorable aspect is their low efficiency, which means sizeable computational time. In [71] and [72], the adaptative EMD and LMD algorithms are proposed. Their main advantage is that no prior knowledge is required, but they suffer from mode mixing problems, possibly leading to signal distortion. In [73] and [74], ensemble EMD and LMD are developed to overcome the problem, but they require many iterative cycles and calculations. In [75], VMD is proposed to address this issue specifically, and it has successfully been applied for de-noising PD or fault signals [76][77]. However, the success of VMD depends highly on the pre-set parameters, including the mode number and bandwidth control parameter. [78] and [79] explore using the ML method for PD de-noising, which is proven to automatically extract PDs in various noise environments. However, ML requires lots of labeled data samples to train the de-noising model, which is impossible in on-site PD measurements.

To remedy these deficiencies in the above de-noising approaches, the non-parametric and self-adaptive methods based on singular value decomposition (SVD) have been explored in recent years. In [80], Abdel-Galil et al. conducted a pioneer study of de-noising via SVD. In [81], an adaptive principal components selection algorithm is developed to automate the SVD-based PD de-noising process. In [82] and [83], some fast SVD algorithms are developed by reducing the rank of the input matrix to be decomposed. In [84] and [85], some hybrid methods combining SVD with WT or EMD are presented, where SVD is used to remove severe discrete spectrum noise components with significantly larger singular values. In all the above papers, the SVD-based de-noising scheme is done as follows: first, a noisy PD signal is embedded into a Hankel matrix; then, applying SVD to the Hankel matrix results in a singular value vector and multiple components; finally, the components with larger singular values are used to reconstruct the noiseless PD or the unwanted discrete spectrum noise that needs to be subtracted. However, the investigation in [86] shows that the de-noising scheme performs poorly for signals with a very low signal-to-noise ratio. In this case, several floors appear in the singular value plot, which makes it very difficult to select the optimal value of the number of dominant contributions. In addition, when the singular values of the PD signal and the discrete spectrum noise have the same magnitude, the de-noising scheme can hardly differentiate them. In [87], a PD de-noising based on the so-called generalized S-transform and module time-frequency matrix is proposed. In this approach, the de-noising performance strongly depends on the accuracy of the estimated frequency of the discrete spectrum noise, which requires high-frequency resolution of the S-transform and thus results in a high-rank matrix, leading to sizeable computational time.

In summary, no solution can simultaneously fix the three critical problems in on-site PD

de-noising, i.e., high-level noise, variable waveforms of PD signals, and limited computing resources.

1.2.3 Partial Discharge Detection

Many PD detection techniques, including Rogowski coils [41][88][89], ultra-high frequent sensors [90], capacity dividers [91][92], and Boni-Whip antenna [93], were presented and proven to detect PD signals on overhead lines effectively. Hashmi *et al*. pioneered the study of detecting PDs produced by leaning/falling trees using Rogowski coils [88]. However, further application of the Rogowski coils is impeded due to its safety problems in installation and signal transmission. To overcome this problem, Fernando *et al*. studied the propagation characteristics of high-frequency components of PD signals on a CC line. They demonstrated that ultra-high frequent sensors can be effective in remotely detecting PDs [90]. Misák *et al*. present using three-phase capacitive detectors to identify PD defects caused by leaning trees [91][92]. For economic reasons, they recently replaced their capacitive sensors with a Boni-Whip antenna [93]. In [94], a method to identify the traveling direction of PD pulses on CC lines is implemented by a hybrid sensor that consists of Rogowski coils and a capacity coupler. Although the above PD detection methods have been proven to be effective in detecting PD in MV overhead distribution networks, the magnitude of PD cannot be quantitatively assessed due to the narrow frequency passband of the used PD sensor, as the frequency range of typical PD pulses is direct current to tens of MHz.

Many PD recognition methods for CC lines have been developed in recent years based on the detection techniques. In [92], statistical methods based on the frequency of peaks in PD patterns are proposed to identify whether the measured CC line has faults or no faults. In [95], the Random Forest Algorithm is used to classify de-noised PD signals from CC lines. In 2018, a public dataset containing many PD signal measurements of CC lines was published on Kaggle [96]. Using the dataset, many CC line fault identification methods based on PD patterns are proposed, such as the TSD-LSTM method [97], CNN-LSTM method [98], and DWT-LSTM method [99]. In [100], the PD-related pulse shape characteristics are used as referential patterns, and a novel machine learning model is proposed for early-stage CC fault detection. In [101], an Edge computing technique is developed to detect PD in overhead distribution networks based on deep neural models. However, all the PD detection methods require many labeled samples to train the models.

In summary, the above PD detection methods cannot quantitatively estimate PD magnitude, and they need many labeled samples for accurate PD recognition, which is almost impossible in field measurement. Therefore, improvement in PD detection of MV overhead distribution networks is required.

1.2.4 Partial Discharge Localization

Traveling-wave (TW) methods, which are the most popular PD location method for power lines, fall into three categories: electromagnetic time reversal (EMTR), time domain reflection (TDR), and arrival time analysis (ATA). Comparison of these methods is listed as Table 1-2, and detailed discussions of these methods are described as follows.

Table 1-2 Comparison of the classical location methods

Challenges	Methods		
	EMTR [95][96]	TDR [97]	ATA [99]
Complex signal reflections	√	×	√
Uncertain line parameters	×	√	√
Complex network structure with multiple branches	×	×	√
Uncertain signal propagation velocity	√	×	×
Synchronization problem	√	√	×
Noise problem	×	×	×

EMTR is a technique used for precise localization of PDs in power lines, e.g., cables [102][103][104][105]. It involves capturing PD signals, reversing them in time, and returning them to the system. The reversed signals converge at the PD source, allowing its location to be determined accurately. However, electromagnetic time reversal has certain limitations. It requires an accurate power line model, making it sensitive to modeling errors. Additionally, reflections and multipath effects can distort the reversed signals, affecting localization accuracy. TDR locates PDs by calculating the difference of TOAs between a pulse and its reflection at the same end [106]. ATA finds PDs by calculating the difference of TOAs of the pulses at double or multiple ends [107]. The complex structures of 10-kV CC lines produce many impedance discontinuities, leading to undefinable reflections. This causes TDR to fail to locate PDs in CC lines. In contrast, the double-sided TW method based on ATA is immune to the reflections, so its ability to locate PDs in CC lines has been validated [108]. However, the difficulty in synchronizing the PD detectors has posed a challenge for the double-sided TW method.

Global position system (GPS) is the most widely used synchronization technique, but its synchronization precision fluctuates and is affected by environmental factors. An alternative synchronization technique was explored in previous papers [109][110]. This technique uses injected pulses to synchronize double-sided PD detectors in CC lines, inspired by the pulse synchronization technique presented in [111]. However, the in-field reliability of this pulse synchronization technique is low because it often fails in a noisy environment where PD pulses or interferences have the same amplitude as the injected pulses.

The physical parameters of CC lines (e.g., structure and height) and their surrounding environment are complex and diverse. This means that signals propagate at various velocities in CC lines, which may generate non-negligible PD location errors [88][112].

Reference [112] describes a multi-end correlation-based method adapted to eliminate varying velocities' effect on PD localization in CC lines. However, the accuracy of this method could be significantly reduced when the waveform of PD pulses in CC lines is distorted by high-frequency attenuation or signal overlapping.

Different electromagnetic interferences can significantly reduce the PD localization accuracy by influencing the determination of the accurate time-of-arrivals of the PD pulses in online PD measurement. In [113], representative time-of-arrival estimate methods were summarized for PD localization of cables, and the energy criterion and phase difference methods were shown to be more accurate than the threshold method, Akaike information criterion, and Gabor centroid method. In [114], the energy criterion method was also more accurate than the peak method, considering the high-frequency attenuation and dispersion characteristics of the PD signals in cables. In [115], the phase difference method was successfully applied in the single-sided PD localization of cables. All the above-presented methods did not deal with noise problems, so they may fail to be used for online PD localization in overhead lines as various noises may couple to the lines from the controlling and switching devices.

In summary, the existing solutions cannot be used for reliable and accurate PD localization of MV overhead distribution networks, primarily due to the synchronization problem, the uncertainty of the signal propagation velocity of overhead lines, and noise interferences.

1.3 Overview of This Dissertation

1.3.1 Main Work of This Dissertation

This dissertation aims to address the technical problems that impede the further application of the traveling wave-based PD diagnosis method to MV overhead distribution networks, to develop advanced algorithms and tools for PD detection and localization. Most of the content focuses on PD signal analysis, subdivided into propagation characteristics study, noise reduction, signal detection, and source localization. To that end, two measurement devices and a diagnosis strategy are developed for the MV overhead distribution network based on the proposed methods and algorithms. These contributions are as follows:

A multiple conductor transmission model is built in PSCAD to analyze the frequency-dependent wave propagation characteristics (attenuation, dispersion, phase constant, and propagation velocity) of three-phase overhead distribution lines. This model considers the influence of alongside apparatuses (e.g., insulators, transformers, etc.). The results can be applied to designing and deploying PD sensors over the entire MV overhead distribution network range.

A fully automatic tool for PD de-noising is developed. The proposed de-noising scheme can adaptively reduce, selectively, both the white noise and the discrete spectrum noise in all the considered (three representative types) PD pulses. Furthermore, this tool is further

improved to reduce its computational complexity, allowing it to be implemented in an embedded system with minimal computational resources. A comprehensive comparison of the proposed algorithm and other state-of-the-art alternatives proves its superior de-noising performance and computational efficiency.

A special notched high-frequency current transformer is developed to overcome the magnetic saturation problem caused by the vast power-frequency load current with little sacrifice in sensitivity and bandwidth. To simplify the design and complex parameter tuning of the high-frequency transformer, a digital compensation algorithm is proposed to improve the transfer characteristic of the developed high-frequency transformer. This allows us to evaluate the PD more accurately, e.g., PD discharge magnitude estimation.

An improved double-sided PD location method is developed. The process is driven by a hybrid synchronization technique, which integrates a pulse-based interaction mechanism and a global positioning system (GPS). The proposed solution offers two benefits. It has the inherent feature of being immune to varying physical parameters of the transmission line, and it has been proven to deliver improved accuracy concerning conventional GPS-based location methods. Based on the technique, a multiple-sided PD location algorithm is further developed for PD localization of MV overhead distribution network with multiple branches.

A windowed phase difference method is proposed to robustly estimate the time-of-arrival (TOA) difference between the noisy PD pulses collected by the detectors in a low signal-to-noise ratio environment. Specifically, this method is immune to the discrete spectrum noise that overlaps with the PD signal in the time and frequency domain, which is impossible to achieve by any time-domain, frequency-domain, or time-and-frequency-domain filter methods.

A cost-effective PD diagnosis strategy is proposed for the MV overhead distribution network. Two types of PD measurement tools are developed. The first is a smart, compact detector for online PD monitoring, offering a flexible, cost-effective solution. The other one is a portable live-line PD assessment system for detailed PD diagnosis, which is controllable and equipped with the advanced functions of PD detection and localization.

1.3.2 Dissertation Outline

The dissertation is organized into the following chapters (see Figure 1-7):

Chapter 2 studies the PD propagation characteristics of a three-phase MV overhead distribution network. First, the three-phase overhead line is modeled, the theoretical formula for calculating the transmission line parameters is derived, and the frequency-dependent propagation characteristics are discussed. Second, the effects of the alongside towers are modeled. Finally, the PD propagation simulation is carried out in PSCAD to examine the effect of line parameters on the critical features of the PD signal.

Chapter 3 develops an automatic and adaptive PD signal extraction tool. First, the signal characteristics of PDs and noise interferences are investigated. Second, an automated algorithm for noise reduction is developed. Then, the implementation of the algorithm in resource-limited embedded systems is presented.

Chapter 4 investigates a methodology for online PD detection and localization of an MV overhead distribution network. First, a special notched high-frequency current transformer is developed, and a digital compensation algorithm is proposed to improve its signal transmission characteristic. Second, an enhanced double-sided PD location method is set, and a windowed phase method for TOA difference estimation is proposed. Finally, a multiple-sided PD location algorithm is developed for a radiate overhead distribution network.

Chapter 5 discusses the application of online PD diagnosis in the MV overhead distribution network. First, a smart and compact detector is developed for online PD monitoring. Then, a portable live-line measurement system is designed for advanced PD diagnosis functions, i.e., localization. Finally, a cost-effective PD measurement strategy is proposed.

Chapter 6 contains the summary and conclusions of the research work. The future developments of the present research work are also discussed.

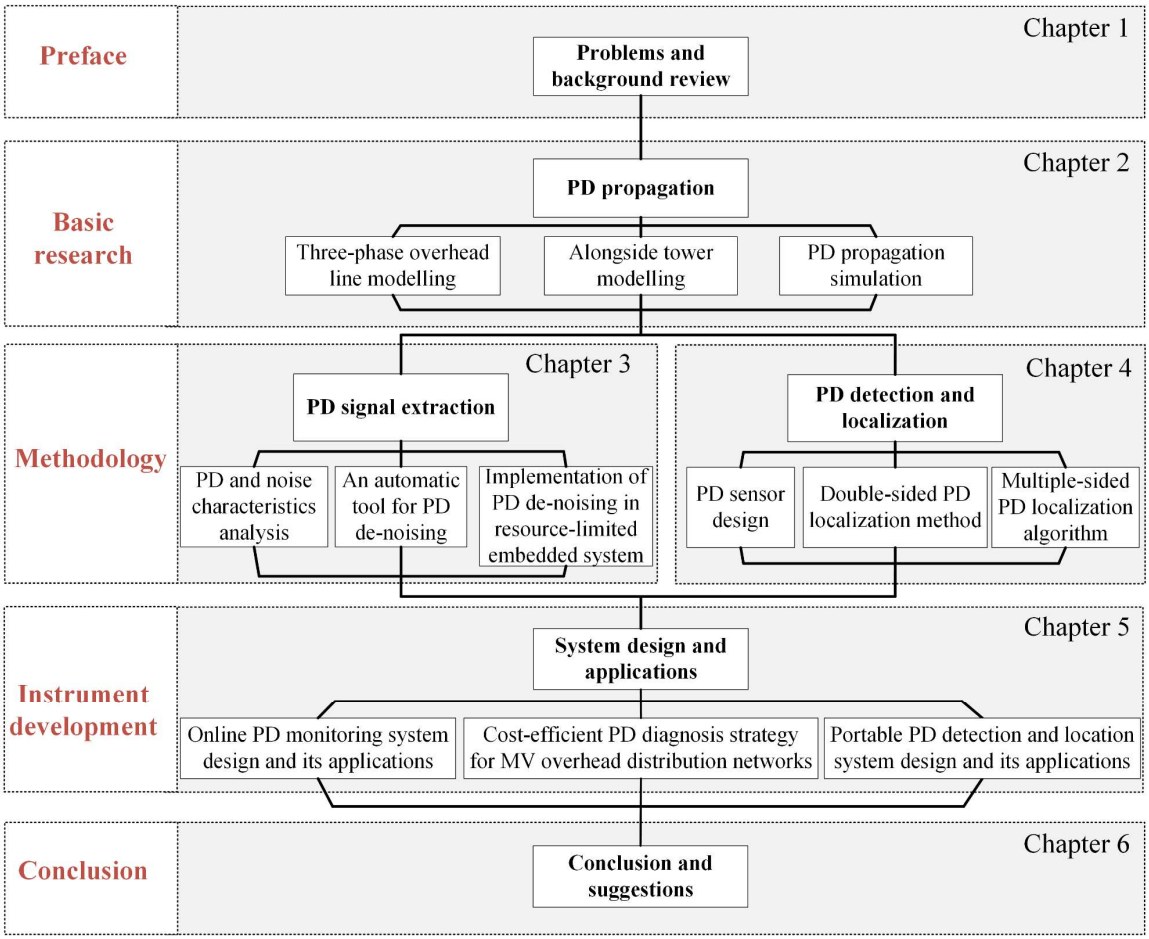

Figure 1-7 Structure diagram of this dissertation.

2 Partial Discharge Propagation in Medium-Voltage Three-Phase Overhead Networks

Partial discharges (PD) may originate in any insulation materials of the MV overhead distribution networks. The discharges induce small pulses on the surrounding overhead conductors, propagating in both directions. Since we can only deploy PD detectors at some locations in the distribution network, the measured PD pulses are altered or re-arranged by the propagation characteristics of the propagation channels in overhead lines. This chapter discusses propagation models of three-phase overhead lines and alongside towers. Simulations and measurements are carried out to verify the models and thoroughly examine the effects of line parameters and structures on PD signal propagation. The developed models allow us to simulate PD signals at any location within an overhead distribution network. The simulation and measurement results provide quantitative and qualitative knowledge on PD propagation in three-phase overhead distribution networks, helping us develop PD detection and location methods and sensor deployment strategies.

2.1 Basic Concepts of Partial Discharge

This section briefly describes the basic concepts of the PD phenomenon, including its cause, model, and characteristics. This builds a primary impression of the PD phenomenon, especially the typical PD signal waveform, helping explain subsequent research. It turns out that the PD signal induced to the overhead line has special time-domain waveform features and a wide frequency spectrum from 0 to tens of MHz.

1）Initiation of Partial Discharge

PD is a localized electrical discharge that occurs within the insulation material of an electrical system. It refers to a concentrated flow of electric charge that does not bridge the insulation barrier between two conductors; instead, it occurs within the dielectric material between them [20]. Although PD defects in overhead distribution networks are diverse, they can be mainly divided into two categories, i.e., internal and surface discharge.

Internal discharge can be caused by the cavities within solid insulation, such as gas-filled voids, delaminations, or cracks in insulators, transformers, etc. In general, the generation of internal PD could be analyzed by considering a cavity in the dielectric material. The cavity is generally filled with air or gas, as shown in Figure 2-1(a). The electric fields inside the insulation (E_{ins}) and in the cavity (E_{cavity}) are given as:

$$E_{\mathrm{ins}} = \frac{D_{\mathrm{e}}}{\varepsilon_{\mathrm{ins}}} \tag{2-1}$$

$$E_{\text{cavity}} = \frac{D_{\text{e}}}{\varepsilon_{\text{cavity}}} \tag{2-2}$$

where D_{e} is the electric flux density in the insulation, $\varepsilon_{\text{cavity}}$ is the permittivity of the air in the cavity, which is approximatively equal to the vacuum permittivity $\varepsilon_0 = 8.85 \times 10^{-12}$ F/m, and ε_{ins} is the permittivity of the insulation, e.g., ceramics insulator with the permittivity from $8\varepsilon_0$ to $10\varepsilon_0$. Since ε_{ins} is much larger than $\varepsilon_{\text{cavity}}$, the electrical field E_{cavity} in the cavity is much larger than E_{ins} in the insulation. As the voltage stress on the whole insulation increases (i.e., E_{ins} increases), E_{cavity} could exceed the inception voltage (e.g., 30kV/cm) of the air in the cavity, leading to the breakdown of the cavity, i.e., generating a PD. Similarly, PD can also occur on the surface of electrical insulation when the tangential field is high, particularly on high-voltage devices' porcelain or polymeric housing. These discharges are called "gliding discharges" or "edge discharges," originating from the edges of the electrode parallel to the dielectric's surface. The PDs produced due to falling trees on covered conductor overhead distribution lines is an example of the surface discharges, as shown in Figure 2-1(b).

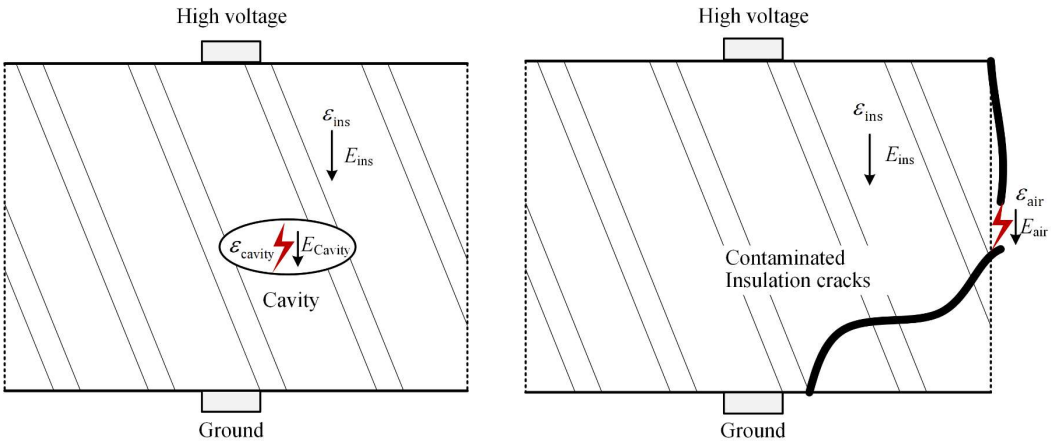

Figure 2-1 Illustration of internal (a) and surface PDs (b) in dielectrics.

2）Three-Capacitance Model and Apparent Discharge Quantity

The three-capacitance model simulates electrical insulation systems' PD phenomena. The three-capacitance model divides the insulation system into three capacitances, i.e., the geometric capacitance (C_A), the interfacial capacitance (C_B), and the trapped charge capacitance (C_C), as shown in Figure 2-2. The first capacitance arises from the physical geometry of the insulation system, while the second refers to the capacitance due to the interface between the insulator and the electrode. The third capacitance represents the charge trapped at the interface due to voltage stress applied to the insulation. This model considers the discharge process due to the interaction between these three capacitances. When a voltage is applied across the insulation system, an electric field is generated that causes PD to occur. The electric field induces charges on the surfaces of the insulation system, resulting

in the formation of charge packets at the interface between the insulator and electrode. These charge packets can then discharge through the trapped charge capacitance, leading to PD.

It is assumed that discharge occurs when the voltage across the capacitance C_C exceeds the inception voltage and ceases to exist when it falls below the extinction voltage, as described in reference [117]. The occurrence of a discharge results in the short-circuiting of C_C, which leads to the rapid flow of current in the circuit due to the voltage difference between C_B and the source. It results in a short transient voltage surge. As depicted in Figure 2-2, the actual charge quantity Q_{real} and the apparent discharge quantity Q_{app} for partial discharge can be computed using the formula presented in reference [117]

$$Q_{real} = \int_0^{\infty} i_{real}(t)\mathrm{d}t = (C_1 + C_2)\Delta V \tag{2-3}$$

$$Q_{app} = \int_0^{\infty} i_{app}(t)\mathrm{d}t = C_1 \Delta V = \frac{C_1}{C_1 + C_2} Q_{real} \tag{2-4}$$

where ΔV is the voltage reduction across the void due to a discharge. The features of charge transfer make it an appealing metric for measuring discharges. These characteristics include:

- Q_{app} is directly proportional to the energy of the discharge.
- Q_{app} is directly linked to the size of the defect.
- Q_{app} can be effortlessly measured with an electrical discharge detector.
- The dangerousness of a discharge is associated with the order of magnitude of Q_{app}, which can be expressed in powers of ten.

In summary, these properties indicate that measuring the charge transfer provides valuable information about discharges and their potential effect on the insulation system.

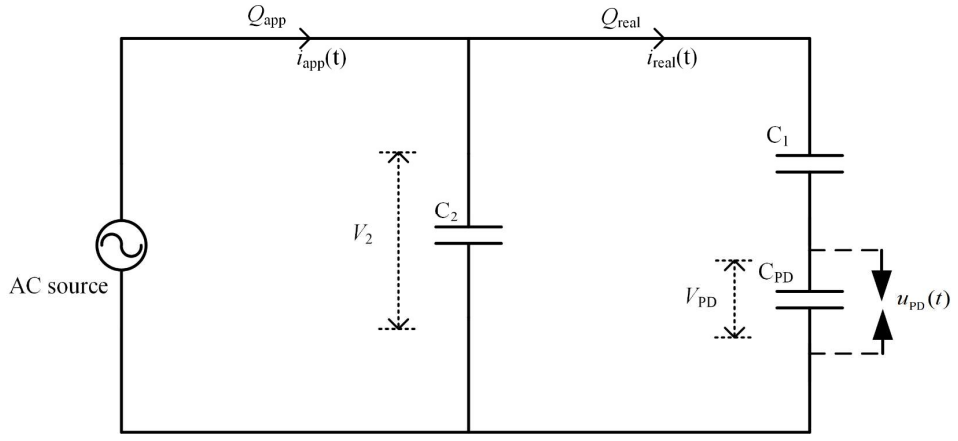

Figure 2-2 Equivalent circuit of the PD process.

3）Partial Discharge Signal Induced to Overhead Lines

The PD process can be approximately equivalent to the Townsend discharge process, in which a current pulse is generated due to the movement of ionized electrons and ions under the stress of an external electric field [118]. The current pulse can induce to the overhead

conductor and propagate in both directions. Figure 2-3 collects time-domain and frequency-domain waveforms of a real PD signal originating from a 10-kV fouling insulator. The PD sensor was placed as close as possible to the insulator to obtain the original PD waveform induced in the overhead line, i.e., without the propagation effect of the overhead line. It can be observed that the measured PD signal has a fast-rising edge and a slow-falling edge, and the frequency spectrum of the PD signal distributes from 0 to several tens of MHz.

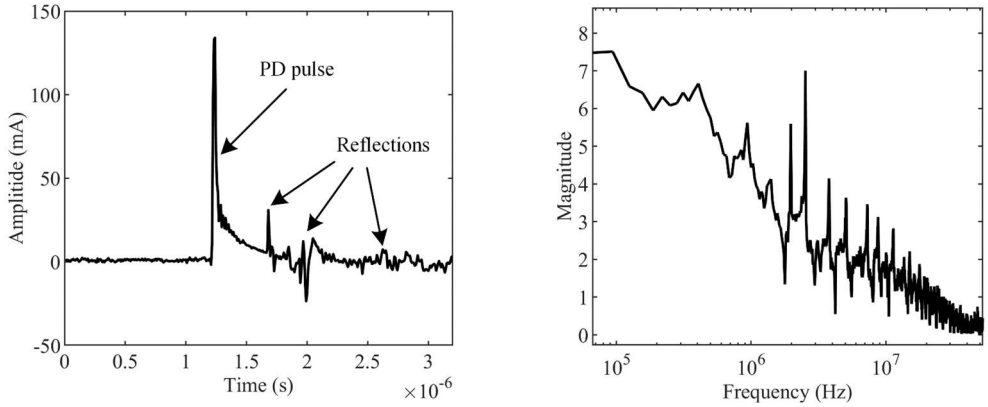

(a) (b)

Figure 2-3 Time- and frequency-domain waveforms of a real PD caused by a 10-kV fouling insulator, measured by a high-frequency current transformer with a frequency bandwidth from 0.1 to 50 MHz.

2.2 Frequency-Dependent Partial Discharge Propagation in Three-phase Overhead Lines

This section first briefly describes the multiple-conductor transmission line model for three-phase overhead lines. The model transforms the four-conductor transmission line into two independent (i.e., decoupled) propagation channels, i.e., phase-to-ground and phase-to-phase channels, greatly simplifying the PD propagation characteristics analysis. Then, the cascading transmission line model for non-uniform overhead lines is developed; this model can describe PD propagation in multiple-segment lines with inconsistent physical parameters, e.g., the earth's resistivity and the overhead line's height. Last but not least, the formula to calculate frequency-dependent transmission line parameters from physical parameters of three-phase overhead lines is derived; the propagation characteristics difference between phase-to-ground (PG) and phase-to-phase (PP) channels is thoroughly discussed; simulation experiments are conducted to analyze the effects of these physical parameters on the propagation constants (i.e., attenuation coefficient and propagation velocity) of the PG and PP channels; finally, laboratory experiment is conducted to validate the developed formulations for calculating the transmission line parameters (or propagation constants) of MV three-phase overhead lines.

2.2.1 Multi-Conductor Transmission Line Model

1）Transmission Line Model

The propagation of PD signals on a three-phase overhead line can be described by a

four-conductor transmission line model [119]. The voltages and currents of the model in the frequency domain can be given via vectors $\mathbf{U}(z,\omega)$ and $\mathbf{I}(z,\omega)$, respectively, which can be defined as

$$\mathbf{U}(z,\omega) = [U_{\mathrm{a}}(z,\omega), U_{\mathrm{b}}(z,\omega), U_{\mathrm{c}}(z,\omega)]^{\mathbf{T}} \tag{2-5}$$

$$\mathbf{I}(z,\omega) = [I_{\mathrm{a}}(z,\omega), I_{\mathrm{b}}(z,\omega), I_{\mathrm{c}}(z,\omega)]^{\mathbf{T}} \tag{2-6}$$

where $U_{\mathrm{a/b/c}}(z,\omega)$ and $I_{\mathrm{a/b/c}}(z,\omega)$ denote the voltages to ground and line currents of three phase conductors over the ground conductor.

The characteristics of the four-conductor transmission line model can be described via a 3×3 impedance matrix $\mathbf{Z}(\omega)$ and a 3×3 admittance matrix $\mathbf{Y}(\omega)$, which are given by

$$\mathbf{Z}(\omega) = \mathbf{R}(\omega) + \mathrm{j}\omega\mathbf{L}(\omega) \tag{2-7}$$

$$\mathbf{Y}(\omega) = \mathbf{G}(\omega) + \mathrm{j}\omega\mathbf{C}(\omega) \tag{2-8}$$

where $\mathbf{R}(\omega)$, $\mathbf{L}(\omega)$, $\mathbf{G}(\omega)$, and $\mathbf{C}(\omega)$ are the per-unit-length resistance, inductance, conductance, and capacitance matrixes. They depend on the four-conductor overhead line's physical structure and the conductors' material characteristics and insulations. Calculations of $\mathbf{Z}(\omega)$ and $\mathbf{Y}(\omega)$ will be discussed in Chapter 2.2.3.

The relationship between the voltages and currents can be described via the Telegrapher's equations, which are defined as

$$\begin{cases} -\dfrac{\partial}{\partial z}\mathbf{U}(z,\omega) = \mathbf{Z}(\omega)\bullet\mathbf{I}(z,\omega) \\ -\dfrac{\partial}{\partial z}\mathbf{I}(z,\omega) = \mathbf{Y}(\omega)\bullet\mathbf{U}(z,\omega) \end{cases} \tag{2-9}$$

Equation (2-9) is a coupled first-order ordinary differential equation with complex coefficients. It can be decoupled as

$$\begin{cases} \dfrac{\partial^2}{\partial z^2}\mathbf{U}(z,\omega) = \mathbf{Z}(\omega)\mathbf{Y}(\omega)\mathbf{U}(z,\omega) \\ \dfrac{\partial^2}{\partial z^2}\mathbf{I}(z,\omega) = \mathbf{Y}(\omega)\mathbf{Z}(\omega)\mathbf{I}(z,\omega) \end{cases} \tag{2-10}$$

In general, $\mathbf{Z}(\omega)$ and $\mathbf{Y}(\omega)$ cannot satisfy the reciprocal rule, i.e., $\mathbf{Z}(\omega)\mathbf{Y}(\omega) \neq \mathbf{Y}(\omega)\mathbf{Z}(\omega)$, causing the coupling among the voltages in $\mathbf{U}(z,\omega)$ or currents in $\mathbf{I}(z,\omega)$. Nevertheless, since the structure of the three-phase overhead line is (approximatively) symmetric, causing $\mathbf{Z}(\omega)$ and $\mathbf{Y}(\omega)$ are both circulant and symmetric:

$$\mathbf{Z}(\omega) = \begin{bmatrix} Z_{\mathrm{p}}(\omega) & Z_{\mathrm{m}}(\omega) & Z_{\mathrm{m}}(\omega) \\ Z_{\mathrm{m}}(\omega) & Z_{\mathrm{p}}(\omega) & Z_{\mathrm{m}}(\omega) \\ Z_{\mathrm{m}}(\omega) & Z_{\mathrm{m}}(\omega) & Z_{\mathrm{p}}(\omega) \end{bmatrix} \tag{2-11}$$

$$\mathbf{Y}(\omega) = \begin{bmatrix} Y_{\mathrm{p}}(\omega) & Y_{\mathrm{m}}(\omega) & Y_{\mathrm{m}}(\omega) \\ Y_{\mathrm{m}}(\omega) & Y_{\mathrm{p}}(\omega) & Y_{\mathrm{m}}(\omega) \\ Y_{\mathrm{m}}(\omega) & Y_{\mathrm{m}}(\omega) & Y_{\mathrm{p}}(\omega) \end{bmatrix} \tag{2-12}$$

where $Z_p(\omega)$ and $Z_m(\omega)$ are the self-impedance of each phase conductor and the mutual impedance between the phase conductors, respectively, and $Y_p(\omega)$ and $Y_m(\omega)$ are the ground admittance of each phase conductor and the mutual admittance between the phase conductors, respectively.

To solve Equation (2-10), the classical Karrenbauer phase-mode transformation referred to as phase A is used, which can be formulated as

$$\mathbf{U}_{012}(z,\omega)=\begin{bmatrix}U_0(z,\omega)\\U_1(z,\omega)\\U_2(z,\omega)\end{bmatrix}=\mathbf{T}\cdot\mathbf{U}(z,\omega) \tag{2-13}$$

$$\mathbf{I}_{012}(z,\omega)=\begin{bmatrix}I_0(z,\omega)\\I_1(z,\omega)\\I_2(z,\omega)\end{bmatrix}=\mathbf{T}\cdot\mathbf{I}(z,\omega) \tag{2-14}$$

where $\mathbf{T}$ is the Karrenbauer phase-mode transformation matrix, which is defined as

$$\mathbf{T}=\frac{1}{3}\cdot\begin{bmatrix}1&1&1\\1&-1&0\\1&0&-1\end{bmatrix} \tag{2-15}$$

Therefore, Equation (2-10) can be rewritten as

$$\begin{cases}\dfrac{\partial^2}{\partial z^2}\mathbf{U}_{012}(z,\omega)=\boldsymbol{\gamma}^2(\omega)\cdot\mathbf{U}_{012}(z,\omega)\\[2ex]\dfrac{\partial^2}{\partial z^2}\mathbf{I}_{012}(z,\omega)=\boldsymbol{\gamma}^2(\omega)\cdot\mathbf{I}_{012}(z,\omega)\end{cases} \tag{2-16}$$

where $\boldsymbol{\gamma}(\omega)$ is a diagonal matrix defined by

$$\begin{aligned}\boldsymbol{\gamma}(\omega)&=\sqrt{\mathbf{Z}_{012}\cdot\mathbf{Y}_{012}}=\sqrt{\mathbf{T}\cdot\mathbf{Z}(\omega)\cdot\mathbf{Y}(\omega)\cdot\mathbf{T}^{-1}}\\&=\begin{bmatrix}\gamma_0(\omega)&0&0\\0&\gamma_1(\omega)&0\\0&0&\gamma_2(\omega)\end{bmatrix}\end{aligned} \tag{2-17}$$

where $\mathbf{Z}_{012}$ and $\mathbf{Y}_{012}$ are the decoupled impedance and admittance matrices, which can be calculated as

$$\begin{aligned}&\mathbf{Z}_{012}(\omega)=\mathbf{T}\cdot\mathbf{Z}(\omega)\cdot\mathbf{T}^{-1}\\&=\begin{bmatrix}Z_{\mathrm{p}}(\omega)+2Z_{\mathrm{m}}(\omega)&0&0\\0&Z_{\mathrm{p}}(\omega)-Z_{\mathrm{m}}(\omega)&0\\0&0&Z_{\mathrm{p}}(\omega)-Z_{\mathrm{m}}(\omega)\end{bmatrix}\end{aligned} \tag{2-18}$$

$$\begin{aligned}&\mathbf{Y}_{012}(\omega)=\mathbf{T}\cdot\mathbf{Y}(\omega)\cdot\mathbf{T}^{-1}\\&=\begin{bmatrix}Y_{\mathrm{p}}(\omega)+2Y_{\mathrm{m}}(\omega)&0&0\\0&Y_{\mathrm{p}}(\omega)-Y_{\mathrm{m}}(\omega)&0\\0&0&Y_{\mathrm{p}}(\omega)-Y_{\mathrm{m}}(\omega)\end{bmatrix}\end{aligned} \tag{2-19}$$

$\boldsymbol{\gamma}(\omega)$ contains the propagation constants of different propagation channels. All voltages

and currents in Equation (2-16) are completely decoupled, and the general solution of $\mathbf{I}_{012}(z,\omega)$ and $\mathbf{U}_{012}(z,\omega)$ can be given by:

$$\begin{cases} \mathbf{I}_{012}(z,\omega) = e^{-\boldsymbol{\gamma}(\omega)z}\cdot\mathbf{I}^{+}_{012}(0,\omega) - e^{\boldsymbol{\gamma}(\omega)z}\cdot\mathbf{I}^{-}_{012}(0,\omega) \\ \mathbf{U}_{012}(z,\omega) = e^{-\boldsymbol{\gamma}(\omega)z}\cdot\mathbf{Z}_{\mathrm{C012}}(\omega)\cdot\mathbf{I}^{+}_{012}(0,\omega) + e^{-\boldsymbol{\gamma}(\omega)z}\cdot\mathbf{Z}_{\mathrm{C012}}(\omega)\cdot\mathbf{I}^{-}_{012}(0,\omega) \end{cases} \tag{2-20}$$

where $\mathbf{I}^{+}_{012}(0)$ and $\mathbf{I}^{-}_{012}(0)$ are the forward and back current waves at 0, respectively, and $\mathbf{Z}_{\mathrm{C012}}(\omega)$ is the characteristic impedance matrix, which is defined as

$$\mathbf{Z}_{\mathrm{C012}}(\omega) = \sqrt{\mathbf{Z}_{012}(\omega)\cdot\mathbf{Y}_{012}(\omega)^{-1}} = \begin{bmatrix} Z_{\mathrm{C0}}(\omega) & 0 & 0 \\ 0 & Z_{\mathrm{C1}}(\omega) & 0 \\ 0 & 0 & Z_{\mathrm{C2}}(\omega) \end{bmatrix} \tag{2-21}$$

where $\mathbf{Z}_{\mathrm{C012}}(\omega)$ describes the relationship between $\mathbf{U}_{012}(z,\omega)$ and $\mathbf{I}_{012}(z,\omega)$.

Finally, $\mathbf{I}_{012}(z,\omega)$ and $\mathbf{U}_{012}(z,\omega)$ can be coupled to $\mathbf{I}(z,\omega)$ and $\mathbf{U}(z,\omega)$ via the inverse Karrenbauer phase-mode transformation. $\mathbf{I}(z,\omega)$ and $\mathbf{U}(z,\omega)$ can be calculated as

$$\begin{cases} \mathbf{I}(z,\omega) = \mathbf{T}^{-1}\cdot\mathbf{I}_{012}(z,\omega) \\ \mathbf{U}(z,\omega) = \mathbf{T}^{-1}\cdot\mathbf{U}_{012}(z,\omega) \end{cases} \tag{2-22}$$

In summary, Telegrapher's equations of the three-phase overhead line can be solved via a three-step procedure, as shown in Figure 2-4 (taking the calculation of the line currents $\mathbf{I}(z,\omega)$ as an example). First, modal transformations are applied to decouple these equations, resulting in decoupling currents $\mathbf{I}_{012}(0,\omega)$ at 0. Then, the decoupled currents at any location are independent and can be calculated by multiplying the propagation constants $\boldsymbol{\gamma}(\omega)$ and $\mathbf{I}_{012}(0,\omega)$. Finally, the line currents $\mathbf{I}(z,\omega)$ are obtained via coupling $\mathbf{I}_{012}(0,\omega)$ via the inverse phase-mode transformation.

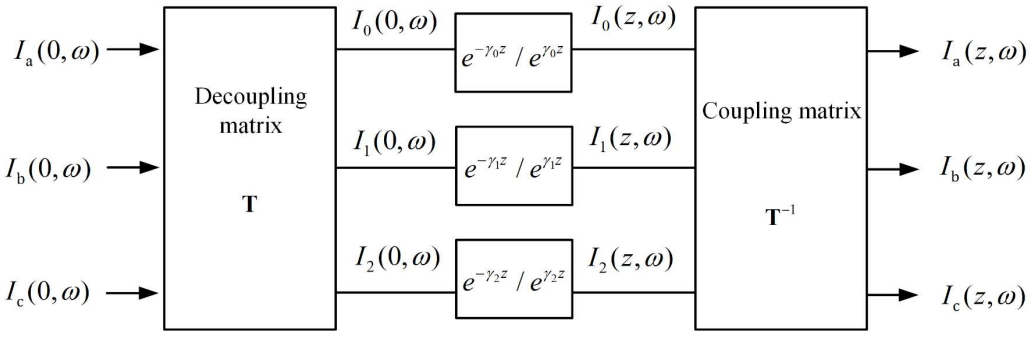

Figure 2-4 Illustration of calculating line currents at any location of the three-phase overhead line via phase-mode transformation method.

2）Propagation Channels in Three-Phase MV Overhead Line

In the last subsection, the coupled three-phase voltages to ground and line currents are transformed into decoupled 0-, 1-, and 2-modal voltages and currents, respectively, which two distinct propagation channels can describe. Therefore, we can describe PD propagation in the three-phase overhead line with two distinct propagation characteristics, which depend on the diagonal elements (i.e., eigenvalues) of $\mathbf{Z}_{012}$ and $\mathbf{Y}_{012,}$ referring to Equation (2-19). The first eigenvalues in $\mathbf{Z}_{012}$ and $\mathbf{Y}_{012}$ represent the phase-to-ground (PG) channel, equal to the sum of the voltages or currents of the three-phase conductors. The propagation

characteristics of the PG channel can be described by its propagation constant $\gamma_{\mathrm{PG}}(\omega)$ and characteristic impedance $Z_{\mathrm{C,PG}}(\omega)$, defined as

$$\gamma_{\mathrm{PG}}(\omega)=\gamma_0(\omega)=\sqrt{(Z_{\mathrm{p}}(\omega)+2Z_{\mathrm{m}}(\omega))(Y_{\mathrm{p}}(\omega)+2Y_{\mathrm{m}}(\omega))} \tag{2-23}$$

$$Z_{\mathrm{C,PG}}(\omega)=Z_{\mathrm{C0}}(\omega)=\sqrt{\frac{Z_{\mathrm{p}}(\omega)+2Z_{\mathrm{m}}(\omega)}{Y_{\mathrm{p}}(\omega)+2Y_{\mathrm{m}}(\omega)}} \tag{2-24}$$

Similarly, the other eigenvalues of $\mathbf{Z}_{012}$ and $\mathbf{Y}_{012}$ define the phase-to-phase (PP) propagation channel, subtraction between the voltages or currents of the three-phase conductors. The PP channel can be described by its propagation constant $\gamma_{\mathrm{PP}}(\omega)$ and characteristic impedance $Z_{\mathrm{C,PP}}(\omega)$, defined as

$$\gamma_{\mathrm{PP}}(\omega)=\gamma_1(\omega)=\gamma_2(\omega)=\sqrt{(Z_{\mathrm{p}}(\omega)-Z_{\mathrm{m}}(\omega))(Y_{\mathrm{p}}(\omega)-Y_{\mathrm{m}}(\omega))} \tag{2-25}$$

$$Z_{\mathrm{C,PP}}(\omega)=Z_{\mathrm{C1}}(\omega)=Z_{\mathrm{C2}}(\omega)=\sqrt{\frac{Z_{\mathrm{p}}(\omega)-Z_{\mathrm{m}}(\omega)}{Y_{\mathrm{p}}(\omega)-Y_{\mathrm{m}}(\omega)}} \tag{2-26}$$

Since the duration of the PD signal is very short, its first pulse and reflections can always be separated by a time axis. If only the first arriving pulse is of interest, the modal currents $\mathbf{I}_{012}^{+}(z,\omega)$ at z can be calculated by

$$\mathbf{I}_{012}^{+}(z,\omega)=\begin{bmatrix} e^{-\gamma_{\mathrm{PG}}(\omega)z} & 0 & 0 \\ 0 & e^{-\gamma_{\mathrm{PP}}(\omega)z} & 0 \\ 0 & 0 & e^{-\gamma_{\mathrm{PP}}(\omega)z} \end{bmatrix}\cdot\mathbf{I}_{012}^{+}(0) \tag{2-27}$$

Taking $\mathbf{I}^{+}(z,\omega)=\ \mathbf{T}^{-1}\cdot\mathbf{I}_{012}^{+}(z,\omega)$ into Equation (2-27) results into

$$\begin{aligned}\mathbf{I}^{+}(z,\omega)&=\mathbf{T}^{-1}\cdot\begin{bmatrix} e^{-\gamma_{\mathrm{PG}}(\omega)z} & 0 & 0 \\ 0 & e^{-\gamma_{\mathrm{PP}}(\omega)z} & 0 \\ 0 & 0 & e^{-\gamma_{\mathrm{PP}}(\omega)z} \end{bmatrix}\cdot\mathbf{T}\cdot\mathbf{I}^{+}(0,\omega)\\ &=\frac{1}{3}\left(e^{-\gamma_{\mathrm{PG}}(\omega)z}\begin{bmatrix}1&1&1\\1&1&1\\1&1&1\end{bmatrix}+e^{-\gamma_{\mathrm{PP}}(\omega)z}\begin{bmatrix}2&-1&-1\\-1&2&-1\\-1&-1&2\end{bmatrix}\right)\mathbf{I}^{+}(0,\omega)\end{aligned} \tag{2-28}$$

where the PG and PP channels are separated and can be respectively described as

$$\begin{cases} I_{\mathrm{PG}}^{+}(z,\omega)=\dfrac{1}{3}\sum_{i=\mathrm{a}}^{\mathrm{c}}I_i^{+}(z,\omega)=\dfrac{1}{3}e^{-\gamma_{\mathrm{PG}}(\omega)z}\sum_{i=\mathrm{a}}^{\mathrm{c}}I_i^{+}(0,\omega) \\ \mathbf{I}_{\mathrm{PP}}^{+}(z,\omega)=\begin{bmatrix}I_{\mathrm{ab}}^{+}(z,\omega)\\I_{\mathrm{ac}}^{+}(z,\omega)\\I_{\mathrm{bc}}^{+}(z,\omega)\end{bmatrix}=\begin{bmatrix}I_{\mathrm{a}}^{+}(z,\omega)-I_{\mathrm{b}}^{+}(z,\omega)\\I_{\mathrm{a}}^{+}(z,\omega)-I_{\mathrm{c}}^{+}(z,\omega)\\I_{\mathrm{b}}^{+}(z,\omega)-I_{\mathrm{c}}^{+}(z,\omega)\end{bmatrix}=e^{-\gamma_{\mathrm{PP}}(\omega)z}\mathbf{I}_{\mathrm{PP}}^{+}(0,\omega) \end{cases} \tag{2-29}$$

where $I_{\mathrm{a/b/c}}^{+}(0,\omega)$ are given by the induced three-phase PD currents $\mathbf{I}_{\mathrm{PD}}=[I_{\mathrm{a}}^{+}(0,\omega),I_{\mathrm{b}}^{+}(0,\omega),I_{\mathrm{c}}^{+}(0,\omega)]^{\mathrm{T}}$ at the PD source.

In summary, the complex propagation characteristics of the three-phase overhead line can be represented by the propagation constants of the PG and PP channels, greatly simplifying the analysis. In other words, we can predict the change of the PD signal as long as the propagation constants (i.e., $\gamma_{\mathrm{PG}}(\omega)$ and $\gamma_{\mathrm{PP}}(\omega)$) and characteristic impedances (i.e.,

$Z_{\mathrm{C,PG}}(\omega)$ and $Z_{\mathrm{C,PP}}(\omega)$) of the PG and PP channels are obtained.

2.2.2 Cascading Transmission Line Model

The former paragraphs' models and measurements apply to connections of overhead lines with uniform structures. In a distribution network, however, the geography always varies along the overhead line, e.g., the height of the overhead line or the conductivity and dielectric constant of the ground. To simplify the model of the non-uniform transmission line, the overhead line can be separated into multiple segments, in which each one can be identified as a uniform line. Each overhead segment can be modeled by the models presented in the former paragraph, and each segment can have different propagation characteristics. A cascade coupling of the single-segment models can be used to obtain a total overhead line model.

One propagation channel (PG or PP) of a line segment can be characterized as a general two-port. One way of describing a general two-port is with a chain parameter $\boldsymbol{\Theta}_{k,l}(\omega)$ or ABCD matrix [119]:

$$\begin{bmatrix} U_k(z,\omega) \\ I_k(z,\omega) \end{bmatrix} = \boldsymbol{\Theta}_{k,l}(\omega) \cdot \begin{bmatrix} U_k(z+z_l,\omega) \\ I_k(z+z_l,\omega) \end{bmatrix} \tag{2-30}$$

where z_l is the length of the l^{th} line segment with the uniform structure, and $\boldsymbol{\Theta}_{k,l}(\omega)$ characterizes the parameters of the k^{th} propagation channel of the l^{th} line segment and can be formulated as:

$$\boldsymbol{\Theta}_{k,l}(\omega) = \begin{bmatrix} \cosh(\gamma_{k,l}(\omega)z_l) & Z_{\mathrm{C}k}\sinh(\gamma_{k,l}(\omega)z_l) \\ Z_{\mathrm{C}k}^{-1}\sinh(\gamma_{k,l}(\omega)z_l) & \cosh(\gamma_{k,l}(\omega)z_l) \end{bmatrix} \tag{2-31}$$

where $\gamma_{k,l}(\omega)$ is the propagation constant of the k^{th} propagation channel of the l^{th} line segment. The impedance of one side of the two-port depends on the load impedance $Z_{\mathrm{load},(k,l)}(\omega)$ at the other side. From Equations (2-30) and (2-31), the input impedance can be derived:

$$Z_{\mathrm{in},(k,l)}(\omega) = \frac{Z_{\mathrm{load},(k,l)}(\omega)\cosh(\gamma_{k,l}(\omega)z_l) + Z_{\mathrm{C},(k,l)}(\omega)\sinh(\gamma_{k,l}(\omega)z_l)}{Z_{\mathrm{load},(k,l)}(\omega)Z_{\mathrm{C},(k,l)}^{-1}(\omega)\sinh(\gamma_{k,l}(\omega)z_l) + \cosh(\gamma_{k,l}(\omega)z_l)} \tag{2-32}$$

where $Z_{\mathrm{C},(k,l)}(\omega)$ is the characteristic impedance of the k^{th} propagation channel of the l^{th} line segment, and $Z_{\mathrm{load},(k,l)}(\omega)$ is equal to $Z_{\mathrm{in},(k,l+1)}(\omega)$ if the l^{th} line segment is connected to $(l+1)^{\mathrm{th}}$ line segment. Similarly, the output impedance can be characterized by the same equation as (2-32) as an overhead line is a symmetrical two-port.

Each propagation channel of the non-uniform overhead line can be equivalent to a set of N cascade-coupled two-ports, which the total chain parameter matrix can describe:

$$\boldsymbol{\Theta}_{\mathrm{T},k}(\omega) = \boldsymbol{\Theta}_{k,1}(\omega) \cdot \boldsymbol{\Theta}_{k,2}(\omega) \ldots \cdot \boldsymbol{\Theta}_{k,l}(\omega) \ldots \cdot \boldsymbol{\Theta}_{k,L}(\omega) \tag{2-33}$$

where L is the number of the line segments. Using $\boldsymbol{\Theta}_{\mathrm{T},k}(\omega)$ and $Z_{\mathrm{load},(k,l)}(\omega) = Z_{\mathrm{in},(k,l+1)}(\omega)$, the total input impedance of this total system with load $Z_{\mathrm{load},k}$ at the output is defined as:

$$Z_{\text{in},(k,l)}(\omega)=\frac{Z_{\text{load},k,l}(\omega)\Theta_{\text{T},k}(1,1)+\Theta_{\text{T},k}(1,2)}{Z_{\text{load},k,l}(\omega)\Theta_{\text{T},k}(2,1)+\Theta_{\text{T},k}(2,2)} \tag{2-34}$$

where $\Theta_{\text{T},k}(i,j)$ represents the i^{th} row and j^{th} column of matrix $\boldsymbol{\Theta}_{\text{T},k}$. Using these equations, the whole overhead line with multiple non-uniform segments can be characterized and incorporated into the (numerous) reflections. However, the PD signal is a pulse with a very short period leading to the first pulse, and its reflections are always separated by time axis. If only the first arriving pulse is of interest, the propagation of the PD pulse can be expressed in a more straightforward formulation as

$$H_k(\omega)=\prod_{l=1}^{L} e^{-\gamma_{k,l}(\omega)z_l}T_{k,(l\to l+1)}(\omega) \tag{2-35}$$

where H_k is the transform function of the k^{th} propagation channel of the while overhead line, and $T_{k,(l\to l+1)}$ is the refraction coefficient in the joint between the l^{th} and $(l+1)^{\text{th}}$ line segments, and it can be formulated as:

$$T_{k,(l\to l+1)}(\omega)=\frac{2Z_{\text{C},(k,l+1)}(\omega)}{Z_{\text{C},(k,l+1)}(\omega)+Z_{\text{C},(k,l)}(\omega)} \tag{2-36}$$

where $Z_{\text{C},(k,L+1)}(\omega)$ (i.e., $l=L$) is equal to the load impedance $Z_{\text{load},k}(\omega)$ It can be observed that the output current or voltage of the non-uniform overhead line is up to the propagation coefficients $\gamma_{k,l}(\omega)$, distances z_l, and the refraction coefficients $T_{k,(l\to l+1)}(\omega)$ at the joints.

2.2.3 Frequency-Dependent Transmission Line Parameters

The transmission line parameters of the three-phase MV overhead line are frequency-dependent due to the effects of the skin effects in overhead conductors and ground plane [120], leading to frequency-dependent propagation characteristics of the transmission line model. The frequency-dependent features are non-negligible for the PD signal since it has a wide frequency band from DC to tens of MHz. This subsection will derive the frequency-dependent propagation constants of a typical three-phase MV overhead line, as shown in Figure 2-5.

1）Impedance Parameters

Figure 2-6 describes the schematic diagram of impedance parameter calculation. Based on Carson's formula [121], the depth $D_{\text{G}}(\omega)$ of complex penetration in the ground is defined as

$$D_{\text{G}}(\omega)=\sqrt{\frac{\rho_{\text{G}}}{j\omega\mu}} \tag{2-37}$$

where ρ_{G} denotes the resistivity of the earth (e.g., $\rho_{\text{G}}\approx 100\Omega\bullet\text{m}$ in [122]); μ is the permeability of vacuum ($\mu=4\pi\times10^{-7}$H/m);

Similarly, the penetration depth $D_{\text{al}}(\omega)$ of the overhead conductors is defined as

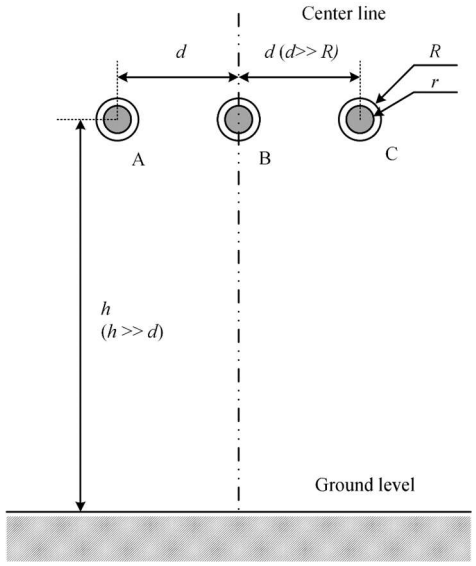

Figure 2-5 Typical structure of MV three-phase overhead lines.

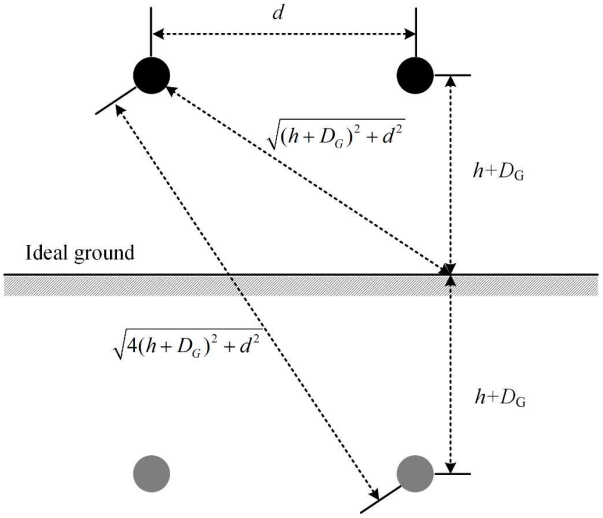

Figure 2-6 Impedance parameter calculation scheme

$$D_{\mathrm{al}}(\omega)=\sqrt{\frac{\rho_{\mathrm{al}}}{\omega\mu}} \tag{2-38}$$

where ρ_{al} denotes the resistivity of the aluminum conductors ($\rho_{\mathrm{al}} \approx 2.7\times10^{-8}$ S/m).

For overhead conductors, their self-impedance $Z_p(\omega)$ can be calculated as

$$Z_{\mathrm{p}}(\omega)=\frac{\rho_{\mathrm{al}}}{2\pi r D_{\mathrm{al}}(\omega)}+\frac{j\omega\mu}{2\pi}\ln\frac{2(h+D_{\mathrm{G}}(\omega))}{r} \tag{2-39}$$

The first term in Equation (2-39) is the alternative-current resistance of the overhead conductors, and the second term contains the self-inductance of the overhead conductors and the resistance of the ground; r is the radius of the aluminum conductors, and h is the height of the conductors above the ground.

The mutual impedance $Z_{\mathrm{m}}(\omega)$ in per-unit length between conductors is approximately given by

$$Z_{\mathrm{m}}(\omega) \approx \frac{1}{3}\left(Z_{\mathrm{ab}}(\omega)+Z_{\mathrm{ac}}(\omega)+Z_{\mathrm{bc}}(\omega)\right) = \frac{j\omega\mu}{3\pi}\ln\frac{\sqrt{4(h+D_{\mathrm{G}}(\omega))^2+d^2}}{d}+\frac{j\omega\mu}{6\pi}\ln\frac{\sqrt{(h+D_{\mathrm{G}}(\omega))^2+d^2}}{d} \quad (2\text{-}40)$$

where $Z_{\mathrm{ab/ac/bc}}(\omega)$ is the mutual impedance between phases A, B, and C, and d is the distance between the conductors.

2）Admittance Parameters

Figure 2-7 describes the schematic diagram of admittance parameter calculation. Generally, the air's conductance value is far less than its susceptance so that it can be ignored. The electric potential parameter can calculate the susceptance parameter [119]. The self-potential parameter of overhead (covered) conductors can be calculated as

$$P_{\mathrm{p}} = \frac{1}{2\pi\varepsilon_0}\ln\frac{2h}{R}+\frac{1}{2\pi\varepsilon_1}\ln\frac{R}{r} \quad (2\text{-}41)$$

where $\varepsilon = 8.854\times10^{-12}$ H/m is the vacuum dielectric constant, R is the radius of the covered conductor, and $\varepsilon_1 \approx 2.3\varepsilon$ is the dielectric constant of the XLPE insulation layer. The above formula assumes the insulation layer does change the electric field distribution in the air medium, causing it to work only if h is much larger than R and r.

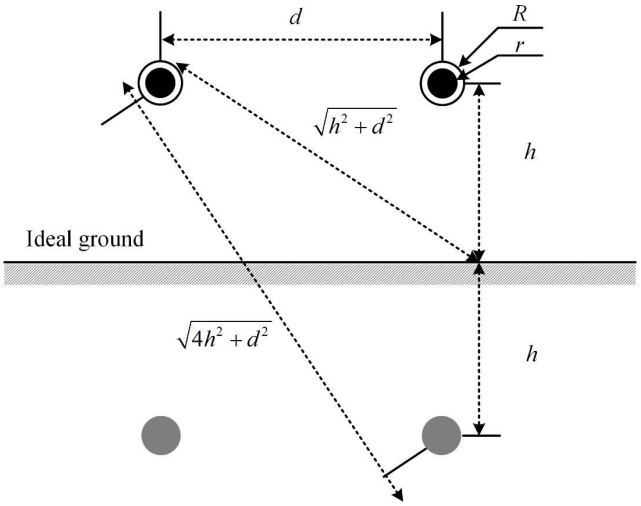

Figure 2-7 Admittance parameter calculation scheme

The mutual potential parameters $P_{\mathrm{ab}}(\omega)$ and $P_{\mathrm{ac}}(\omega)$ between phase conductors can be calculated as

$$P_{\mathrm{ab}}(\omega) = \frac{1}{2\pi\varepsilon_0}\ln\frac{\sqrt{4h^2+d^2}}{d} \quad (2\text{-}42)$$

$$P_{\mathrm{ac}}(\omega) = \frac{1}{2\pi\varepsilon_0}\ln\frac{\sqrt{4h^2+4d^2}}{2d} \quad (2\text{-}43)$$

Since d is much smaller than h for the MV overhead line, P_{m} can be approximately

defined as

$$P_{\mathrm{m}} \approx \frac{1}{3}\left(P_{\mathrm{ab}}(\omega)+P_{\mathrm{ac}}(\omega)+P_{\mathrm{bc}}(\omega)\right) \tag{2-44}$$

As the formulation of calculating P_{p} and P_{m} assumes the insulation layer does change the electric field distribution in the air medium, causing it to work only if h and d are much larger than R and r.

The admittance matrix can be calculated from P_{p} and P_{m} [119], resulting into

$$\begin{cases} Y_{\mathrm{p}}(\omega) = j\omega\left(\dfrac{P_{\mathrm{p}}+P_{\mathrm{m}}}{P_{\mathrm{p}}^2+P_{\mathrm{p}}P_{\mathrm{m}}-2P_{\mathrm{m}}^2}\right) \\ Y_{\mathrm{m}}(\omega) = j\omega\left(\dfrac{-P_{\mathrm{m}}}{P_{\mathrm{p}}^2+P_{\mathrm{p}}P_{\mathrm{m}}-2P_{\mathrm{m}}^2}\right) \end{cases} \tag{2-45}$$

In the above formulations for calculating P_{p} and P_{m}, the effect of the XLPE layer is approximated. To validate the feasibility of this approximation, a simulation experiment is carried out in CMOSOL, a finite element analysis software. This software allows us to numerically calculate P_{p} and P_{m} of the three-phase overhead line with very high accuracy (e.g., the relative error is set to less than 0.001 in this simulation). Figure 2-8 and Figure 2-9 show the comparison results between COMSOL simulations and the proposed approximation formulations. It can be observed that the errors between the COMSOL simulation and the proposed formulations gradually become more significant as r increases. Nevertheless, the errors can be ignored as if r is much smaller than the height and spacing of the overhead conductors, i.e., $r < 0.05$ m. This demonstrates that the proposed formulations can accurately describe the MV overhead lines since their radius (i.e., a few centimeters) is always much smaller than their height and spacing (i.e., a few or ten meters).

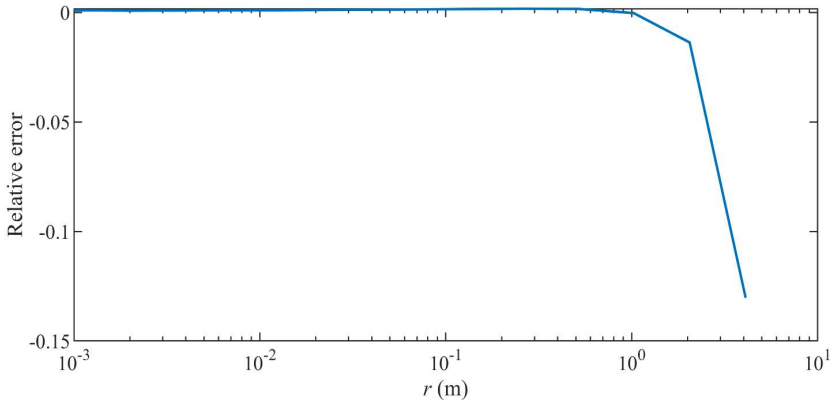

Figure 2-8 Relative error of the self-potential parameters between the developed formulation and the COMSOL simulation, with varying r ($R = 2r$, h =12 m, d =0.4 m, and ρ_{G}=100 $\Omega \bullet$ m.

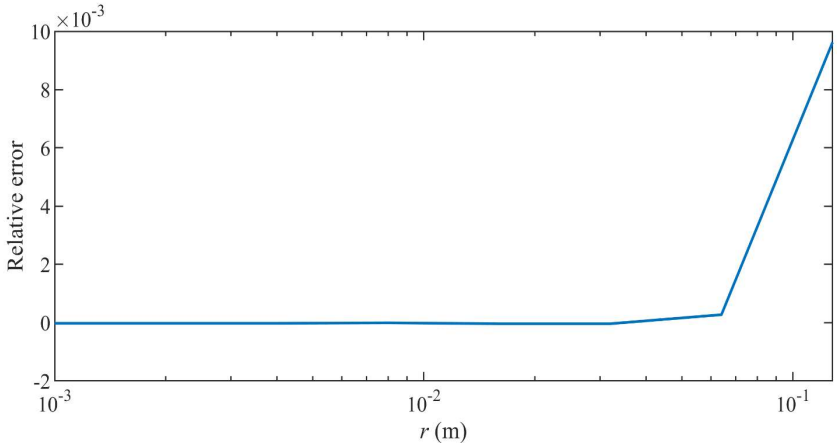

Figure 2-9 Relative error of the mutual potential parameters between the developed formulation and the COMSOL simulation, with varying r ($R = 2r$, h =12 m, d =0.4 m, and ρ_G=100 Ω • m).

3）Propagation Differences Between Phase-to-Ground and Phase-to-Phase channels

According to Equation (2-23) and (2-25), the propagation constants of the PG and PP channels are given as

$$\gamma_{PG}(\omega) = \sqrt{(Z_p(\omega) + 2Z_m(\omega))(Y_p(\omega) + 2Y_m(\omega))} = \alpha_{PG}(\omega) + j\beta_{PG}(\omega) \tag{2-46}$$

$$\gamma_{PP}(\omega) = \sqrt{(Z_p(\omega) - Z_m(\omega))(Y_p(\omega) - Y_m(\omega))} = \alpha_{PP}(\omega) + j\beta_{PP}(\omega) \tag{2-47}$$

where $\alpha_{PG}(\omega)$ and $\alpha_{PP}(\omega)$ are the real parts of $\gamma_{PG}(\omega)$ and $\gamma_{PP}(\omega)$, respectively, and they are named as the attenuation coefficients, which represent the energy loss characteristics of PD propagation in the corresponding channel; $\beta_{PG}(\omega)$ and $\beta_{PP}(\omega)$ are the imaginary parts of $\gamma_{PG}(\omega)$ and $\gamma_{PP}(\omega)$, respectively, and they are named phase constants, which character the phase shift of PD propagation in the corresponding channel. Accordingly, the phase velocities $v_{PG}(\omega)$ and $v_{PP}(\omega)$ of the PG and PP channels are defined as

$$v_{PG}(\omega) = \frac{\omega}{\beta_{PG}(\omega)} \tag{2-48}$$

$$v_{PP}(\omega) = \frac{\omega}{\beta_{PP}(\omega)} \tag{2-49}$$

Considering the structure and electrical parameters of the typical MV three-phase overhead line, Figure 2-10 displays the frequency-dependent attenuation coefficients and phase velocities of a 10-kV overhead line's PG and PP channels via the developed analytical model and the simulation experiment in PSCAD. To sum up,

(1) The results of the developed analytical formulations are almost the same as those of the simulation experiment in PSCAD, verifying the accuracy and feasibility of the developed approximate formulations for calculating the impedance and admittance parameters.

(2) Both attenuation coefficients $\alpha_{PG}(\omega)$ and $\alpha_{PP}(\omega)$ increase as the frequency increases, which will lead to the energy loss of the PD signal when propagating in

the MV overhead line. The attenuation coefficient $\alpha_{PG}(\omega)$ of the PG channel is significantly larger than that of the PP channel, causing the PG-modal of the PD signal to attenuate faster and cannot propagate a long distance. This implies that detecting PD in MV overhead lines is better by analyzing the PP voltages and currents (i.e., the PP-modal signal).

(3) Both the velocities $v_{PG}(\omega)$ and $v_{PP}(\omega)$ increase as the frequency increases, leading to dispersion of the PD signal when propagating in the MV overhead line. The gradient of the phase velocity $v_{PG}(\omega)$ of the PG channel is significantly larger than that of the PP channel, causing more severe dispersion. Moreover, the significant variation of $v_{PG}(\omega)$ can pose a difficulty in choosing the correct velocity value in PD localization, which strongly depends on PD signal characteristics. In contrast, the velocity variation of the PP channel is much smaller than that of the PG channel, easing the velocity value setting in PD localization.

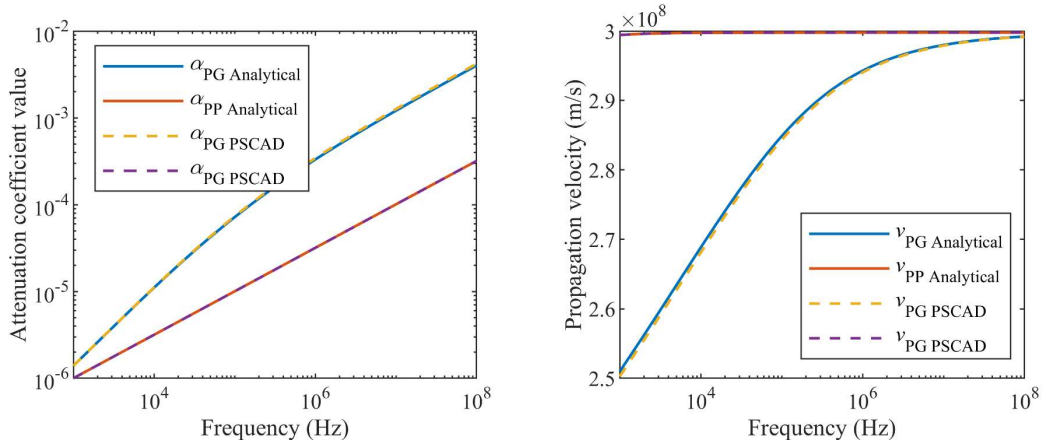

(a) (b)

Figure 2-10 Attenuation coefficients (a) and propagation velocities (b) of the PG and PP channels of three-phase bare overhead lines (h=12 m, d=0.4 m, r=0.004 m, ρ_G=100 Ω • m, and R=0.004 m).

Figure 2-11 compares propagation constants between three-phase covered and bare conductors. It can be observed that the XLPE layer hardly affects the attenuation coefficients of the PG and PP channels. However, it significantly decreases the propagation velocities of the PG and PP channels. The decrease in propagation velocity of the PP channel is considerably more significant than that of the PG channel.

Figure 2-12 collects the waveforms of the line, PG-channel, and PP-channel currents of a real PD signal in a 10-kV three-phase overhead line. The PD signal was detected via two high-frequency transformers mounted at 0 m and 3784 m away from a fouling PD-affect insulator connected to phase conductor A. In Figure 2-12(a), it can be observed that at the PD source, the signal magnitude in the PG channel (i.e., $i_a + i_b + i_c$) is almost equal to that in the PP channel (i.e., $i_a - i_b$ or $i_a - i_c$). In Figure 2-12(b), at a 3784-m distance from the PD source, the amplitude of i_a is approximately two times that of i_b or i_c; the polarity of i_a is opposite to i_b and i_c; the signal magnitude in the PP channel is still significant while

that in the PG channel is almost equal to zero. Comparing Figure 2-12(a) with (b), it can be observed that the PD signal becomes more “short” (due to attenuation) and “fat” (due to dispersion) as the signal in the PG channel can propagation a significantly shorter distance than that in PP channel since the attenuation in PG channel is considerably more severe.

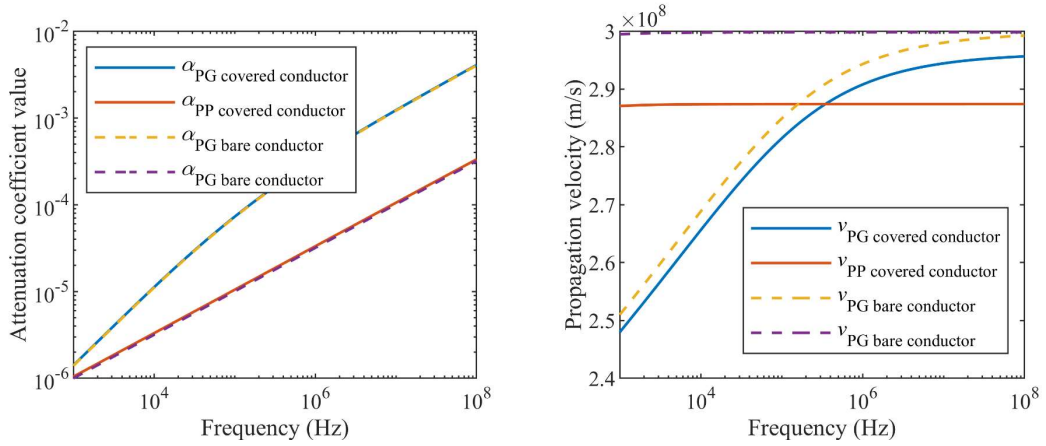

(a) (b)

Figure 2-11 Attenuation coefficients (a) and propagation velocities (b) of the PG and PP channels between three-phase covered (R=0.008 m) and bare (R=0.004 m) overhead lines. (h=12 m, d=0.4 m, r=0.004 m, ρ_G=100 Ω • m)

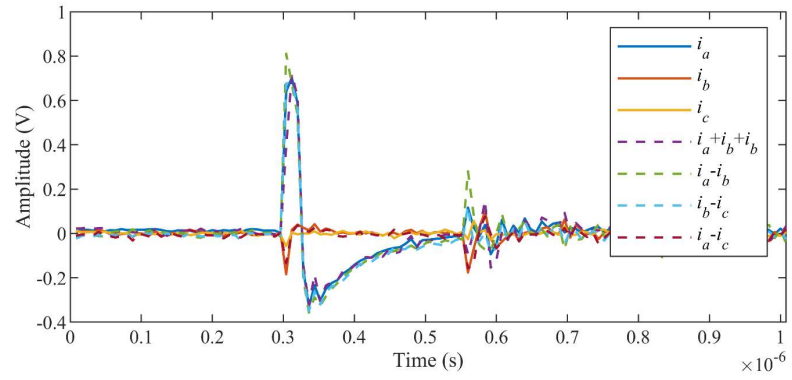

(a)

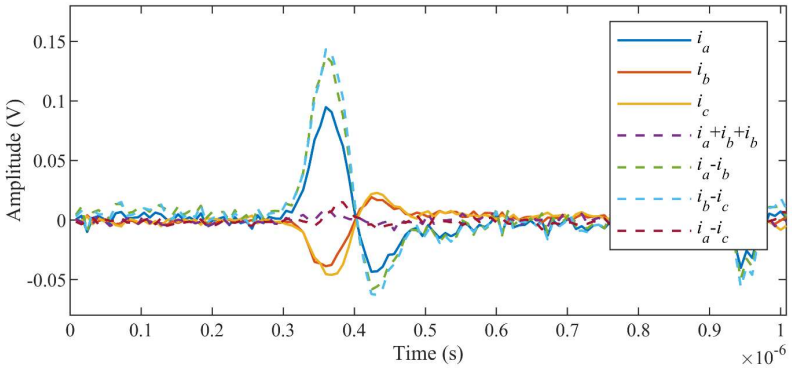

(b)

Figure 2-12 Time-domain waveforms of line, PG-channel, and PP-channel currents of a real PD signal detected at 0 m and 3784 away from the PD-affected fouling insulator in phase conductor A.

4）Simulation Analysis: Effect of Line Parameters on Propagation Constants

A simulation experience was carried out to understand the effect of the physical parameters of the MV three-phase overhead line on its propagation characteristics based on the developed models. Figure 2-13, Figure 2-14, Figure 2-15, Figure 2-16, and Figure 2-17 collect the simulation results of the attenuation coefficients and propagation velocities of the PG and PP channels with varying h, d, r, ρ_G, and R, respectively, which will be discussed in the followings.

In Figure 2-13(a), it can be observed that the attenuation coefficient $\alpha_{PG}(\omega)$ of the PG channel decreases as the height h of the overhead line increases. The decrement of $\alpha_{PG}(\omega)$ becomes more significant as the frequency increases. In contrast, the attenuation coefficient $\alpha_{PP}(\omega)$ of the PP channel is hardly affected by h, as shown in Figure 2-13(b). In Figure 2-13(c), it can be observed that the propagation velocity $v_{PG}(\omega)$ of the PG channel becomes larger as h increases. The increment of $v_{PG}(\omega)$ becomes smaller as the frequency increases. In contrast, the propagation velocity $v_{PP}(\omega)$ of the PG channel is hardly affected by h, as shown in Figure 2-13(d).

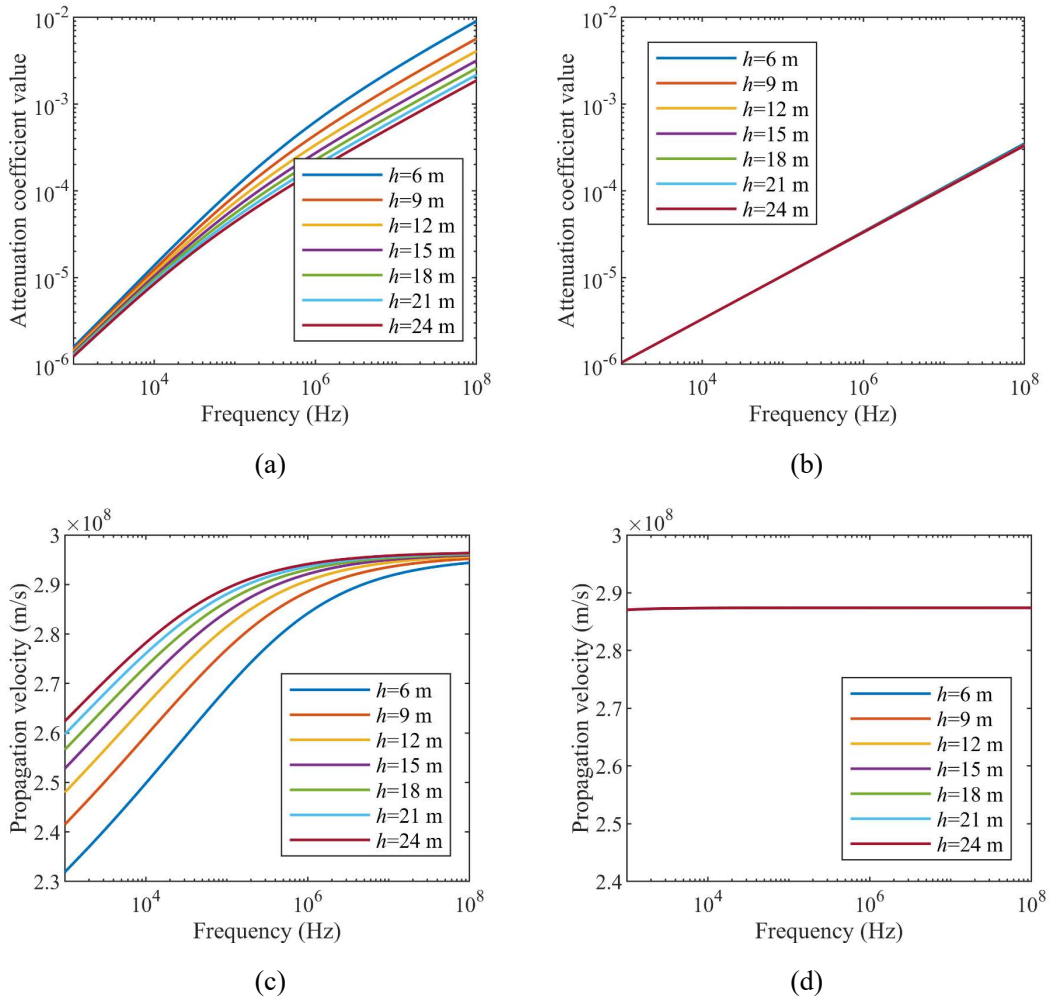

Figure 2-13 Effect of h on the propagation constants of the PG and PP channels (d=0.4 m, r=0.004 m, ρ_G=100 Ω • m, and R=0.008 m): (a) $\alpha_{PG}(\omega)$; (b) $\alpha_{PP}(\omega)$; (c) $v_{PG}(\omega)$; (d) $v_{PP}(\omega)$.

In Figure 2-14(a), it can be observed that the attenuation coefficient $\alpha_{PG}(\omega)$ of the PG channel slightly increases as the distance d between the overhead phase conductors increases. In contrast, the attenuation coefficient $\alpha_{PP}(\omega)$ of the PP channel slightly decreases as d increases, as shown in Figure 2-14(b). In Figure 2-14(c), it can be observed that the propagation velocity $v_{PG}(\omega)$ of the PG channel slightly decreases as d increases. The decrement of $v_{PG}(\omega)$ becomes smaller as the frequency increases. In contrast, the propagation velocity $v_{PP}(\omega)$ of the PG channel slightly increases as d increases, as shown in Figure 2-14(d).

In Figure 2-15(a), it can be observed that the attenuation coefficient $\alpha_{PG}(\omega)$ of the PG channel is hardly affected by the radius r. In contrast, the PP channel's attenuation coefficient $\alpha_{PP}(\omega)$ of the PP channel significantly decreases as r increases, as shown in Figure 2-15(b). In Figure 2-15(c), it can be observed that the propagation velocity $v_{PG}(\omega)$ of the PG channel slightly decreases as d increases. The decrement of $v_{PG}(\omega)$ becomes smaller as the frequency increases. In contrast, the propagation velocity $v_{PP}(\omega)$ of the PG channel slightly increases as d increases, as shown in Figure 2-15(d).

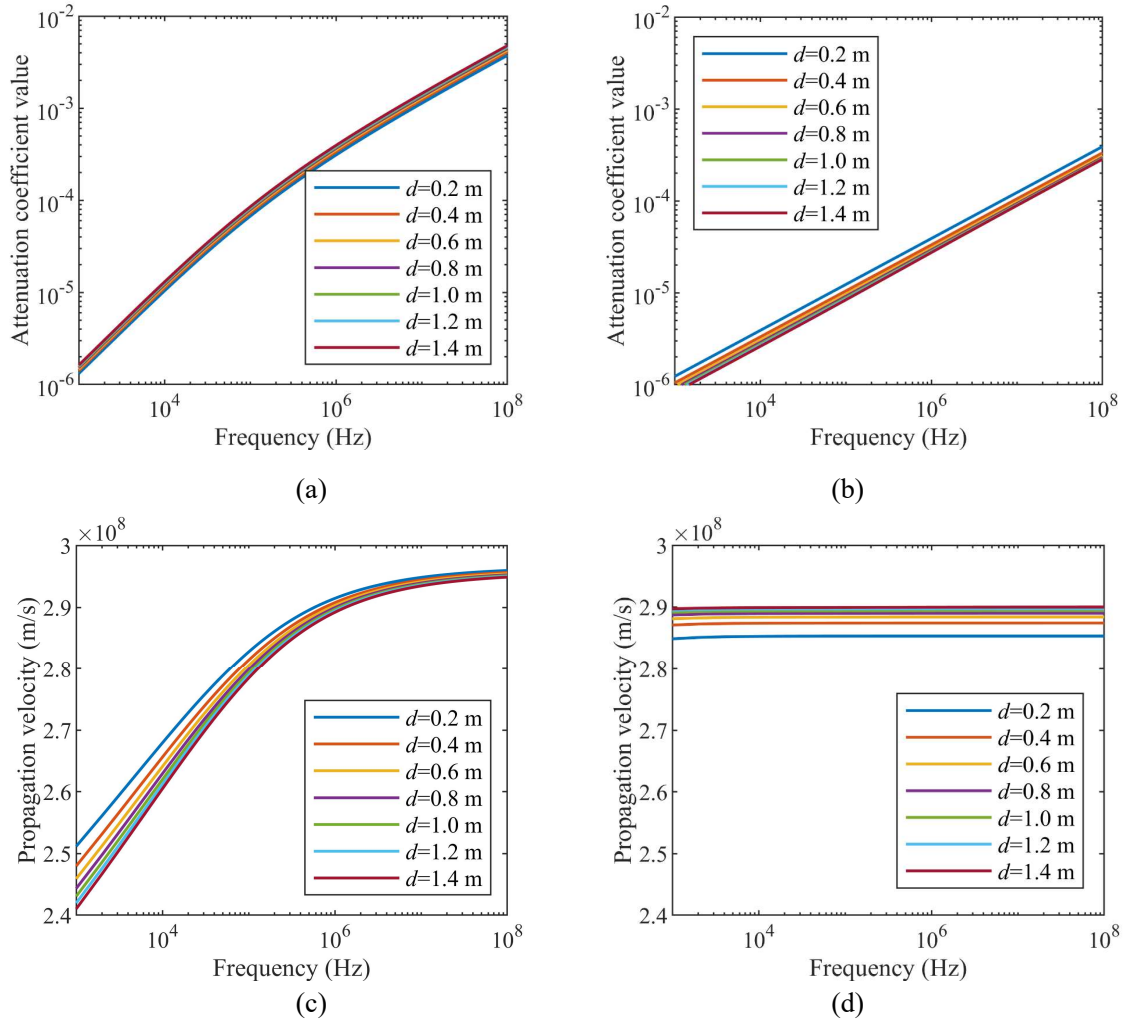

Figure 2-14 Effect of d on the propagation constants of the PG and PP channels (h=12 m, r=0.004 m, ρ_G=100 Ω • m, and R=0.008 m): (a) $\alpha_{PG}(\omega)$; (b) $\alpha_{PP}(\omega)$; (c) $v_{PG}(\omega)$; (d) $v_{PP}(\omega)$.

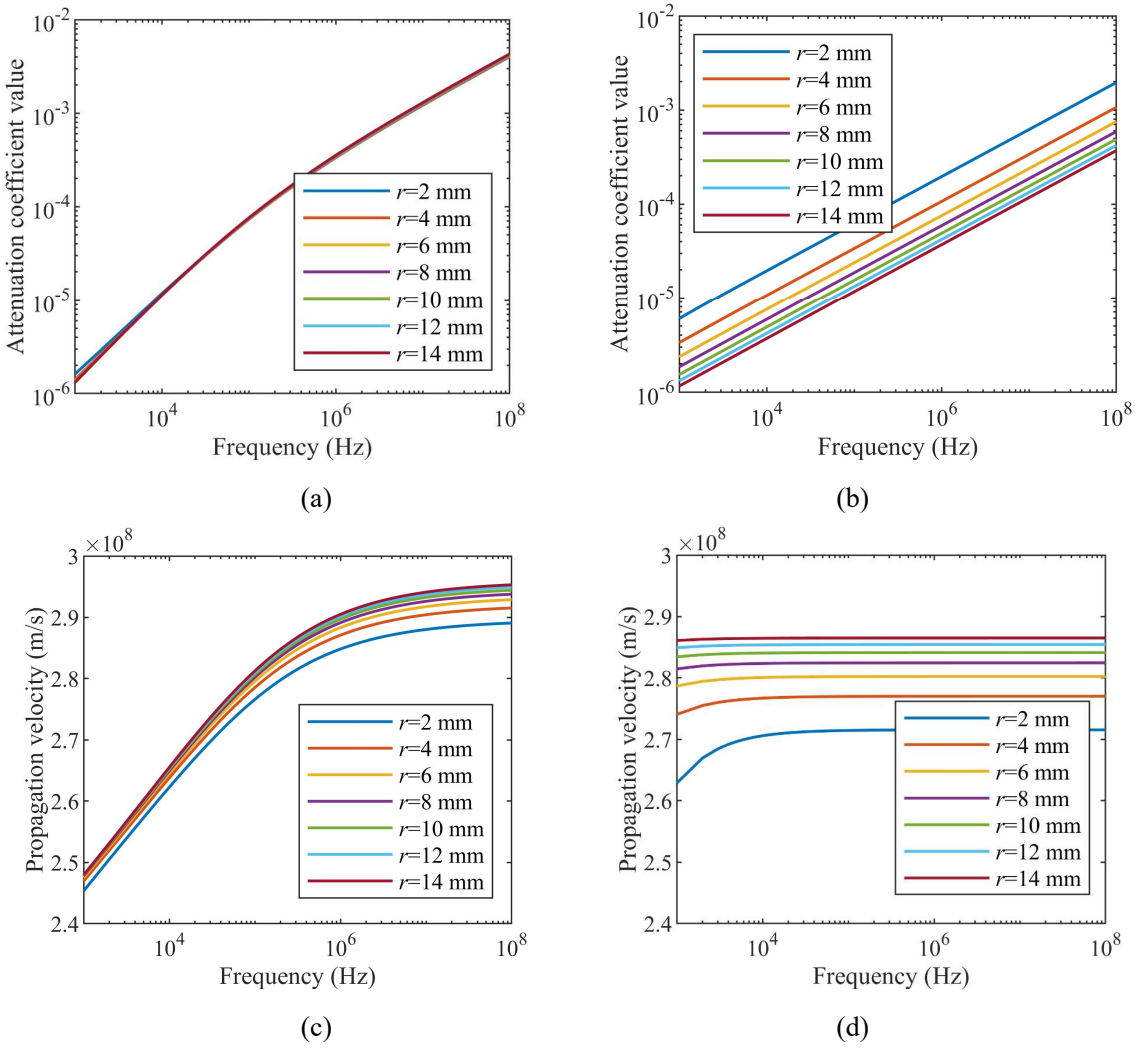

Figure 2-15 Effect of r on the propagation constants of the PG and PP channels (h=12 m, d=0.4 m, ρ_G=100 Ω • m, and R=0.008 m): (a) $\alpha_{PG}(\omega)$; (b) $\alpha_{PP}(\omega)$; (c) $v_{PG}(\omega)$; (d) $v_{PP}(\omega)$.

In Figure 2-16(a), it can be observed that the attenuation coefficient $\alpha_{PG}(\omega)$ of the PG channel becomes more significant as the resistivity ρ_G of the earth increases. The increment of $\alpha_{PG}(\omega)$ is significantly more critical as the frequency increases. In contrast, the attenuation coefficient $\alpha_{PP}(\omega)$ of the PP channel is hardly affected by ρ_G, as shown in Figure 2-16(b). In Figure 2-16(c), it can be observed that the propagation velocity $v_{PG}(\omega)$ of the PG channel becomes significantly smaller as ρ_G increases. In contrast, the propagation velocity $v_{PP}(\omega)$ of the PP channel is hardly affected by ρ_G, as shown in Figure 2-16(d).

In Figure 2-17(a) and (b), it can be observed that the attenuation coefficients of the PG and PP channels are hardly affected by the thickness of the XLPE layer. In Figure 2-17(c), it can be observed that the propagation velocity $v_{PG}(\omega)$ of the PG channel becomes significantly smaller as the thickness of the XLPE layer increases. Similarly, the propagation velocity $v_{PP}(\omega)$ of the PP channel becomes considerably smaller as the thickness of the XLPE layer rises, as shown in Figure 2-17(d).

In summary, the propagation characteristics of the PG channel strongly depend on h

and ρ_G, but are insensitive to d and r; the propagation characteristics of the PP channel strongly depend on r but are not sensitive to h, d, and ρ_G. Moreover, the propagation velocities of PG and PP channels are sensitive to the thickness of the XLPE layer. Based on the conclusion, it can be inferred that:

(1) The PD signal in the PG channel is susceptible to h and ρ_G, which are always varying along the overhead line due to the non-uniform geography, leading to complex influences on the signal features. The results can pose a significant challenge to diagnosing PD characteristics of the MV overhead distribution network.

(2) In contrast, the PD signal in the PP channel is hardly influenced by the surrounding environment (i.e., the line height and the ground resistivity), causing the PD signal in any location to be easier estimated, which mainly depends on the radius of the overhead conductors. In other words, The PD signal in the PP channel can more robustly reveal the features of the PD source, e.g., the magnitude, location, and waveform. Therefore, PD detection by analyzing the PP-modal signal can be better.

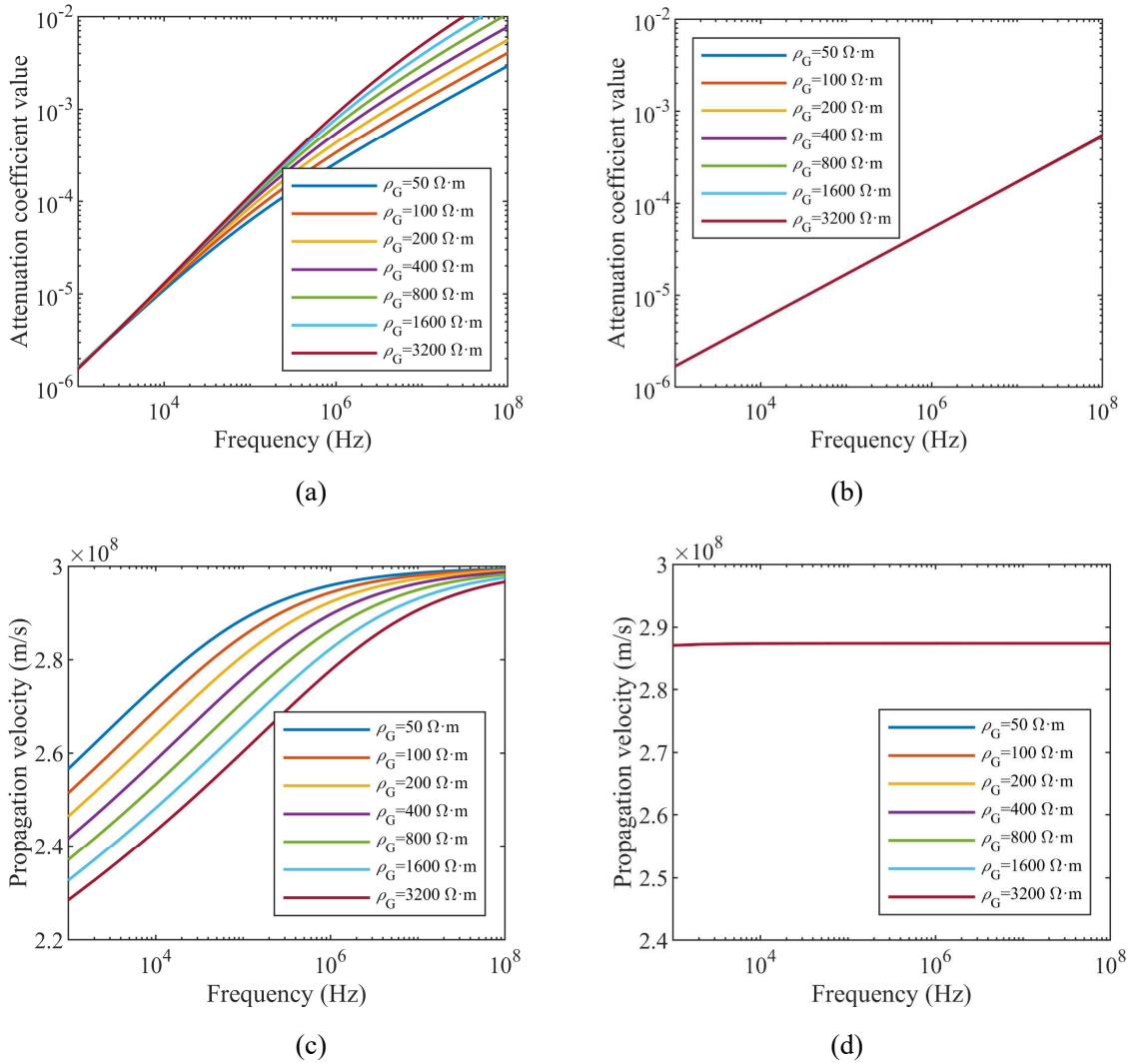

Figure 2-16 Effect of ρ_G on the propagation constants of the PG and PP channels (h=12 m, d=0.4 m, r=0.004 m, and R=0.008 m): (a) $\alpha_{PG}(\omega)$; (b) $\alpha_{PP}(\omega)$; (c) $v_{PG}(\omega)$; (d) $v_{PP}(\omega)$.

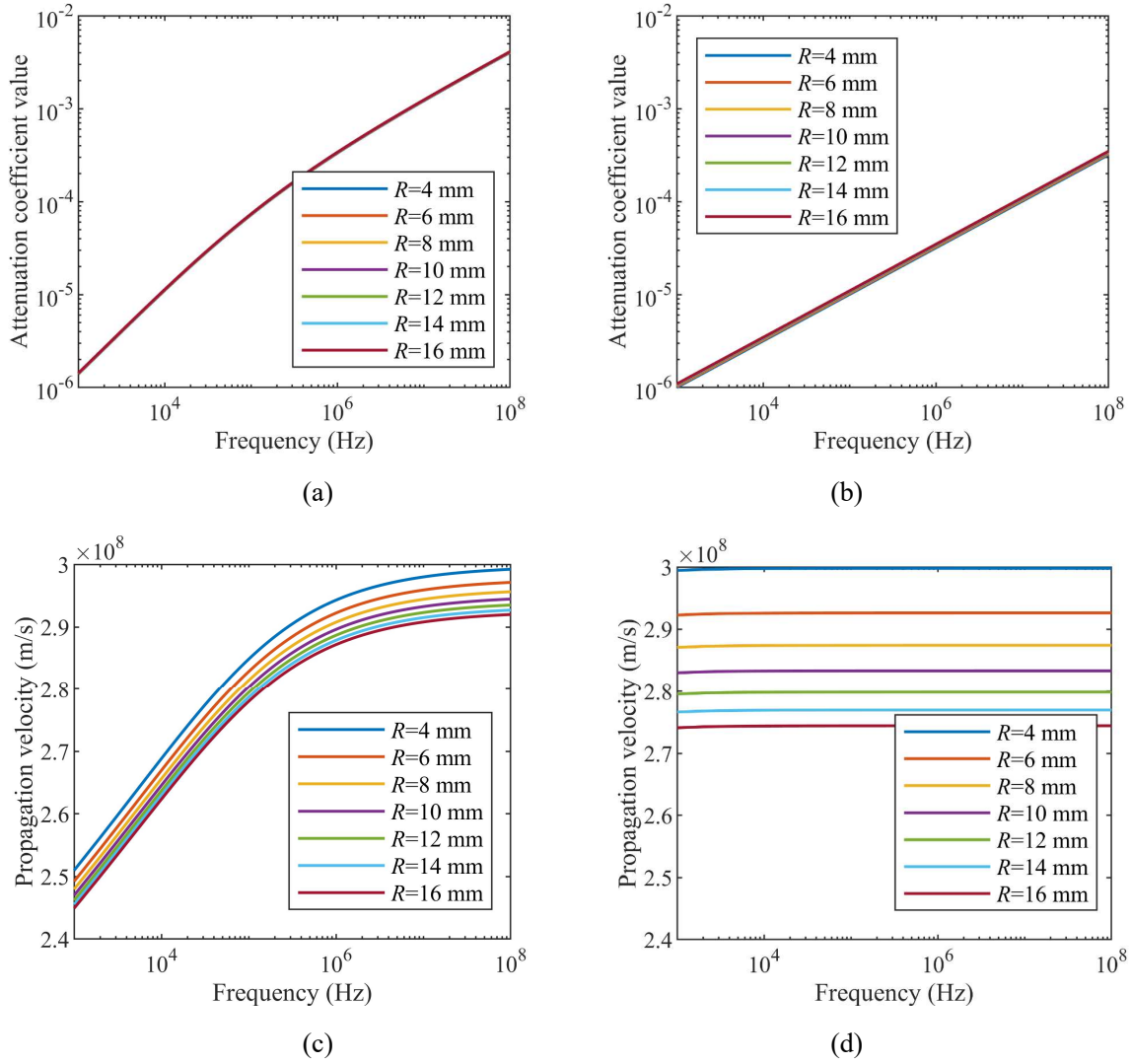

Figure 2-17 Effect of R on the propagation constants of the PG and PP channels (h=12 m, d=0.4 m, r=0.004 m, and ρ_G=100 Ω • m): (a) $\alpha_{PG}(\omega)$; (b) $\alpha_{PP}(\omega)$; (c) $v_{PG}(\omega)$; (d) $v_{PP}(\omega)$.

5）Propagation Constants Measurement Method

Besides the developed analytical model, the propagation constants can be measured via the time-domain reflection method. The time-domain reflection method is a common technique used to measure the propagation constant of transmission lines. The principle behind this method is based on the fact that when a signal is transmitted along a transmission line, it shows a reflection at any point where there is a change in the characteristic impedance of the line [54]. These reflections result in echoes that can be detected and analyzed to determine the transmission line's properties. To use the time-domain reflection method to measure the propagation constant of a transmission line, a test signal is first sent down the line from the source side. The signal propagates along the line until it encounters an impedance mismatch, causing a portion of the signal to be reflected towards the source. This reflected signal travels back along the line toward the source, interacting with the original signal. By analyzing the interaction between the original signal and the reflected

signal, it is possible to determine the transmission line's properties, including its characteristic impedance, propagation constant, and the location of any impedance mismatches along the line. The propagation constants of the PG and PP channels can be calculated as

$$\gamma_{\mathrm{PG}}(\omega) = -\frac{1}{2\wp}\ln\left(\frac{I_{\mathrm{a}}^{-}(0,\omega)+I_{\mathrm{b}}^{-}(0,\omega)+I_{\mathrm{c}}^{-}(0,\omega)}{I_{\mathrm{a}}^{+}(0,\omega)+I_{\mathrm{b}}^{+}(0,\omega)+I_{\mathrm{c}}^{+}(0,\omega)}\right) \tag{2-50}$$

$$\gamma_{\mathrm{PP}}(\omega) = -\frac{1}{2\wp}\ln\frac{1}{3}\left(\frac{I_{\mathrm{a}}^{-}(0,\omega)-I_{\mathrm{b}}^{-}(0,\omega)}{I_{\mathrm{a}}^{+}(0,\omega)-I_{\mathrm{b}}^{+}(0,\omega)}+\frac{I_{\mathrm{b}}^{-}(0,\omega)-I_{\mathrm{c}}^{-}(0,\omega)}{I_{\mathrm{b}}^{+}(0,\omega)-I_{\mathrm{c}}^{+}(0,\omega)}+\frac{I_{\mathrm{a}}^{-}(0,\omega)-I_{\mathrm{c}}^{-}(0,\omega)}{I_{\mathrm{a}}^{+}(0,\omega)-I_{\mathrm{c}}^{+}(0,\omega)}\right) \tag{2-51}$$

where $I_{\mathrm{a/b/c}}^{+}(0,\omega)$ and $I_{\mathrm{a/b/c}}^{-}(0,\omega)$ the forward and backward currents of phase conductor A, B, and C at the location of the PD detectors, respectively, and $\wp$ is the distance between the PD detectors and the open end. The time-domain reflection method measures the time delay and amplitude of these reflections and uses this information to calculate the propagation constant of the transmission line.

A laboratory experiment was conducted to measure the propagation of the overhead covered conductor line, as shown in Figure 2-18. The physical parameters of a 100-m three-phase overhead line are listed in Table 2-1. A pulse generator was mounted on the start side of the overhead line, and it can generate a single-polarity pulse. Three PD detectors (i.e., high-frequency current transformers) are mounted 50 m (i.e., $\wp = 50$ m) from the start. The end side of the overhead line is open.

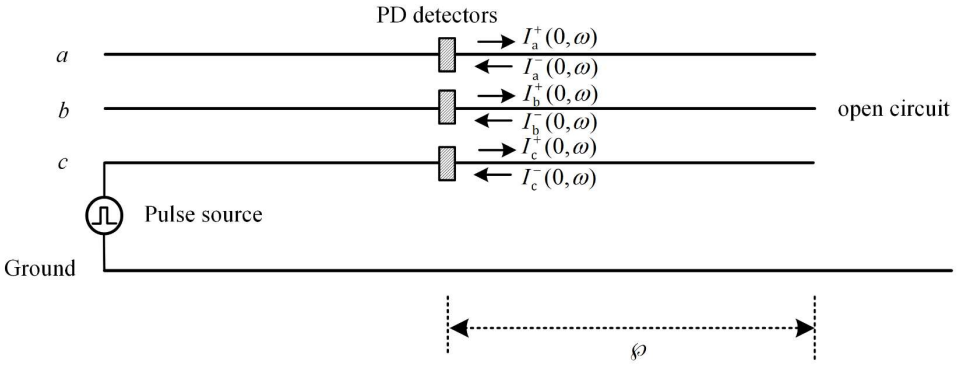

Figure 2-18 Layout of the pulse generator and PD detectors for the propagation parameter measurement of a three-phase overhead line via the time-domain reflection method.

Figure 2-19 collects the waveforms of PP and PG channels, which are calculated via the current waveforms of three-phase PD detectors. It can be observed that the attenuation and dispersion phenomenon in the PG channel is more significant than that in the PP channel. To further distinguish their difference, the two channels' attenuation coefficients and propagation velocities are calculated via Equations (2-46)-(2-51). Moreover, the analytical attenuation coefficients and propagation velocities were also calculated via Equations

(2-37)-(2-49), as shown in Figure 2-20. It is essential to point out that the amplitude of both ends of the original and reflected signals should be the same to avoid truncation errors; moreover, each lot of the truncated signals is supplemented with 2000 sampling points of amplitude 0 V to improve the resolution in the frequency domain analysis. It can be observed that the measured results are consistent with the simulated analytical results, demonstrating the effectiveness of the developed models of a three-phase overhead line; the attenuation coefficients of the PG channel are more significant than that of the PP channel; the propagation velocities of PG channel are significantly less than that of PP channel, and they are sensitive to frequency.

Table 2-1 Physical parameters of the three-phase overhead CC line

Parameter	values	Description
L	100 m	The length of the overhead conductors
h	1.5 m	The average height of the overhead conductors
r	0.0048 m	The radius of the bare overhead conductors
R	0.0082 m	The radius of the covered overhead conductors
d	0.3 m	The distance between the overhead conductors
ρ_G	138 Ω · m	The resistivity of the earth
ρ_{al}	2.7×10^{-8} S/m	The resistivity of the aluminum conductors
ε	8.854 × 10−12 H/m	The permittivity of the air
μ	4π × 10−7 H/m	The permeability of the air

2.3 Influence of Alongside Towers: Reflections and Refractions

The PD signal's frequency components of interest are up to tens of MHz in overhead distribution networks. In such a frequency range, the stray parameters of the alongside towers cannot be ignored, unlike the fault transients with a center frequency of tens of kHz [123]. Therefore, modeling the effect of the alongside apparatuses is crucial for accurately describing the PD propagation characteristics in the overhead distribution network. However, to our best knowledge, no published paper or materials has ever discussed or presented the influence of the MV towers on a signal (i.e., PD signal) with frequency components of tens of MHz (as shown in Figure 2-3). Accordingly, this section focuses on modeling the MV towers in the frequency range from DC to MHz. This section first describes the high-frequency equivalent circuit of four typical towers by modeling their detailed components. Finally, the time-domain reflection method based on the non-invasive inductive pulse injection technique is presented to measure the equivalent circuit parameters of the towers, and the accuracy of developed models for the towers is validated via field measurements.

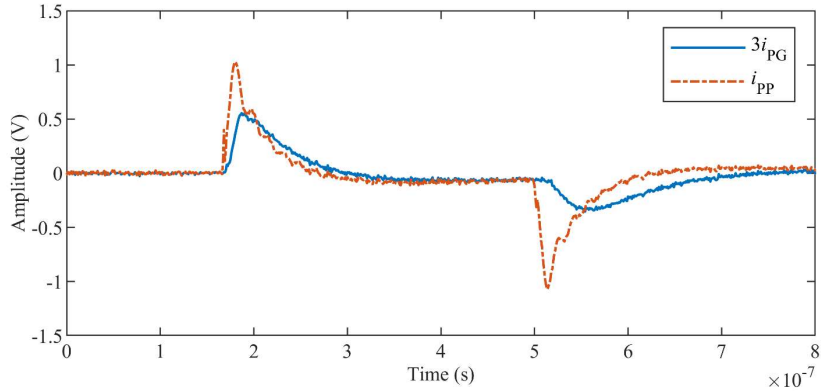

Figure 2-19 Current waveforms of the PG and PP channels in the three-phase overhead covered conductor line.

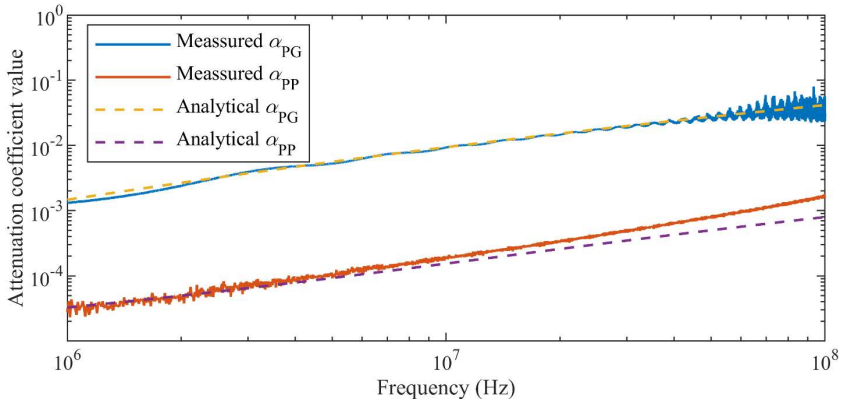

(a)

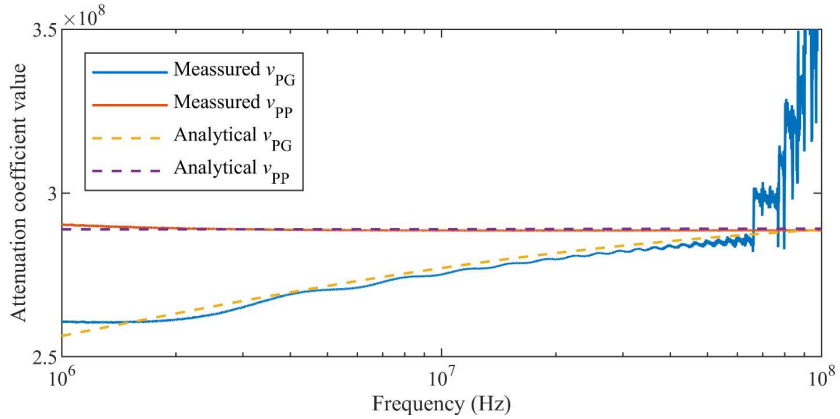

(b)

Figure 2-20 Results of attenuation coefficients (a) and propagation velocities (b) of the 100-m 10-kV three-phase overhead covered conductors in the laboratory.

2.3.1 Genetic Model of Alongside Towers

The tower's influence on PD propagation can generally be described via a 3×3 state transform matrix $\mathbf{\Phi}_{\text{tower}}(\omega)$, as shown in Figure 2-21. The line currents $\mathbf{I}_{\text{out}}(z,\omega) = [I_{a,\text{out}}(z,\omega), I_{b,\text{out}}(z,\omega), I_{c,\text{out}}(z,\omega)]^{\text{T}}$ after the tower can be defined as

$$\mathbf{I}_{\text{out}}(z,\omega) = \mathbf{\Phi}_{\text{tower}}(\omega) \cdot \mathbf{I}_{\text{in}}(z,\omega) \tag{2-52}$$

where $\mathbf{I}_{\text{in}}(z,\omega)=\left[I_{a,\text{out}}(z,\omega),I_{b,\text{out}}(z,\omega),I_{c,\text{out}}(z,\omega)\right]^{\text{T}}$ is the line currents before the tower. In the following subsection, we will derive the formulas of the state transform matrices.

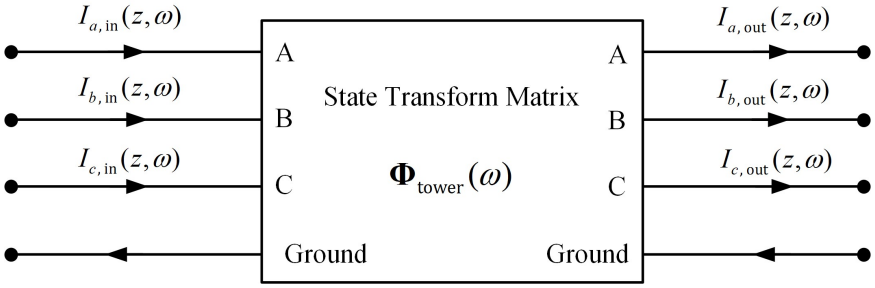

Figure 2-21 State transform matrix of the tower.

Since the sizes of the alongside apparatuses on the tower are significantly smaller than the wavelength corresponding to the concerned frequency components (i.e., < 50 MHz) in the PD signal, the symmetrical tower can be modeled as a lumped-parameter circuit, which can be described as via the impedance and admittance matrices $\mathbf{Z}_{\text{tower}}$ and $\mathbf{Y}_{\text{tower}}$ as

$$\mathbf{Z}_{\text{tower}}=\begin{bmatrix} Z'_p & Z'_m & Z'_m \\ Z'_m & Z'_p & Z'_m \\ Z'_m & Z'_m & Z'_p \end{bmatrix} \tag{2-53}$$

$$\mathbf{Y}_{\text{tower}}=\begin{bmatrix} Y'_p & Y'_m & Y'_m \\ Y'_m & Y'_p & Y'_m \\ Y'_m & Y'_m & Y'_p \end{bmatrix} \tag{2-54}$$

where Z'_p and Z'_m denote the self- and mutual impedances of the phase conductors, respectively, and Y'_p and Y'_m represent the self- and mutual admittances of the phase conductors, respectively. Since the non-diagonal elements (i.e., Z'_m and Y'_m) of $\mathbf{Z}_{\text{tower}}$ and $\mathbf{Y}_{\text{tower}}$ are non-zero, leading to the coupling between the line currents. Like the three-phase transmission line, $\mathbf{Z}_{\text{tower}}$ and $\mathbf{Y}_{\text{tower}}$ can be decoupled via the Karrenbauer phase-mode transformation. The decoupled impedance and admittance matrices $\mathbf{Z}_{\text{tower012}}$ and $\mathbf{Y}_{\text{tower012}}$ can be calculated as

$$\begin{aligned}\mathbf{Z}_{\text{tower012}}&=\begin{bmatrix} Z'_{\text{PG}} & 0 & 0 \\ 0 & Z'_{\text{PP}} & 0 \\ 0 & 0 & Z'_{\text{PP}} \end{bmatrix}=\mathbf{T}\cdot\mathbf{Z}_{\text{tower}}\cdot\mathbf{T}^{-1}\\ &=\begin{bmatrix} Z'_P+2Z'_m & 0 & 0 \\ 0 & Z'_P-Z'_m & 0 \\ 0 & 0 & Z'_P-Z'_m \end{bmatrix}\end{aligned} \tag{2-55}$$

$$\begin{aligned}\mathbf{Y}_{\text{tower012}}&=\begin{bmatrix} Y'_{\text{PG}} & 0 & 0 \\ 0 & Y'_{\text{PP}} & 0 \\ 0 & 0 & Y'_{\text{PP}} \end{bmatrix}=\mathbf{T}\cdot\mathbf{Y}_{\text{tower}}\cdot\mathbf{T}^{-1}\\ &=\begin{bmatrix} Y'_P+2Y'_m & 0 & 0 \\ 0 & Y'_P-Y'_m & 0 \\ 0 & 0 & Y'_P-Y'_m \end{bmatrix}\end{aligned} \tag{2-56}$$

where Z'_{PG} and Z'_{PP} denote the impedances in the PG and PP channels, respectively, and Y'_{PG} and Y'_{PP} represent the admittances in the PG and PP channels, respectively. Since the PG and PP channels are decoupled, a two-conductor Peterson's equivalent circuit can be used to calculate the reflection and refraction coefficients of any one channel, as shown in Figure 2-22, taking the PG channel as an example. The reflection and refraction coefficients $\mathrm{T_{PG}}$ and $\mathrm{\Gamma_{PG}}$ can be defined as

$$T_{\mathrm{PG}} = 2\frac{\frac{1}{Y'_{\mathrm{PG}}} // Z_{\mathrm{C,PG}}}{Z_{\mathrm{C,PG}} + Z'_{\mathrm{PG}} + \frac{1}{Y'_{\mathrm{PG}}} // Z_{\mathrm{C,PG}}} \tag{2-57}$$

$$\Gamma_{\mathrm{PG}} = \frac{Z_{\mathrm{C,PG}} - Z'_{\mathrm{PG}} - \frac{1}{Y'_{\mathrm{PG}}} // Z_{\mathrm{C,PG}}}{Z_{\mathrm{C,PG}} + Z'_{\mathrm{PG}} + \frac{1}{Y'_{\mathrm{PG}}} // Z_{\mathrm{C,PG}}} \tag{2-58}$$

where $Z_{\mathrm{C,PG}}$ is the PG-channel characteristics impedance of the three-phase overhead line. Similarly, the reflection and refraction coefficients $\mathrm{T_{PP}}$ and $\mathrm{\Gamma_{PP}}$ in the PP channel can be obtained as the same in the PG channel.

If only the first PD pulse is of interest, the decoupled state transform matrix $\mathbf{\Phi}_{\mathrm{tower012}}(\omega)$ can be defined as

$$\mathbf{\Phi}_{\mathrm{tower012}}(\omega) = \begin{bmatrix} T_{\mathrm{PG}} & 0 & 0 \\ 0 & T_{\mathrm{PP}} & 0 \\ 0 & 0 & T_{\mathrm{PP}} \end{bmatrix} \tag{2-59}$$

Accordingly, the coupled state transform matrix can be obtained via the inverse Karrenbauer phase-mode transformation, and it can be calculated as

$$\mathbf{\Phi}_{\mathrm{tower}}(\omega) = \mathbf{T}^{-1} \cdot \mathbf{\Phi}_{\mathrm{tower012}}(\omega) \cdot \mathbf{T} \tag{2-60}$$

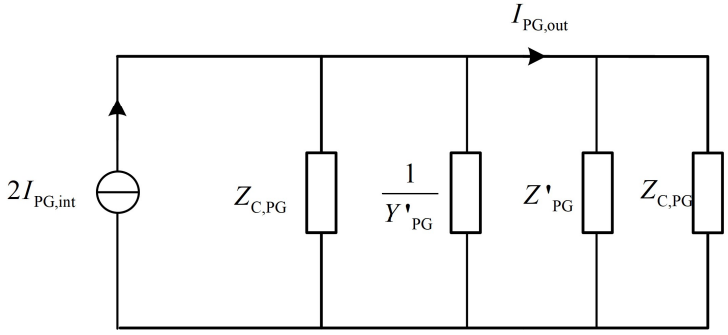

Figure 2-22 Peterson's equivalent circuit of the PG channel at the tower.

2.3.2 Equivalent Circuits of Tower Models

In the MV overhead distribution network, the towers can be divided into four categories: supporting tower, branch tower, transformer tower, and breaker tower. These towers comprise multiple power apparatuses, including insulators, arresters, power transformers, potential transformers, current transformers, breakers, etc. The tower models can be obtained by combining models of the power apparatuses. This subsection first presents the models of

the power apparatuses in the PG and PP channels. Then, the simplified models for the four typical towers are developed. Finally, the measurement experiments were carried out to validate the effectiveness of the developed tower models.

1）Simplified Equivalent Circuits of Shunt or Series Apparatuses on Towers

The MV overhead distribution network includes a mass of alongside apparatuses, which can generally be divided into two categories: the shunt apparatuses and the series apparatuses. The shunt apparatuses include insulators, arrestors, power transformers, and potential transformers; the series consists of breakers, current transformers, and connecting lines. Table 2-2 collects the simplified three-phase equivalent circuit models of these apparatuses and equivalent circuits in PG and PP channels. Details of the models are described as follows.

Table 2-2 Simplified equivalent circuits of the alongside apparatuses

Types	Power apparatuses	Simplified three-phase equivalent circuit	Equivalent circuit in PG mode		Equivalent circuit in PP mode
Shunt apparatuses	Insulator Arrestor	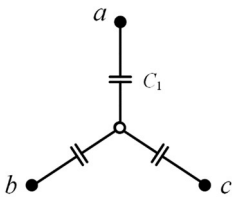	 (neutral grounding)	/ (ungrou -nding)	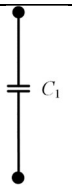 (neutral grounding or ungrounding)
	Power or potential Transformer	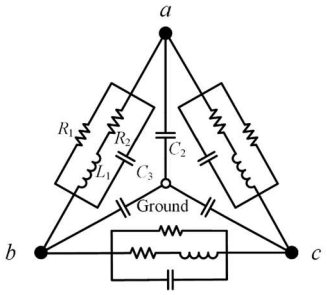			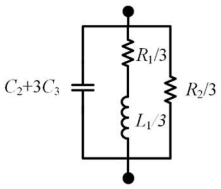
Series apparatuses	Breaker Current Transformer Connecting line	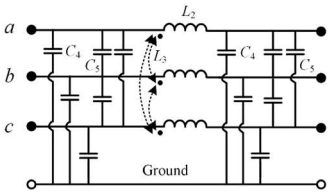	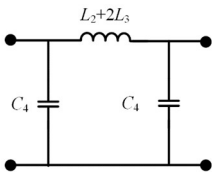		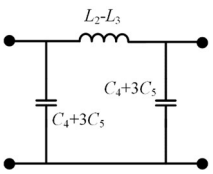

The insulators and arrestors connect the tower's overhead line and metal cross-arm. Insulators support the overhead line from the ground; arrestors protect the overhead line and other apparatuses from lightning and system transient overvoltage. Generally, they can be

equivalent to a capacitance for the high-frequency PD signal. If the metal cross-arm connected to the insulators is connected to the ground, the value of the equivalent capacitance in the PG channel is equal to that of the PP channel; if not, the value of the equivalent capacitance in the PG channel is equal to zero.

Power or potential transformers in the overhead distribution network are always mounted on the middle and ends of the system. In China, almost all transformers are connected to the three-phase MV overhead line via Delta Connection; the equivalent circuit of the transformers can be modeled as shown in Table 2-2. R_1, R_2, L_1, and C_3 denote the equivalent circuit of the interphase windings; C_2 denote the phase to ground capacitance. The transformer can be identical to the capacitance C_2 in the PG channel, while it needs to be described by R_1, R_2, L_1, C_2, and C_3 in the PP channel.

The series apparatuses, including breakers, current transformers, and connection lines, can generally be equivalent to a π-type circuit, as shown in Table 2-2. C_4 and C_5 are used to describe the input or output self- or mutual capacitances, L_2 and L_3 are used to describe the self- or mutual inductances. The series apparatuses can be characterized by C_4, C_5, L_2, and L_3 in PP and PG channels.

2）Equivalent Circuits of Four Typical Towers

The overhead distribution network always consists of three-phase overhead lines and towers. In general, the towers can be divided into four categories: support towers, branch towers, transformer towers, and breaker towers. Each tower includes one or multiple types of apparatuses. The equivalent circuits of these towers are developed based on the equivalent circuits of the apparatuses presented in the last subsection, and they are listed in Table 2-3. More details of these equivalent circuits are described as follows.

The support tower includes three-phase insulators and one three-phase overhead line. If the metal cross-arm connected to the insulators is connected to the ground, the equivalent circuit in PG and PP channels can be described via a capacitance; if not, the equivalent circuit in the PP channel can still be characterized via a capacitance, while the effect of the insulators on PD propagation in PG channel can be ignored.

Branch towers include three-phase insulators, one overhead line, and multiple branches. If the metal cross-arm connected to the insulators is connected to the ground, the equivalent circuit in PG and PP channels can be described via a capacitor and impedance in parallel; if not, the equivalent circuit in PP channel can still be characterized via a capacitor and impedance in parallel, while the equivalent circuit in PG channel can still be described via an impedance. The impedance is associated with the number of branches N.

Transformer towers include multiple apparatuses, i.e., insulators, arrestors, connecting lines, and a power transformer. The equivalent circuit of the transformer tower is obtained by combining various equivalent circuits of these apparatuses in series or parallel, as shown in the fourth row in Table 2-3. Since the metal cross-arm connected to all apparatuses in the transformer tower is always connected to the ground, the effect of these apparatuses cannot be ignored.

The breaker tower includes insulators, arrestors, potential and current transformers (i.e.,

PT and CT), connecting lines, and a breaker. Similar to the transformer tower, the equivalent circuit of the breaker tower is obtained by combining multiple equivalent circuits of these apparatuses in series or parallel, as shown in the fifth row in Table 2-3. The metal cross-arm connected to all apparatuses in the breaker tower is always connected to the ground.

Table 2-3 Simplified equivalent circuits of the alongside towers

Types	Pictures	Simplified equivalent circuit in PG channel		Simplified equivalent circuit in PP channel
Support tower (including insulators)		 (neutral grounding)	/ (neutral ungrounding	 (neutral grounding or ungrounding)
Branch tower (including insulators and multiple branches)		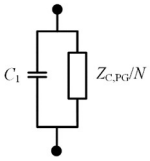		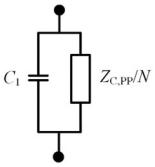
Transformer tower (including insulators, arrestors, connecting lines, and a power transformer)		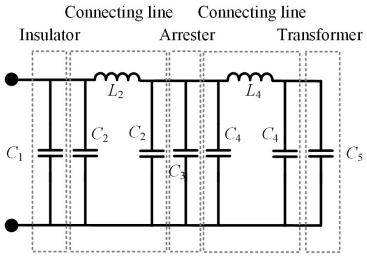		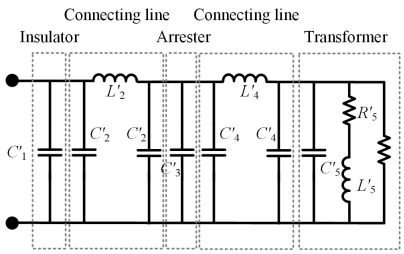
Breaker tower (including insulators, arrestors, potential and current transformers (i.e., PT and CT), connecting lines, and a breaker)		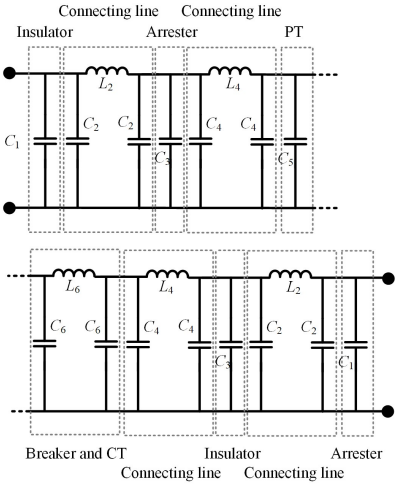		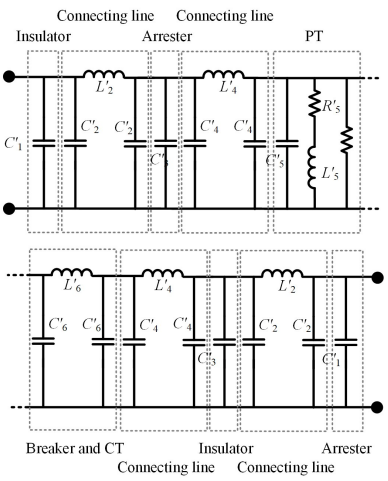

2.3.3 Online Measurement of the Propagation Characteristics of the Towers

The propagation characteristics of the towers can be described via the reflection and refraction coefficients in PG and PP channels, i.e., $\Gamma_{\mathrm{PG}}(\omega)$, $\Gamma_{\mathrm{PP}}(\omega)$, $T_{\mathrm{PG}}(\omega)$, and $T_{\mathrm{PP}}(\omega)$. They can be obtained based on the time-domain reflection technique, as shown in Figure 2-23. A pulse injector is non-invasively mounted on one phase of the overhead line; three PD detectors are mounted close to the pulse injector; another three PD detectors are mounted on the tower's output. The pulse injector can generate a single-polarity spike pulse and inject the pulse into the overhead line via inductive coils. The PD detectors use high-frequency current transformers as their sensors, and their frequency passband ranges from 0.1 MHz to 100 MHz. It is important to point out that the distance $\wp$ between the left PD detectors is about 50 m. Too small $\wp$ can lead to difficulty in separating the direct pulse and its reflection; too large $\wp$ can lead to non-negligible attenuation and dispersion errors.

By analyzing the collected signals, $\Gamma_{\mathrm{PG}}(\omega)$, $\Gamma_{\mathrm{PP}}(\omega)$, $T_{\mathrm{PG}}(\omega)$, and $T_{\mathrm{PP}}(\omega)$ can be obtained as:

$$T_{\mathrm{PG}}(\omega)=\frac{I_{\mathrm{a,out}}(\wp,\omega)+I_{\mathrm{b,out}}(\wp,\omega)+I_{\mathrm{c,out}}(\wp,\omega)}{I_{\mathrm{a}}^{+}(0,\omega)+I_{\mathrm{b}}^{+}(0,\omega)+I_{\mathrm{c}}^{+}(0,\omega)} \tag{2-61}$$

$$\Gamma_{\mathrm{PG}}(\omega)=\frac{I_{\mathrm{a}}^{-}(0,\omega)+I_{\mathrm{b}}^{-}(0,\omega)+I_{\mathrm{c}}^{-}(0,\omega)}{I_{\mathrm{a}}^{+}(0,\omega)+I_{\mathrm{b}}^{+}(0,\omega)+I_{\mathrm{c}}^{+}(0,\omega)} \tag{2-62}$$

$$\begin{aligned}T_{\mathrm{PP}}(\omega)=\frac{1}{3}\Bigg(&\frac{I_{\mathrm{a,out}}(\wp,\omega)-I_{\mathrm{b,out}}(\wp,\omega)}{I_{\mathrm{a}}^{+}(0,\omega)-I_{\mathrm{b}}^{+}(0,\omega)}+\frac{I_{\mathrm{b,out}}(\wp,\omega)-I_{\mathrm{c,out}}(\wp,\omega)}{I_{\mathrm{b}}^{+}(0,\omega)-I_{\mathrm{c}}^{+}(0,\omega)}\\&+\frac{I_{\mathrm{a,out}}(\wp,\omega)-I_{\mathrm{c,out}}(\wp,\omega)}{I_{\mathrm{a}}^{+}(0,\omega)-I_{\mathrm{c}}^{+}(0,\omega)}\Bigg)\end{aligned} \tag{2-63}$$

$$\begin{aligned}\Gamma_{\mathrm{PP}}(\omega)=\frac{1}{3}\Bigg(&\frac{I_{\mathrm{a}}^{-}(0,\omega)-I_{\mathrm{b}}^{-}(0,\omega)}{I_{\mathrm{a}}^{+}(0,\omega)-I_{\mathrm{b}}^{+}(0,\omega)}+\frac{I_{\mathrm{b}}^{-}(0,\omega)-I_{\mathrm{c}}^{-}(0,\omega)}{I_{\mathrm{b}}^{+}(0,\omega)-I_{\mathrm{c}}^{+}(0,\omega)}\\&+\frac{I_{\mathrm{a}}^{-}(0,\omega)-I_{\mathrm{c}}^{-}(0,\omega)}{I_{\mathrm{a}}^{+}(0,\omega)-I_{\mathrm{c}}^{+}(0,\omega)}\Bigg)\end{aligned} \tag{2-64}$$

where $I_{\mathrm{a/b/c}}^{+}(0,\omega)$ and $I_{\mathrm{a/b/c}}^{-}(0,\omega)$ are the direct and reflected pulses collected by the left PD detectors, and $I_{\mathrm{a/b/c,out}}(\wp,\omega)$ is the refracted pulse collected by the right PD detectors.

Figure 2-24 collects the waveforms of the left and right PD monitors to measure a support tower's reflection and refraction coefficients. The amplitude and pulse width of the injected signal is 20 V and 40 ns. The sampling ratio of the data acquisition unit is 500MS/s. It can be observed that the support tower can lead to a significant reflection, validating that the tower's effect is non-negligible. The pulses in the dashed boxes are extracted to calculate

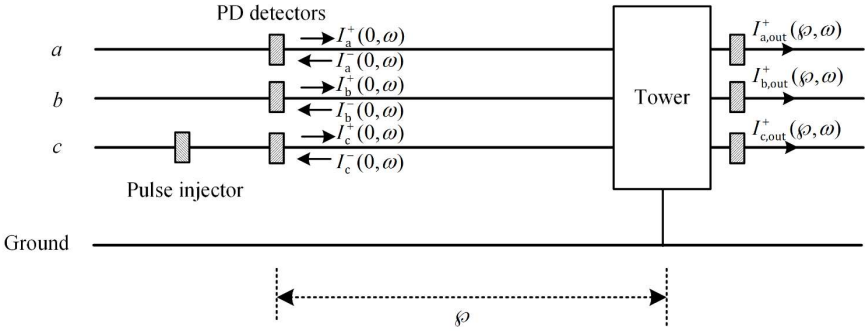

Figure 2-23 Illustration of online measurement of the reflection and refraction coefficients of the tower.

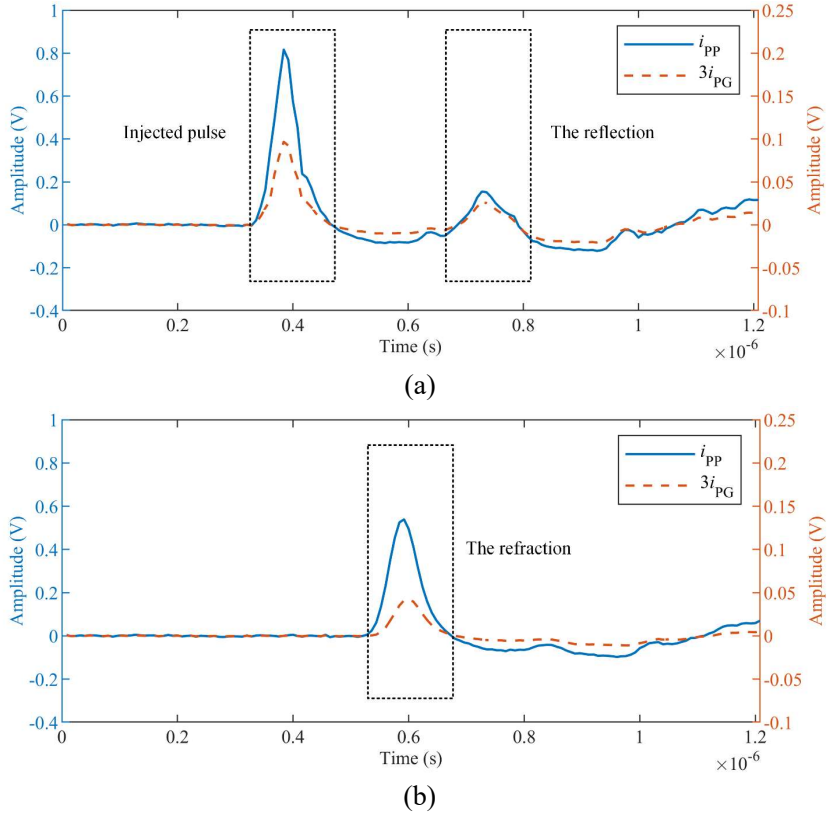

Figure 2-24 Reflection and refraction waveforms of the PG and PP channels, measured by the left (a) and right (b) PD detectors in Figure 2-23, respectively.

the reflection and refraction coefficients. It is essential to point out that the amplitude of both ends of the intercepted signal should be the same to avoid truncation errors; moreover, each lot of the truncated signals is supplemented with 2000 sampling points of amplitude 0 V to improve the resolution in the frequency domain analysis. The calculated reflection and refraction coefficients are shown in Figure 2-25. It can be observed that the measured results are consistent with the analytical value, demonstrating the effectiveness of the proposed model of the support tower. Moreover, the reflection coefficients in the PG channel are significantly more significant than those in the PP channel, meaning that the PD signal in the PG channel will lose more energy to get through the tower. The result proves that detecting PD in the PP channel can be better.

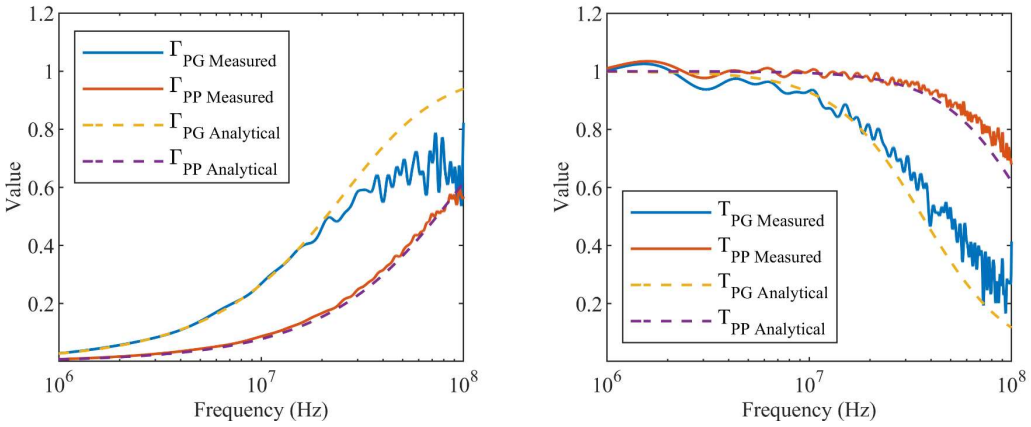

(a) (b)

Figure 2-25 Measured and analytical (C_1=10 pF) results of the supporting tower.

Figure 2-26, Figure 2-27, and Figure 2-28 collect the measured and analytical results of branch, transformer, and breaker towers. It can be observed that the analytical results are consistent with the measurements, demonstrating the effectiveness of the proposed models. The reflection coefficients of the branch tower increase from 1/3 as the frequency increases. The reflection and refraction coefficients of the transformer tower have multiple peaks and valleys, meaning that parts of the energy of the PD signal can be lost. The reflection coefficients of the breaker tower are almost equal to 1, meaning that most energy of the PD signal will be lost when the PD signal gets through the breaker tower.

Many of the above four types of towers are distributed in the MV overhead distribution network with a spacing of about 100 meters. In the network, the support rod is the most, the branch and transformer tower are the second, and the circuit breaker tower is the least. Therefore, the effect of the tower must be considered in the PD detection process, including the deployment of PD detectors, the parameter design of PD detectors, and the evaluation of PD magnitude and location, which are discussed as follows:

(1) Reflections at the towers can reduce the maximum propagation distance of a PD signal, e.g., most energy of a PD signal will be lost when the signal gets through the breaker tower. Therefore, the spacing between PD detectors should fully consider the

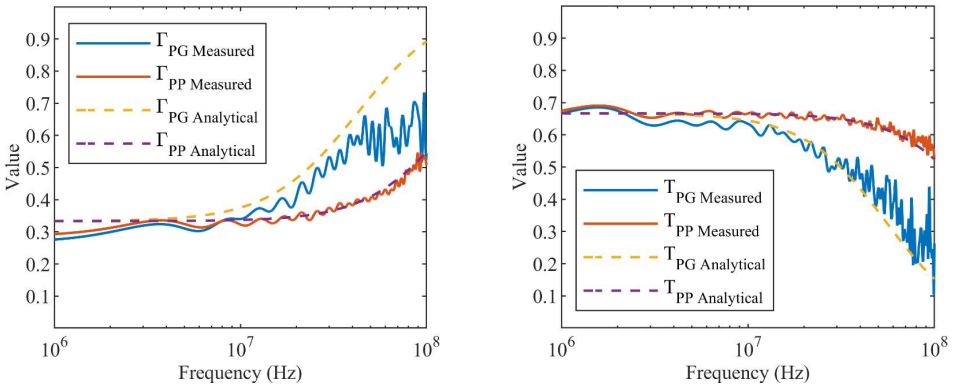

(a) (b)

Figure 2-26 Measured and analytical results of the branch tower (C_1=10 pF and N=1).

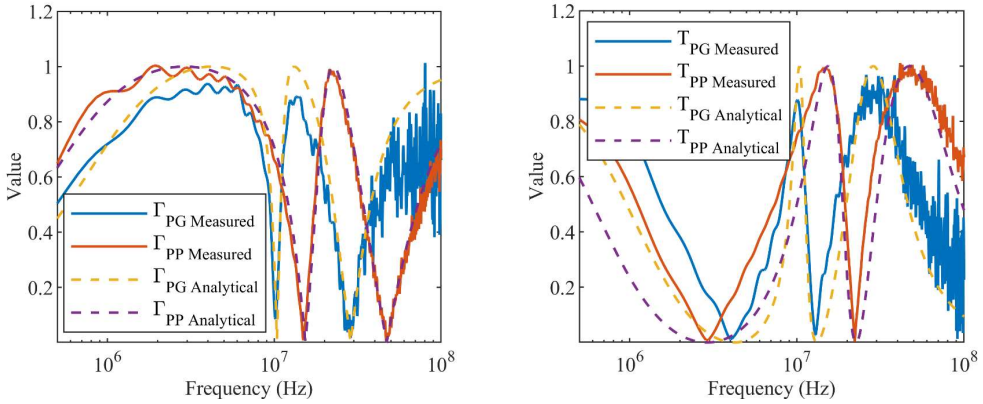

(a) (b)

Figure 2-27 Measured and analytical results of the transformer tower. (Parameter values of the theoretical model: C_1=10 pF, C_2=1 pF, C_3=100 pF, C_4=1 pF, C_5=200 pF, C'_1=10 pF, C'_2=5 pF, C'_3=100 pF, C'_4=5 pF, L'_2=0.85 uH, L'_4=0.85 uH, C'_5=1700 pF, L'_5=1.2 H, R'_{51}=20 kΩ, and R'_{52}=220 kΩ).

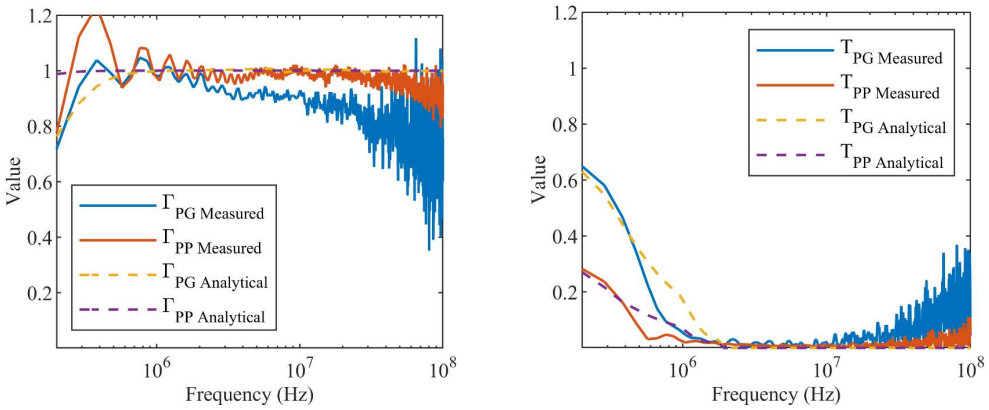

(a) (b)

Figure 2-28 Measured and analytical results of the breaker tower (Parameter values of the theoretical model: C_1=10 pF, C_2=1 pF, C_3=100 pF, C_4=1 pF, C_5=2000 pF, C_6=20 pF, L_2=3 uH, L_4=3 uH, L_6=500 pF C'_1=10 pF, C'_2=5 pF, C'_3=100 pF, C'_4=5 pF, C'_5=17000 pF, C'_6=60 pF, L'_2=0.85 uH, L'_4=0.85 uH, L'_6=500 uH, L'_5=12 H, R'_{51}=20 kΩ, and R'_{52}=220 kΩ).

influence of the towers to avoid missing detection.

(2) The propagation characteristics analysis of the towers helps us optimize the PD detector's design. For example, since the reflection coefficients of the transformer tower have multiple peaks and valleys, which depend on the structures and components of the tower, it is challenging to select the correct frequency sub-bands in which the signal attenuation is minimal. Therefore, ultra-wideband PD detectors can perform better since they won't miss the optimal sub-band.

(3) The attenuation and phase shift caused by the tower can lead to errors in PD detection and localization. On the one hand, the attenuation can reduce the magnitude of the PD signal collected by the PD detector at a remote distance, and the reflection may overlap with the original PD signal, leading to magnitude errors.

On the other hand, the phase shift can lead to additional time delays of the PD signal, reducing the accuracy of PD localization. The influence of alongside towers on PD detection and localization will be thoroughly discussed in the next section.

2.4 Simulation Experiment of the effects of line parameters and alongside towers on PD signal characteristics

This section discusses PD propagation characteristics in MV overhead distribution networks via the simulation experiment in PSCAD. The layout of the simulation experiments and parameters of the PD source are presented first. Then, the effects of propagation distances, non-uniform transmission line parameters, and alongside towers are thoroughly discussed via the simulations. Since the effects of line parameters have been discussed in Chapter 2.2.3, it is not considered in this simulation.

2.4.1 Layout of the Simulation Platform

1）Key Parameters of Partial Discharge Signal

A PD signal starting at time zero can be approximately modeled at the PD source by a double exponential pulse [57], as shown in Figure 2-29. The features of the PD pulse can be described via five time-domain parameters, i.e., the time-of-arrival t_{TOA}, the rising time t_{R}, the duration time t_{D}, the peak V_{peak}, and the discharge magnitude Q. These parameters play a crucial role in PD magnitude and location evaluation and classification [20][124][125]. These five parameters can be used to quantitatively evaluate the propagation effect on PD time-domain waveform.

2）PD Simulator

In this simulation, the PD signal is simulated via a pulse calibrator provided by IEC 60270 standard [20]. Figure 2-30 collects the sketch map of using the calibrator to generate a standard PD signal in equipment under test. The PD calibrator includes a square-wave generator with a voltage of U_0 and a capacitance of C_0. R_{m} is used to equivalent as the load. The discharge magnitude Q_0 of the generated pulse on the load can be defined as

$$Q_0 = U_0 C_0 \tag{2-65}$$

where Q_0 has nothing to do with the load; therefore, the pulse calibrator can be used to simulate a PD signal on any equipment under test, including the overhead line.

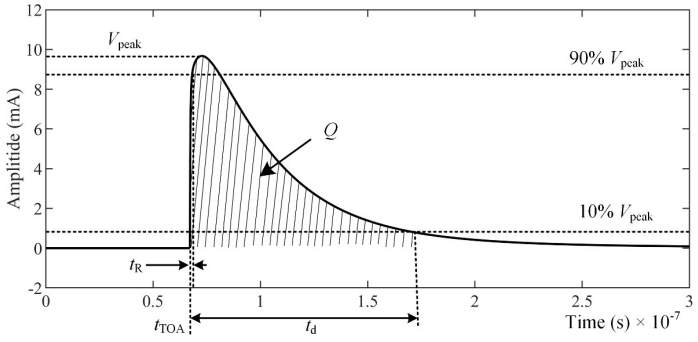

Figure 2-29 Waveform parameters of the typical PD current pulse at the PD source.

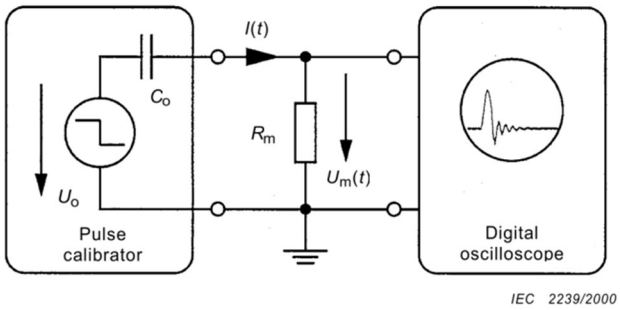

Figure 2-30 PD simulation circuit based on a pulse calibrator provided by IEC 60270 standard [20].

3）Layout of Simulation Circuits

An overhead distribution network simulation model was set up in the PSCAD platform, as shown in Figure 2-31. The model includes a pulse calibrator, 2000-m three-phase overhead lines with the model of JKLGYJ-10, and multiple towers. The pulse calibrator was connected between one phase of the overhead line, and U_0 and C_0 in the calibrator are set as 10 V and 0.096 nF, respectively, resulting in a PD pulse with a discharge magnitude of 0.96 nC. The structure of the three-phase overhead lines is shown on the right of Figure 2-31, and their physical parameters are listed in Table 2-4. The ground resistivity is set as 100 Ω·m, a value suggested in [122]. The towers are connected to the overhead line with a spacing of 100 m; they are represented in the PSCAD via the equivalent circuits developed in Chapter 2.3. The double sides of the overhead line are connected to two infinitely long (i.e., >100 km) overhead lines with the same parameters as the middle overhead line

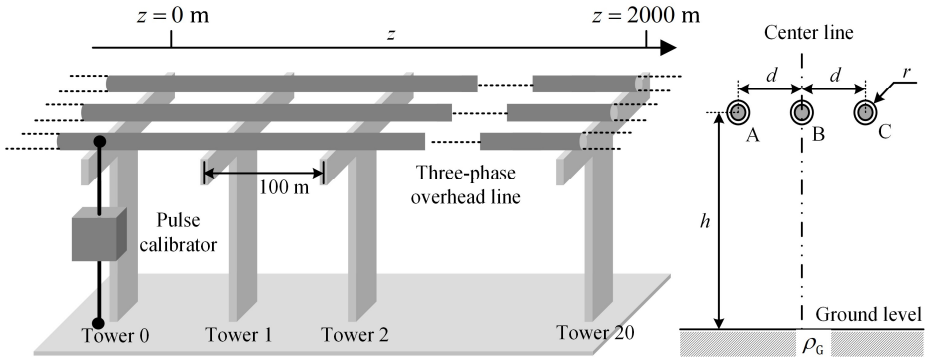

Figure 2-31 Layout of the simulation platform in PSCAD.

2.4.1 Effect of Propagation Distance

This subsection discusses the effect of the propagation distance on PD signal characteristics in three-phase conductors. Since the effects on voltages and currents are similar, only the current waveforms are displayed. In this simulation, the equivalent circuits of the towers were not connected to the overhead line, i.e., the alongside towers' effects were ignored to explain the effect of propagation distance better.

Figure 2-32 collects the current signals in the three-phase overhead line. It can be observed that as the propagation distance increases, the amplitude of the current in the PD-affected phase conductor decreases. Still, those of the other two-phase conductors

Table 2-4 Parameters of the three-phase overhead line

Parameter	values	Description
h	12 m	The average height of the overhead conductors
r	0.0048 m	The radius of the bare overhead conductors
R	0.0048 m	The radius of the covered overhead conductors
d	0.4 m	The distance between the overhead conductors
ρ_G	100 Ω·m	The resistivity of the earth
ρ_{al}	2.7×10^{-8} S/m	The resistivity of the aluminum conductors
ϵ	8.854 × 10−12 H/m	The permittivity of the air
μ	4π × 10−7 H/m	The permeability of the air

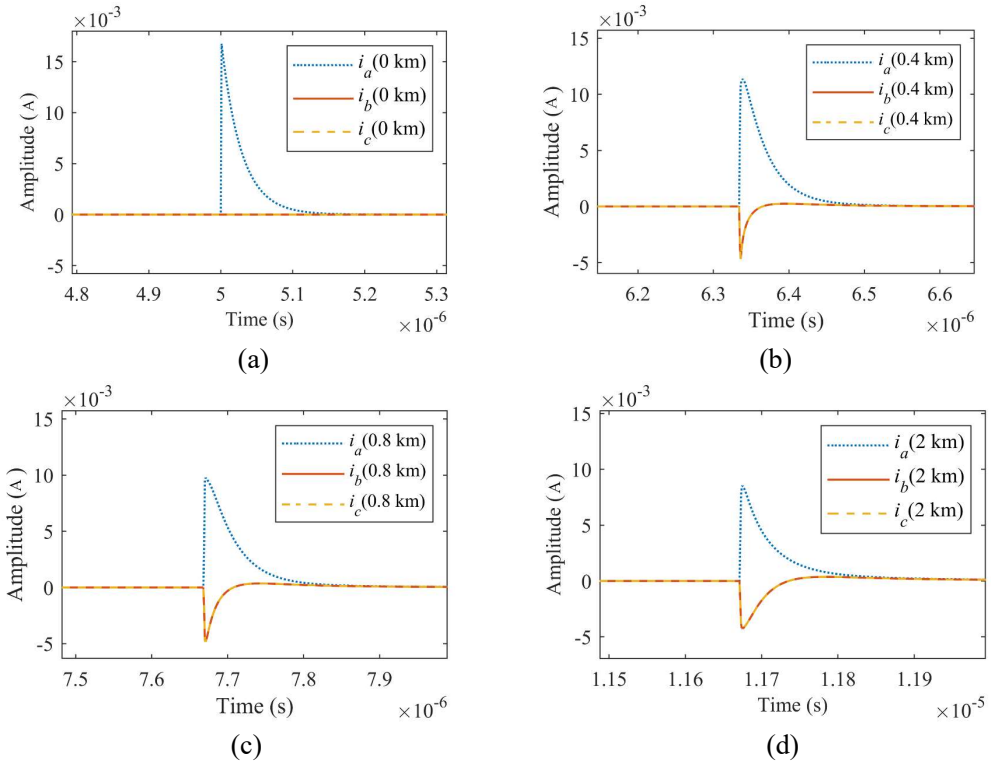

Figure 2-32 Three-phase current waveforms of the simulated PD pulse at varying distances.

increase when the propagation distance is more significant than a critical value (e.g., 1.6 km), and the amplitudes of the other two-phase conductors are almost half that of the PD-affected phase. The result reveals that we can detect the PD signal from any one-phase conductor, allowing us to decrease the number of PD detectors by reducing the budget. However, we must collect the three-phase conductors' data to identify which conductor is affected by the PD defect.

Figure 2-33 and Figure 2-34 collect the time-domain and frequency-domain waveforms of the transformed current signals in PG and PP channels, respectively. It can be observed

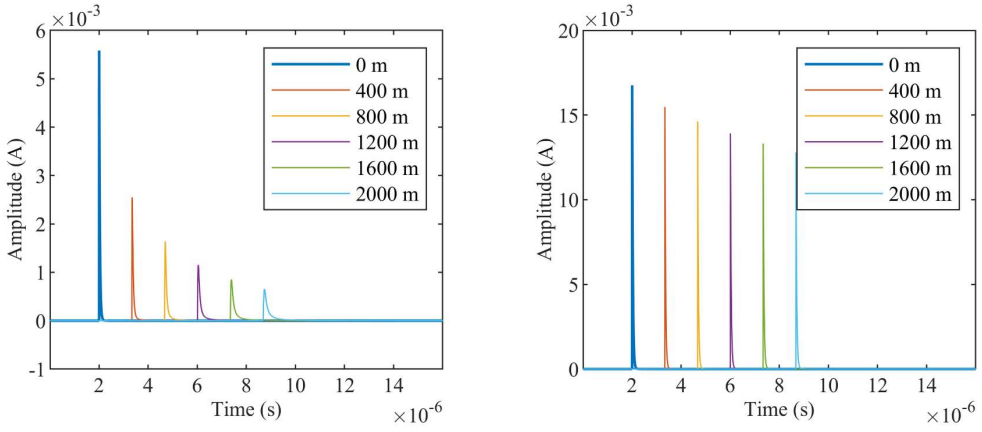

Figure 2-33 PD current waveforms of the PG (a) and PP (b) channels at different distances.

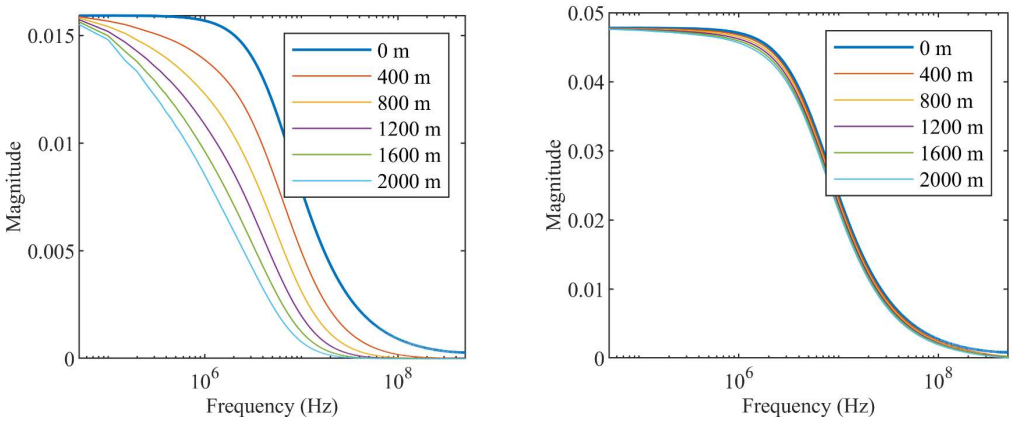

Figure 2-34 Frequency spectrum of the PD currents in the PG (a) and PP (b) channels at different distances.

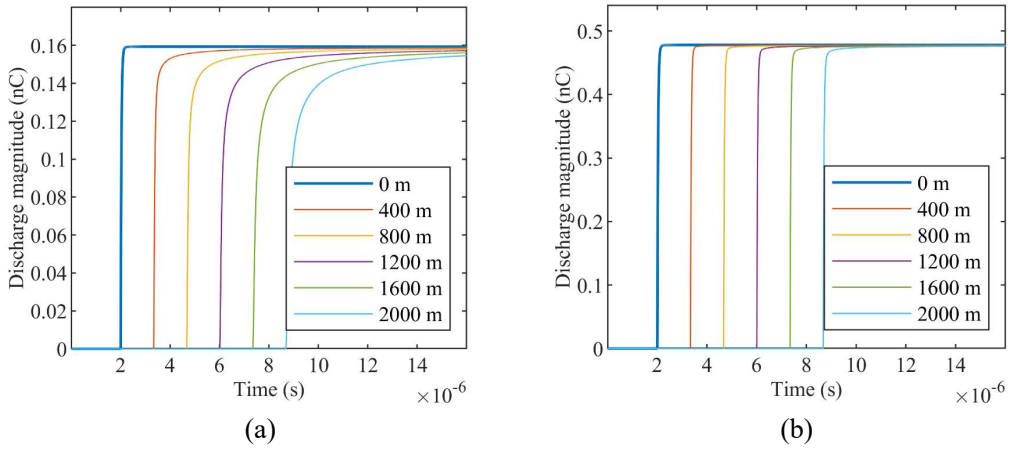

Figure 2-35 Integral curve of the PD currents in the PG (a) and PP (b) channels at different distances.

that the amplitude attenuation of the PD pulses in the PG channel is more significant than that in the PP channel. This reveals that PD detection in the PP channel can be better than in

the PG channel. Moreover, the discharge magnitudes were obtained by integrating the PD pulses' time-domain waveforms, as shown in Figure 2-35. It can be observed that the final integral values of all PD pulses are equal in PG or PP channels. This reveals that the discharge magnitude of the PD pulse is almost affected by the propagation distance.

Figure 2-36 collects the propagation distance's effect on the PD pulses' key parameters. It can be observed that as the propagation distance increases, the peaks of the PD pulses significantly decrease, the rising and falling times of the pulses increase, and the discharge magnitudes of the pulses are almost constant. Moreover, the parameter variations of PD pulses in the PP channel are much more minor than in the PG channel.

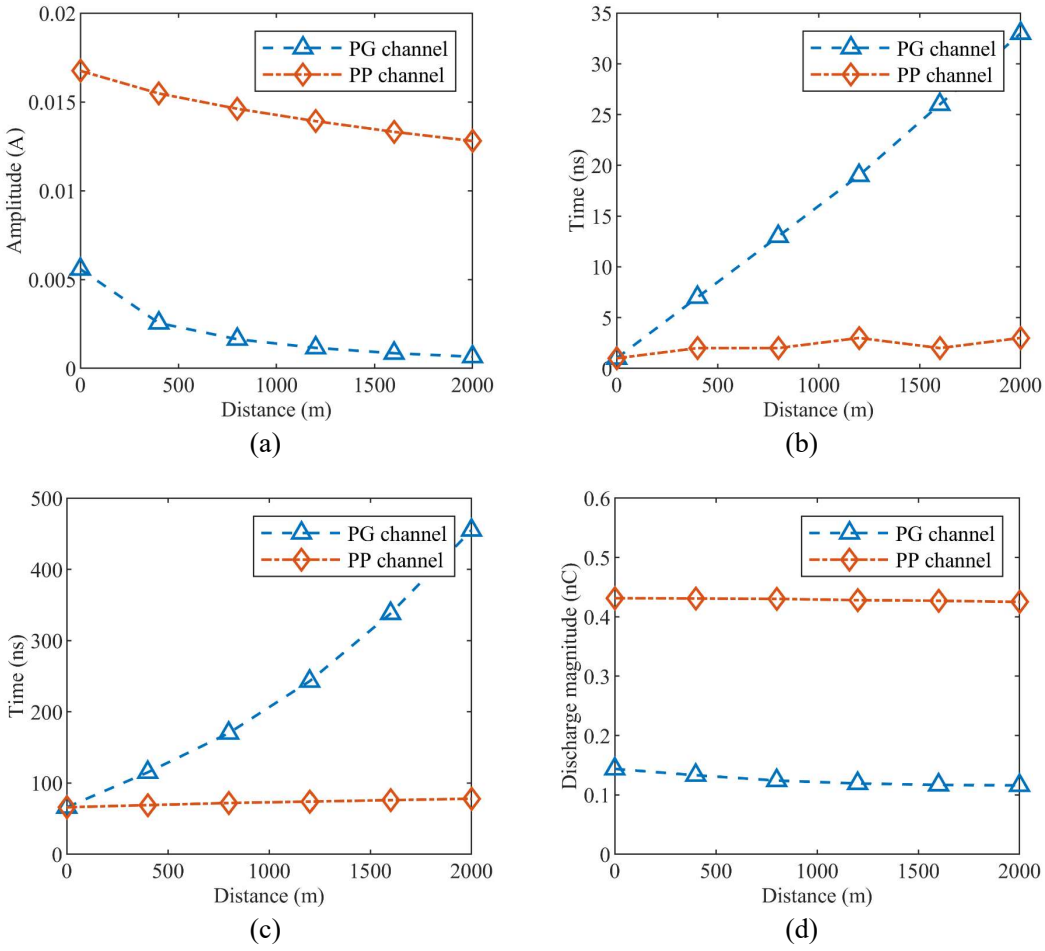

Figure 2-36 Effect of the propagation distance on the waveform parameters of the PD signal: (a) Peak, (b) Rising time, (c) Duration time, (d) Discharge magnitude.

2.4.2 Effect of Non-Uniform Transmission Line Parameters

This subsection discusses the effect of non-uniform transmission line parameters on PD signal characteristics in PG and PP channels. Since line height h and ground resistivity ρ_G are always variable, which depends on geographical topography and soil parameters under the MV overhead line, we carried out two simulation experiments: one is the effect of varying h on PD propagation characteristics; the other one is the effect of different ρ_G. Moreover, it is essential to point out that since the other transmission line parameters (e.g.,

the radius of the overhead conductor) are often consistent along the overhead line, the effects of their non-uniformity are not considered in this work. Moreover, the equivalent circuits of the towers were not connected to the overhead line, i.e., the alongside towers' effects were ignored better to explain the effect of the non-uniform transmission line parameters.

1）Case I: Effect of Varying Height h

In this case, the heights of the line section between two adjacent towers are reduced by Δh one by one from Tower 0 to Tower 20. The height of the first line section is always set as 12 m. For example, if Δh is set as 0.1, the heights of the 20 line sections from Tower 0 to Tower 20 equal 12 m, 11.9 m, 11.8 m,…, and 10.1 m. It is essential to point out that the larger Δh, the more uneven the overhead line is.

Figure 2-37 and Figure 2-38 collect the time-domain waveforms and their integration of the signals in PG and PP channels, measured at Tower 20. It can be observed that as Δh increases, the amplitude of the PD signal in the PG channel is significantly reduced. In contrast, the PD signal in the PP channel is almost invariable. Figure 2-39 collects the effect of Δh on five critical parameters of PD signals. It can be observed that as Δh increases, the peaks of the PD pulses in the PG channel decrease, the rising and falling time of the pulses significantly increase, the discharge magnitudes of the pulses are slightly raised, and

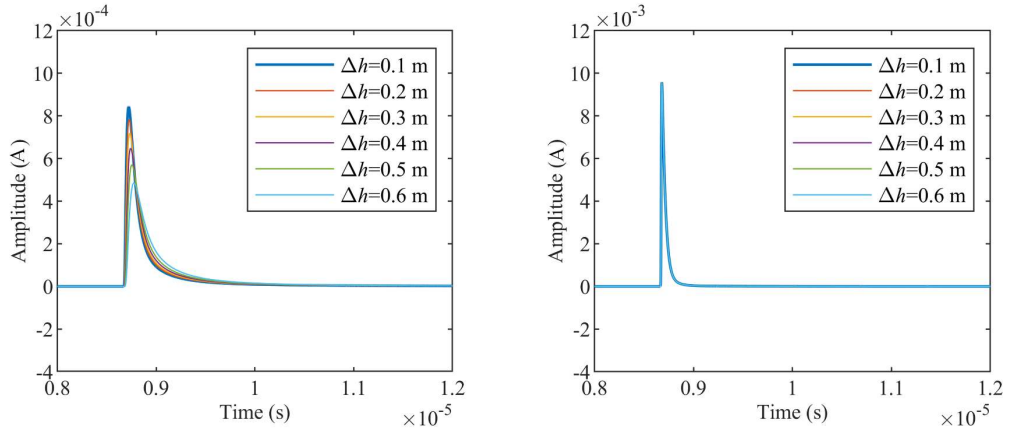

Figure 2-37 PD current waveforms of PG (a) and PP (b) channels with varying Δh.

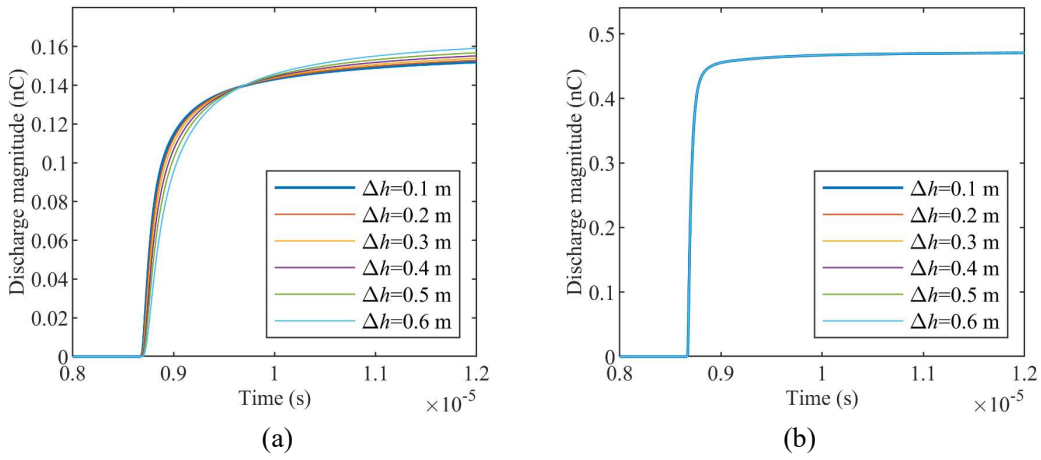

Figure 2-38 Integral curve of the PD currents in PG (a) and PP (b) channels with varying Δh.

the time-of-arrival of the pulses significantly increase. In contrast, all parameters of PD pulses in the PP channel are immune to the variation of Δh. This reveals that varying line heights hardly affect the PD signal in the PP channel.

In summary, the signal in the PG channel is susceptible to the change in the line height, while that in the PP channel is almost immune to the change in the line height.

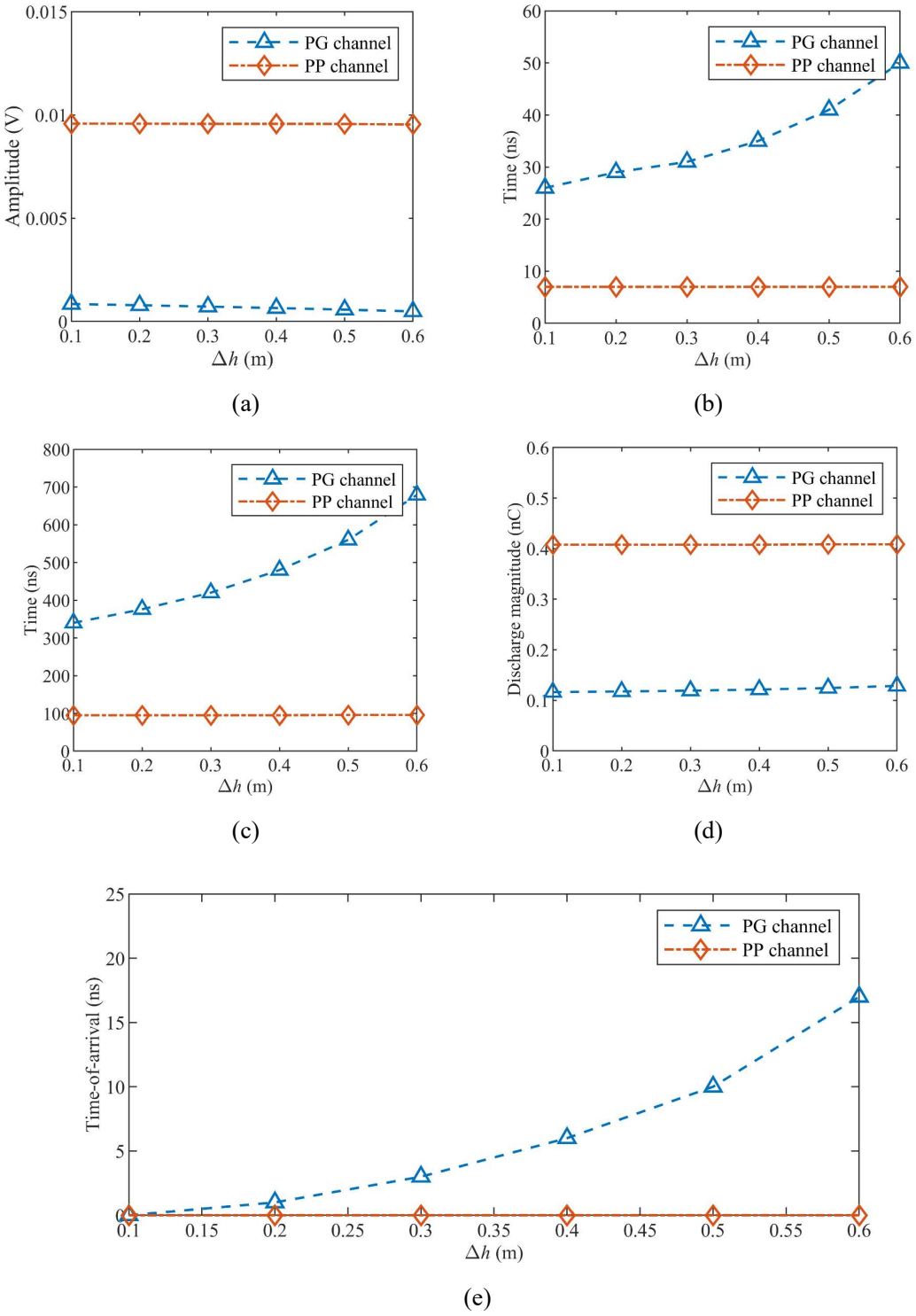

Figure 2-39 Effect of Δh on the waveforms parameters of the PD signal: (a) Peak; (b) Rising time; (c) Duration time; (d) Discharge magnitude; (e) Time-of-arrival.

2）Case II: Effect of Varying Resistivity ρ_G of the Ground

In this case, the ground resistivity ρ_G of the line section between two adjacent towers is increased by $\Delta\rho_G$ one by one from Tower 0 to Tower 20. The ground resistivity of the first line section is always set as 100 Ω·m. As an example, if $\Delta\rho_G$ is set as 100 Ω·m, the ground resistivities of the 20 line sections from Tower 0 to Tower 20 are equal to 100 Ω·m, 110 Ω·m, 120 Ω·m,…, and 290 Ω·m It is essential to point out that the larger $\Delta\rho_G$, the more uneven the overhead line is.

Figure 2-40 and Figure 2-41 collect the time-domain waveforms, their integration, and frequency-domain waveforms of the signals in PG and PP channels, measured at Tower 20. It can be observed that as $\Delta\rho_G$ increases, the amplitude of the PD signal in the PG channel is significantly reduced. In contrast, the PD signal in the PP channel is almost invariable. Figure 2-42 collects the effect of $\Delta\rho_G$ on five critical parameters of PD signals. It can be observed that as $\Delta\rho_G$ increases, the peaks of the PD pulses in the PG channel decrease, the rising and falling time of the pulses significantly increase, the discharge magnitudes of the pulses are slightly increased, and the time-of-arrival of the pulses significantly increase. In contrast, all parameters of PD pulses in the PP channel are immune to the variation of $\Delta\rho_G$. This reveals that ground resistivity variation hardly affects the PP channel PD signal.

In summary, the signal in the PG channel is susceptible to the change of ground resistivity, while that in the PP channel is almost immune to the change of ground resistivity.

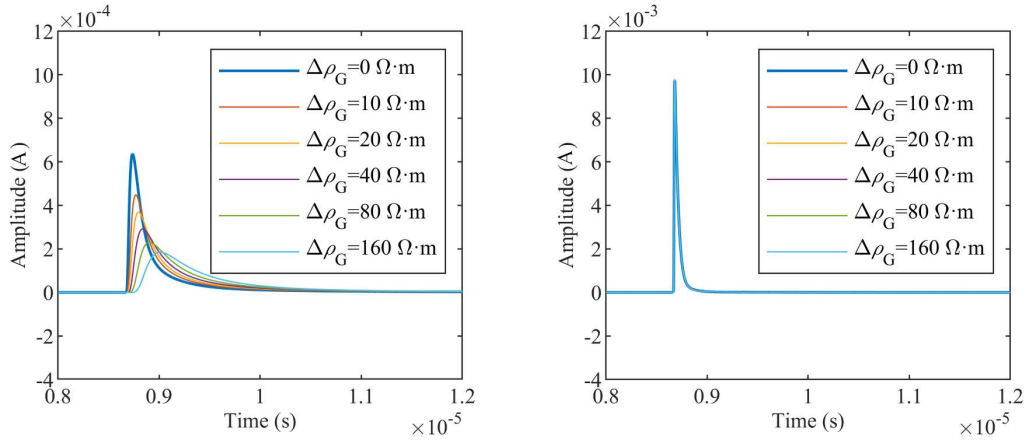

(a) (b)

Figure 2-40 PD current waveforms of the PG (a) and PP (b) channels with varying ρ_G.

2.4.3 Effect of Alongside Towers

1）Case III: Effect of the Support Towers

In this case, all towers from Tower 0 to 20 are set as the support tower, i.e., the equivalent circuit of the support tower is connected in parallel to the three-phase overhead line in the simulation circuit. The capacitance of the equivalent circuit is set from 0 pF to 32 pF. The metal cross-arms of all towers are not connected to the ground. The simulation results are discussed in the following.

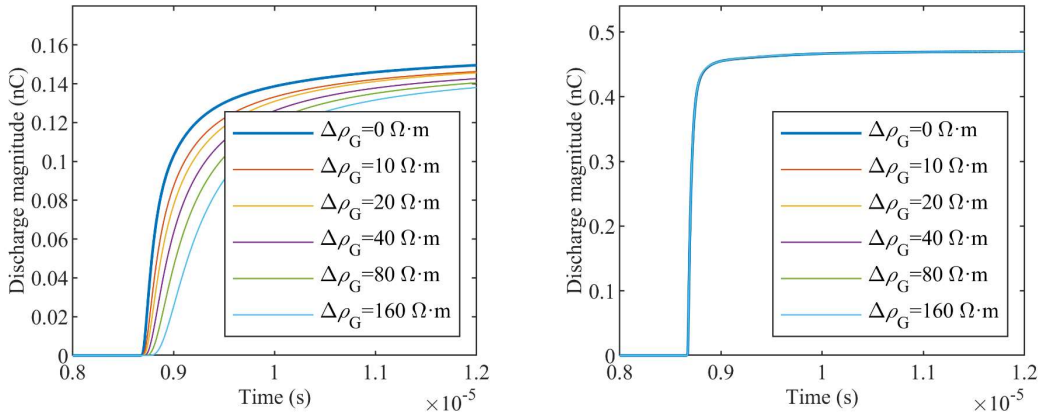

Figure 2-41 Integral curve of the PD currents in the PG (a) and PP (b) channels with varying ρ_G.

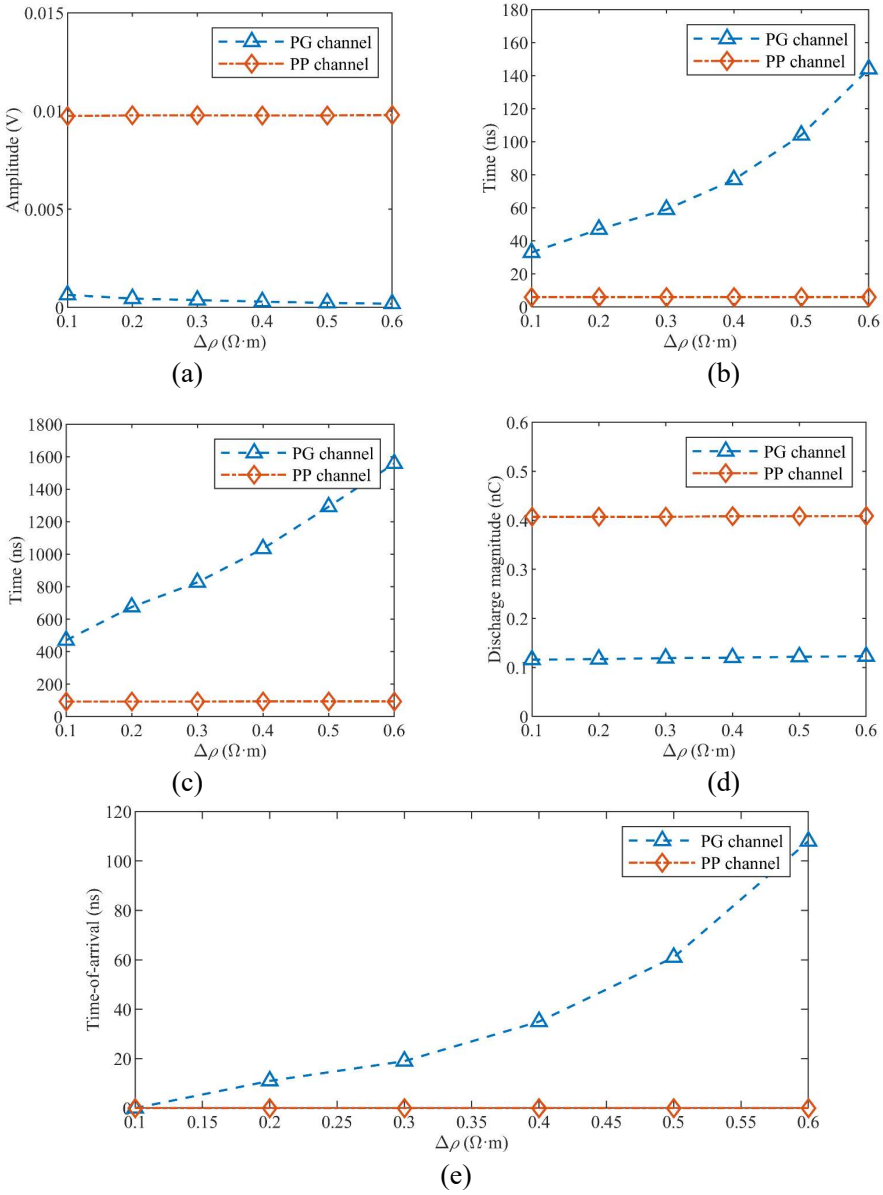

Figure 2-42 The effect of ρ_G on the waveform parameters of the PD signal: (a) Peak, (b) Rising time, (c) Duration time, (d) Discharge magnitude, (e) Time-of-arrival.

Figure 2-43 collects the PD current signal of the PG and PP channels at Tower 20. It can be observed that the support towers without grounding hardly affect the PD signals in the PG channel. In contrast, the amplitude of the PD signal in the PP channel reduces as the value of the capacitance increases. Moreover, the support towers can lead to a significant time delay of the PD pulse in the PP channel, and the time delay increases as the capacitance increases. Significant reflections in the PD signal in the PP channel can be observed.

Figure 2-44 collects the integration of the time-domain signal in Figure 2-43. It can be observed that the integration curves in the PG channel are immune to variations in the capacitance. In contrast, the integration curves in the PP channel are susceptible to taking in the capacitance, and they include some oscillations caused by the reflections. Nevertheless, all curves' final (stable) values are almost the same, meaning that the support tower does not affect the discharge magnitude of the PD signal.

Figure 2-45 collects the effect of support towers on five critical parameters of PD signals. It can be observed that as the capacitance increases, the peaks of the PD pulses in the

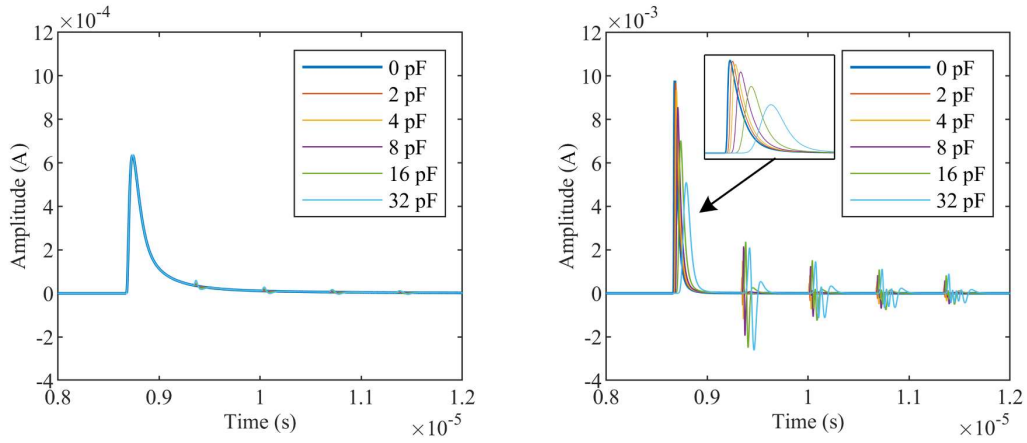

Figure 2-43 PD current waveforms in the PG (a) and PP (b) channels at 2000 m with varying capacitance of the insulators.

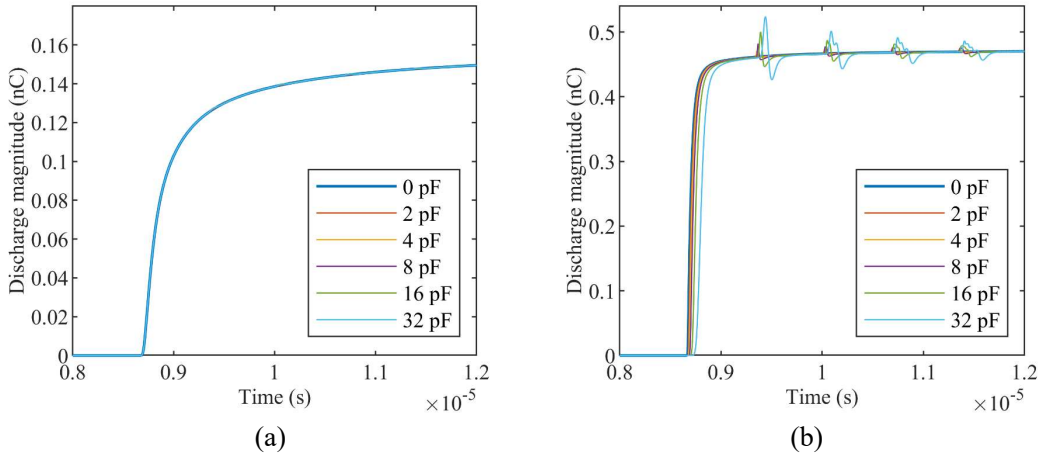

Figure 2-44 Integral curve of the PD currents in the PG and PP channels at 2000 m with varying capacitance of the insulators.

PP channel decrease, the rising and falling times of the pulses significantly increase, the discharge magnitudes of the pulses are almost invariable, and the time-of-arrival of the pulses significantly increases. In contrast, all parameters of PD pulses in the PG channel are immune to the variation of the capacitance value.

In summary, the support towers without grounding hardly affect the PD signal in the PG channel. In contrast, the support towers can lead to significant signal attenuation and time delay in the PP channel but hardly affect the discharge magnitude of the PD signal.

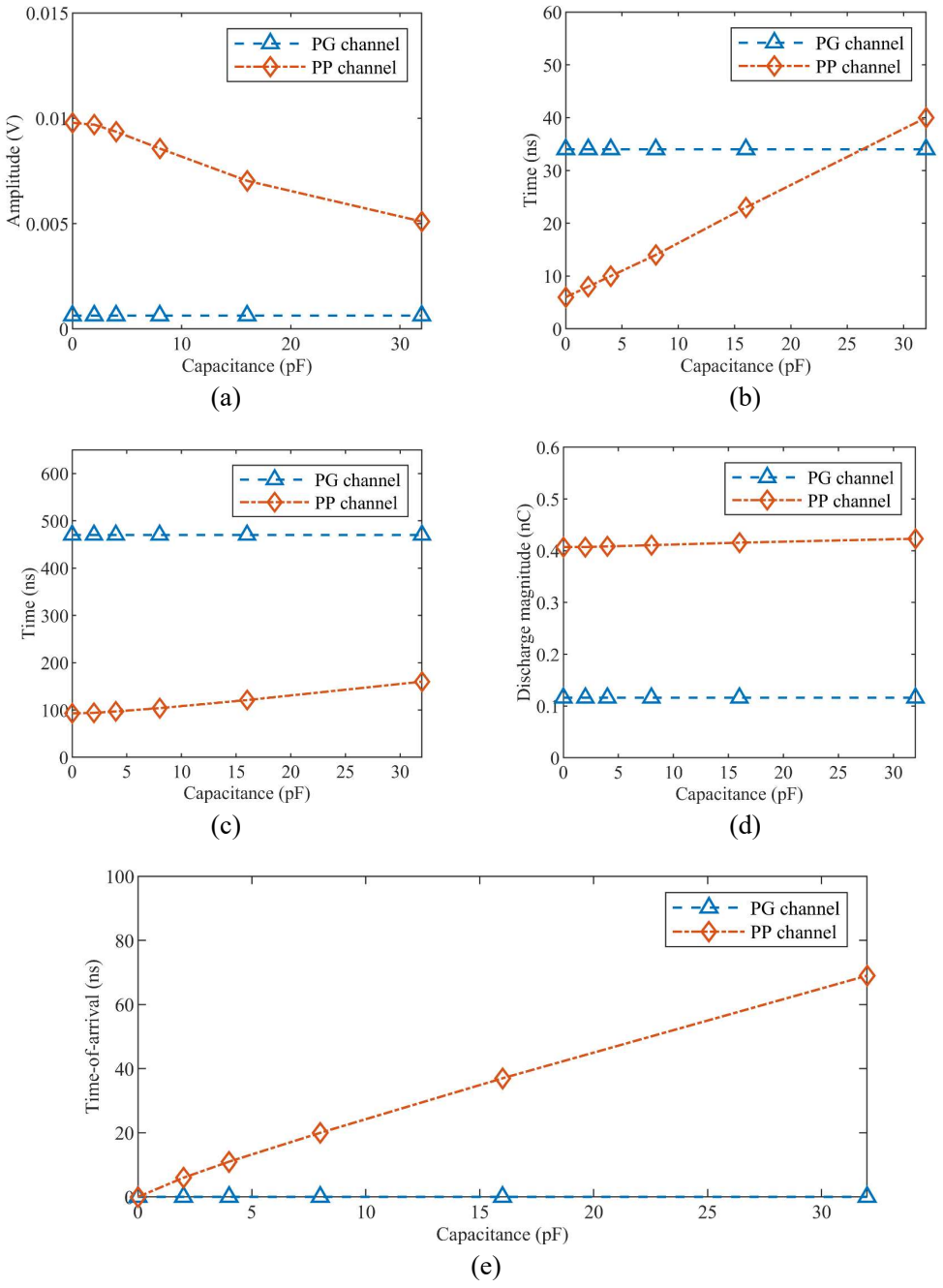

Figure 2-45 The effect of the capacitance of the insulators on critical parameters of the PD signal detected at 2000 m: (a) Peak; (b) Rising time; (c) Duration time; (d) Discharge magnitude; (e) Time-of-arrival.

2）Case IV: Effect of the Transformer Towers in the Middle of the Line

In this case, parts of the towers are set as the transformer tower and the others as the support tower. The distance between two adjacent transformer towers is 400 m. The number of the transformer towers can be set from 0 to 5. For example, if the number of transformer towers is 3, Towers 4, 8, and 12 will be selected as the transformer tower, and the others are set as the support tower.

Figure 2-46 collects the time-domain waveform of the PD current signals of the PG and PP channels at Tower 20. It can be observed that the transformer towers can lead to significant amplitude attenuation and signal distortion in PG and PP channels. In the PP channel, significant reflections can be observed. As the number of transformer towers increases, the amplitude attenuation and signal distortion become more significant.

Figure 2-47 collects the integration of the time-domain signal in Figure 2-46. It can be observed that the integration curves in PG and PP channels are fluctuant, which is caused by

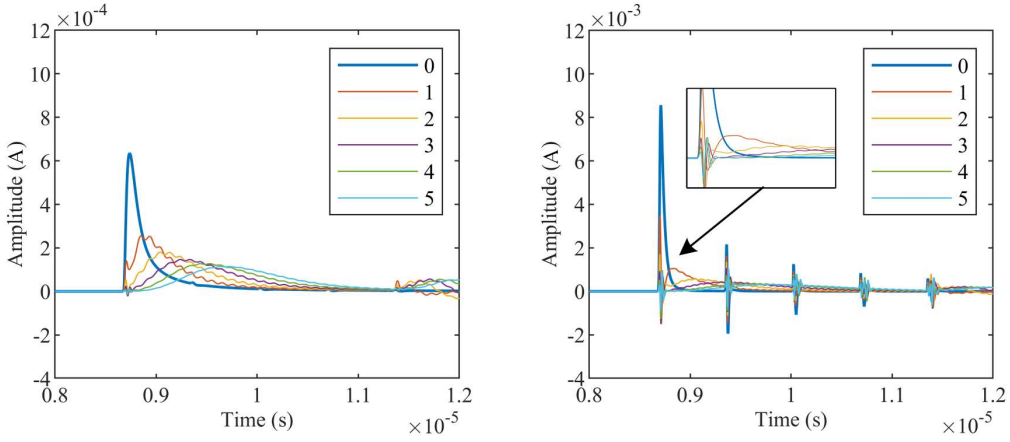

(a) (b)

Figure 2-46 PD current waveforms in the PG (a) and PP (b) channels with varying numbers of the transformer tower at the middle of the line.

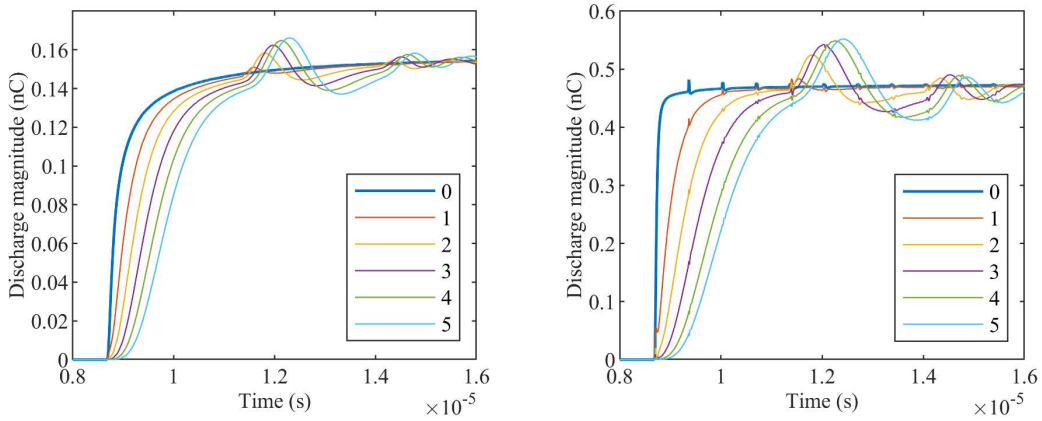

(a) (b)

Figure 2-47 Integral curve of the PD currents in the PG and PP channels with varying numbers of the transformer tower at the middle of the line.

the reflections. Nevertheless, all curves' final (stable) values are almost the same, meaning that the transformer tower does not affect the PD discharge magnitude. However, the integration curve fluctuations make discharge magnitude estimation challenging.

In summary, the transformer tower can lead to significant amplitude attenuation that can signal distortion of the PD signal in PG and PP channels, which poses a difficulty in detecting the PD signal.

3）Case V: Effect of the Transformer Tower at the Terminal of the Line

In this case, Tower 20 is set as the transformer tower, i.e., the circuit model of the transformer tower is connected to the overhead line at Tower 20, and the others are selected as the support tower. Moreover, the overhead line outside Tower 20 is removed to simulate that Tower 20 is a terminal transformer tower, which is common in the MV overhead distribution network.

Figure 2-48 collects the time-domain waveform of the PD current signals of the PG and PP channels at Tower 20. It can be observed that the terminal transformer towers can lead to significant amplitude increases and signal distortion in PG and PP channels. The amplitude

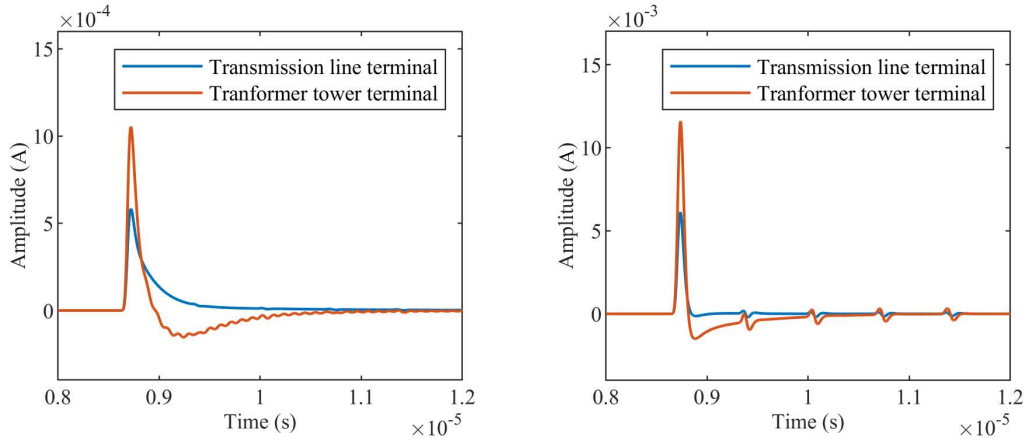

Figure 2-48 PD current waveforms in the PG (a) and PP (b) channels at 2000 m with a transformer tower terminal mounted at Tower 20.

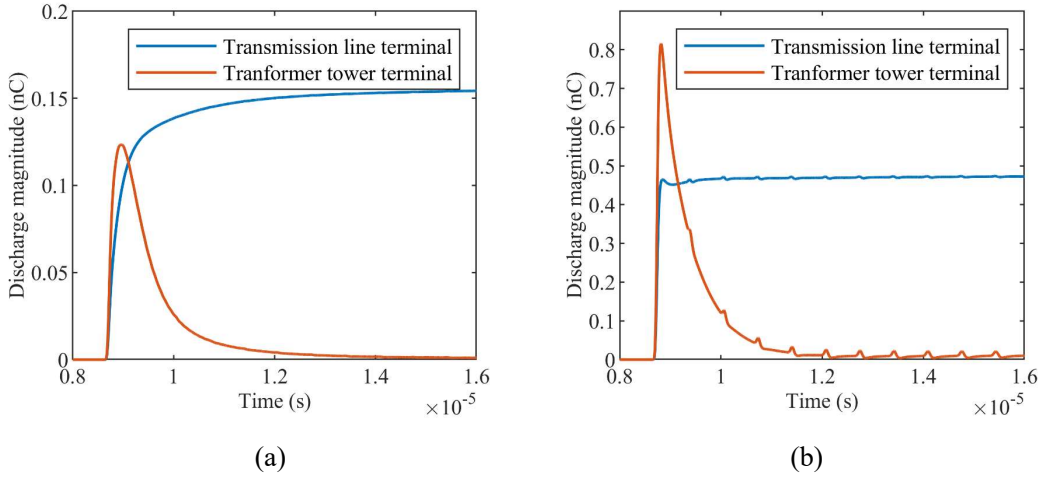

Figure 2-49 Integral curve of the PD currents in the PG (a) and PP (b) channels at 2000 m.

of the PD signal detected at the terminal transformer tower is almost double that in the overhead line without the terminal transformer tower. This reveals that the sensitivity of PD measurement via the PD detectors mounted close to the terminal transformer tower can be improved.

Figure 2-49 collects the integration of the time-domain signal in Figure 2-48. It can be observed that the maximum of the integration curve is larger than the real discharge magnitude, and the final (stable) values of all curves are close to zero, making it almost impossible to determine the correct discharge magnitude.

In summary, the terminal transformer tower can improve the PD signal amplitude, but it leads to challenges in estimating the PD discharge magnitude.

4）Case VI: Effect of the Breaker Tower at the Terminal of the Line

In this case, Tower 20 is set as the breaker tower, i.e., the circuit model of the breaker tower is connected to the overhead line at Tower 20, and the others are selected as the support tower. Moreover, the overhead line outside Tower 20 remains to simulate that Tower 20 is a terminal breaker tower, which is the start of a distribution feeder.

Figure 2-50 collects the time-domain waveform of the PD current signals in the PG and PP channels at Tower 20. It can be observed that the terminal breaker towers can lead to significant amplitude increases and signal distortions. The amplitude of the PD signal detected at the terminal breaker tower is almost double that in the overhead line without the terminal breaker tower. This reveals that the sensitivity of PD measurement via the PD detectors mounted close to the terminal breaker tower can be improved.

Figure 2-51 collects the integration of the time-domain signal in Figure 2-50. It can be observed that the final (stable) values of all curves are close to the correct discharge magnitude, revealing that the terminal breaker tower does not affect the PD discharge magnitude determination.

In summary, the breaker tower can improve the PD signal amplitude, but it hardly affects estimating the PD discharge magnitude.

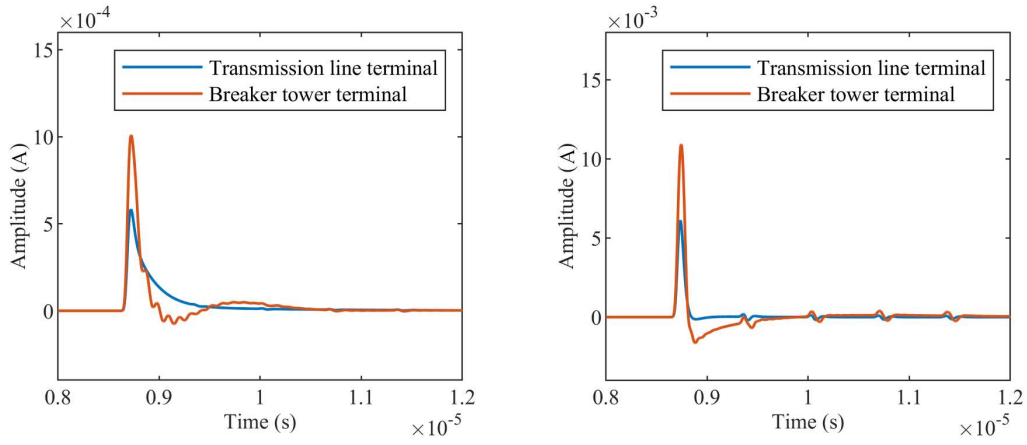

(a) (b)

Figure 2-50 PD current waveforms in the PG (a) and PP (b) channels at 2000 m with a breaker tower terminal mounted at Tower 20.

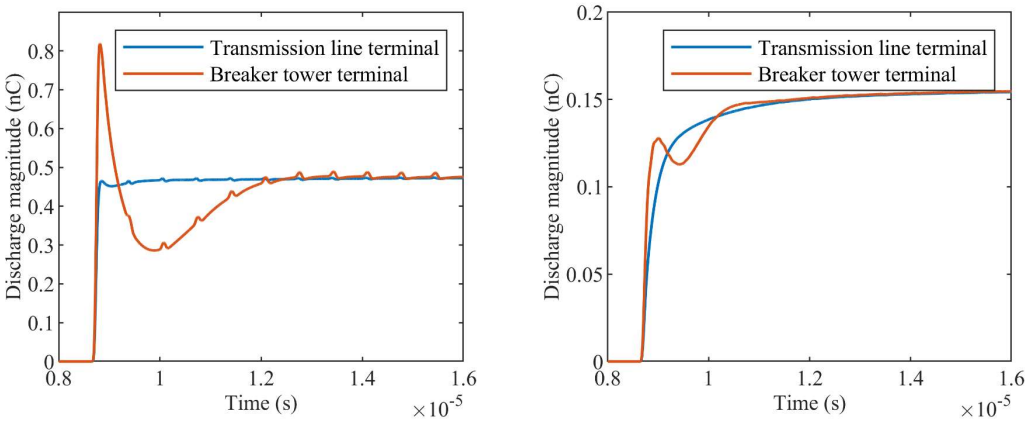

Figure 2-51 Integral curve of the PD currents in the PG (a) and PP (b) channels at 2000 m.

2.5 Conclusion

This chapter develops the models and formulas for calculating the propagation constants of MV three-phase overhead lines and alongside towers, i.e., attenuation coefficient, propagation velocity, and reflection and refraction coefficients. The effectiveness and accuracy of these formulas are validated via simulation and laboratory experiments. Combined with the multiple-conductor transmission line model, the developed formulas allow us to accurately describe the PD propagation characteristics of MV overhead distribution networks. Furthermore, simulation experiments are conducted to quantitatively evaluate the effects of line parameters and structures on PD signal propagation. Several crucial results are summarized as follows:

(1) PD propagation characteristics in PG and PP channels of MV overhead lines are significantly different. On the one hand, the attenuation coefficient of the PP channel is much less than that of the PG channel. For example, the attenuation coefficient of the PP channel is about 2×10^{-5} at the frequency of 1 MHz for a typical 10-kV overhead CC line, while that of the PG channel is about 3×10^{-4}, resulting in the PD signal in the PP channel can propagate a significantly longer distance than that in PG channel. On the other hand, the propagation velocity of the PP channel is almost constant in the frequency range from a few tens of kHz to several tens of MHz. In contrast, the PG channel significantly increases as the frequency increases. The frequency-dependent propagation velocity of the PG channel could lead to difficulty in determining the optimal velocity value for PD localization. Moreover, the simulation results show that the PP channel's propagation constants are hardly affected by the non-uniformity of the overhead line caused by varying ground resistivity and line heights; in contrast, those in the PG channel are susceptible to the non-uniformity of the overhead line. The above results reveal that the sensitivity and accuracy of PD detection and localization based on the signal in the PP channel could be higher than that in the PG channel.

(2) The influence of the alongside towers on PD propagation is proven to be non-negligible. On the one hand, the alongside towers could lead to significant reflections, but weak refractions of PD signals, e.g., breaker and transformer towers. These towers can attenuate most of the energy of PD signals, thus significantly reducing PD detection sensitivity if these towers are located between the PD source and the PD sensor. On the other hand, the alongside towers could lead to additional time delays of the PD signal, e.g., the supporting towers. Although the time delay of a single tower is insignificant, e.g., a few ns, accumulation of the time delays of multiple supporting towers could reach tens of ns, leading to a non-negligible PD location error.

(3) The apparent discharge quantity of a PD signal is almost immune to the increased propagation distance, but the PD sensor's location significantly influences it. Although a PD signal generally attenuates as its propagation distance increases, integrating the PD time-domain signal (i.e., its apparent discharge magnitude) is almost constant as long as the PD signal does not go through a branch. However, once the reflections overlap on the original PD signal, e.g., if the PD sensor is deployed close to the transformer and breaker towers, estimating the correct apparent discharge quantity of the PD signal could be challenging.

In summary, the above conclusions reveal several crucial PD propagation characteristics in MV three-phase overhead distribution networks. These can be used as essential references in developing accurate and reliable PD detection and location methods.

3 Partial Discharge Signal Extraction: Adaptive and Efficient Noise Reduction

The sensitivity and accuracy of PD detection are significantly reduced by field interferences, with unavoidable detrimental effects induced by white noise and discrete spectrum disturbances. However, de-noising PD signals is challenging, primarily due to various PD waveforms, high-level field noises, and limited computing resources. This chapter describes an adaptive and efficient PD de-noising algorithm based on the improved spectral decomposition of the noisy PD signal. Furthermore, implementing the algorithm in resource-limited embedded systems commonly used for PD monitoring is discussed. The performance of the proposed de-noising algorithm is first demonstrated on a synthetic PD signal and compared with state-of-the-art alternatives. Finally, the proposed approach's strength and effectiveness are further validated on measured data.

3.1 Partial Discharge and Noise Signal Characteristics

1）Partial Discharge Signal Characteristics

PD is a localized electrical discharge that only partially bridges the insulation between conductors and can or cannot occur adjacent to a conductor [20]. According to many laboratory studies, the PD process can be approximately equivalent to the Townsend discharge process, in which a current pulse is generated due to the movement of ionized electrons and ions under the stress of an external electric field [118]. The electrons move faster due to their lighter weight, leading to a fast-rising edge of the current pulse, whereas the ions move slowly due to their heavier weight, leading to a slow-falling edge.

Therefore, at the PD source, a PD signal start at time zero can be approximately modeled by a double exponential pulse (DEP), which can be formulated as [57]

$$\mathrm{DEP}(t) = A_1 \cdot (e^{-t/\tau_1} - e^{-t/\tau_2}) \tag{3-1}$$

where A_1 is the amplitude, and τ_1 and τ_2 ($\tau_1 > \tau_2$) are the time constants. DEP signal is often detected in line-type power equipment, such as cables and overhead lines. However, most detected PD signals are oscillating pulses due to the effects of both the propagation path and the transfer function of the used sensor. Therefore, single exponential and double exponential attenuation oscillation pulses (SEOP and DEOP) are used [84]. They are formulated as:

$$\mathrm{SEOP}(t) = A_2 \cdot e^{-t/\tau_3} \cdot \sin(2\pi f_{c1} t) \tag{3-2}$$

$$\mathrm{DEOP}(t) = A_3 \cdot (e^{-t/\tau_4} - e^{-t/\tau_5}) \cdot \sin(2\pi f_{c2} t) \tag{3-3}$$

where A_2 and A_3 are the amplitude parameters, τ_3, τ_4, and τ_5 are time constants, and f_{c1} and f_{c2}

are the oscillation frequencies.

In this work, the three pulses (DEP, SEOP, and DEOP) are concatenated sequentially to generate the signal shown in Figure 3-1. The above signal represents an initial synthetic test case that simulates the simultaneous occurrence of multiple PDs, a common phenomenon in field measurements. Also, it offers a fully controllable test case, highlighting and verifying the features and strengths of the proposed de-noising scheme for increasing levels of superimposed noise. The parameters of DEP, SEOP, and DEOP signals used in this paper are listed in Tab. I. The PD signal is uniformly sampled at a sampling frequency and stored in a vector. For the signals in Figure 3-1, the number of sampling points is 9000.

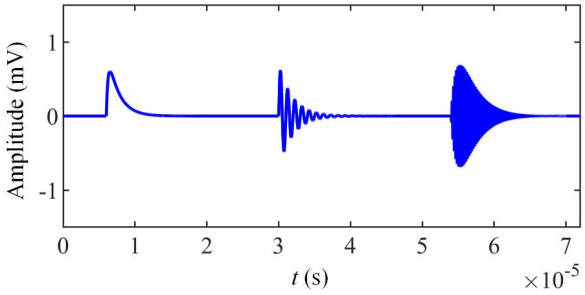

Figure 3-1 Synthetic noiseless PD signal.

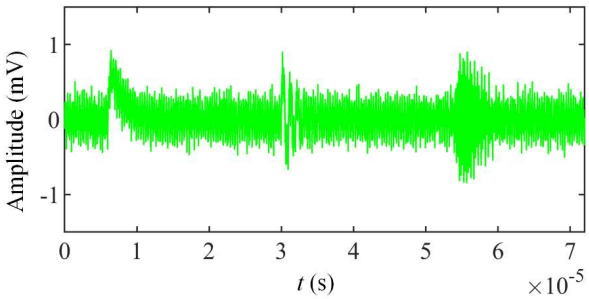

Figure 3-2 Synthetic noisy PD signal with a signal-to-noise ratio of -1.55dB.

Table 3-1 Parameters of the synthetic PD signal of Figure 3-1

Parameter	A_1 /mV	A_2 /mV	A_3 /mV	τ_1 /ns	τ_2 /ns
Value	1	0.7	1.8	150	23
Parameter	τ_3 /ns	τ_4 /ns	τ_5 /ns	f_{c1} /MHz	f_{c2} /MHz
Value	200	77	230	1	5

2）Noise Signal Characteristics

In on-site PD measurements, the sensitivity and accuracy of PD detection are always reduced by two types of noise: (i) the white noise and (ii) the discrete spectrum noise. Discrete spectrum noise mainly arises from carrier communication, radio communication, high-order harmonic, etc., while white noise is caused primarily by equipment thermal noise, ground noise, rand noise, etc. [32]. In this work, the frequencies of two harmonics in the discrete spectrum noise are set to 3 and 7 MHz, and their corresponding amplitudes are set to

0.15 and 0.1 mV, respectively. White noise is a zero mean Gaussian sequence with 0.1 mV standard deviation.

The above disturbances are added to the noise-free PD signal to generate the noisy signal shown in Figure 3-2. It is essential to point out that a critical low signal-to-noise ratio characterizes the synthetic noisy signal in the Figure. Thus, it is a challenging test case that can be effectively used to verify the proposed de-noising solution's benefits and compare it with state-of-the-art alternatives.

3.2 An Improved Automatic Tool for Partial Discharge De-noising

This section develops a fully automatic tool for de-noising PD signals occurring in electrical power networks and recorded in on-site measurements. The proposed method is based on the spectral decomposition of the measured PD signal via the joint application of the short-time Fourier transform and the singular value decomposition. The estimated noiseless signal is reconstructed via a clever selection of the dominant contributions. This allows us to filter out the different spurious components, including the white and discrete spectrum noise. The method offers a viable solution that can be easily integrated within the measurement apparatus, with unavoidable beneficial effects in detecting essential signal parameters for PD localization. The performance of the proposed tool is first demonstrated on a synthetic test signal and then applied to real measured data. A cross-comparison of the proposed method and other state-of-the-art alternatives is included in the study.

3.2.1 Principles

This subsection presents the proposed automatic tool for PD de-noising, as illustrated in Figure 3-3. The principles of the tool are briefly described as follows.

First, the time-domain signal is transformed into a time-frequency spectrogram via STFT. This step represents the most critical initial data processing since the local features of a nonstationary PD signal cannot be well expressed in the time domain or the frequency domain only. Hence, a time-frequency analysis is more suitable for representing a PD signal with its inherent pulsed characteristics.

Second, the spectrogram is preprocessed via a soft masking function to reduce part of the white noise, and then it is decomposed into multiple components via SVD. This step can automatically separate the PD pulses, white noise, and discrete spectrum noise from the original spectrogram, allowing us to select the dominant components easily.

Then, each component is transformed back to time-domain sub-signals via inverse STFT. This step enables perfect reconstructions of the time-domain signals.

Finally, the sub-signals with distinct pulsed characteristics are selected via Principal Component Analysis and kurtosis criteria, and they are finally summed to reconstruct the de-noised PD signal.

Furthermore, a six-step procedure is developed to better explain the proposed tool, as shown in Figure 3-4, along with data processing following all the blocks involved from left to right. More details of the six steps are described in the following subsections.

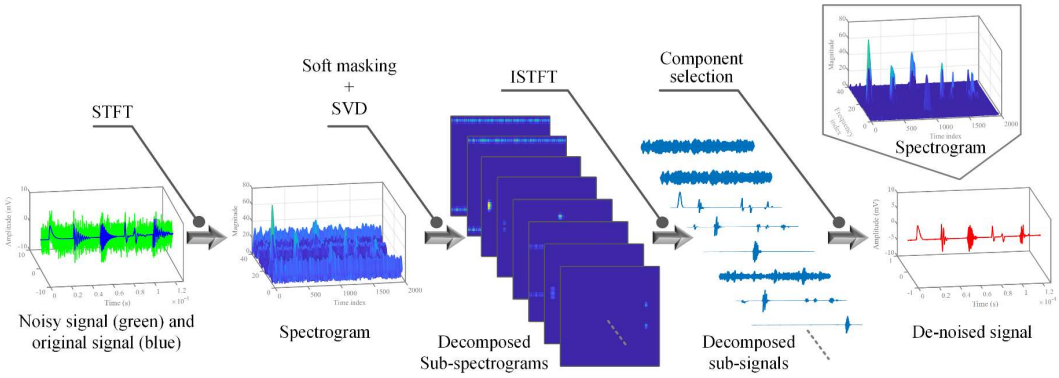

Figure 3-3 Illustration of the proposed PD de-noising method.

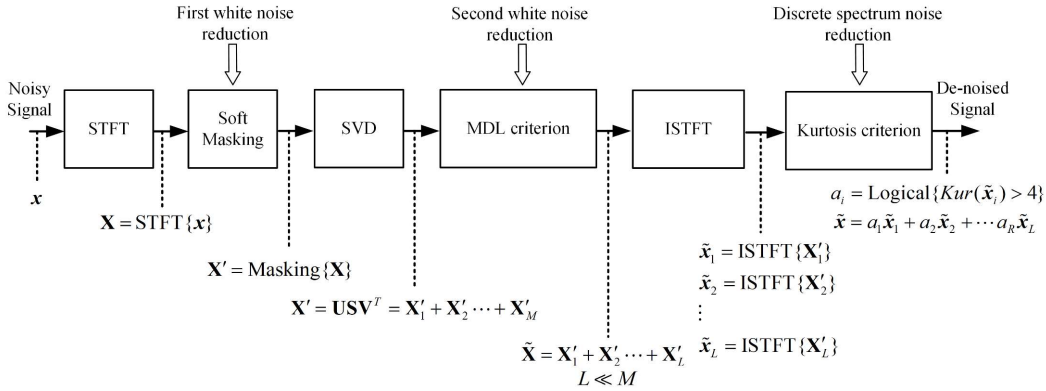

Figure 3-4 Step-by-step automatic procedure of the proposed de-noising method.

1）Time-Frequency Transform via STFT (step 1)

According to the procedure of Figure 3-4, the sampled noisy PD signal like the one shown in Figure 3-2 is stored in a vector $\boldsymbol{x}=[x(t_1),x(t_2),\ldots,x(t_K)]^T$ defined as:

$$x(t_k)=s(t_k)+w(t_k),\ t_k=(k-1)\Delta t,\ k=1,2,\ldots,K \tag{3-4}$$

where $s(t_k)$ is the discretized noise-free PD signal, $w(t_k)$ represents the superimposed noise (e.g., white and discrete spectrum noise), $\Delta t=1/f_s$ is the sampling interval, and K is the number of time samples (e.g., 9000 in the example signal). Then, $\boldsymbol{x}$ is transformed into a spectrogram $\mathbf{X}$ via the STFT.

This step represents the most critical initial data processing since the local features of a nonstationary PD signal cannot be well expressed in the time domain or the frequency domain only. Hence, a time-frequency analysis is more suitable for representing a PD signal with its inherent pulsed characteristics.

STFT is a widely used time-frequency tool for studying nonstationary signals, and it has been proven to be effectively used in this field [126]. The discrete STFT of the discrete signal x can be written as:

$$X(f_m,t_n)=\sum_{k=1}^{K}x(t_k)g(t_k-t_n)e^{-j2\pi t_k f_m}\Delta t \tag{3-5}$$

whereas a Gaussian window function with a length of M (e g., 200 in the following illustrative example in this subsection), $t_n = (n-1)\Delta t$ ($n = 1, 2, \cdots, N$, N=K-M+1) and $f_m = (2m-M)/(2M\Delta t)$ （ $m = 1, 2, \cdots, M$) are the discrete-time and frequency, respectively, and $X(f_m, t_n)$ (also labeled as $X_{m,n}$) is the element in the m^{th} row and n^{th} column of the spectrogram $\mathbf{X} \in \mathbb{C}^{M \times N}$. The absolute value of the spectrogram $\mathbf{X}$ obtained by applying STFT to the synthetic noisy signal in Figure 3-2 is shown in Figure 3-5, in which the PD pulses emerge clearly while they are drowned out by noise in the time domain.

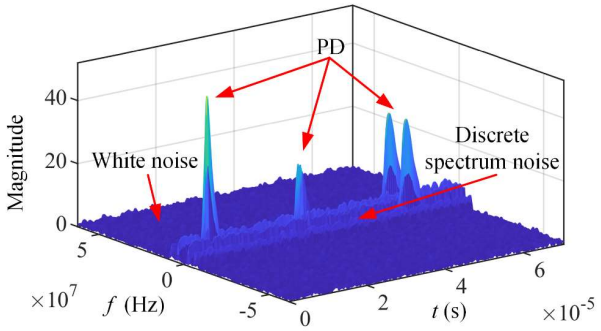

Figure 3-5 Magnitude of the spectrogram of the synthetic noisy signal shown in Figure 3-2 and the location of the different signal components.

2）Soft Masking (step 2)

White noise is preliminarily reduced by applying the following soft masking to the spectrogram **X**, resulting in an updated spectrogram $\mathbf{X}'$.

Figure 3-5 shows the magnitude of **X**, highlighting that both the PD signal and the discrete spectrum noise are localized in the specific zones of the spectrogram characterized by a remarkably high amplitude (in magnitude). On the other hand, white noise produces a uniformly distributed background. This magnitude difference between the dominant signal (e.g., PD signal) and the white noise allows us to first preliminarily filter out the noise by applying the following soft masking on the spectrogram [127]:

$$X'_{m,n} = \begin{cases} T_{m,n} \cdot X_{m,n} & \text{if } |X_{m,n}| < 3\varepsilon \\ X_{m,n} & \text{if } |X_{m,n}| \geq 3\varepsilon \end{cases} \tag{3-6}$$

where ε is the standard deviation of **X**. The threshold value of 3ε is suitably adjusted based on the signal-to-noise ratio and is chosen according to [128], and $T_{m,n}$ are the attenuation coefficients defined as:

$$T_{m,n} = \left| \frac{X_{m,n}}{3\varepsilon} \right|^q \tag{3-7}$$

where q is the attenuation control factor. A significant value of q increases the white noise suppression, but at the same time, it leads to considerable distortion of the PD signal. Therefore, the value of q should be set carefully, and it will be thoroughly discussed in

Chapter 3.2.2. In this subsection's illustrative example, q is set to 1. After the soft masking, the spectrogram $\mathbf{X}$ is updated to a new one, in which parts of white noise are removed while discrete spectrum noise and some residual white noise still exist. Finally, it is essential to point out that soft masking improves the signal-to-noise ratio of the PD signal, thus facilitating the subsequent matrix factorization and component selection.

3）Matrix Factorization via SVD (step 3)

In this step, the spectrogram $\mathbf{X}'$ is decomposed into M components via the singular value decomposition, allowing the split of the original signal into multiple distinguishable components, in which the functional PD signal, the discrete spectrum noise, and the remaining white noise can be separated. This can also be justified by the different localization of signal components in Figure 3-5, which are characterized by different shapes and strengths in magnitude.

Applying SVD to the spectrogram $\mathbf{X}'$ (with $M < N$) can generate three decomposed matrices, yielding:

$$\begin{aligned} \mathbf{X}' &= \mathbf{U}\mathbf{S}\mathbf{V}^H \\ &= \sigma_1 \boldsymbol{u}_1 \boldsymbol{v}_1^H + \sigma_2 \boldsymbol{u}_2 \boldsymbol{v}_2^H + \cdots \sigma_M \boldsymbol{u}_M \boldsymbol{v}_M^H \\ &= \mathbf{X}'_1 + \mathbf{X}'_2 + \cdots + \mathbf{X}'_M \end{aligned} \tag{3-8}$$

where $\mathbf{U}$ is a $M \times M$ orthonormal matrix ($\mathbf{U}= [\boldsymbol{u}_1, \boldsymbol{u}_2, \cdots, \boldsymbol{u}_N]$, $\boldsymbol{u}_i \in \mathbb{C}^{M\times 1}$), $\mathbf{S}$ is a real $M \times N$ rectangular matrix with the singular values $\sigma_1 > \sigma_2 > \cdots > \sigma_M$ in the diagonal entries, $\mathbf{V}$ is $M \times M$ a square orthonormal matrix ($\mathbf{V}= [\boldsymbol{v}_1, \boldsymbol{v}_2, \cdots, \boldsymbol{v}_M], \boldsymbol{v}_i \in \mathbb{C}^{M\times 1}$), and $\mathbf{X}'_i$ is the i^{th} decomposed component of $\mathbf{X}'$. PD de-noising can be achieved by selecting the components that best represent the contribution of the noiseless PD signal.

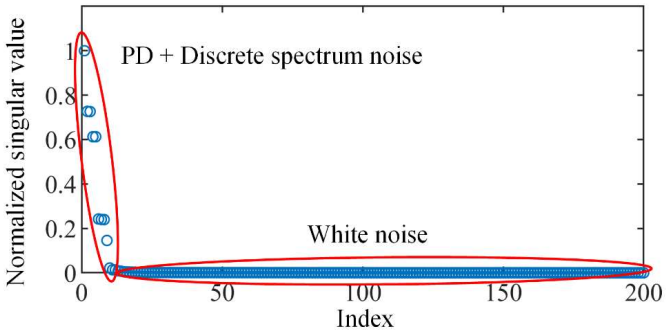

Figure 3-6 Singular values of the spectrogram $\mathbf{X}'$.

Roughly speaking, it can be verified that the more concentrated and large-amplitude objects (e.g., the PD signal and the discrete spectrum noise) in the spectrogram $\mathbf{X}'$ correspond to the components with larger singular values. In contrast, the scattered and low-amplitude objects (e.g., the white noise) correspond to the components with small singular values, as highlighted in Figure 3-6. Therefore, the mix of the PD signal and the discrete spectrum noise can be extracted by selecting the principal components associated

with larger singular values, thus reducing the residual white noise.

4）Principal Components Selection via Minimum Description Length (MDL) criterion (step 4)

This step implements an automatic rule for selecting the optimal L ($L \ll M$) components from the dominant singular values, as shown in Figure 3-6.

Traditionally, the principal components associated with larger singular values in the SVD are selected via the threshold criterion $\sigma_{l+1}/\sigma_1 \geq \delta$ ($l = 0,1,\ldots,M-1$), where an artificial threshold value refers to the spectrogram's signal-to-noise ratio $\mathbf{X}'$. Since we do not know the signal-to-noise ratio, which depends on the PD signal and noise level, we use the MDL criterion to select the number of the principal components automatically. The function of the MDL with respect to the singular values of the spectrogram $\mathbf{X}'$ is defined as [129][130]:

$$\mathrm{MDL}(l) = -N \log \left(\frac{\prod_{i=l+1}^{M} \sigma_i}{\left(\frac{1}{M-l} \sum_{i=l+1}^{M} \sigma_i \right)^{M-l}} \right) + \frac{1}{2} l(2M-l) \log N \tag{3-9}$$

where σ_i is the i^{th} singular value of $\mathbf{X}'$, M is the number of singular values (or rows) of $\mathbf{X}'$, and N ($N > M$) is the number of the columns of $\mathbf{X}'$. The number of effective singular values can be determined by minimizing MDL(l) as [129][130]:

$$L = \arg \min_{0 \leq l \leq M-1} \mathrm{MDL}(l) \tag{3-10}$$

To better explain the effect of the above criterion, the MDL curve of the singular value vector of Figure 3-6 is shown in Figure 3-7. L=12 corresponds to the minimum of the MDL curve, defining that only the first 12 components, instead of 200 in total, can successfully be used to represent the dominant contributions of the spectrogram $\mathbf{X}'$. Therefore, $\mathbf{X}'$ can be updated to a compressed spectrogram $\tilde{\mathbf{X}} = \mathbf{X}'_1 + \mathbf{X}'_2 \cdots + \mathbf{X}'_L$ ($\mathbf{X}'_i \in \mathbb{C}^{M \times N}$, $i = 1,2,\ldots,L$) by selecting the first L components, thereby removing most of the remaining white noise.

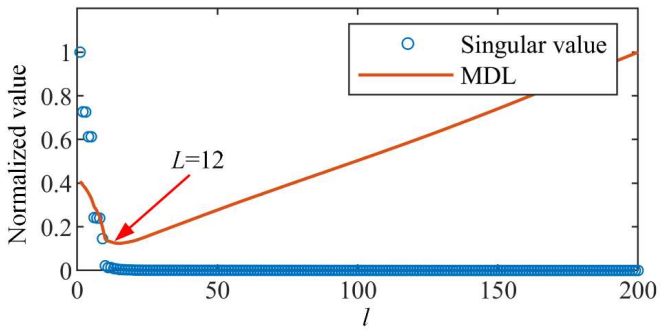

Figure 3-7 MDL curve of the singular values.

5）Time-Domain Signal Reconstruction via Inverse STFT (step 5)

Each component in the spectrogram $\tilde{\mathbf{X}}$ is transformed back to the time domain via Inverse STFT (ISTFT), resulting in *L* signal modes, in which the PD signal and the discrete spectrum noise are distinguishable. The conversing back to the time domain is essential not only for retrieving the estimated noiseless PD signal but also because, as observed before, the singular values of the PD signal and the discrete spectrum noise may have the same magnitude, making their possible separation hard.

Hence, each component $\mathbf{X}_i'$ of the spectrogram $\tilde{\mathbf{X}}$ is converted back to the time domain via inverse STFT:

$$\tilde{x}_i(t_k) = \frac{1}{M}\sum_{n=1}^{N}\sum_{m=1}^{M} X_i'(f_m, t_n) g(t_k - t_n) e^{j2\pi t_k f_m} \tag{3-11}$$

where $\tilde{x}_i(t_k)$ is the i^{th} reconstructed signal mode, and $X'(f_m, t_n)$ (also labeled as $X'_{m,n}$) is the element in the m^{th} row and n^{th} column of the sub-spectrogram $\mathbf{X}_i'$.

Again, for example, in a signal of Figure 3-2, the *L* reconstructed signal modes $\tilde{\boldsymbol{x}}_1$, $\tilde{\boldsymbol{x}}_2$, …, and $\tilde{\boldsymbol{x}}_L$ are shown in Figure 3-8. From visual inspection, it can be observed that the PD signal and the discrete spectrum noise are spread in different contributions or modes (e.g., #1, #4, #5, #8, #9, #10, #11, #12). This observation suggests it is also possible to filter out the discrete spectrum noise and estimate the noiseless PD signal by selecting the most modes with an impulse-like shape. This is done in the next, i.e., last, step.

6）Mode Selection via Kurtosis Criterion (step 6)

The Kurtosis parameter separates the contributions associated with the PD signal from those arising from the discrete spectrum noise in the *L* reconstructed modes. Kurtosis is a statistical measure of whether the data are heavy-tailed or light-tailed relative to a normal distribution [131]. Qualitatively, sequences with high kurtosis parameters tend to have heavy tails or outliers. Sequences with low kurtosis values tend to have light tails or lack outliers. In the reconstructed modes, the signal components associated with the pulses (e.g., PD signal) perform like some outliers, thus producing a considerable kurtosis value, whereas periodic signals (e.g., the discrete spectrum noise) have a low kurtosis value.

The Kurtosis value of a discretized signal is defined as:

$$Kur(\tilde{x}_i) = \frac{\frac{1}{K}\sum_{k=1}^{K}\left[\tilde{x}_i(t_k) - \overline{x}_i\right]^4}{\left(\frac{1}{K}\sum_{k=1}^{K}\left[\tilde{x}_i(t_k) - \overline{x}_i\right]^2\right)^2} \tag{3-12}$$

where $\tilde{x}_i$ is the i^{th} signal reconstructed by the i^{th} component, and $\overline{x}_i$ is the average of $\tilde{x}_i$.

The calculated kurtosis values of the modes collected in Figure 3-8 are shown in Figure 3-9. From this figure, we can see the modes more closely related to the PD signal are those

with larger kurtosis values (i.e., #1, #4, #5, #8, #9, #10, #11, #12).

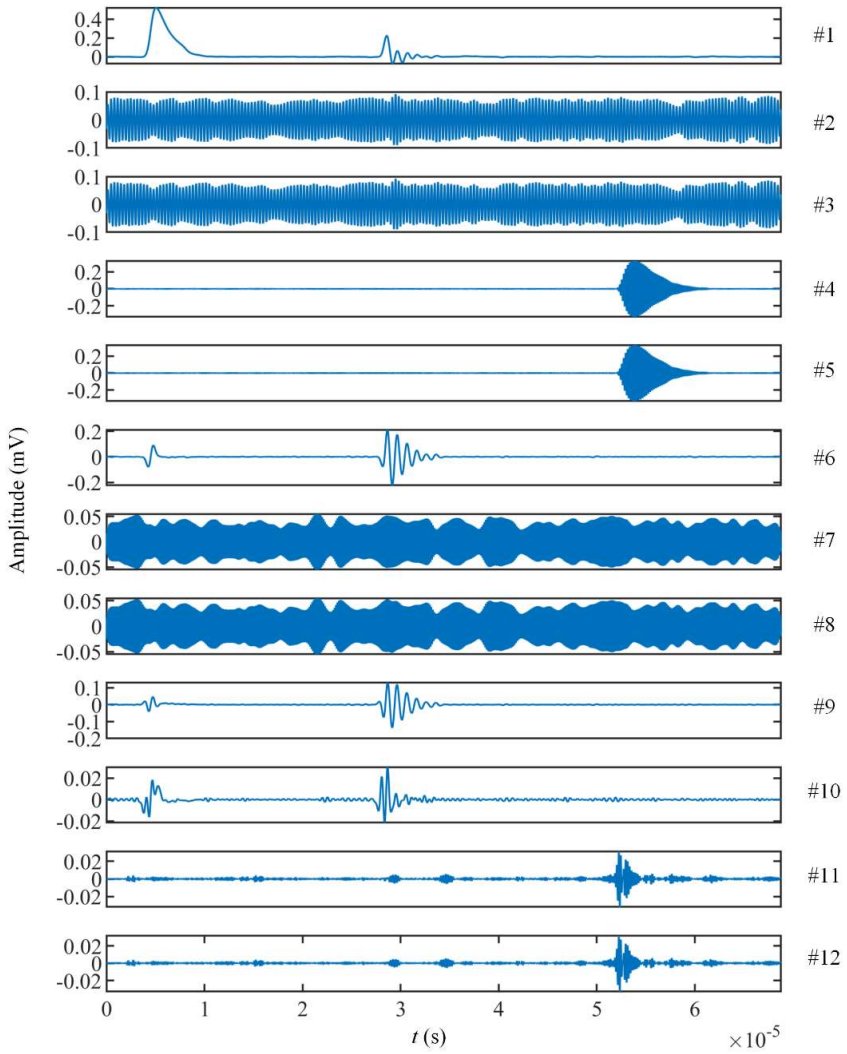

Figure 3-8 Signal modes reconstructed from the first twelve components with larger singular values.

The modes with more considerable kurtosis value are selected to reconstruct the final estimated noiseless signal $\tilde{\boldsymbol{x}}$, which can be rewritten as:

$$\tilde{\boldsymbol{x}} = a_1\tilde{\boldsymbol{x}}_1 + a_2\tilde{\boldsymbol{x}}_2 + \cdots a_L\tilde{\boldsymbol{x}}_L \tag{3-13}$$

where $a_i = \text{Logical}\{kur\{\tilde{\boldsymbol{x}}_i\} > \beta\}$,where Logical$\{.\}$ is the logical judgment function and returns 1 or 0. β is a threshold set to 4, an empirical value suggested in [84][131]. The final estimated noiseless signal $\tilde{x}$ via Equation (3-13) is shown in Figure 3-10, where most white noise and discrete spectrum noise are successfully removed.

3.2.2 Results of De-Noising Synthetic Signal

This Section collects the results of applying the proposed tool to the synthetic PD test case. The simulations use MATLAB software on an Intel(R) Core i7-10750H processor with a 2.60-GHz clock frequency and 16 GB RAM. In the simulations, three evaluation metrics

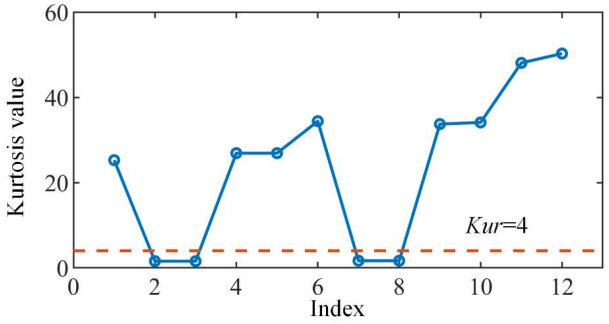

Figure 3-9 Kurtosis value of the modes in Figure 3-8.

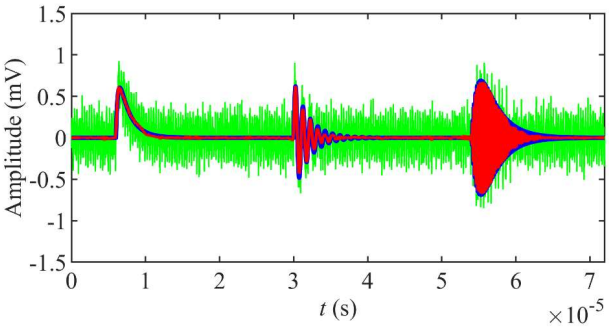

Figure 3-10 De-noised signal obtained by summing modes #1, #4, #5, #8, #9, #10, #11, and #12 in Figure 3-8. The green, blue, and red lines denote the noisy, the original, and the de-noised signals, respectively.

are defined to quantitatively assess the de-noising performance of the proposed algorithm, which is compared with the alternative WT [62], EMD [73], and H-ASVD [81] tools. Also, as mentioned before, in the proposed algorithm, only two parameters (the window length in the STFT and the attenuation control factor of the soft masking) must be determined in advance; a rule for their choice is also presented.

1）Evaluation Metrics

Three evaluation metrics are defined below to quantify the quality of the estimated noiseless PD signal [84] ($s(t_k)$ and $\tilde{x}(t_k)$ denote the discrete noise-free and de-noised signals, respectively).

（1）Signal-to-noise ratio (SNR) is used to measure the background noise reduction:

$$\mathrm{SNR}(s(t),\tilde{x}(t)) = 10\cdot\log_{10}\frac{\sum_{k=1}^{K} s^2(t_k)}{\sum_{k=1}^{K}\left[\tilde{x}(t_k)-s(t_k)\right]^2} \tag{3-14}$$

（2）Normalized correlation coefficient (NCC) is used to evaluate waveform similarity between the original and de-noised signals. It is defined as:

$$\mathrm{NCC}(s(t),\tilde{x}(t)) == \frac{\sum_{k=1}^{K} s(t_k)\cdot\tilde{x}(t_k)}{\sqrt{\left[\sum_{k=1}^{K} s^2(t_k)\right]\cdot\left[\sum_{k=0}^{K-1}\tilde{x}^2(t_k)\right]}} \tag{3-15}$$

（3）Root-mean-square error (RMSE) is used to evaluate the waveform distortion of the de-noised signal compared with the original signal:

$$\mathrm{RMSE}(s(t),\tilde{x}(t)) == \sqrt{\frac{1}{K}\sum_{k=1}^{K}\left[\tilde{x}(t_k)-s(t_k)\right]^2} \tag{3-16}$$

Higher *SNR* and *NCC* and lower *RMSE* represent a better de-noising performance.

2）Comparison with the Classical Hankel Matrix-Based SVD De-Noising Method

Two main differences between the proposed STFT-SVD and the Hankel matrix-based SVD methods are listed as follows:

(1) The singular value selection for the ASVD algorithm is carried out on the time-domain representation of the input data via the Hankel matrix. On the other hand, in the proposed STFT-SVD algorithm, the selection of the singular value is carried out in the time-frequency domain since it is outstanding to study a non-stationary signal (i.e., the PD signal). The time-frequency representation has two benefits. One is that the PD-associated elements in the time-frequency matrix have a significantly more significant value than that of noise, thus leading to larger singular values. The other one is that the time-frequency matrix allows us to apply the soft masking to improve the SNR of the PD signal, thus facilitating the subsequent matrix factorization and singular values selection. Although the singular value plot of the STFT-SVD seems more straightforward to handle than that of the ASVD, additional computations are required for the STFT to transform the time-domain signal into the time-frequency spectrogram.

(2) The singular value criteria used by the proposed STFT-SVD method differ from the one used by the ASVD. The STFT-SVD algorithm uses the minimum description length (MDL) criterion for selecting singular values. At the same time, the ASVD approach selects the singular values for which the standard deviations (STDs) floor is more significant than zero [81][86].

The above differences motivate the improved resilience of the proposed method to the multiple-step phenomena compared to the ASVD. Additional details are provided below to support the conclusion further.

As a qualitative proof of what has been stated above, Figure 3-11 and Figure 3-12 collect the singular values of the synthetic signal, which are computed via the ASVD and the proposed STFT-SVD method for an SNR=-7dB and -20 dB, respectively. Figure 3-11 shows that when the *SNR* is “high,” the STFT-SVD and ASVD can successfully select the effective singular values. However, as shown in Figure 3-12, for a low *SNR*, it can be observed that the ASVD fails to choose the effective singular values due to the multiple steps phenomenon (as the paper [86] raises). On the other hand, the proposed STFT-SVD algorithm shows a smoother behavior for the singular values magnitude, with a well-defined knee-point. This, together with the MDL, allows us to select the optimal number of the practical singular values suitably. The above analysis highlights that the multiple steps phenomenon is heavily reduced by the proposed STFT-SVD method.

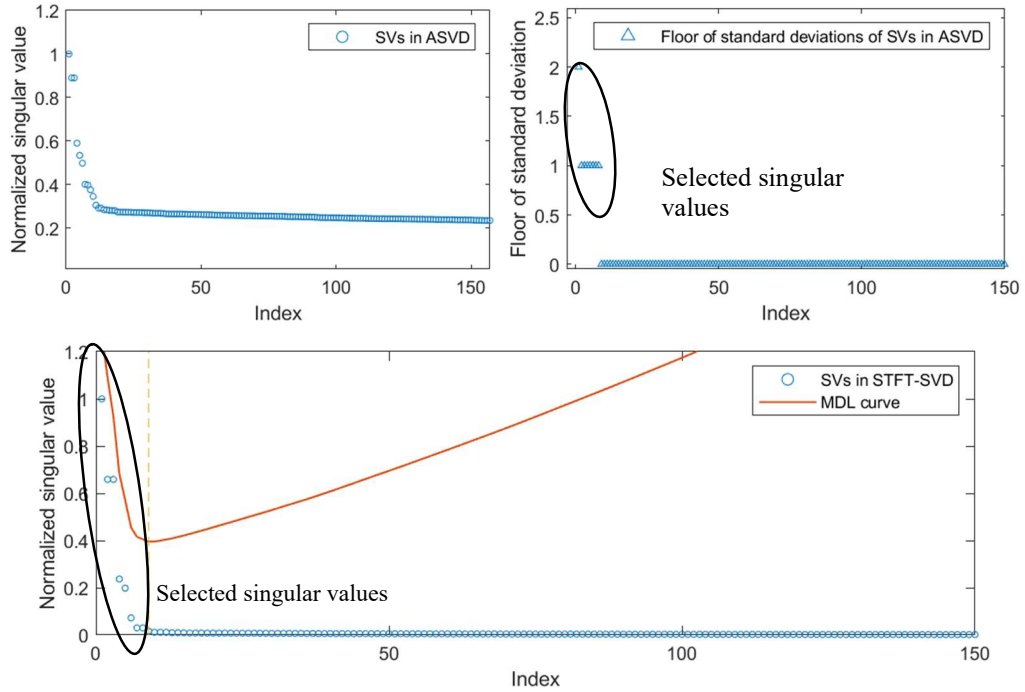

Figure 3-11 singular values plots of the ASVD and STFT-SVD methods under SNR of -7 dB.

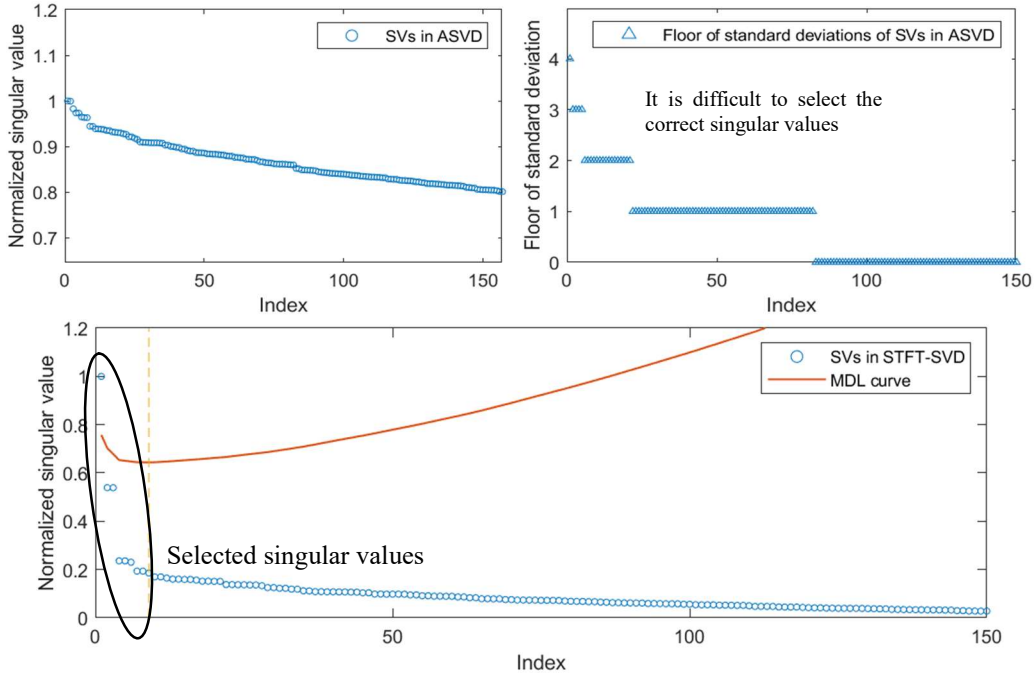

Figure 3-12 singular values plots of the ASVD and STFT-SVD methods under SNR of -20 dB.

3）Effect of the Window Length in STFT

The window length M in STFT, which is equal to the number of rows of the time-frequency spectrogram $\mathbf{X}$, is inversely proportional to the frequency resolution Δf of the spectrogram, which can be formulated as

$$\Delta f = \frac{f_s}{M} \tag{3-17}$$

For a fixed value of the sampling frequency f_s, a small window length can lead to a large frequency resolution of the spectrogram, which may be insufficient to distinguish a PD signal from the noise, especially the discrete spectrum noise. In contrast, a considerably considerable window length can lead to a small frequency resolution, resulting in redundant computations.

We de-noise the noisy PD signal synthesized in Chapter 3.1 via the proposed algorithm with varying window lengths and noise levels. The window length M is changed from 40 to 800 sampling points, the SNR of the noisy signal is changed from -1.55 to -15.5-dB by increasing the amplitudes of the two types of noises in equal proportions, and the attenuation control factor q of the soft masking in Equation (3-7) is set as 1.

The fundamental effect of the size of window width (M) is reflected in the spectrogram obtained by the STFT, as shown in Figure 3-13. As M increases, the number of the rows (i.e., the frequency resolution) of the spectrogram increases, allowing us to identify the PD pulses more clearly. Therefore, M should be set large enough so that the spectrogram has a sufficient frequency resolution to separate PD signals and noises. It is important to remark that increasing M, and thus the number of rows of the spectrogram, unavoidably increases the computational cost required by the subsequent SVD.

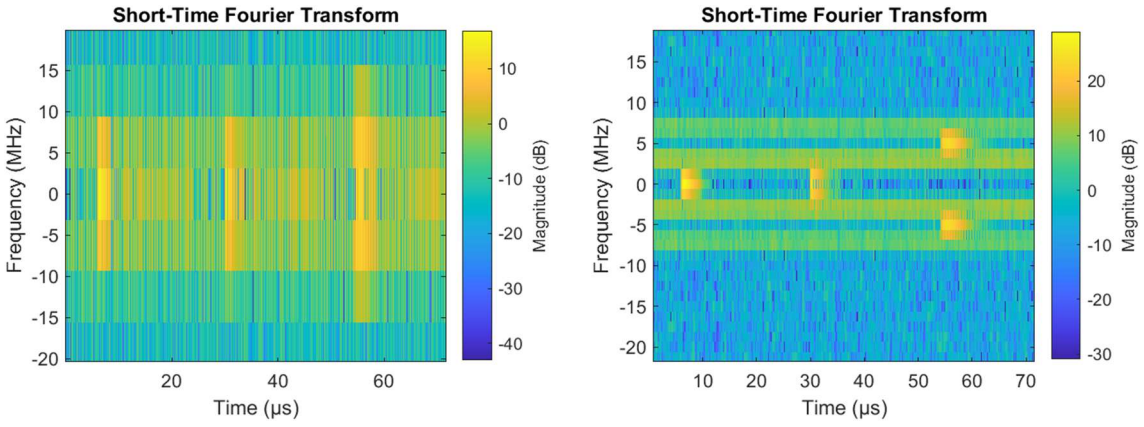

(a) M=20

(b) M=100

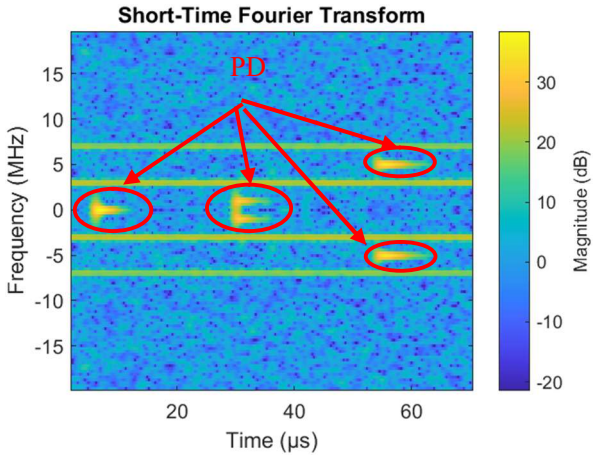

(c) M=400

Figure 3-13 Spectrograms of the synthetic noisy signal with various M.

Figure 3-14 collects the spectrograms and final de-noising results of the synthetic noisy signals. It can be observed that although the sharpness and clarity of the spectrograms vary with the value of *M*, which is set from 160 to 1600, the final de-noising results are almost equivalent. This means that the overall algorithm is robust even if a suboptimal value of *M* is selected during the STFT step. In other words, the outcome of the additional test is that the algorithm exhibits a low sensitivity to *M*.

Figure 3-15 provides a compact picture of the effect of the window length *M* in STFT on the de-noising performance of the proposed algorithm through the defined two evaluation metrics, *SNR* and *RMSE*. It can be observed that the de-noising performance improves as the window length increases in the initial part of the curves, and then it becomes nearly flat once the number of sampling points exceeds the critical value of 200. This critical value is equivalent to the frequency resolution of the spectrogram of 0.625MHz, which is just sufficient to distinguish the last two PD pulses with dominant frequencies of 1MHz and 5MHz, respectively, from the discrete spectrum noise with dominant frequencies of 3MHz and 7MHz. Once the window length is smaller than the critical value, the frequency resolution of the spectrogram is insufficient to distinguish the PD pulses from the discrete spectrum noise, resulting in a significant drop in the de-noising performance as shown in the front parts of the curves in Figure 3-15. Therefore, the window length should not be too small.

Figure 3-16 shows the effect of the window length *M* on the computational time of the proposed algorithm. It can be observed that the efficiency decreases as the window length increases, suggesting a selection of the smallest value of *M* may lead to sufficiently good performance indexes (such as those considered in Figure 3-15).

Referring to the frequency pass-band of the used PD sensor, an empirical formula allows us to determine the window length *M*:

$$M \geq \frac{f_s}{\Delta f} = \frac{\alpha \cdot f_s}{f_{\text{high}} - f_{\text{low}}} \tag{3-18}$$

where f_{high} and f_{low} are the upper and lower cutoff frequencies of the used PD sensor, and α is the ratio between the passband frequency of the sensor and the acceptable frequency resolution. In practical applications, it is recommended to set α a bit larger than some dozens (e.g., 20 to 60) to ensure sufficient frequency resolution of the spectrogram for good de-noising performance and simultaneously less computation time.

4）Effect of the Attenuation Control Factor in the Soft Masking

Similar to *M*, the effect of attenuation control factors *q* is also reflected in the spectrogram obtained via the STFT. As *q* increases, a sharper spectrogram after the soft masking can be obtained, as shown in Figure 3-17. In principle, the larger q is, the more noise is reduced, as shown in Figure 3-18. It can be observed that the result in Figure 3-18(a) (q=1) has a significant improvement in the de-noising performance than that in Figure 3-18(b) (q=0). In addition, increasing *q* will not bring significant gains in de-noising performance, as shown in Figure 3-18(b), (c), and (d). It can be observed that the de-noising

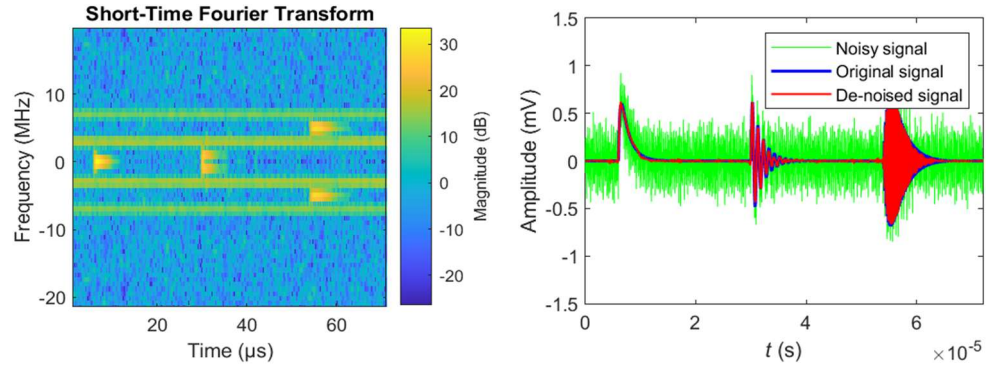

(a) M=160

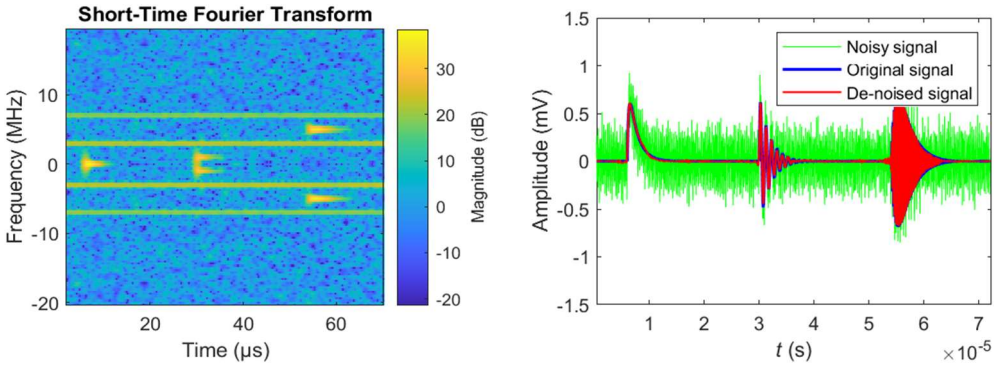

(b) M=400

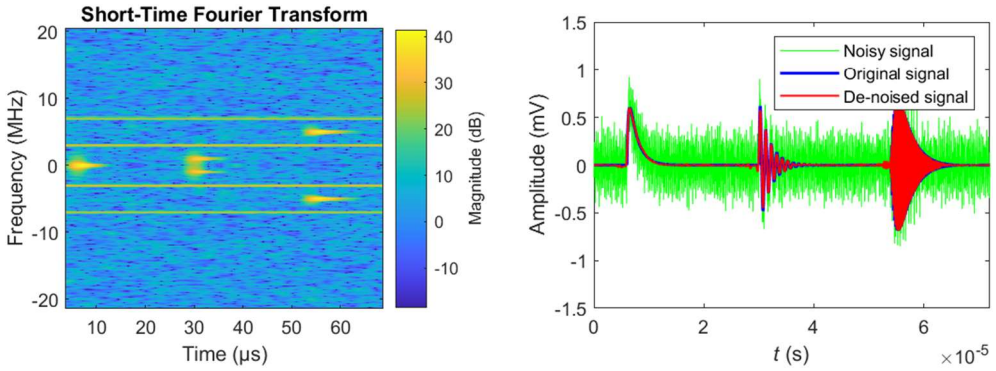

(c) M=800

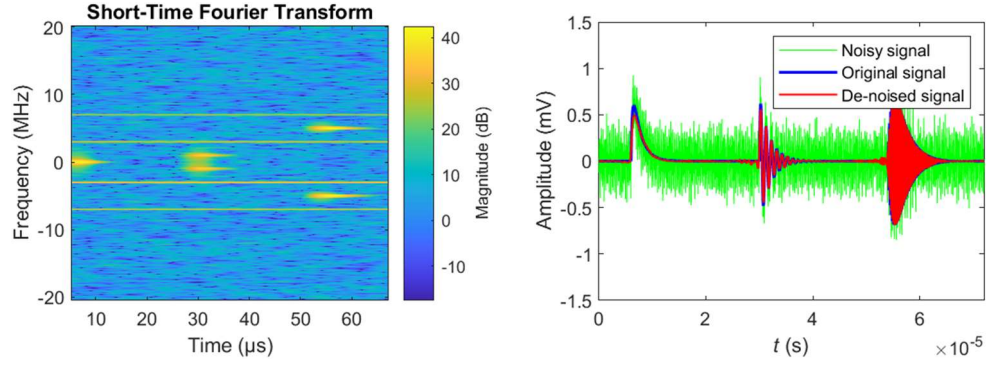

(d) M=1600

Figure 3-14 Spectrograms and de-noising results of the synthetic noisy signal with various M.

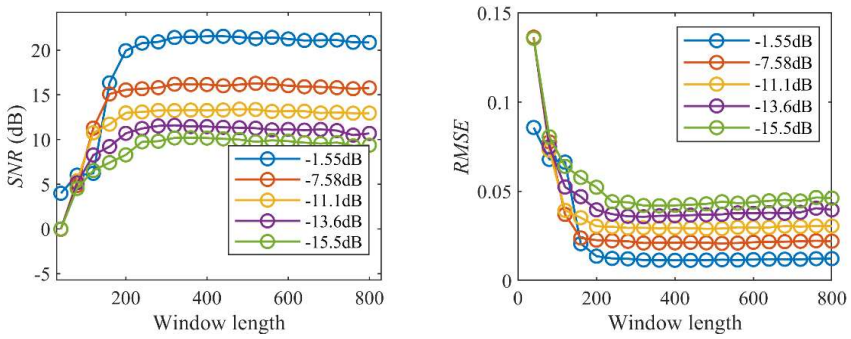

(a) (b)

Figure 3-15 Effect of the window length M on (a) SNR and (b) RMSE in varying noise levels.

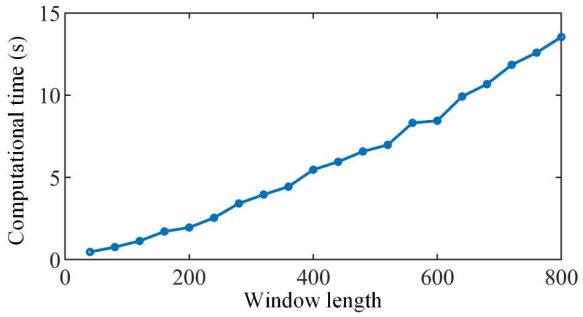

Figure 3-16 Effect of the window length M on the overall computational time required by the proposed algorithm.

results with q=1, 2, and 4 are similar and all acceptable. Therefore, the selection of q is not demanding in practice. In addition, it is also important to mention that a too-large value of q could decrease the de-noising performance (see Figure 3-15) since it can introduce some distortion in the reconstructed PD signal.

The effect of the attenuation control factor of the soft masking on the two evaluation metrics *SNR* and *RMSE* is shown in Figure 3-19, where the attenuation control factor, q, is changed from 0 to 6, the SNR of the noisy signal is changed from -1.55 to -15.5-dB, and α in (18) is set as 48. The above value corresponds to the window length $M = 48 \cdot 125\ \text{MHz} / (30\ \text{MHz} - 0.5\ \text{MHz}) \approx 200$ sampling points if a PD sensor with a pass-band from 0.5 MHz to 30 MHz is used, which is sufficient to detect the synthetic PD signal. It can be observed that with the increase of the attenuation control factor, the de-noising performance is improved at first, indicating that soft masking works effectively and then gradually deteriorates. The initial increase in the de-noising performance is because white noise is removed; the subsequent drop in de-noising performance is because part of the useful PD signal is also removed, resulting in some signal distortions. In addition, comparing the optimal q values for different noise levels, it can be found that a relatively small q value produces the best noise reduction effect at low noise levels. In contrast, a rather significant q value has the best noise reduction effect at high noise levels. Referring to the simulation results, the attenuation control factor, q, is recommended to be set between 0.5 and 2.5, and it should be relatively large for high noise levels and rather small for low noise levels.

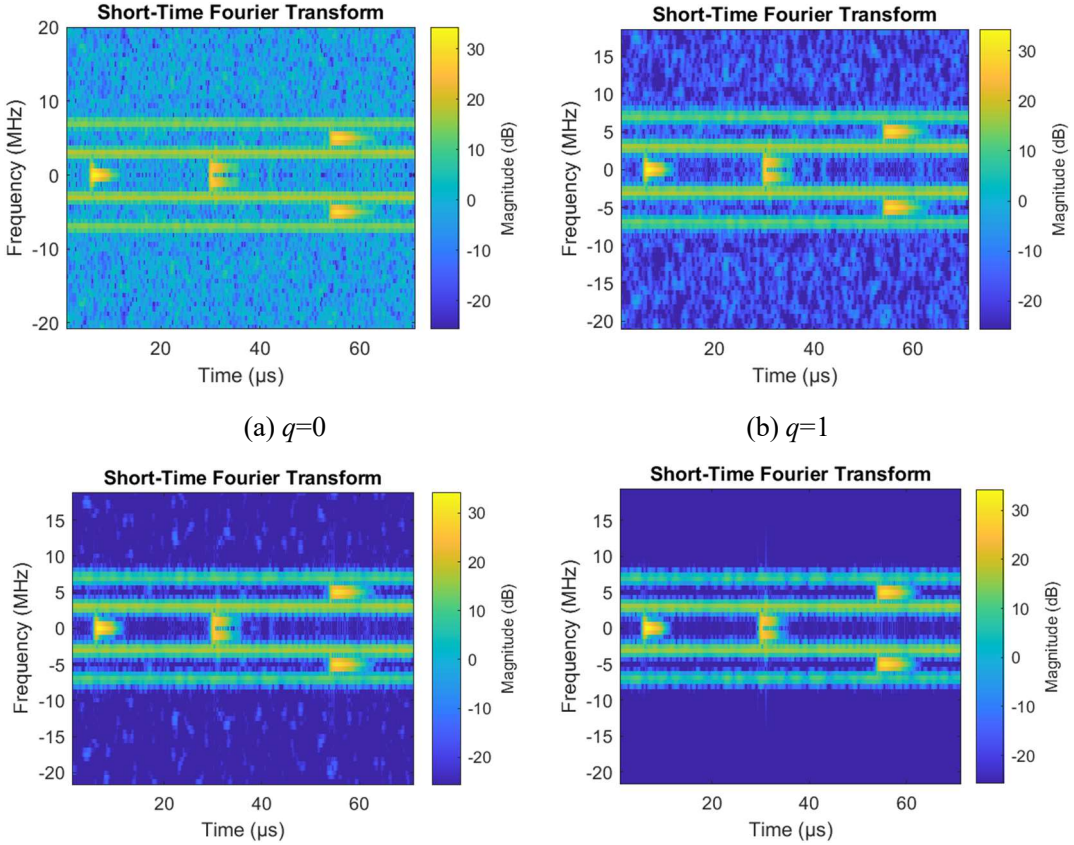

(a) q=0 (b) q=1

(c) q=2 (d) q=4

Figure 3-17 Spectrograms after the soft masking with various q (M=200).

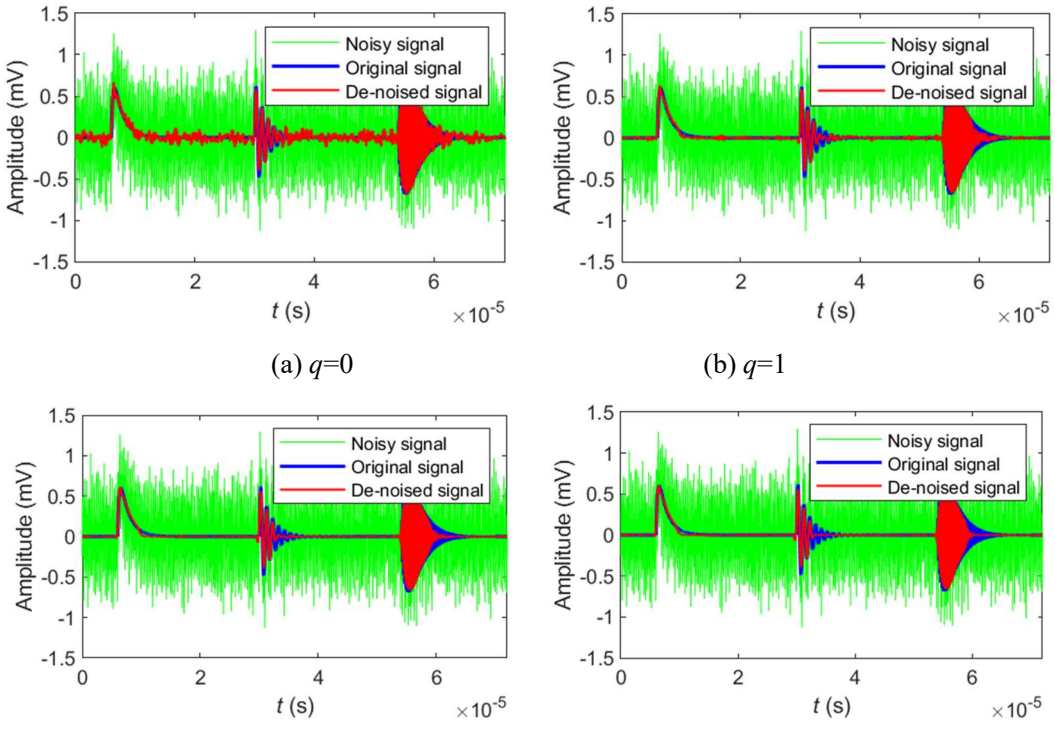

(a) q=0 (b) q=1

(c) q=2 (d) q=4

Figure 3-18 De-noising results of the synthetic noisy signal with various q (M=200).

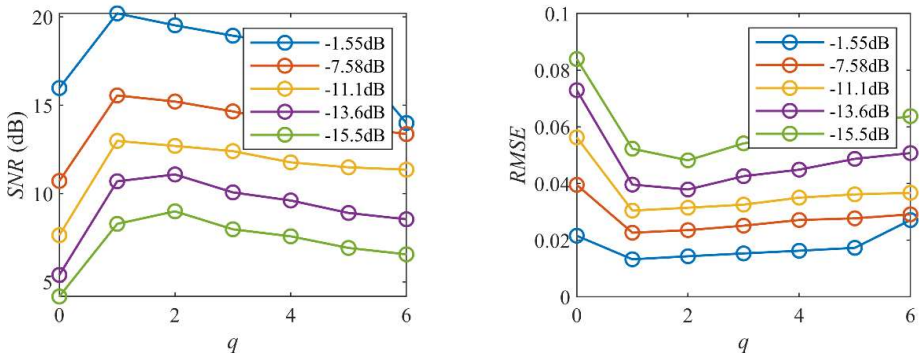

(a) (b)

Figure 3-19 Effect of the attenuation control factor q on (a) SNR and (b) RMSE in varying noise levels. (q equal to 0 denotes the soft masking is disenabled)

5）De-noising Result Comparison

Figure 3-20 collects the results of de-noising the simulated PD signal with high-level noise (*SNR*=-11.10dB) via the proposed STFT-SVD, H-ASVD, WT, and EMD algorithms. It can be seen from Figure 3-20(a) that the H-ASVD algorithm can hardly remove the discrete spectrum noise. In Figure 3-20(b), the WT algorithm behaves well for the first and second pulses but fails to reconstruct the third pulse. The difference in the noise reduction effect on the PD pulses is attributed to the selected mother wavelet (dB8); the failure of the last PD pulse de-noising is due to the insufficient frequency resolution requiring to separate the PD pulses (with a dominant frequency of 5MHz) with the discrete spectral noises with sinusoidal components at 3MHz and 7MHz. In Figure 3-20(c), the EMD technique can only vaguely discriminate the PD signal, and many white noise and waveform distortions remain. In Figure 3-20(d), compared with the results of H-ASVD, WT, and EMD algorithms, the proposed STFT- SVD algorithm can be effectively used to reduce both the white noise and the discrete spectrum noise in all three types of PD pulses, although a small amount of noise remains. In Figure 3-20(e), where the soft masking is enabled, the de-noising performance is improved, thus proving the benefit of this additional step in the de-noising procedure.

The evaluation metrics of all the algorithms are listed in Table 3-2, where it can be observed that the proposed STFT-SVD algorithm with the soft masking has the most significant signal-to-noise ratio (the highest *SNR*) and the minor waveform distortion (the lowest *RMSE* and the highest *NCC*).

3.2.1 Results of De-Noising Measured Real PD Signal

This Section collects the results of the application of the proposed de-noising tool to the measurements carried out by a typical ultra-wideband PD sensor (high-frequency current transformer (HFCT)) widely used for on-site PD measurement in cables, transformers, motors, switchgear, overhead lines, etc. The de-noising performance is compared to those obtained through the alternative WT, EMD, and H-ASVD algorithms.

In this first real application test case, the proposed STFT-SVD algorithm is applied to a PD signal measured using a HFCT to demonstrate its de-noising performance. To have a

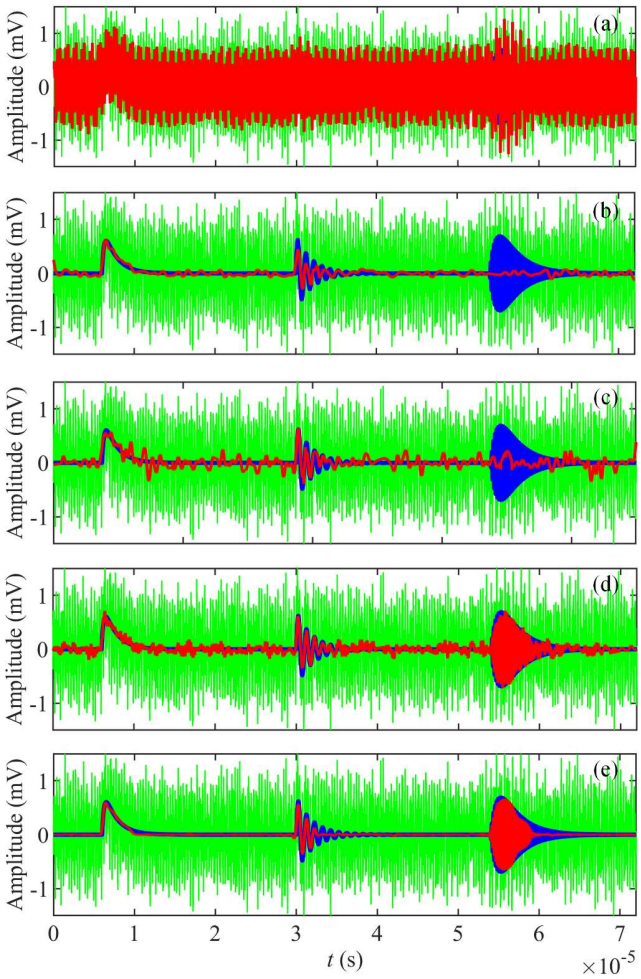

Figure 3-20 De-noising results of (a) H-ASVD (the size of Hankel matrix: 450×9000), (b) WT (the mother wavelet: dB8), (c) EMD (the ensemble number: 300), (d) the proposed STFT-SVD without the soft masking (M=200, q=0), and (e) the proposed STFT-SVD with the soft masking (M=200, q=2). The green, blue, and red lines denote the noisy (SNR=-11.10 dB), the original, and the de-noised signals.

Table 3-2 Evaluation metrics comparison of the algorithms

Method	*SNR* (dB)	*NCC*	*RMSE*
STFT-SVD (L=200, q=0)	7.53	0.912	0.057
STFT-SVD (L=200, q=2)	12.97	0.975	0.030
WT	2.10	0.627	0.107
EMD	0.236	0.518	0.132
H-ASVD	-9.17	0.273	0.390

controlled environment and test, two measurements are carried out: one is related to a PD signal with the smallest possible noise corruption, and the other involves the contribution of the noise only, being this latter associated with another conductor and time window where only the spurious disturbance is recorded. The PD signal originates from a soiled insulator in a 10-kV covered conductor (CC) line, as shown in Figure 3-21. The passband frequency of

the HFCT is 0.5-30 MHz, and the sampling frequency for data collection is 125 MHz.

Figure 3-22 collects the time waveforms and the corresponding frequency spectra of the measured PD signal and noise. Specifically, panel (a) corresponds to the PD signal measured as close as possible to the insulator to reduce noise's detrimental effects and produce a reference response, which is eventually compared with the reconstructed PD. Panel (b) and panel (c) correspond to the noisy contrition and the PD noisy response, respectively. The PD noisy response is generated by summing the noiseless and the noisy waveforms. It is essential to point out that the noisy waveform of Figure 3-22(b) includes both the effects of the white noise and the discrete spectrum noise. Also, for this case, the PD pulse, for both the time- and the frequency-domain waveforms, is massively cluttered by the effect of the sizeable superimposed noise, thus making the de-noising a challenge.

De-noising starts from the time-domain measured response of Figure 3-22(c) using all the considered algorithms. In the proposed STFT-SVD algorithm, the tuning parameters are defined as follows. According to (3-18) and the suggested range of α between 20 to 60, M should be chosen between 83 and 254. It is essential to point out that the discussion of the role of M in Chapter 3.2.1 and the additional simulation analyses have proven that the overall accuracy of the method has a very low sensitivity to this parameter. For this test case, the window width value is set to 200 sampling points (corresponding to the ratio $\alpha \approx 48$), which enables the frequency resolution to be 0.625 MHz. A similar reasoning and behavior holds for the other parameter (i.e., the attenuation control factor in the soft masking), which is set to 2 due to the high-level noise.

Figure 3-23 offers the results of the cross-comparison. It illustrates the proposed tool's superior performance, which yields an excellent reconstructed PD signal (see Figure 3-23(d)). From the responses in the figure, we can observe that the H-ASVD algorithm fails to remove the discrete spectrum noise (see Figure 3-23(a)), the WT algorithm effectively reduces most of the noise but leads to a visible distortion (see Figure 3-23(b)), and the EMD algorithm can only discriminate the PD signal vaguely and leads to a significant distortion (see Figure 3-23(c)). To sum up, this test has proven the excellent features of the proposed de-noising tool for in-field measurements via HFCT.

(a) (b)

Figure 3-21 Layout of the high-frequency current transformer on a 10-kV CC line (a) and picture of the PD defect on an insulator caused by fouling (b).

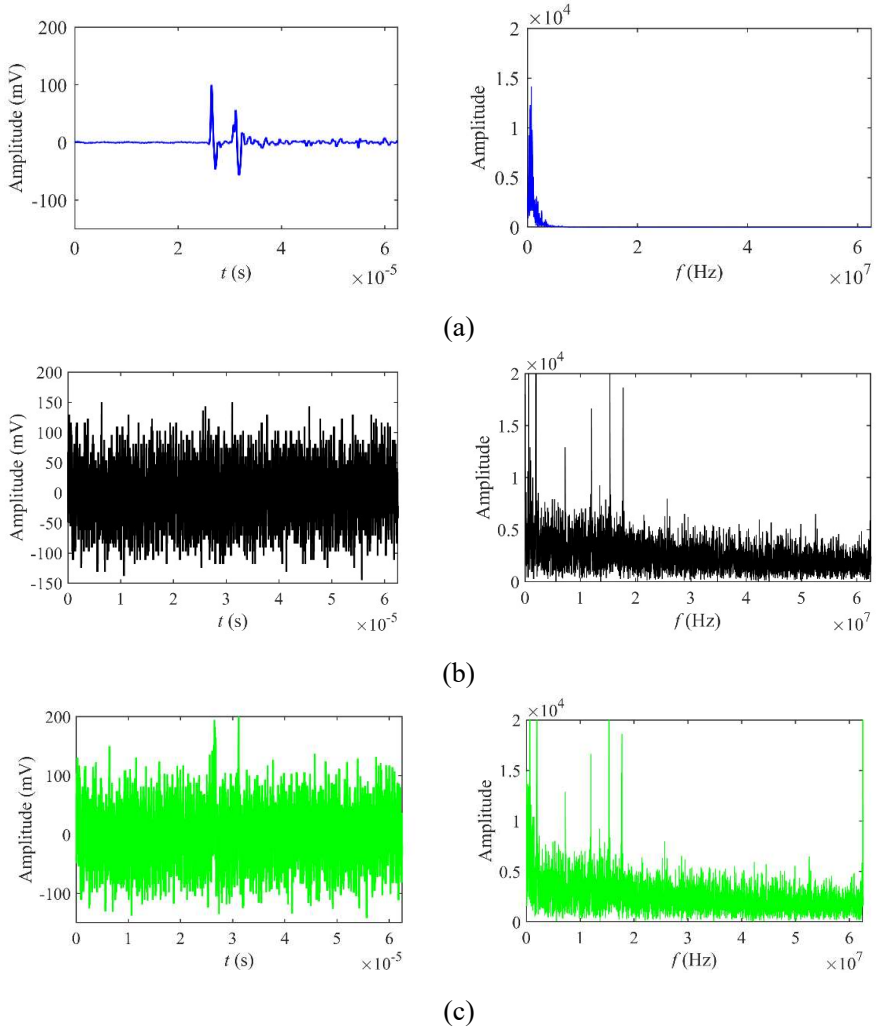

Figure 3-22 Time-domain waveforms and frequency-domain spectrums of the HFCT-measured PD signal (a), the HFCT-measured noise (b), and their combination (c).

3.3 Adaptive and Efficient Partial Discharge De-noising Algorithm for Implementation in Resource-Limited Embedded Systems

This section addresses developing and implementing a practical algorithm for PD monitoring of weakly insulated apparatuses in electrical power systems. The proposed solution addresses the challenges of field noise filtering and hardware selection. On one side, field noise has unavoidable detrimental effects on monitoring, thus demanding a clever and robust solution. On the other hand, the implementation of limited resource hardware is a crucial requirement for a practical design, allowing to reduce production costs. This work describes an adaptive and efficient PD de-noising algorithm based on the improved spectral decomposition of the noisy PD signal. PD pulses are accurately extracted from the noisy signal by cleverly selecting the dominant components via a low-rank singular value decomposition of the time-frequency spectrogram of the signal, thus reducing the size of the involved matrices and the computational complexity. The performance of the proposed de-noising algorithm is first demonstrated on a synthetic PD signal and compared with

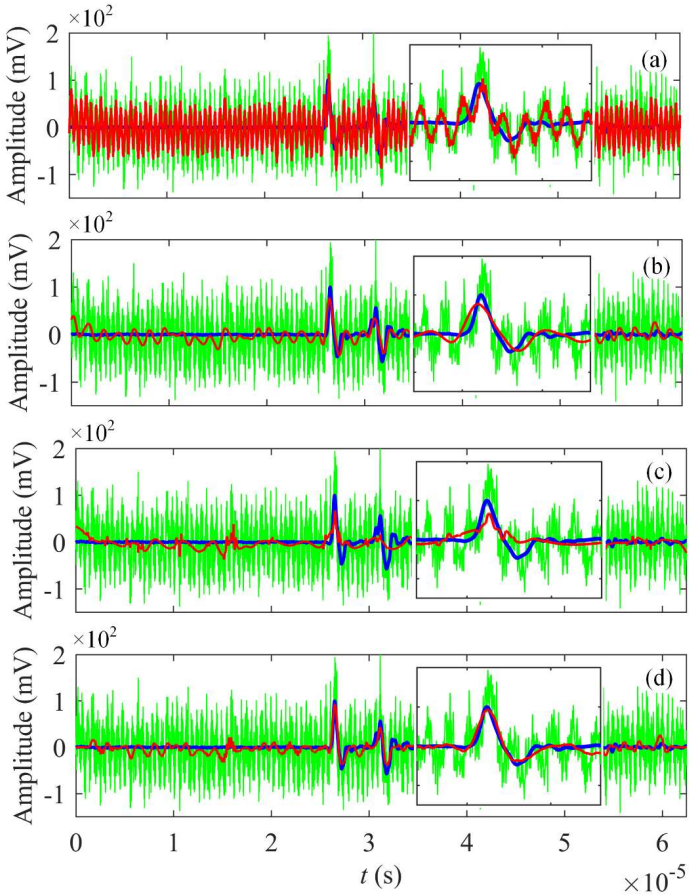

Figure 3-23 De-noising results of actual noisy PD signal by (a) H-ASVD (the size of Hankel matrix: 390×7810), (b) WT (the mother wavelet: dB8), (c) EMD (the ensemble number: 300), and (d) the proposed STFT-SVD (M=200, q=2). The green, blue, and red lines denote the noisy, original, and de-noised signals. The insets zoom in on the PD pulses.

state-of-the-art alternative techniques implemented on three embedded systems commonly used for PD monitoring. Finally, the strength and the effectiveness of the proposed approach are further validated on experimental data based on the measurement of Internet-of-Thing-based PD monitors, demonstrating its better de-noising performance in improving the sensitivity and accuracy of the PD monitors.

3.3.1 Algorithm Improvements

To reduce the computational complexity of the STFT-SVD algorithm, the more efficient STFT-RSVD algorithm is developed, as shown in Figure 3-24. Compared with the STFT-SVD algorithm, the proposed algorithm has three improvements, which will be discussed and formulated in the following.

Improvement 1: Kurtosis criteria are added between the STFT and SVD steps, aiming at avoiding applying the expensive SVD to the useless data without PDs.

PD pulses have a short duration, leading to outliers in the local area of the spectrogram (i.e., $\mathbf{X} \in \mathbb{C}^{M \times L}$ obtained via the STFT). At the same time, white and discrete spectrum noises are continuous and tend to lack outliers in the time dimension (i.e., each row of the spectrogram). Such a statistical difference between PD pulses and white and discrete

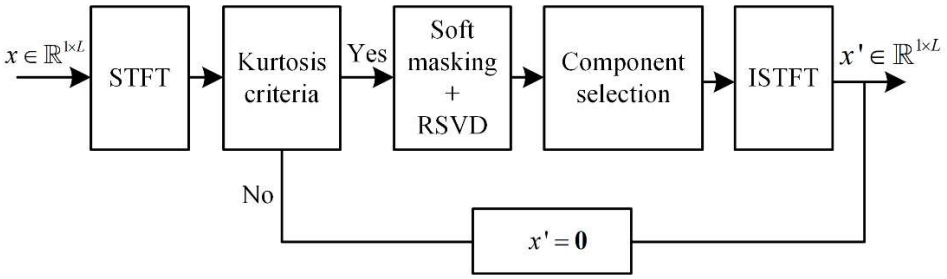

Figure 3-24 Block diagram of the improved STFT-RSVD algorithm.

spectrum noises allows us to identify whether one or multiple PD pulses occur in the signal sequence by detecting these outliers. Since the real parts of the spectrogram have similar outliers as the spectrogram, PD identification can be achieved by applying kurtosis criteria directly to the real parts of each row of the obtained spectrogram to reduce computational cost. The criteria are formulated as

$$\begin{cases} \text{yes}, & \left(\sum_{i=1}^{M} \text{logical}(kur(\mathbf{X}_i^{\text{re}}) > \beta)\right) \geq \varepsilon \\ \text{no}, & \left(\sum_{i=1}^{M} \text{logical}\left(kur\left(\mathbf{X}_i^{\text{re}}\right) > \beta\right)\right) < \varepsilon \end{cases} \tag{3-19}$$

where $\mathbf{X}_i^{\text{re}}$ is the real parts of the i^{th} row of the spectrogram, M is the total number of rows of the spectrogram (also the length of the Gaussian window in STFT), β is a threshold set to 4, an empirical value suggested in [131], ε is a threshold to identify whether a PD occurs and is better to be selected as 2~5 since too small or large ε may lead to wrong or missed PD identification, $kur(\bullet)$ is the kurtosis calculation function, and logical($\bullet$) is the logical function and returns 0 or 1. The computational complexity of the criteria is up to that of the kurtosis calculation function, i.e., $\mathrm{O}(2MN)$, where N is the total number of columns of the spectrogram, determined by $N = \lfloor (K - M + H)/H \rfloor$, where K is the sampling number of the signal, and H is the window hops of the STFT. Moreover, it is essential to point out that applying the kurtosis criteria to the spectrogram is better than the time-domain signal since outliers caused by PDs are more significant.

Improvement 2: RSVD is used to decompose the time-frequency spectrogram automatically. Compared with the SVD, the RSVD requires less memory, leading to significantly smaller computational complexity.

Since the elements belonging to the PD signal always concentrate at the local area of the spectrogram $\mathbf{X}$, we can perform low-rank approximation to reduce the size of the input matrix of the expensive sequent SVD, which can be achieved via the randomized algorithm described in [132]. The randomized algorithm and SVD combination are named randomized SVD (RSVD) [133]. The noisy input matrix $\mathbf{X} \in \mathbb{C}^{M\times N}$ (obtained via the STFT) is decomposed into four matrices via RSVD, yielding:

$$\mathbf{X} = \mathbf{Q}\mathbf{U}_{\mathrm{Q}}\mathbf{S}_{\mathrm{Q}}\mathbf{V}_{\mathrm{Q}}^{H} \tag{3-20}$$

where $\mathbf{Q} \in \mathbb{C}^{M\times P}$ is a given matrix with P ($P \ll M,\ N$) orthonormal columns which can

be obtained via the randomized algorithm [133], $\mathbf{U}_{\mathrm{Q}}$ is a $P \times P$ left orthonormal matrix ($\mathbf{U}_{\mathrm{Q}}$=[$\boldsymbol{u}_1, \boldsymbol{u}_2, \ldots, \boldsymbol{u}_P$], $\boldsymbol{u}_i \in \mathbb{C}^{P\times 1}$), $\mathbf{S}_{\mathrm{Q}}$ is a real $P \times P$ rectangular matrix with the singular values $\sigma_1 > \sigma_2 > \cdots > \sigma_P$ in the diagonal entries, and $\mathbf{V}_{\mathrm{Q}}$ is a $P \times N$ right orthonormal matrix ($\mathbf{V}_{\mathrm{Q}}$=[$\boldsymbol{v}_1, \boldsymbol{v}_2, \ldots, \boldsymbol{v}_P$],$\boldsymbol{v}_i \in \mathbb{C}^{N\times 1}$). The total computational complexity of the RSVD is $\mathrm{O}(4MN\log P + 4(M+N)P^2)$ [133], which is much less than that of the classical SVD (i.e., $\mathrm{O}(4NM^2)$) as P can be set much less than M and N.

In RSVD, only one parameter (i.e., P) is required to be set in advance. On the one hand, we want the basis matrix $\mathbf{Q}$ to contain as few columns as possible to reduce the computational complexity. On the other hand, accurately approximating the input matrix is even more critical. Therefore, P can be slightly larger than the PD components' estimated rank to guarantee this approximation's accuracy. Accordingly, an empirical rule to roughly determine P can be formulated as

$$P = M\frac{\Delta f_{\mathrm{PD}}}{f_s} + r \tag{3-21}$$

where M can be determined by the empirical formula provided in (3-18), Δf_{PD} is the estimated frequency bandwidth of the PD signal, f_s is the sampling frequency, the term of $M \cdot \Delta f_{\mathrm{PD}}/f_s$ denotes the estimated rank of the PD components, and r is the redundancy factor in guaranteeing reliable noise reduction performance. It can be set from 3 to 5 [133].

Improvement 3: The component selection is carried out before the ISTFT step to avoid executing the computationally expensive ISTFT multiple times, significantly reducing the computational complexity of this step.

In the STFT-SVD method in Chapter 3.2, pulse-type component selection is achieved by applying kurtosis criteria to the sub-signals reconstructed using ISTFT for each component, leading to substantial computation costs. Alternatively, since the right orthonormal eigenvectors $\boldsymbol{v}_1, \boldsymbol{v}, \ldots,$ and $\boldsymbol{v}_P$ (obtained via RSVD) also contain the time-dimension characteristics of the components, we can apply kurtosis criteria to the eigenvectors to select pulse-type components before ISTFT, thus avoiding executing the ISTFT multiple times. The components with larger kurtosis values are chosen to reconstruct the noiseless matrix $\mathbf{X}' \in \mathbb{C}^{M\times N}$, which can be formulated as:

$$\mathbf{X}' = a_1\sigma_1\mathbf{Q}\boldsymbol{u}_1\boldsymbol{v}_1^H + a_2\sigma_2\mathbf{Q}\boldsymbol{u}_2\boldsymbol{v}_2^H + \cdots + a_P\sigma_P\mathbf{Q}\boldsymbol{u}_P\boldsymbol{v}_P^H \tag{3-22}$$

where $a_i = \mathrm{logical}\{kur(\boldsymbol{v}_i^{\mathrm{re}}) > 4\}$, where $\boldsymbol{v}_i^{\mathrm{re}}$ is the real parts of the right eigenvector $\boldsymbol{v}_i$, and $\mathbf{Q}\boldsymbol{u}_i$ can be directly obtained in (2), and thus it does not lead to computational costs in (4) [133]. The total computational complexity of the component selection and spectrogram reconstruction can be calculated as $\mathrm{O}(2NP + 4MNP')$, where P' is the number of the selected components, and it is always much less than P.

An overall comparison between the computational complexity of the improved STFT-RSVD algorithm and the STFT-SVD algorithm in Chapter 3.2 at each algorithm step is listed in Tab. 1. It can be observed that the added kurtosis criteria between STFT and

RSVD leads to a negligible additional computational cost while applying RSVD to decompose the spectrogram and exchanging the order between the component selection and ISTFT can significantly reduce the computational complexity. Moreover, it is essential to point out that although some other time-frequency transform tools (e.g., continuous wavelet transform, Wigner-Ville distribution, Hilbert-Huang transform, etc.) are optional to obtain the spectrogram, we still select the STFT since it is the most time-saving one [134].

Table 3-3 Computational complexity comparison between the STFT-SVD and the proposed STFT-RSVD algorithms

The improved STFT-RSVD algorithm			The STFT-SVD algorithm in Chapter 3.2	
Steps	Computational complexity		Steps	Computational complexity
STFT+ Kurtosis criteria	$O(MN\log M + 3MN)$	$\approx$	STFT	$O(MN\log M + MN)$
Soft masking	$O(4MN)$	$=$	Soft masking	$O(4MN)$
RSVD	$O\left(4MN\log P + 4(M+N)P^2\right)$ $(P \ll M, N)$	$\ll$	SVD	$O(4M^2N)$
Component selection	$O(2NP + 4MNP')(P' \ll P, R)$	$\ll$	ISTFT	$O(MNR\log M + 5MNR)$
ISTFT	$O(MN\log M + MN)$		Component selection	$2NR$

M denotes the row number of the spectrogram; N denotes the number of columns of the spectrogram, determined by $N = \lfloor (K - M + H)/H \rfloor$, where K is the sampling number of the signal, and H is the window hops of the STFT; R denotes the number of the components obtained via principal component analysis in the STFT-SVD algorithm; P denotes the number of columns of the given matrix $\mathbf{Q}$ in RSVD; P' denotes the number of the selected components in the proposed STFT-RSVD algorithm.

3.3.2 Implementation in Embedded Systems

In on-site PD monitoring, PD diagnosis, including signal extraction, recognition, and analysis, is always completed in embedded systems instead of personal computers due to their nominal cost, volume, power consumption, functionalities, flexible hardware programming, etc. Many types of embedded systems with varying hardware resources have been used for PD monitoring in different application scenarios, which depend on the testing object and the budget cost.

Three representative types of embedded systems are often used for PD diagnosis: System on Chip (SoC), Microprocessor Unit (MPU), and Microprogrammed Control Unit (MCU). SoC is a system-level chip with very abundant hardware resources (i.e.,

field-programmable gate array, multiple cores, high-speed processors, and extensive random-access memories (RAM)), but on the contrary, it has a very high cost and power consumption; it is often used for advanced PD diagnosis of recognition, classification, and localization, e.g., the PD location system for medium-voltage switchgear and cables [135][136]. MPU is a kind of integrated Central Processing Unit with multiple cores, high-speed processors, and more functionalities but may have small random-access memories; it is often used for PD detection, recognition, and classification, e.g., online PD monitoring for high-voltage motors, gas insulation systems, and transformers [137]. MCU is a chip-level chip with fewer hardware resources (i.e., a single core, a low-speed processor, less RAM), but it has a low cost and power consumption; it is often used for low-cost and low-power PD detection, e.g., the online IoT-based PD monitors for widely distributed medium-voltage overhead lines, cables, and switchgear [138][140].

On the embedded systems side, in this work, three representative chips corresponding to the above SoC, MPU, and MCU have been selected to test the performance of the proposed algorithm and its alternatives. Their characteristic parameters and reference prices are listed in Tab. II. The used evaluation boards integrate all the hardware needed for programming and debugging the chips, namely the JTAG interface for ZYNQ7035 and the ST-LINK/V2 interface for STM32MP157 and STM32L476. The input or output PD signals are stored in the program memory (flash memory), while the intermediate signals or matrices are stored in the RAM. All three devices have been clocked at their maximum speeds.

On the computer side, communication with the above interfaces has been established using KELL 5.0 (for STM32MP157 and STM32L476) and VIVADO (for ZYNQ7035), free software for debugging and programming ARM and other systems. Once the program runs for a series of tests, the numerical outputs can be examined or exported through the debuggers, interrupting the program at convenient points. The timing of the single routines is computed by the software itself, using the SysTick timer built into the ARM cores.

Since the recommended software (i.e., KELL 5.0 and VIVADO) only supports debugging and programming in the embedded systems in C Language, we must implement the PD de-noising algorithms in C Language. However, the C-languages of the most cost-efficient versions of some sub-functions in the algorithms (e.g., STFT and SVD) are unavailable. Alternatively, we programmed the algorithm in MATLAB codes and used a transcoding tool named MATLAB CODER to translate the MATLAB codes into C codes. On the one hand, the MATLAB software platform can provide all the latest sub-functions required in the algorithm. On the other hand, the MATLAB CODER allows us to allocate the dynamic memory to execute the algorithm according to the size of the RAM in the embedded systems, and it can automatically generate corresponding C codes [140]. This work sets the dynamic memories of ZYNQ7035, STM32MP157, and STM32L476 as 900 Mbytes, 700 Kbytes, and 100 Kbytes, respectively. Moreover, the MATLAB CODER includes the OpenMV interface, which can generate the C codes that can be executed in parallel with multiple cores, e.g., in ZYNQ7035 or STM32MP157. This can further reduce the computational cost of the embedded algorithms.

Table 3-4 Features of three representative embedded systems commonly used for PD monitoring

Serial number	Device models	Pictures of the used evaluation board	Types	ARM cores	Clock frequency	Memory (RAM)	Price of the device	Application scenarios
Device 1	ZYNQ70 -35	 (AX7350,ALINX)	SoC	2×Cortex-A9+ Kintex-7	800 MHz	1 Gbytes	1280 USD	Advanced PD diagnosis: recognition, classification, and localization [135][136]
Device 2	STM32 M-P157	 (ATK-DLMP157M, ALIENTEK)	MPU	Cortex-M4 + Cortex-A7	209 MHz +800 MHz	708 Kbytes	109 USD	PD detection, recognition, and classification [137]
Device 3	STM32L -476	 (STM32 Nucleo-L476RG, ST)	MCU	Cortex-M4	80 MHZ	125 Kbytes	12 USD	Low-cost and low-power PD detection and recognition [138][140]

3.3.3 Results of De-Noising Synthetic Signal

A generic PD signal with an extremely low signal-to-noise ratio is synthesized to assess the de-noising algorithms quantitatively. The feasibility of the proposed algorithm is validated via de-noising the synthetic PD signal in Device 1. The effects of the input parameters of the proposed algorithm on its computing costs are simulated in Device 1. The de-noising performance of the proposed algorithm and its alternative algorithms is compared in Devices 1, 2, and 3.

1）Synthetic Noisy PD Signal

Figure 3-25 collects the time-domain and frequency-domain waveforms of the synthetic PD signal. Since the synthetic signal includes multiple PD pulses with various waveforms, which simulate a general case in field PD measurement, it can be used as a qualified test sample to evaluate the de-noising performance of the proposed algorithm and its alternative solutions. The sampling rate of the synthetic signal is 125 MS/s, and the sampling number is 16000.

The PD current pulse can be modeled at the PD source by a double exponential pulse, e.g., pulse 1 in Figure 3-25(a). However, most detected PD signals are oscillating pulses due to the effects of both the propagation path and the transfer function of the used sensor. Therefore, single exponential and double exponential attenuation oscillation pulses, e.g., pulses 2 and 3 in Figure 3-25(a), are used. Nevertheless, the real PD signals can be more complex than these tree models, e.g., pulses 4 and 5 in Figure 3-25(a). Pulse 4 originates from a fouling insulator and is detected by the high-frequency current transformer, as provided in [36]. Pulse 5 originates from the leaning tree and is detected by the same

high-frequency current transformer. It is essential to point out that the high-frequency current transformer was deployed close to the defects to reduce the influence of the field noise as much as possible.

Discrete spectrum noise and white noise are added to the synthetic PD signal. The frequencies of the two harmonics in the discrete spectrum noise are set to 2.5 and 7 MHz, and their corresponding amplitudes are set to 1.5 and 1 mV, respectively, while the standard deviation of the white noise is set to 1 mV. It is essential to note that the synthetic noise includes very high-level noise. Thus, it can be used to validate and assess the de-noising performance of the proposed algorithm for a PD signal with an extremely low signal-to-noise ratio.

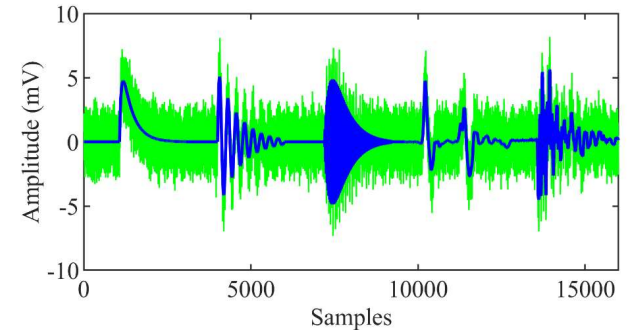

(a)

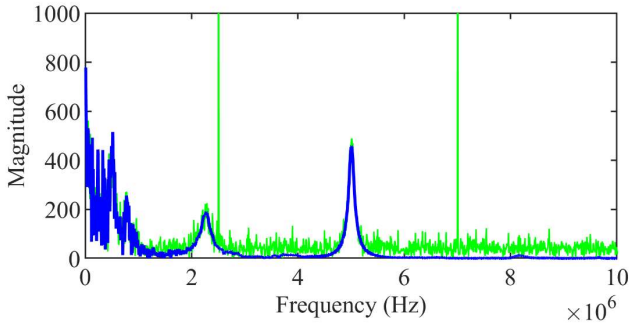

(b)

Figure 3-25 Time-domain (a) and frequency-domain (b) waveforms of the synthetic noiseless and noisy PD signals. The green and blue lines denote the noisy and original signals, respectively.

2）Validation Experiment (in Devices 1)

In Chapter 3.3.1, three improvements in the proposed STFT-RSVD algorithm are developed, aiming at reducing its computational complexity without influencing its de-noising performance. To validate the feasibility of the improvements, the de-noising experiment of the proposed STFT-RSVD algorithm was carried out in the synthetic PD signal in Device 1, which was compared with the STFT-SVD method in [26]. The parameters of the STFT-RSVD algorithm were set as M=320, H=10, and P =20, according to the empirical equations in Chapter 3.3.1 and [26].

Figure 3-26 collects the plots of the kurtosis values of the real parts of rows of the spectrograms calculated for the noisy PD signal. The index axis denotes the serial number of

rows of the spectrogram. It can be observed that the kurtosis values of the noise spectrogram are less than the threshold, while parts of the noisy PD signal are significantly larger than the threshold. According to Equation (3-19), the class of the spectrogram of the noise will be identified to be "No," while that of the noisy PD signal will be "Yes," validating the feasibility of the added kurtosis criteria.

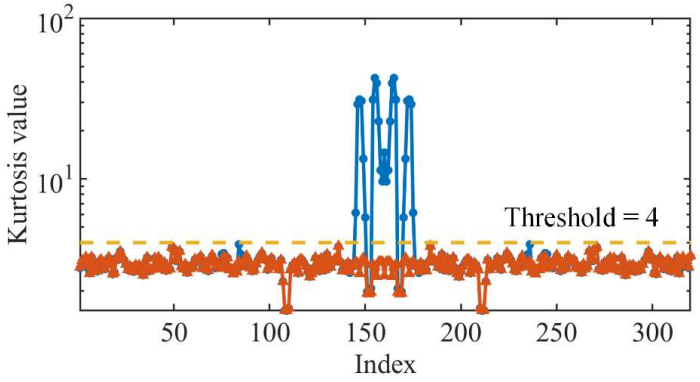

Figure 3-26 Kurtosis values of real parts of rows of the spectrograms of the noise (triangle labels) and noisy PD signal (round labels) (M=320, H=10, and P =20).

Figure 3-27 collects the plots of the kurtosis values of the reconstructed sub-signals obtained via applying ISTFT to each component in the STFT-SVD algorithm and the real parts of the right orthonormal eigenvectors obtained via the RSVD. The index axel denotes the serial number of the components obtained via the RSVD. It can be observed that the kurtosis values of the real parts of the right orthonormal eigenvectors are generally similar to that of the reconstructed sub-signals, verifying the feasibility of selecting the pulse-type components by applying kurtosis criteria to the right orthonormal eigenvectors. Although the difference between the kurtosis values of the two curves tends to be more prominent as the index increases, the result of the component selection via the threshold criteria is hardly influenced. Moreover, since the components' energy significantly reduces as the index rises, discriminant error on the element with a more extensive index severely affects the final de-noising result.

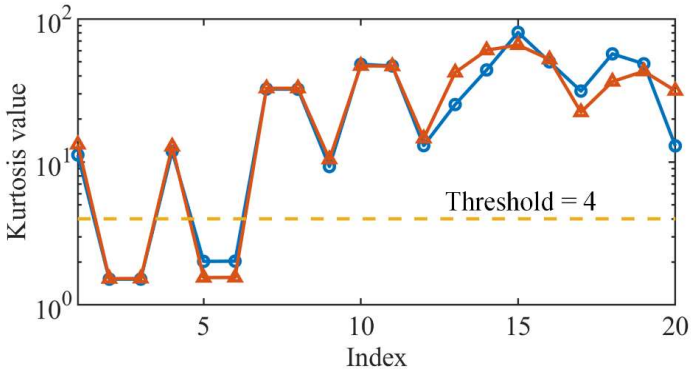

Figure 3-27 Kurtosis values of the reconstructed sub-signals obtained via applying ISTFT to each component (round labels) and the real parts of the right orthonormal eigenvectors obtained via the RSVD (triangle labels) (M=320, H=10, and P =20).

Figure 3-28 and Figure 3-29 collect the de-noised signals and computation time of the STFT-SVD method and the proposed STFT-RSVD algorithm, respectively. In Figure 3-28, it can be observed that their de-noising results are almost coincident as their errors are negligible. In contrast, the computation time of the proposed STFT-RSVD algorithm is significantly less than that of the STFT-SVD algorithm, especially in terms of the SVD or RSVD, component selection, and ISTFT steps. The results demonstrate the essential benefits of the RSVD and exchanging the order between component selection and ISTFT in reducing computational complexity.

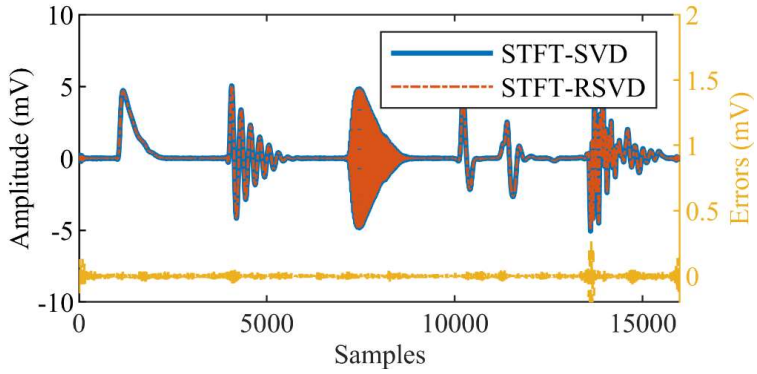

Figure 3-28 De-noising results of the STFT-SVD and the improved STFT-RSVD algorithms (M=320, H=10, and P =20).

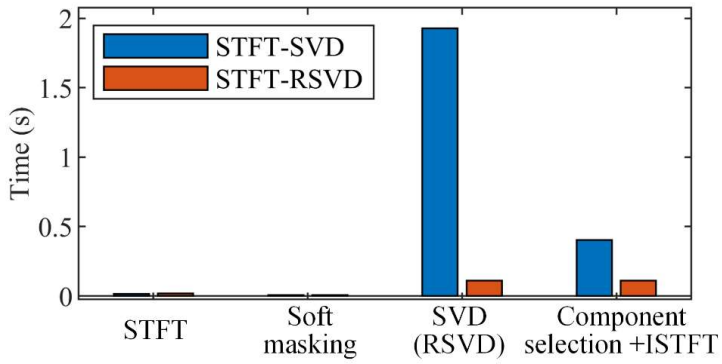

Figure 3-29 Computation times of all steps in the STFT-SVD (a) and STFT-RSVD (b) algorithms (M=320, H=10, and P =20).

3）Parameter Effect Simulation (in Devices 1)

The computational complexity of the proposed STFT-RSVD algorithm is associated with its three parameters, i.e., window length M of STFT; window hops H of STFT, and the estimated rank P of the spectrogram of the noiseless PD. Therefore, this subsection will investigate their effect on the computing cost of the proposed algorithm via de-noising the synthetic PD signal in Device 1. Moreover, since down-sampling the PD signal is commonly applied to reduce the computational burden of the used embedded systems, its effect on the proposed algorithm is also evaluated.

Figure 3-30 collects the curves of *SNR*s and the overall computational time of the proposed algorithm against the window length M. H and P are set as 10 and 20,

respectively. It can be observed that the de-noising performance improves as M increases in the initial part of the curves. It becomes nearly flat once the number of sampling points exceeds the critical value of 100, and finally, it declines slowly as M continues to increase. The computation time of the proposed algorithm gradually increases as M increases since the size of the spectrogram (i.e., the number of rows) increases too. Moreover, the increased size can lead to a significantly increased memory requirement. Therefore, considering both the de-noise performance and efficiency, selecting the smallest value of M may lead to sufficiently good performance indexes.

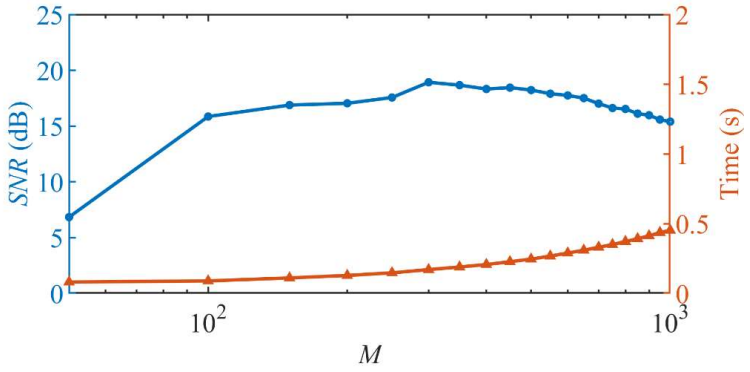

Figure 3-30 Effect of window length M on SNR and the overall computational time required by the proposed STFT-RSVD algorithm (H=10, P = 20).

Figure 3-31 collects the curves of *SNR*s and the overall computational time of the proposed algorithm against the window hops H. M and P are set as 320 and 20, respectively. It can be observed that the de-noising performance stays nearly flat as H increases in the initial part of the curve. It decreases slowly, and finally, it oscillates and decreases faster once H exceeds the critical value of 12. The computation time of the proposed algorithm significantly decreases as H increases since the size of the spectrogram (i.e., the number of columns) decreases. Considering the de-noise performance and efficiency, selecting the critical value of H may lead to sufficiently good performance indexes.

Figure 3-32 collects the curves of *SNR*s and the overall computational time of the proposed algorithm against the estimated rank P. H and M are set as 10 and 320, respectively. It can be observed that the de-noising performance improves as P increases in the initial part of the curves, and then it becomes nearly flat once P exceeds the critical value of 12. Therefore, as suggested in equation (3), P should be set to be somewhat more significant than the estimated rank of the PD components in the proposed STFT-RSVD algorithm, as such a value of P can lead to the same de-noising performance as the STFT-SVD algorithm but significantly reduced computational cost, which verifies the critical benefit of the RSVD.

Figure 3-33 collects the curves of *SNR*s and the overall computational time of the proposed algorithm against the down-sampling intervals. M, H, and P are set as 160, 10, and 20, respectively. It can be observed that as the down-sampling intervals increase, the

de-noising performance decreases linearly while its computation time decreases exponentially. This means that down-sampling the input noisy PD signal can be a feasible trade-off solution if the computing resources of the used embedded system are severely insufficient.

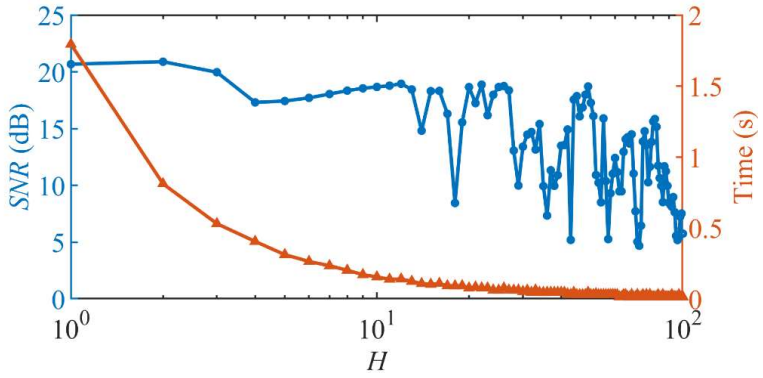

Figure 3-31 Effect of window hops H on SNR and the overall computational time required by the proposed STFT-RSVD algorithm ($M = 320$, $P = 20$).

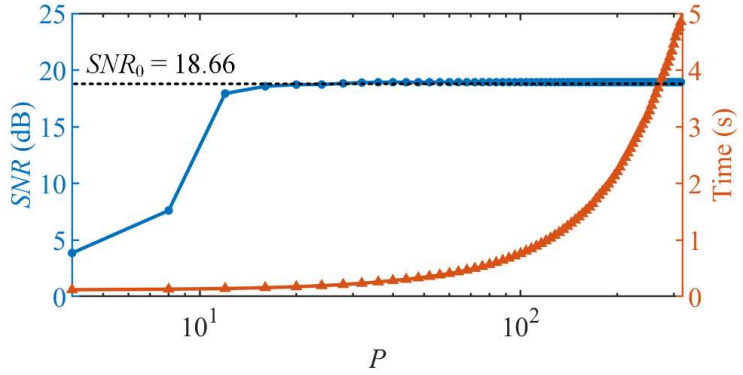

Figure 3-32 Effect of P in RSVD on SNR and the overall computational time required by the proposed STFT-RSVD algorithm ($M = 320$, $H = 10$). (SNR 0 is the SNR of the de-noised signal obtained via the STFT-SVD algorithm [26]).

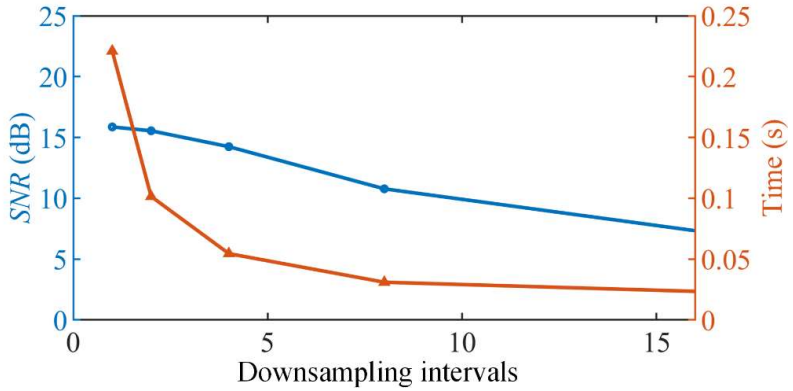

Figure 3-33 Effect of down-sampling intervals on SNR and the overall computational time required by the proposed STFT-RSVD algorithm ($M = 160$, $H = 10$, and $P = 20$).

4）De-noising Result (in Devices 1, 2, and 3)

De-noising the synthetic noisy PD signal via the proposed algorithm and its alternatives (i.e., WT [62], EMD [73], AST-SVD [82], H-FSVD [83], and S-SVD [87]) was carried out in Devices 1, 2, and 3. We selected three group parameters for the proposed STFT-RSVD algorithm in this experiment: (i) M=80, H=1, and P=20; (ii) M=40, H=5, P=12; (iii) M=20, H=10, P=8, which all satisfy the empirical equations in Chapter 3.3.1 and in [26]. The first group of parameters was used in the proposed algorithm executed in Device 1, while the second and last were in Device 2 and 3, respectively. Moreover, since the memories of Devices 2 and 3 are minimal, the synthetic signal is down-sampled with eight intervals before de-noising.

The de-noising results are shown in Figure 3-34. In Figure 3-34(a), the WT algorithm behaves well for the first pulse but fails to reconstruct the third pulse. The difference in the noise reduction effect on the PD pulses is attributed to the selected mother wavelet (dB8). In Figure 3-34(b), the EMD technique can only discriminate the PD signal vaguely; discrete spectrum noises and waveform distortions remain; it fails to reconstruct the third and last pulses. In Figure 3-34(c), the H-FSVD fails to reduce the discrete spectrum noise since its principal component analysis cannot distinguish PD and discrete spectrum noise. In Figure 3-34(d), the AST-SVD algorithm cannot remove the discrete spectrum noise as the H-FSVD. In Figure 3-34(e), the S-SVD algorithm removes most of the noise but fails to reconstruct the first pulse, and waveform distortions can be observed in the other pulses. In Figure 3-34(f), (g), and (h), compared with the results of WT, EMD, H-FSVD, AST-SVD, and S-SVD algorithms, the proposed STFT- SVD algorithm can effectively reduce both the white noise and the discrete spectrum noise in all five types of PD pulses, demonstrating its more strong adaptability to de-noise various noisy PD signal with an extremely low signal-to-noise ratio.

All the algorithms' evaluation metrics (SNR and computing times) are listed in Table 3-5.For de-noising performance, it can be observed that the proposed STFT-RSVD algorithm with parameter settings of M=80, H=1, and P=20 has the highest *SNR*. For computing time, in Device 1, it can be observed that as M decreases and H increases (i.e., the size of the time-frequency matrix decreases), the computational time of the proposed STFT-RSVD algorithm decreases exponentially; the STFT-RSVD algorithm requires significantly less computing time than other SVD-based algorithms (i.e., H-FSVD, AST-SVD, and S-SVD); although the STFT-RSVD algorithm requires slightly more computational time than the WT technique, it provides significantly better de-noising performance, as discussed in the last paragraph. Moreover, it is essential to note that the H-FSVD, AST-SVD, and S-SVD algorithms cannot be implemented in Devices 2 and 3 due to the limited memories, which cannot execute the expensive SVD operation in these algorithms. In contrast, the proposed STFT-RSVD algorithm can be implemented in Devices 2 and 3 as long as the proper parameters are selected, demonstrating the most crucial benefit that the proposed algorithm can be implemented in different embedded systems with varying hardware resources by tuning the three parameters, i.e., the window length M, the window hops H, and the estimated rank.

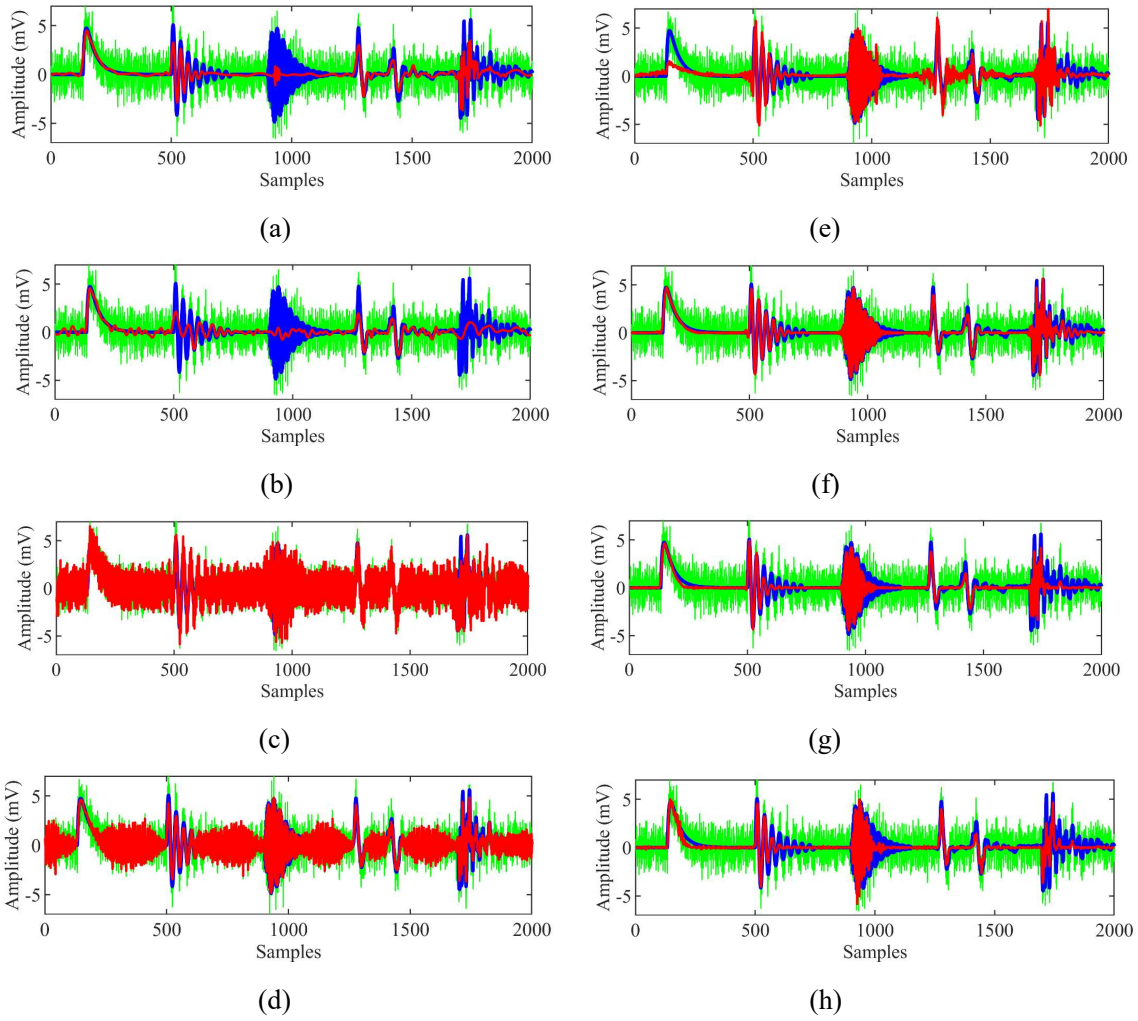

Figure 3-34 De-noising results of (a) WT (the mother wavelet: dB8; decomposition level: 5) in Device 1, (b) EMD in Device 1, (c) H-FSVD (the size of Hankel matrix: 500×2000) in Device 1, (d) AST-SVD (the size of the sliding window: 200; the size of Hankel matrix: 100×200) in Device 1, (e) S-SVD (the adjustable factor of S-transform: 1) in Device 1, (f) the proposed STFT-RSVD ($M = 80$, $H = 1$, and $P = 20$) in Device 1, (g) the proposed STFT-SVD ($M = 40$, $H = 5$, and $P = 12$) in Device 2, (h) the proposed STFT-SVD ($M = 20$, $H = 10$, and $P = 6$) in Device 3. The green, blue, and red lines denote the noisy, original, and de-noised signals.

3.3.4 Results of De-Noising Measured Real PD Signal

The proposed STFT-SVD algorithm and its alternative (i.e., the WT and EMD algorithms) are implemented in another PD monitor with the same hardware. The noisy PD data obtained via the PD monitor is imported into the PD monitor via its serial port. PD pulses in this data were caused by a fouling insulator. Since the memory of the processor (i.e., STM32L476) is minimal, causing it impossible to directly de-noise the whole data (i.e., with a length of 20 ms) at one time, we use a sliding window200 to split the data into multiple segmentations, which are de-noised individually. Since the frequency bandwidth of the PD data collected by the PD monitor (i.e., the envelope of the PD signal) is always less than 1 MHz [38], the window length M should be set as at least 15 (i.e., more than $\alpha \times 5$ MHz/1 MHz according to the empirical equation in [26], where α is set as 3) to guarantee a

Table 3-5 Evaluation metrics comparison of the algorithms

Method	*SNR* (dB)	Computation time (s)		
		Device 1	Device 2	Device 3
STFT-RSVD (*M*=80, *H*=1, *P*=20)	12.223	0.137	/	/
STFT-RSVD (*M*=40, *H*=5, *P*=12)	9.175	0.023	0.051	/
STFT-RSVD (*M*=20, *H*=10, *P*=6)	7.697	0.011	0.018	0.876
WT	3.654	0.005	0.011	0.489
EMD	3.059	0.007	0.016	0.728
H-FSVD	-0.575	0.109	/	/
AST-SVD	3.229	0.434	/	/
S-SVD	0.813	0.842	/	/

*Remark: "/" means that the memory is insufficient to run the algorithm. Moreover, since the minimal memory of Device 1, the signal is divided into five segments of equal length (i.e., 400 sampling points), which are de-noised one by one in Device 3; on the contrary, the whole signal is directly de-noised in Device 1 and 2 without segmentation.

sufficient frequency resolution of the spectrogram. On the other hand, M cannot be set too large due to the limit of its random access memory (i.e., 125 Kbytes) in STM32L476. Therefore, we selected three group parameters for the proposed STFT-RSVD algorithm in this experiment: (i) M=25, H=2, and P=10; (ii) M=20, H=4, P=8; (iii) M=15, H=6, P=5, where the possible values of H and P are set according to the suggestion of the simulation result in Chapter 3.3.4 and the empirical equation (4) provided in Chapter 3.3.1.

The de-noising results of the proposed algorithm and its alternatives are collected in Figure 3-35. It can be observed that the WT algorithm can only discriminate the PD signal vaguely, and leads to a significant distortion and energy loss. The EMD algorithm almost fails to de-noising most PD pulses. In contrast, the proposed algorithm yields perfect reconstructed PD pulses, causing most PD pulses (some even completely drowned in the noise) to be detected and their energy loss significantly less than the WT algorithm. Moreover, the proposed algorithm with the three-parameter settings yields similar de-noised results, demonstrating that the de-noising performance of the algorithm is insensitive to its parameters. It makes applying to various industrial applications easy without intensively tuning the parameters.

Figure 3-36 collects the computing times of the proposed algorithm in the sliding windows. The indexes in the horizontal axis denote the serial numbers of the signal segmentations obtained via sliding the time window on the data in Figure 3-35 from left to right. It can be observed that the computation times of the signal segmentations without PD pulses are significantly less than that with PD pulses, demonstrating the critical benefit of the

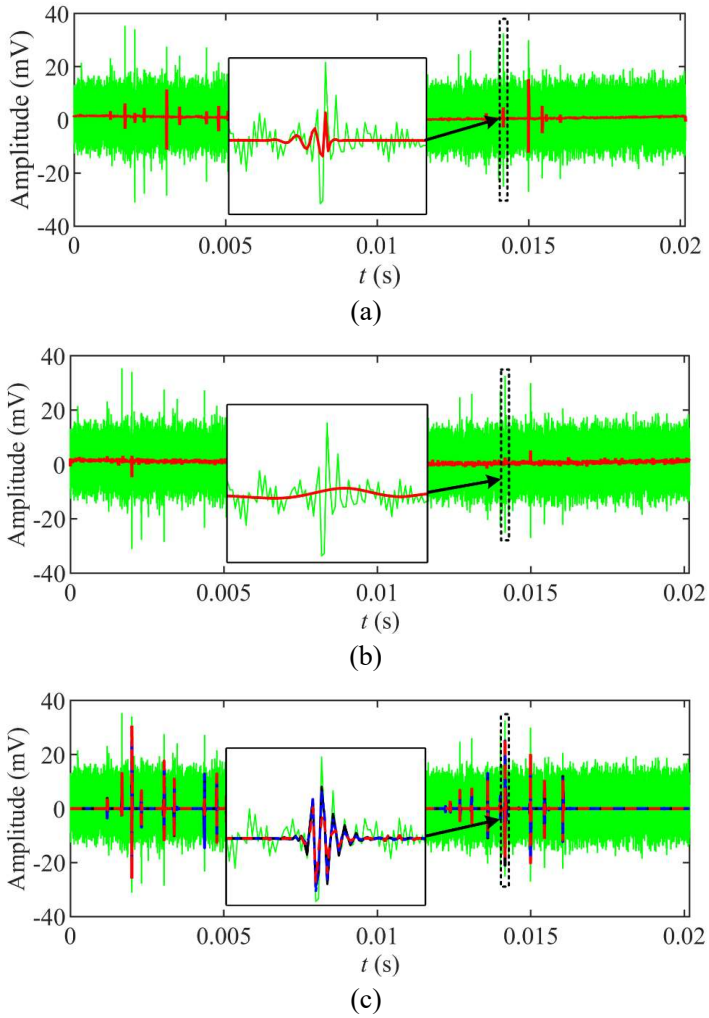

Figure 3-35 De-noising results of (a) WT (the mother wavelet: dB8; decomposition level: 5) in Device 3, (b) EMD in Device 3, (c) the proposed STFT-RSVD in Device 3 (black line: $M = 25$, $H = 2$, and $P = 10$; blue line: $M = 20$, $H = 4$, and $P = 8$; red line: $M = 15$, $H = 6$, and $P = 5$;). The green and red lines denote the noisy and de-noised signal.

kurtosis criteria between STFT and RSVD, i.e., avoiding unnecessary calculations of useless data. Moreover, it can be observed that the computing times of the signal segmentations with PD pulses using the third parameter setting are significantly less than that of the first and second parameter settings. This reveals that reasonably adjusting the parameters of the proposed algorithm (that is, reducing M and P and increasing H within the critical range) can significantly reduce its computation time without influencing its de-noising performance. The total computing times of applying the proposed algorithm and its alternatives to the whole data in Figure 3-35 are listed in Table 3-6. It can be observed that the proposed algorithms with the second and third parameter settings require significantly less computation time than that of the WT and EMD algorithms, primarily due to the unnecessary calculations of the useless data being avoided in the proposed algorithm. Moreover, it is essential to point out that the total computation time of the proposed algorithm (i.e., tens of seconds) is significantly less than the test interval (i.e., half an hour)

of the PD monitors, allowing it to be used in these monitors.

The collected 33 noisy PD data are successively de-noised via the proposed algorithm (with parameters of M=15, H=6, P=5). Figure 3-37 contains the statistical phase-resolved spectrum of the original data and the de-noised results, that is, the acknowledged data form widely used to diagnose PD magnitude and types [141]. The statistical phase-resolved spectrums display information about the amplitude and the position of the recorded PD events, which occur in possibly different locations within the period of the sinusoidal power source. The blue dots represent the cloud of points associated with the PD events. Each dot is placed in an (x,y) position where x is the phase location, and y is the pulse amplitude (i.e., the maximum value of the absolute values of the (de-noised) signal in the sliding time window). It can be observed that it is indeed difficult to identify any PD activities in the spectrum of the original signal due to the high-level noise; visible PD activities can be observed in the spectrum obtained via the WT algorithm, but it causes a significant energy loss and misses to detect parts of PD pulses; the spectrum of the EMD algorithm reveals a small number of PD events; in contrast, the proposed algorithm yields a significantly more precise and more accurate phase-resolved spectrum, which can be undoubtedly identified as one with significant PD activities and can be a qualified input for the subsequent PD recognition and classification. It reveals that the proposed algorithm can significantly improve the sensitivity and accuracy of PD detection via the monitors and has a better de-noising performance than the state-of-the-art alternatives.

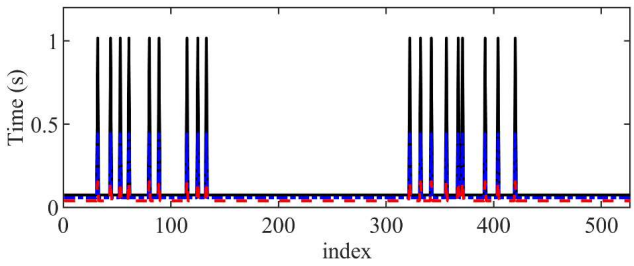

Figure 3-36 Computation times in the de-noising time window sliding on the noisy signal via the proposed STFT-RSVD algorithm. (black line: $M = 25$, $H = 2$, and $P = 10$; blue line: $M = 20$, $H = 4$, and $P = 8$; red line: $M = 15$, $H = 6$, and $P = 5$;).

Table 3-6 Computing times of applying the algorithms to de-noising 20-ms data in the PD monitor

Method	Total computation time (s)
WT	48.052
EMD	45.381
STFT-RSVD (M=25, H=2, P=10)	50.089
STFT-RSVD (M=20, H=4, P=8)	36.592
STFT-RSVD (M=15, H=6, P=5)	22.693

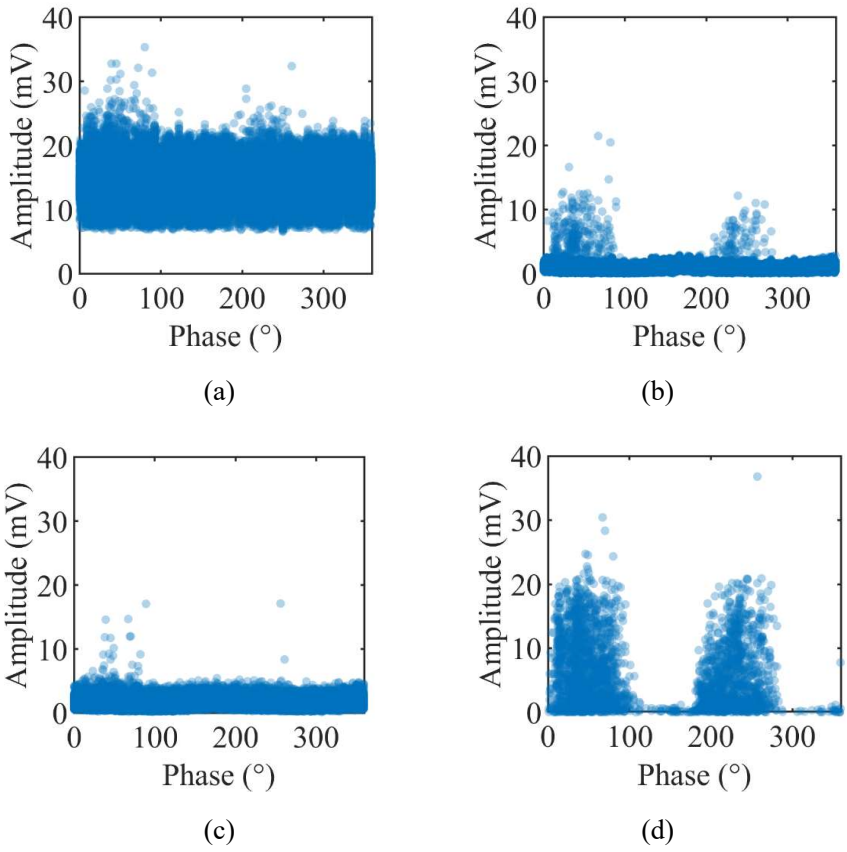

Figure 3-37 Statistical phase-resolved spectrum of PD events detected in (a) the measured noisy signals; (b) the de-noised signals obtained via WT; (c) the de-noised signals obtained via EMD; (d) the de-noised signals obtained via the proposed STFT-RSVD.

3.4 Conclusion

An automatic PD de-noising algorithm is proposed in the first half of this chapter. It is based on a well-defined automated procedure that involves the joint application of the STFT and the SVD tools. The former time-frequency transform separates the PD signal's functional behavior, the possibly superimposed discrete spectrum noise, and the background disturbance of white noise. The latter matrix decomposition allows separating all the signal contributions in terms of the dominant terms (or modes) and filtering out all the noisy terms. The algorithm also embeds some additional features, including a soft-masking mechanism and the optimal selection of the terms leading to the accurate estimation of the noiseless PD signal. The proposed method is demonstrated on a first test case involving a synthetic PD signal, which is fully controllable and can be used to validate and stress the tool in extreme conditions (e.g., with a significant impact of noise). Then, a second test case is considered, where the real measured data are processed and de-noised. The SNR of the noisy signal was significantly improved from -11.10 dB to 12.97dB. A cross-comparison with some state-of-the-art alternatives is carried out for all the test cases, demonstrating that the proposed algorithm causes significantly less waveform distortion than other state-of-the-art

alternatives.

In the last half of this chapter, the STFT-SVD method is further improved to reduce the proposed algorithm's computational complexity. Compared with the previous STFT-SVD algorithm, the computation efficiency of the developed STFT-RSVD algorithm is significantly increased by more than ten times. This allows it to be easily integrated into the embedded systems with minimal hardware resources. The computational complexity of the developed algorithm is reduced via three improvements, including adding kurtosis criteria before matrix factorization to avoid unnecessary computation of useless data, decomposing the spectrogram using a more efficient RSVD algorithm, and selecting dominate components via a more straightforward approach. The simulation experiment and application case demonstrate the developed algorithm's superior de-noising performance and computational efficiency compared with the state-of-the-art solutions.

4 Non-invasive Partial Discharge Detection and Multiple-Sided Localization

Accurate PD detection and localization enable efficient and reliable condition-based maintenance of MV overhead distribution networks. This chapter describes improved methods or algorithms for PD detection and localization of MV overhead distribution networks. First, a special notched high-frequency current transformer is designed for PD detection, and a digital compensation method is developed to improve the performance of the high-frequency current transformer. Then, an innovative PD location technique is proposed. PD localization is carried out via an improved double-sided traveling-wave method. The method exhibits two superior features: the double-sided testing units are accurately synchronized via the joint application of Global Position Systems and a pulse-based interaction process, and a windowed phase difference method is proposed and integrated into the system to estimate the time-of-arrival difference in low signal-to-noise ratio environment robustly. Furthermore, based on the double-sided location method, a multiple-sided location algorithm is developed to determine the PD source in feeders with multiple branches. Its feasibility and robustness are validated via Monte Carlo simulations.

4.1 Improved High-Frequency Current Transformer

This section presents a non-invasive method to detect PDs in MV overhead distribution networks. The technique addresses the challenging problems of i) power-frequency interference and magnetic saturation caused by the hundred-ampere load currents in the overhead line and ii) signal reconstruction of the PD current in the overhead line. The method is based on the magnetic field induction principle and uses an improved notched high-frequency current transformer (HFCT) to detect PDs. The developed HFCT sensor is equivalent to a band-pass filter, thus can reduce the power-frequency interference; moreover, the improved HFCT does not have the magnetic saturation problem of the classical HFCT, thus allowing us to use it on the natural overhead line with high load currents. A digital compensation method is developed to reconstruct the PD current in the overhead line from the output of the HFCT. The proposed method uses the surrogate model to describe the transform function of the HFCT, and thus, it does not rely on a specific model. This means there is no requirement to extract parameters from the HFCT as long as its frequency response is measured and processed. Finally, the feasibility and effectiveness of the developed HFCT and digital compensation method are validated via laboratory experiments.

4.1.1 Principles

This subsection describes modeling a notched HFCT to detect PD in an overhead line.

Two classical HFCT models are reviewed first to explain the basic principle of the HFCT. Then, a general surrogate model, which regards the HFCT as a "black box," is developed to describe the transform function of the HFCT. The model can avoid measuring the internal parameters of the HFCT, which is complicated and time-consuming.

1）Classical HFCT Models

HFCT is used as the sensor for PD detection of MV overhead line in this work because of its high sensitivity, wide frequency band, and non-invasive installability. The PD traveling wave current in the overhead line can generate a magnetic field around the line. This allows us to measure this PD non-invasively by detecting the magnetic field without connecting the measurement unit to the overhead line. HFCT, a commonly used magnetic or current measurement tool mounted on the earth wire, has been widely used in PD detection of cables, transformers, motors, etc [142]. The apparent discharge quantity of a PD pulse can be calculated by integrating the output of the HFCT [147]. However, the classical HFCT cannot be directly used for the overhead line due to the magnetic saturation problem caused by the hundreds-ampere load currents in the overhead line. Therefore, a modified HFCT is designed in this work; the HFCT consists of a notched magnetic core and coils, as shown in Figure 4-1. The PD signal propagating in the overhead line is detected by measuring the output voltage on the two terminals of the coils. The simplified equivalent circuit of the HFCT is shown in Figure 4-2 (a). The output voltage $U_{\text{out}}(\omega)$ in the frequency domain can be defined as

$$U_{\text{out}}(\omega) = \frac{j\omega R_{\text{out}} M}{L_{\text{rc}} C_{\text{rc}} R_{\text{out}} (\text{j}\omega)^2 + (L_{\text{rc}} + R_{\text{rc}} C_{\text{rc}}) \text{j}\omega + (R_{\text{out}} + R_{\text{rc}})} I_{\text{in}}(\omega) \tag{4-1}$$

where $I_{\text{in}}(\omega)$ is the Fourier transform of the input signal $i_{\text{in}}(t)$, M is the mutual inductance between the overhead line and the coils, L_{rc}, C_{rc}, and R_{rc} are the equivalent inductance, capacitance, and resistance of the coils, respectively, and R_{out} is the load resistance. The transform function of the simplified model can thus be derived as

$$H_{\text{simplified}}(\omega) = \frac{U_{\text{out}}(\omega)}{I_{\text{in}}(\omega)} = \frac{\text{j}\omega R_{\text{out}} M}{L_{\text{rc}} C_{\text{rc}} R_{\text{out}} (\text{j}\omega)^2 + (L_{\text{rc}} + R_{\text{rc}} C_{\text{rc}}) \text{j}\omega + (R_{\text{out}} + R_{\text{rc}})} \tag{4-2}$$

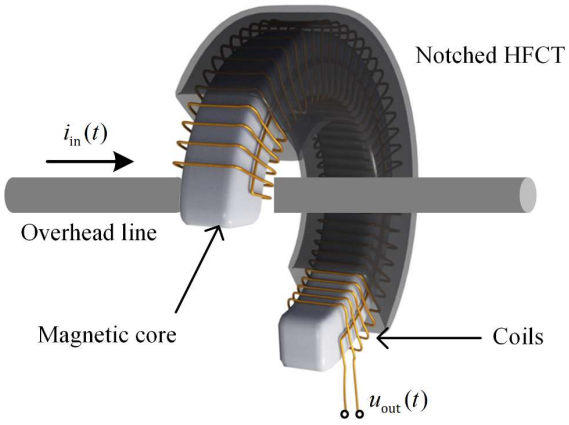

Figure 4-1 Schematic diagram of the designed HFCT with a notch.

In Equation (4-2), analytical expressions of the circuit parameters of the coils can be obtained according to the physical parameters of the coils [142]. Moreover, the circuit parameters can be measured by analyzing the input impedance from the output port of the HFCT. However, the model ignores the influence of the stray parameters, e.g., the capacitance between the coils and the metal shielding, causing the model to not accurately describe the transform function of the HFCT in the high-frequency range, i.e., more than ten MHz. Alternatively, [143] proposes a more accurate model for the (shielded) HFCT. Its equivalent circuit is shown in Figure 4-2 (b). The model can be formulated as

$$H_{\text{general}}(\omega)=\frac{\mathrm{j}\omega R_{\text{out}} M\sqrt{\frac{\mathrm{j}\omega L_{\text{rc}}+Z_{\text{rc}}}{\mathrm{j}\omega C_{\text{rc}}}}\sinh\left(\sqrt{(\mathrm{j}\omega L_{\text{rc}}+Z_{\text{rc}})\mathrm{j}\omega C_{\text{rc}}}\Delta x\right)}{(\mathrm{j}\omega L_{\text{rc}}+Z_{\text{rc}})}\cdot \frac{1}{\left(\sqrt{\frac{\mathrm{j}\omega L_{\text{rc}}+Z_{\text{rc}}}{\mathrm{j}\omega C_{\text{rc}}}}\sinh\left(\sqrt{(\mathrm{j}\omega L_{\text{rc}}+Z_{\text{rc}})\mathrm{j}\omega C_{\text{rc}}}\Delta x\right)+R_{\text{out}}\cosh(\sqrt{(\mathrm{j}\omega L_{\text{rc}}+Z_{\text{rc}})\mathrm{j}\omega C_{\text{rc}}}\Delta x)\right)} \tag{4-3}$$

where M is the unit-length mutual inductance between the overhead line and the coils, Z'_{rc} L'_{rc}, C'_{rc}, and R'_{rc} are the unit-length equivalent impedance, inductance, capacitance, and resistance of the coils, respectively, and R_{out} is the load resistance. Although the transform function $H(\omega)$ can accurately describe the transform function of the HFCT, determining the circuit parameters of the notched HFCT is challenging since their values cannot be measured, and their analytical expression cannot be obtained. Moreover, since the magnetic core has a notch, the unit-length inductances of the coils are theoretically different, leading to a more complicated circuit model of the HFCT.

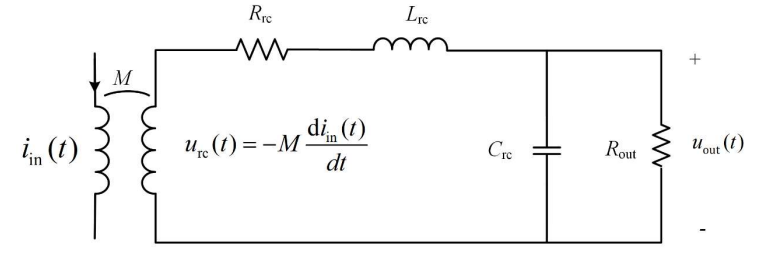

(a)

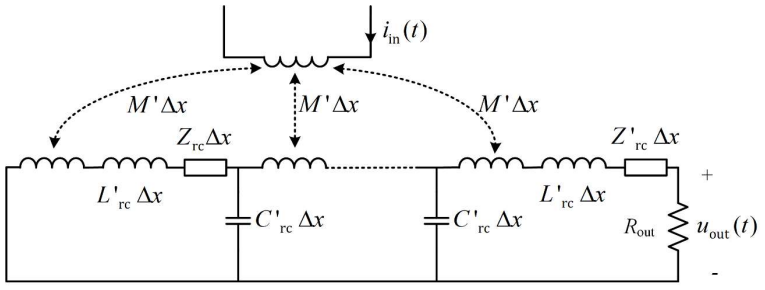

(b)

Figure 4-2 Equivalent circuits of (a) the simplified model and (b) the general model of the HFCT.

2）Surrogate Model for the Modified HFCT

A surrogate model, also known as an approximation or a metamodel, is a simplified mathematical or computational model used to approximate the behavior of a complex model. The HFCT can be generally regarded as a passive two-port network, as shown in Figure 4-3. In the context of a passive two-port network, a surrogate model can be employed to predict the input-output relationship of the network without the need for detailed simulations or measurements. The use of surrogate models for two-port networks offers several advantages. Firstly, it significantly reduces the computational cost associated with analyzing the behavior of the network. Instead of performing numerous time-consuming simulations or measurements, the surrogate model provides a rapid estimation of the network response, allowing us to optimize the performance of the two-port network efficiently. By utilizing the surrogate model, we can quickly assess the performance of different design configurations, evaluate trade-offs, and identify optimal solutions. This accelerates the design process and allows efficient exploration of various design parameters.

Since the equivalent two-port network of the HFCT is passive and linear, the transform function $H_{\text{surrogate}}(s)$ of the HFCT (i.e., between $U_{\text{out}}(s)$ and $I_{\text{in}}(s)$) can be defined in the form of the rational polynomial as

$$H_{\text{general}}(s) = \frac{U_{\text{out}}(s)}{I_{\text{in}}(s)} \approx H_{\text{surrogate}}(s) = \alpha s \cdot \frac{\prod_{i=1}^{i=N_z}(s+z_i)}{\prod_{j=1}^{j=N_p}(s+p_j)} \tag{4-4}$$

where s is equal to $j\omega$, α is the gain, N_z and N_p ($N_z < N_p$) is the number of zeros, and poles, z_i is the value of the i^{th} zero, and p_j is the value of the j^{th} pole. The expression on the far right of Equation (4-4) consists of two terms: the one is the integration element, i.e., αs, that models the mutual inductance of the HFCT; the other one is the fraction that describes the stray parameters and the load resistance of the HFCT in high frequency range. The larger N_z and N_p are, the smaller the error between $H_{\text{general}}(s)$ and $H_{\text{surrogate}}(s)$ is. Nevertheless, N_z and N_p should not be set to too large to reduce the complexity of the model and unnecessary computational cost. The values of the zeros and poles can be obtained by measuring the transform characteristics of the two-port network.

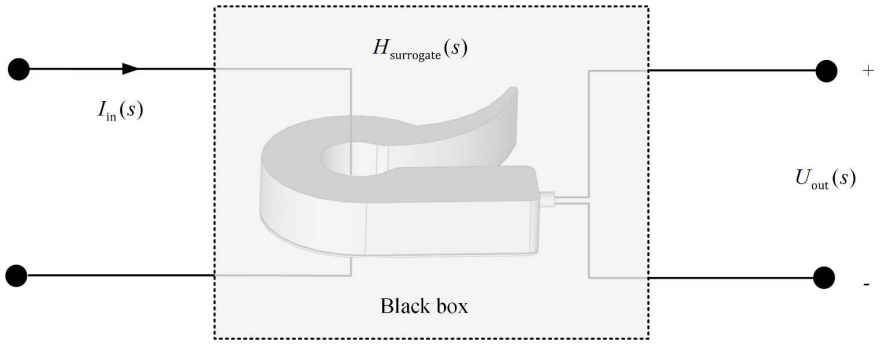

Figure 4-3 Surrogate (black box) model of the designed HFCT.

4.1.2 Digital Compensation of the Sensor's Output

In on-site PD measurement, the frequency passband of the HFCT is expected to be as wide as possible to capture more information about the PD signal, which is crucial for PD recognition, location, and classification. Figure 4-4 shows the frequency spectrums of the typical double-exponential PD pulse and the transform function of a HFCT. It can be observed that the PD signal has a broad frequency spectrum from DC to tens of MHz, which cannot be covered by the frequency spectrum of the HFCT, leading to inevitable waveform distortions on the output of the HFCT. Moreover, the phase shift of the HFCT is expected to be as small as possible to reduce the waveform distortion. However, simultaneously implementing the two above objectives can be challenging, requiring that we fine-tune each parameter of the HFCT. Alternatively, we use a digital compensation approach to broaden the frequency passband of the HFCT and eliminate the phase shift caused by the HFCT, as shown in Figure 4-5.

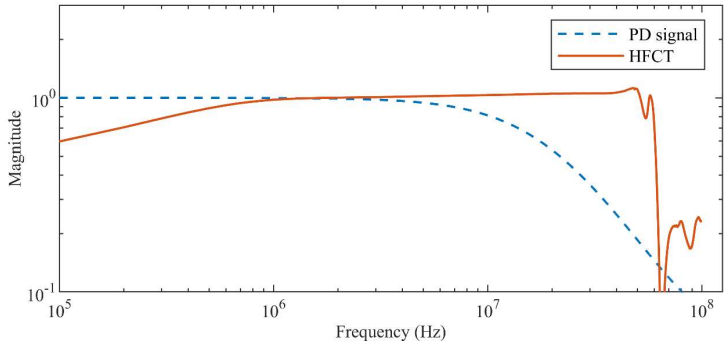

Figure 4-4 Comparison of frequency spectrums between the typical double-exponential PD pulse and the transform function of a HFCT.

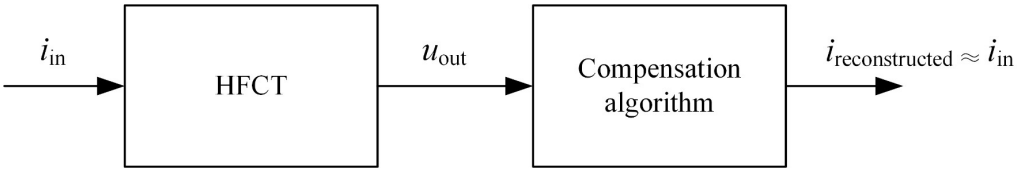

Figure 4-5 Idea of compensating output voltage of the designed HFCT.

The digital compensation technique can be employed to reconstruct the input signal of the HFCT from its output signal. The method aims to mitigate the effects of sensor imperfections, such as frequency response variations, phase shifts, or noise. Digital compensation of the output of the HFCT can be completed via a five-step procedure (see Figure 4-6):

(1) **Characterization**: Begin by characterizing the HFCT's behavior and understanding its imperfections. This involves measuring or modeling the sensor's frequency response and phase response.

(2) **System Identification:** Estimate the sensor's transfer function or impulse response based on the surrogate model described in the last subsection. This can be done by measuring the transform function of the HFCT via a vector analyzer. To simplify the

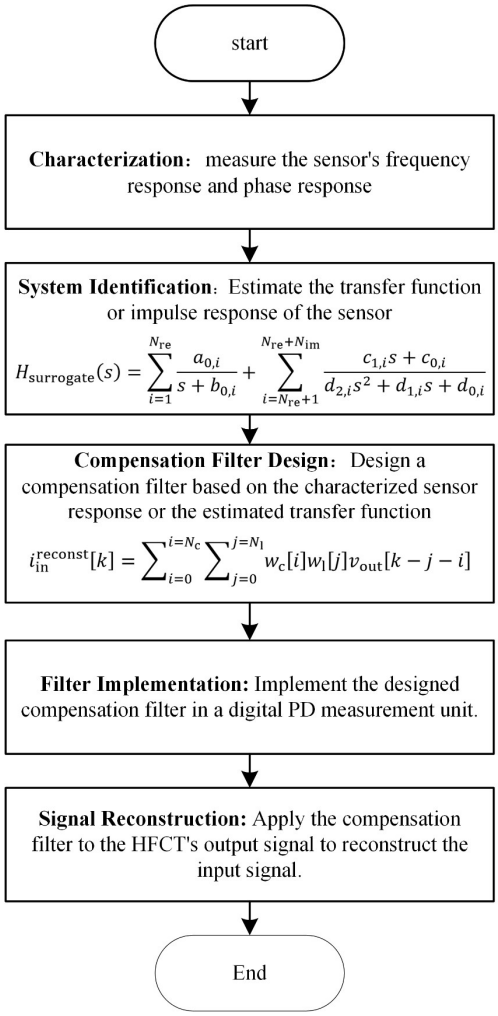

Figure 4-6 Flowchart of the digital compensation approach.

sequence calculation, the surrogate model in Equation (4-4) can be rewritten as (i.e., a combination of real poles and complex poles):

$$H_{\text{surrogate}}(s) = \sum_{i=1}^{N_{\text{re}}} \frac{a_{0,i}}{s+b_{0,i}} + \sum_{i=N_{\text{re}}+1}^{N_{\text{re}}+N_{\text{im}}} \frac{c_{1,i}s+c_{0,i}}{d_{2,i}s^2+d_{1,i}s+d_{0,i}} \tag{4-5}$$

where $a_{0,i}$, $b_{0,i}$, $c_{0,i}$, $c_{1,i}$, $d_{0,i}$, $d_{1,i}s$, and $d_{2,i}$ are the constants of the model, N_{re} and N_{im} is the number of the real and complex poles. The constant can be obtained via the Vector Fitting Tool provided in [144].

(3) **Compensation Filter Design:** Design a compensation filter based on the characterized sensor response or the estimated transfer function. The compensation filter aims to invert or compensate for the sensor's imperfections. To avoid transforming a stable transfer function into an unstable one during the conversion from the s-domain to the z-domain (using bilinear transformation), the transfer function mentioned above has been maintained in a fractional form, i.e.,

$$H_{\text{surrogate}}(z)=\sum_{i=1}^{N_{\text{re}}}\frac{a_{0,i}}{\frac{2}{T_s}\frac{1-z^{-1}}{1+z^{-1}}+b_{0,i}}+\sum_{i=N_{\text{re}}+1}^{N_{\text{re}}+N_{\text{im}}}\frac{c_{1,i}\frac{2}{T_s}\frac{1-z^{-1}}{1+z^{-1}}+c_{0,i}}{d_{2,i}\left(\frac{2}{T_s}\frac{1-z^{-1}}{1+z^{-1}}\right)^2+d_{1,i}s\frac{2}{T_s}\frac{1-z^{-1}}{1+z^{-1}}+d_{0,i}} \tag{4-6}$$

where T_s is the sampling interval. The inverse of the transform function in z-domain, ${H_{\text{surrogate}}}^{-1}(z)$, can be derived as

$$\begin{aligned}{H_{\text{surrogate}}}^{-1}(z)&=\frac{I_{\text{in}}^{\text{reconst}}(z)}{U_{\text{out}}(z)}\\&=\sum_{i=1}^{N_{\text{re}}}\frac{{a'}_{0,i}+{a'}_{1,i}z^{-1}}{{b'}_{0,i}+{b'}_{1,i}z^{-1}}+\sum_{i=N_{\text{re}}+1}^{N_{\text{re}}+N_{\text{im}}}\frac{{c'}_{0,i}+{c'}_{1,i}z^{-1}+{c'}_{2,i}z^{-1}}{{d'}_{0,i}+{d'}_{1,i}z^{-1}+{d'}_{2,i}z^{-1}}\end{aligned} \tag{4-7}$$

where $I_{\text{in}}^{\text{reconst}}(z)$ is the reconstructed PD current. It can be calculated as

$$i_{\text{in}}^{\text{reconst}}[k]=\sum_{i=1}^{N_{\text{re}}}{i_{\text{in}}^{\text{reconst}}}^{\text{re}}[k]+\sum_{i=N_{\text{re}}+1}^{N_{\text{re}}+N_{\text{im}}}{i_{\text{in}}^{\text{reconst}}}^{\text{im}}[k] \tag{4-8}$$

where ${i_{\text{in}}^{\text{reconst}}}^{\text{re}}[k]$ and ${i_{\text{in}}^{\text{reconst}}}^{\text{im}}[k]$ can be calculated as

$$\begin{aligned}{i_{\text{in}}^{\text{reconst}}}^{\text{re}}[k]&=\frac{{a'}_{0,i}v_{\text{out}}[k]+{a'}_{1,i}v_{\text{out}}[k-1]-{b'}_{1,i}{i_{\text{in}}^{\text{reconst}}}^{\text{re}}[k-1]}{{b'}_{0,i}}\\{i_{\text{in}}^{\text{reconst}}}^{\text{im}}[k]&=\frac{{c'}_{0,i}v_{\text{out}}[k]+{c'}_{1,i}v_{\text{out}}[k-1]+{c'}_{2,i}v_{\text{out}}[k-2]}{{b'}_{0,i}}\\&\quad-\frac{{d'}_{1,i}{i_{\text{in}}^{\text{reconst}}}^{\text{im}}[k-1]+{d'}_{2,i}{i_{\text{in}}^{\text{reconst}}}^{\text{im}}[k-2]}{{b'}_{0,i}}\end{aligned} \tag{4-9}$$

In general, the above compensation formulation can be simplified as a Finite Impulse Response (FIR) filter, i.e.,

$$i_{\text{in}}^{\text{reconst}}[k]=\sum\nolimits_{i=0}^{i=N_{\text{c}}-1}w_{\text{c}}[i]v_{\text{out}}[k-i] \tag{4-10}$$

where $w_{\text{c}}[i]$ is the coefficient of the FIR filter, and it can be obtained via Equation (4-6)-(4-9), and N_{c} is the length of the FIR filter. The gain of the HFCT in the high-frequency range (e.g., more than 50 MHz) is much smaller than that in a few MHz, leading to a very high gain of the FIR (i.e., the inverse of the transform function of the HFCT) in the high-frequency range. This can amplify the influence of the high-frequency noise in v_{out}, which can lead to significant waveform distortion of $i_{\text{in}}^{\text{reconst}}$. To address this problem, a low-pass FIR filter (e.g., the upper cut-off frequency of 50MHz) is added into Equation (4-10) to reduce the high-frequency noise in v_{out}. Equation (4-10) is rewritten as

$$i_{\text{in}}^{\text{reconst}}[k]=\sum\nolimits_{i=0}^{i=N_{\text{c}}-1}\sum\nolimits_{j=0}^{j=N_{\text{l}}-1}w_{\text{c}}[i]w_{\text{l}}[j]v_{\text{out}}[k-j-i] \tag{4-11}$$

where $w_{\text{l}}[i]$ is the coefficient of the low-pass FIR filter, and N_{l} is the length of the FIR filter and can be set to be equal to N_{c}.

(4) **Filter Implementation:** Implement the designed compensation filter in a digital PD measurement unit. This involves implementing the compensation filter as a digital algorithm or code that can be applied to the HFCT's output signal.

(5) **Signal Reconstruction:** Apply the compensation filter to the HFCT's output signal to reconstruct the input signal. The compensation filter modifies the sensor's output signal to compensate for its imperfections and recover the original input signal as closely as possible.

4.1.3 Laboratory Validation

The section first describes the details of designing a notched HFCT sensor. Then, the approach to measure the frequency and phase responses of the HFCT is presented, and estimating parameters in the surrogate model of the HFCT is discussed. Finally, the feasibility and effectiveness of the proposed digital compensation algorithm are validated via the laboratory experiment of reconstructing the PD pulse simulated via a PD calibrator.

1）Sensor Design and Transform Function Measurement

Figure 4-7 collects the picture and internal structure of the designed HFCT. The HFCT uses a notched magnetic core to avoid the magnetic saturation caused by the power-frequency currents in the overhead line. The physical parameters of the HFCT are listed in Table 4-1. The parameters are selected according to the design rule of the classical HFCT. Nevertheless, it is essential to point out that the number of the designed HFCT (i.e., 15) is significantly larger than that of classical HFCT to compensate for the reduced mutual inductance caused by the notched magnetic core.

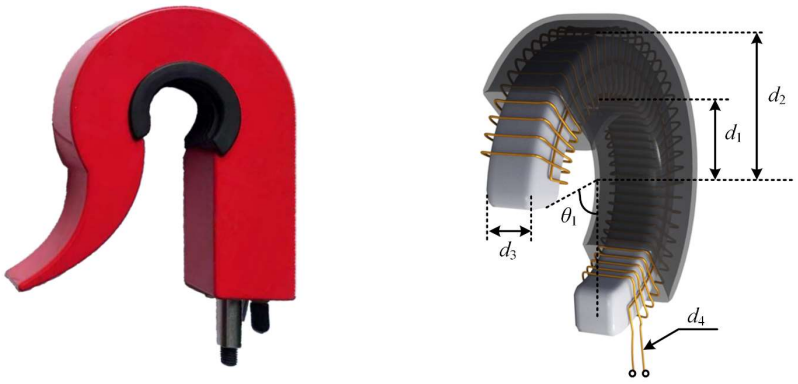

(a) (b)

Figure 4-7 Picture and internal structure of the designed HFCT.

A testing platform in the lab is set up to obtain the frequency and phase responses of the developed HFCT, as shown in Figure 4-8. A vector network analyzer (VNA) is used to measure the frequency and phase responses. It generates a range of frequencies and measures the sensor's response at each frequency. The VNA captures both the magnitude (amplitude) and phase of the sensor's response, providing a comprehensive understanding of its behavior. The VNA determines how the sensor performs across different frequencies by analyzing the frequency response. It can identify resonant frequencies, bandwidth limitations, and

deviations from an ideal response. The phase response measurement reveals the time delay or phase shift introduced by the sensor. Additionally, a VNA offers calibration capabilities to ensure accurate measurements. It compensates for any systematic errors caused by cables, connectors, or other components. The VNA's software tools enable data analysis, visualization, and computation of network parameters like S-parameters, impedance, and reflection coefficients. Since the vector analyzer can only generate a voltage signal, a 50-Ω resistance is connected to the vector analyzer's left port, and a wire in series with the resistance goes through the developed HFCT. Moreover, it needs to explain that since the output of the HFCT is transformed into an optical signal for security reasons (which will be described in detail in the following subsection), an optical-to-electrical converter is used to convert the optical signal into the electrical signal that the VNA can detect.

Table 4-1 Parameters of the designed HFCT

Parameters	Labels	Values
The inner radius of the magnetic core	d_1	30 mm
The outer radius of the magnetic core	d_2	15 mm
Height of the magnetic core	d_3	12 mm
The number of coils	N	15
Radius of the coil conductor	d_4	0.5 mm
The angle of the gap	θ_1	90°
Relative permeability of the magnetic core	μ_{core}	2000

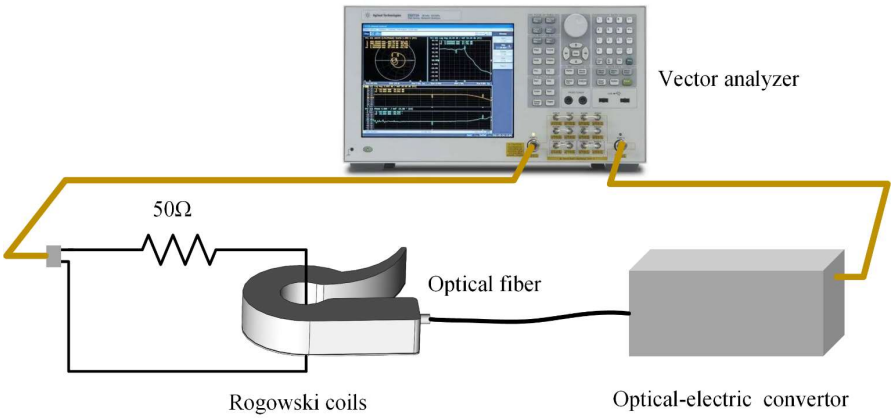

Figure 4-8 Experiment platform of amplitude-frequency characteristic response measurement.

This work uses S-parameters obtained via the VNA (PicoVNA 3) to calculate the frequency and phase responses. The responses $H(s)$ of the developed HFCT can be obtained as

$$H(s)=S_{21}(s)\frac{1+S_{11}(s)}{1-S_{11}(s)}R_{\text{VNA}},\ s=j\omega \tag{4-12}$$

where $S_{21}(s)$ is the forward transmission coefficient, $S_{11}(s)$ is the input reflection coefficient, and R_{VNA} is the output impedance of the VNA. Moreover, Figure 4-9 collected the calculated frequency and phase responses of the HFCT. It is important to note that the time delay in $S_{21}(s)$ caused by the optical transmission is manually compensated. It can be observed that the detection sensitivity of the HFCT is approximately 5.6 mV/mA, and its −6 dB frequency bandwidth is approximately 0.2 MHz-50 MHz; the phase response varies from +50 degrees to -250 degrees. It is important to point out that the magnitude of the frequency response decreases rapidly from 50 MHz, which is caused by the embedded low-pass filter with an upper cut-off frequency (which will be described in detail in the next subsection).

Figure 4-10 shows the results of using the Vector Fitting Tool provided in [144] to calculate the constants in the surrogate model of the developed HFCT. The number of the poles of the model is set as 2, 4, and 6. It can be observed that as the number of the poles increases, the fitting errors become smaller. The surrogate model with six poles is sufficient to describe the performance of the HFCT in the frequency band of interest, i.e., less than 50 MHz. The obtained constants of the surrogate model will be used for input signal reconstruction in the following validation experiment.

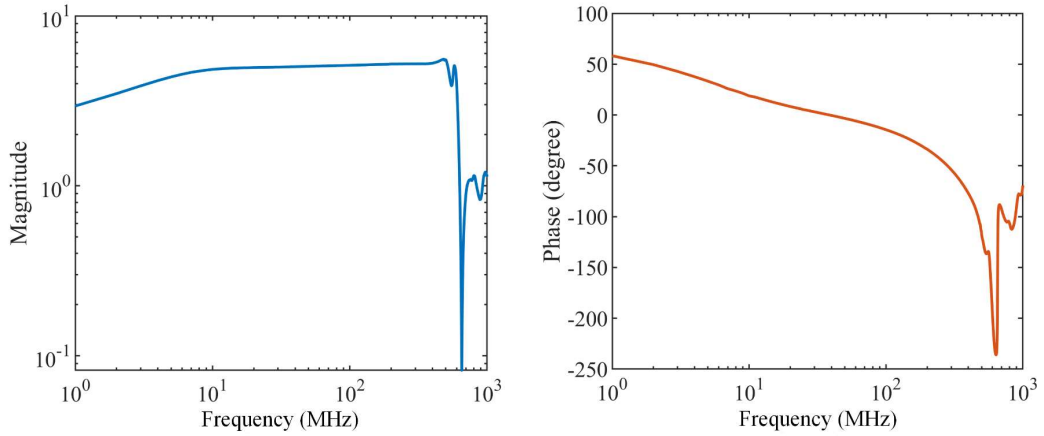

(a) (b)

Figure 4-9 Frequency (a) and phase (b) responses of the designed HFCT.

2）Validation Experiment

PD simulation experiment was carried out in the lab to validate the feasibility and effectiveness of the proposed digital compensation algorithm. The experiment platform is shown in Figure 4-11. A standard PD calibrator generates a PD pulse; a capacitance with a value of 50 nF is used to simulate the equipment under testing; resistance with a value of 50 Ω is used to detect the current across the HFCT.

Figure 4-12 collects the waveforms of the input current, output voltage, and the reconstructed input currents. It can be observed that the waveform of the output voltage is significantly different from the input current, inevitably leading to errors in the PD discharge magnitude estimation; the reconstructed signal with filtering almost overlaps with the measured input current, demonstrating the effectiveness of the proposed digital

compensation algorithm; the reconstructed signal without filtering includes significant high-frequency oscillations, demonstrating the importance of adding the low-pass filtering in the compensation Filter in Equation (4-11).

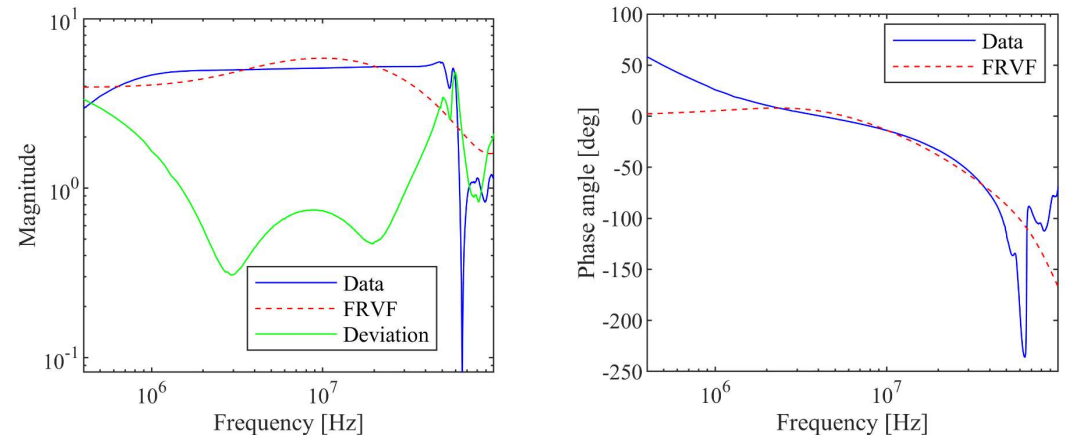

(a)

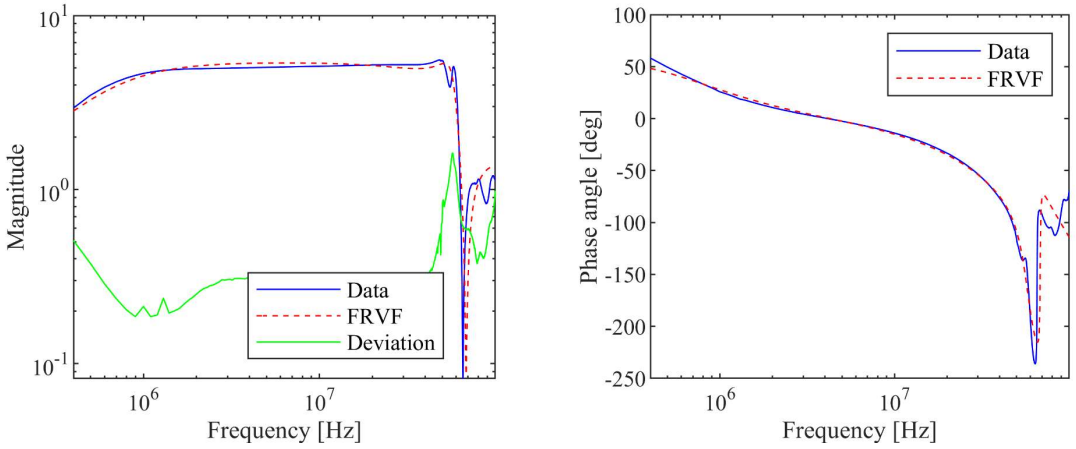

(b)

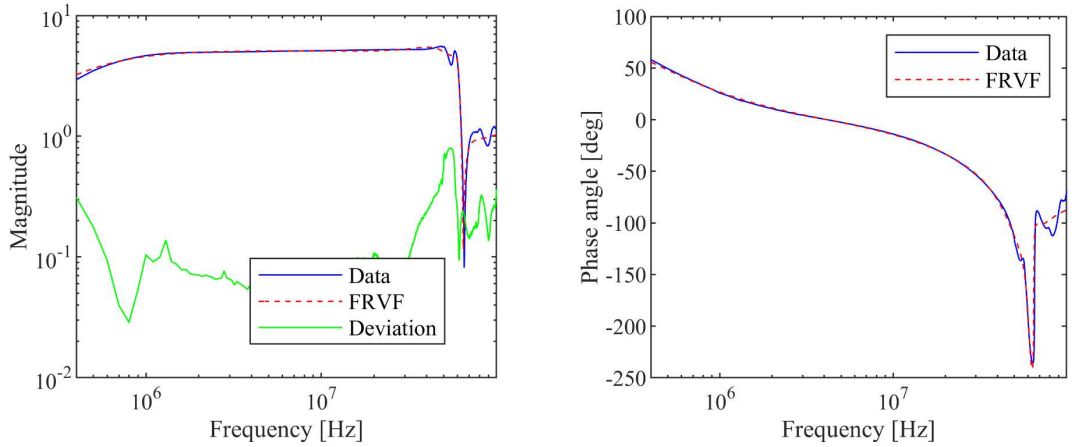

(c)

Figure 4-10 Vector fitting results with (a) 2 poles, (b) 4 poles, and (c) 6 poles

Table 4-2 collects the effect of the number of poles in the surrogate model on the quality of the reconstructed signal. The error between the measured and reconstructed input currents is defined as

$$\text{Error} = \frac{\sqrt[2]{\frac{\sum_{k=1}^{K}(i_{\text{in}}[k]-i_{\text{reconst}}[k])^2}{K}}}{\max(|i_{\text{in}}|)} \cdot 100\% \tag{4-13}$$

where i_{in} and i_{reconst} are the measured and reconstructed input currents, and K is the sampling number of the signals. As the number of poles increases, the error decreases significantly first, which is caused by the fact that the surrogate model of a more significant number of poles can more accurately approximate the transform function of the HFCT. Once the number of the poles is more significant than 6, the error reduction is minimal. Moreover, the error in the case with filtering in the compensation filter is significantly less than without, demonstrating the critical benefit of the low-pass filtering in the compensation Filter in Equation (4-11).

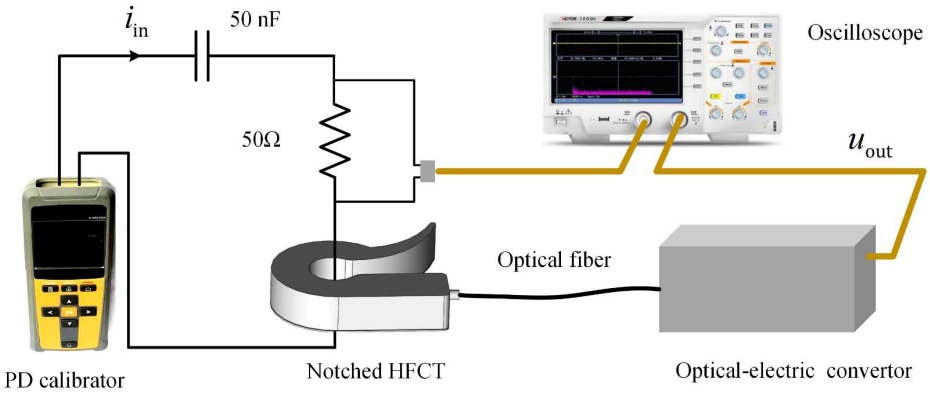

Figure 4-11 Experiment platform of the PD simulation.

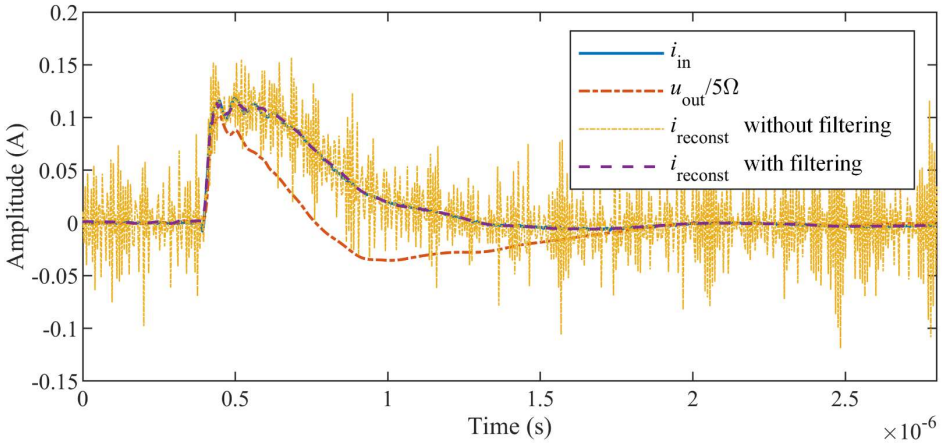

Figure 4-12 Input, output, and reconstructed PD signals via the proposed compensation method based on the surrogate model with six poles.

Table 4-2 Comparison of errors between the input signal and reconstructed signal using the surrogate model with varying poles

Number of poles of the used surrogate model	Error (%)	
	With filtering	Without filtering
2	10.8	94.1
4	5.4	102.5
6	2.1	106.4
8	1.9	121.9
10	1.8	123.4
12	1.8	122.9

4.2 Improved Double-Sided Partial Discharge Localization Based on Pulse Injection Synchronization Mechanism

This section describes an improved double-sided PD location method. The method exhibits three superior features:

(1) The method is driven by a hybrid detection technique, which integrates a pulse-based synchronization mechanism and a global positioning system (GPS). The proposed solution offers several benefits. It has the inherent feature of being immune to varying physical parameters of the transmission line, and it has been proven to deliver improved accuracy with respect to the conventional GPS-based location method.

(2) A windowed phase difference method is proposed to robustly estimate the time-of-arrival difference between PD pules in a low signal-to-noise ratio environment.

(3) An enhanced algorithm is developed to improve the robustness of on-site PD measurement to high-level noise. The proposed algorithm relies on a well-established automatic procedure requiring neither parameter tuning nor expert intervention.

The strength and the effectiveness of the proposed approaches are validated on simulation and laboratory experiments, along with the comparison with the state-of-the-art solutions.

4.2.1 Principles

Figure 4-13 shows the sketch map of the double-sided PD localization of the three-phase overhead line. Two measurement units are mounted on the double sides of the target overhead line. The PD source's location is calculated by analyzing the time-of-arrival difference (TOA) between the PD pulses detected by the two units. To explain the PD location method better, the classical double-sided traveling wave location method is first reviewed, and then the improved method is described in detail.

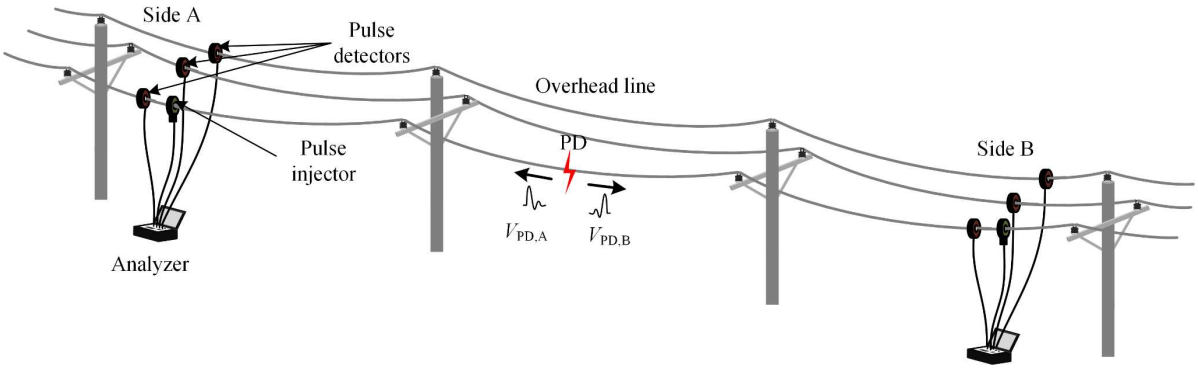

Figure 4-13 Sketch map of double-sided PD detection and localization scheme.

1）Classical Partial Discharge Location Method

The fundamental principle of the method is shown in Figure 4-14. As a PD defect occurs on an overhead line or its tips, the TW pulses produced by the defect propagate to both sides along the overhead line. Thus, the location of the PD defect can be determined by calculating the difference of TOAs of the TW pulses between the two PD detectors mounted on the two sides of the overhead line. The distance from a PD to Side A can be calculated as:

$$l_{PD} = \frac{L_{AB} + [t_A - (t_B + \Delta t_{syn})] \cdot v}{2} \tag{4-14}$$

where t_A and t_B are the TOAs of PD pulses at Side A and B, L_{AB} is the length of the overhead line, Δt_{syn} is the synchronization error between the two PD detectors, and v is the velocity of the PD signal propagating in the overhead line. According to Equation (4-14), it can be observed that the errors or inconsistencies in determining PD source locations are due to synchronization, TOA, and propagation velocity errors. The sources of the errors will be thoroughly discussed in the following paragraph.

The synchronization error mainly comes from the uncertain fluctuations in GPS timing accuracy, caused by the varying weather and the irregular geography. The TOA error is mainly caused by field noise interferences and signal dispersion as illustrated in Figure 2-36. Last but not the least, the propagation velocity uncertainty mainly comes from unknown overhead line parameters and the alongside towers, as illustrated in Chapter II. On the one hand, the propagation velocity is associated with the physical parameters of the overhead line. For example, the propagation velocity of PG or PP channels strongly depends on the line height, the ground resistivity, and the thickness of the insulation layer, as shown in Figure 2-13, Figure 2-16, and Figure 2-15, respectively. On the other hand, the mean propagation velocity of the whole line is changed by the time delays caused by the alongside tower. For example, since supporting towers are always distributed on the 10-kV overhead line at intervals of about 50 meters, the time delay caused by a supporting tower (e.g., more than tens of ns, as shown in Figure 2-43) can significantly affect the mean propagation velocity of the 50-m overhead line. Therefore, these errors must be minimized for accurate PD localization in the on-site PD measurement of MV overhead lines, which will be discussed in the following sub-sections.

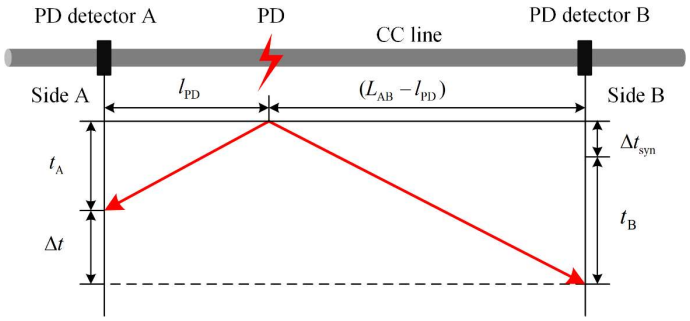

Figure 4-14 Schematic of the classical double-sided PD localization on an overhead line section.

2）Improved Partial Discharge Location Method

Synchronization and propagation velocity errors are the most critical aspects of the double-sided TW method above. To minimize them, GPSM, a hybrid time-synchronization technique, is devised. It integrates a pulse-based synchronization mechanism (PSM) and a GPS. GPSM enables accurate (due to the PSM) and reliable (due to the GPS) synchronization of the double-sided PD detectors and the signal propagation velocity calculation. A seven-step overview of the working procedure of GPSM is detailed below (see Figure 4-15 and Figure 4-16).

(1) Two PD detectors and two pulse injectors are mounted on each side of a target segment of the overhead line.

(2) PD detectors on Side A and B both start to acquire data when their respective GPS triggers activate them. PSM is only triggered within a short pre-set time window.

(3) On side A, at the beginning of the time window, a high-amplitude pulse $V_{SYN,A1}$ is generated and inductively injected into the overhead line at time t_1 by the pulse injector.

(4) $V_{SYN,A1}$ propagates from side A along the overhead line and arrives, in an altered form, at side B after propagation time T. This altered pulse is denoted $V_{SYN,B1}$.

(5) The PD detector on side B captures $V_{SYN,B1}$ at time t_2. Another high amplitude pulse, $V_{SYN,B2}$, is generated and inductively injected into the overhead line at t_3. The latter parameter, t_3, is controllable and is set to be significantly larger than $(t_1+\Delta t_{syn}+T)$ to ensure that $V_{SYN,B2}$ occurs later than $V_{SYN,B1}$, i.e., $t_2<t_3$. Since Δt_{syn} fluctuates within a few microseconds at most, and T can be approximately estimated with the length of the overhead line, it is easy to ensure $t_2<t_3$ by setting a large enough interval (e.g., T+20 μs) between t_3 and t_1.

(6) $V_{SYN,B2}$ propagates from side B along the overhead line and arrives, in an altered form, at Side A after time T, at t_4. This altered pulse is denoted $V_{SYN,A2}$. At this time, PSM is completed, and the time window soon ends. In the PSM, synchronization of the double-sided PD detectors and estimation of the propagation velocity can be achieved, as described below.

First, by calculating the TOAs of the injected pulses, the propagation time T from Side A to Side B can be calculated as:

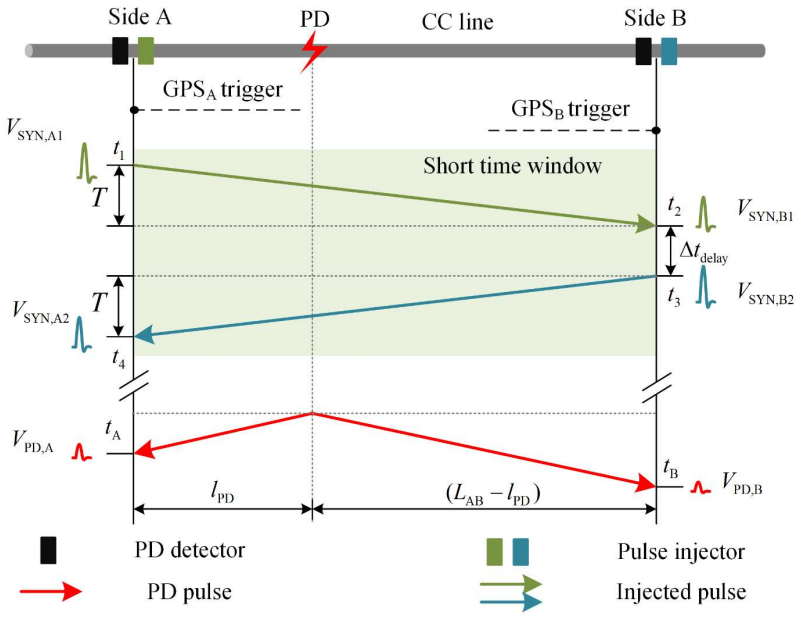

Figure 4-15 Illustration of the improved PD location method for overhead lines based on the proposed GPSM.

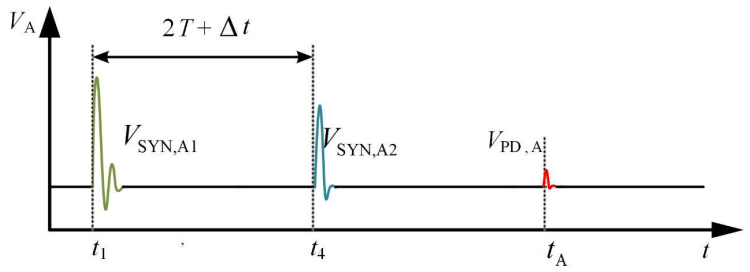

(a)

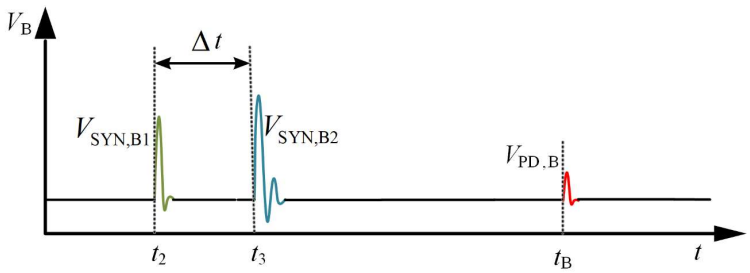

(b)

Figure 4-16 Time sequence of injected pulses and the PD pulse at Side A (a) and Side B (b).

$$T=\frac{(t_4-t_1)-(t_3-t_2)}{2} \tag{4-15}$$

Second, it is assumed that t_1 represents the absolute time reference for the signal acquired on Side A. Thus, as the absolute TOA difference between $V_{SYN,A1}$ and $V_{SYN,B1}$ equals propagation time T, the absolute time reference for the signal acquired on Side B is (t_2-T). Therefore, Δt_{syn}. in Equation (4-14) can be calculated as:

$$\Delta t_{syn}=t_1-t_2+T \tag{4-16}$$

Third, using the calculated propagation time T and the length L_{AB} of the measured overhead line segment, the signal propagation velocity (v) of the target overhead line segment can be calculated as:

$$v = \frac{L_{AB}}{T} \tag{4-17}$$

(7) The double-sided PD detectors continue to acquire PD data for more than one power-frequency cycle. Two pulses, $V_{PD,A}$ and $V_{PD,B}$, originating from the same PD activity, represent the test results for Side A and B, respectively. In addition, t_A and t_B are the arrival times of $V_{PD,A}$ and $V_{PD,B}$, respectively. Therefore, incorporating Equation (4-14), (4-15), (4-16) and (4-17), the PD location (l_{PD}) can be calculated as:

$$l_{PD} = \frac{L_{AB} \cdot [(t_A - t_B) - (t_1 - t_2)]}{(t_4 - t_1) - (t_3 - t_2)} \tag{4-18}$$

In contrast to Equation (4-14), Equation (4-18) eliminates synchronization and propagation velocity errors, thus enabling more accurate PD localization.

4.2.2 Time-of-Arrival Estimation

According to Equation (4-18), the PD localization accuracy depends on the estimation accuracy of TOAs of the injected and PD pulses. Since the injected pulses are controllable and their amplitude and rising time can be deliberately set to be high and fast, respectively, the TOAs of the injected pulses t_1, t_2, t_3, and t_4 can be easily determined via the simple threshold method. In contrast, determining the TOAs of the PD pulses is challenging as their amplitudes are always low, causing them to be susceptible to background noise interferences [32]. In this subsection, a windowed phase difference method is developed to robustly estimate the TOA difference of the PD pulses (i.e., the sub-equation $\Delta t = (t_A - t_B)$ in Equation (4-18)) to reduce the influence of the noise interferences. The classical phase difference method is first reviewed to explain the method better, and the developed method is subsequently described.

1）Classical Phase Difference Method

Let us consider two noisy sub-signals, $x_A(t)$ and $x_B(t)$, obtained by sliding a time window with the length T_{win} on $u_A(t)$ and $u_B(t)$, respectively. T_{win} can be conveniently chosen to be two to three times the propagation time T of the PD pulses traveling in the entire overhead line. In the time window, $x_A(t)$ and $x_B(t)$ contain a PD pulse, respectively, and the pulses in $x_A(t)$ and $x_B(t)$ originate from the same PD activity.

While PD pulses between $x_A(t)$ and $x_B(t)$ are related, since noises between $x_A(t)$ and $x_B(t)$ are generally unrelated, correlation analysis between $x_A(t)$ and $x_B(t)$ can reduce the influence of the noises on determining their TOA difference [145]. The phase difference method is a representative correlation analysis approach to estimate the TOA difference between two related signals [115][146]. It provides the TOA difference estimation

only based on the cross-power spectrum phase, i.e., the frequency domain representation phase of the cross-correlation between the two signals $x_A(t)$ and $x_B(t)$. The phase difference method is completed in the following three steps.

Step 1) Cross-power spectrum $\Psi(\omega)$ of $x_A(t)$ and $x_B(t)$ is calculated as

$$\Psi(\omega) = \frac{X_A(\omega) \bullet X_B^*(\omega)}{|X_A(\omega) \bullet X_B^*(\omega)|} \tag{4-19}$$

where $X_A(\omega) \in \mathbb{C}$ is the Fourier transform of $x_A(t)$ and $X_B^*(\omega) \in \mathbb{C}$ is the complex conjugation of the Fourier transform of $x_B(t)$. The $\Psi(\omega)$ modulus (i.e., $|\Psi(\omega)|$) is identically equal to 1, and the phase of $\Psi(\omega)$ (i.e., $\angle\Psi(\omega)$) is equal to the phase difference between $X_A(\omega)$ and $X_B(\omega)$.

Step 2) Generalised cross-correlation $R(\tau)$ of the two signals $x_A(t)$ and $x_B(t)$ is defined as the inverse Fourier transform of $\Psi(\omega)$, i.e.

$$R(\tau) = \frac{1}{2\pi} \int_{-\pi}^{\pi} \Psi(\omega) \bullet e^{j\omega\tau} \, d\omega \tag{4-20}$$

Step 3) The TOA difference Δt between the pulses in $x_A(t)$ and $x_B(t)$ is estimated by searching for the maximum absolute value of $R(\tau)$, as follows [28]:

$$\Delta t = \arg\max_{\tau} |R(\tau)| \tag{4-21}$$

where Δt is always positive because Equation (8) assumes that the PD pulse in $x_A(t)$ is later than that in $x_B(t)$ (i.e., $t_A > t_B$). If the PD pulse in $x_A(t)$ is earlier than that in $x_B(t)$, Δt should be redefined as $(\Delta t - T_{win})$. The chronological order of the two PD pulses in $x_A(t)$ and $x_B(t)$ can be conveniently determined by comparing the times corresponding to their peaks.

2）The improved windowed phase difference method

According to Equation (4-20), it can be observed that $R(\tau)$ uses all the frequency components in $\Psi(\omega)$. This is a good strategy and can make the result robust if the target signals have a wide frequency spectrum distribution. However, in practice, the main energy of the frequency spectrum of PD signals measured in overhead lines is always limited in a relatively narrow frequency sub-band (e.g., a few MHz). At the same time, noises are almost distributed in the entire frequency pass-band (e.g., tens or hundreds of MHz) [32][57][58]. Therefore, selecting the PD-associated frequency sub-band in $\Psi(\omega)$ to calculate $R(\tau)$ can improve the robustness of the TOA difference estimation. Since the exact central value of the frequency sub-band of PD pulses is unknown in field measurement, depending on the material, size, and location of the PD source [60][61], we apply a sliding frequency-domain window on $\Psi(\omega)$. Equation (4-20) can be rewritten as

$$r(\tau, l) = \frac{1}{2\pi} \int_{-\pi}^{\pi} \Psi(\omega) \bullet G(|\omega| - \omega_l) \bullet e^{j\omega\tau} \, d\omega \tag{4-22}$$

where ω_l is the frequency offset corresponding to sub-band l, $G(\bullet)$ is a symmetric Gaussian frequency-domain window, centered at $\omega = 0$ with frequency support $[-B_G, B_G]$. In principle, the B_G value depends on the frequency components of the measured PD signal.

Since the main energy of the frequency bandwidth of the PD signals measured in MV overhead lines or cables is always within a few MHz [41][88], B_G can be conveniently set as a few MHz, e.g., 2 MHz, which is used in the subsequent laboratory and field experiments and is validated to be feasible.

A two-dimensional generalized cross-correlation spectrum $r(\tau, l)$ can be obtained by sweeping the cross-power spectrum $\Psi(\omega)$ over the frequency sub-bands:

$$\omega_l = l \bullet H_G, \qquad l = 0,1,\cdots,L-1 \tag{4-23}$$

where H_G is the frequency hop, and L is the number of sub-bands and can be chosen to cover those frequencies up to the Nyquist limit of $L = \lfloor(\pi - B_G + H_G)/H_G\rfloor$. In principle, the smaller the H_G value, the higher the resolution of $r(\tau, l)$ is. On the other hand, too small H_G can lead to additional computational overhead. Therefore, the H_G is recommended to be empirically set as about one-fifth of B_G.

To eliminate the influence of noises, we need first to identify the sub-band l_0 containing most of the PD signal components and then estimate Δt by searching for the maximum absolute value of $r(\tau, l_0)$ as formulated in Equation (4-22). Since the sub-band with PD signal can produce a more considerable maximum absolute value of $r(\tau, l_0)$ than that of noises, the above two steps can be completed simultaneously by searching the maximum absolute value of $r(\tau, l)$, which is formulated as

$$\Delta t = arg \max_{\tau} |r(\tau, l)| \tag{4-24}$$

Similar to Equation (4-21), Δt in Equation (4-24) should be redefined as $(\Delta t - T_{\text{win}})$ if the PD pulse in $x_{\text{A}}(t)$ is earlier than that in $x_{\text{B}}(t)$.

Moreover, some possible concerns are clarified when the proposed method is used for the farm wind overhead lines.

First, it is essential to point out that since the physical structures and electrical parameters of the terminals at both ends of the overhead line are always symmetrical, the waveforms between PD signals collected by the double-sided PD detectors are similar despite the difference in their magnitudes. This is the premise of the phase difference method effectiveness, based on the correlation between the PD signals.

Second, the overhead lines' high-frequency attenuation and dispersion nature can cause the PD waveform to become 'shorter' and 'fatter,' as discussed in Chapter 1. If the PD source is not located in the overhead line middle (i.e., $L_{\text{AB}}/2$), the waveforms between the PD signals detected at both ends of the overhead line can differ, more or less. Nevertheless, in [115], it has been proven that the influence of the attenuation and dispersion characteristics on the phase difference method accuracy is negligible.

In addition, since the running overhead line is connected to other overhead lines, some reflections caused by the impedance discontinuities (i.e., other overhead line terminals) can be detected after the PD signal. The reflection magnitude is significantly lower than that of the PD signal due to the high-frequency attenuation nature of the overhead lines. In [113], it has been proven that the low-amplitude reflections hardly reduced the phase difference

method accuracy.

3）Simulation Validation

In this subsection, the proposed TOA difference estimate method is applied to synthetic noisy PD signals, which are fully controllable and can validate and stress the method in extreme conditions (e.g., with a significant effect of noise). Simultaneously, the proposed method is compared with the state-of-the-art alternatives, the energy criterion method [113] and the phase difference method [115].

The synthetic noisy PD signals were obtained by proportionally adding noises on noiseless PD signals. The noiseless PD signals are the simulated pulses measured by the developed system in the laboratory overhead line, as shown in Figure 4-17. The onsets of the two noiseless pulses can be visually identified, and their TOA difference is calculated as 24 sampling points. Figure 4-17 (b) shows that the noises were measured in an on-shore wind farm. It can be observed that the noises contain both representative white noise and discrete spectrum noise. In addition, the center frequency of the discrete spectrum noise is close to that of the PD pulses. Thus, the noises can simulate the worst noise case in field measurement.

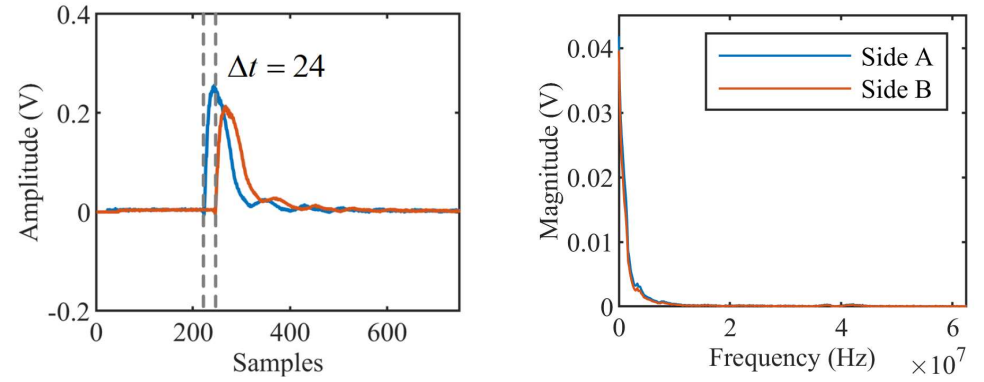

(a)

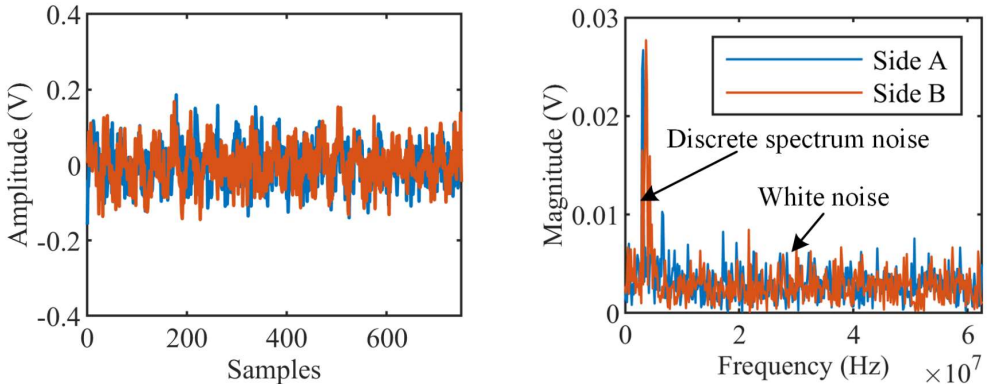

(b)

Figure 4-17 Time-domain and frequency-domain waveforms of the PD pulses and noises collected by the developed system: (a) Simulated noiseless PD signals measured in the laboratory overhead line and (b) The noises measured in an on-shore wind farm

The waveforms of the synthetic noisy PD signals, their cross-power spectrum phase curve, and the TOA difference estimate results are shown in Figure 4-18. Three possible situations are considered: (i) Case I: no noise, (ii) Case II: low-level noise, and (iii) Case III: high-level noise. According to the recommended parameter selection of the proposed method in the first subsection in Chapter 4.4.2, the frequency support B_G is set as 2 MHz (i.e., 12 sampling points when the sampling frequency is 125 MHz, and the total number of sampling points is 750). The value of the frequency hop H_G turns out to be 0.4 MHz (i.e., two sampling points). In Case I, no noise is added to the synthetic PD signals, and thus, their cross-power spectrum phase curve (i.e., $\angle\Psi(\omega)$ is almost perfect to be used in the phase difference method for TOA difference estimation, as shown in the first row and the first column in Figure 4-18. Because the TOA difference between the various frequency components of the two signals is constant, the phase difference between the two PD signals increases as the frequency increases, causing the phase curve to be a sawtooth wave. The

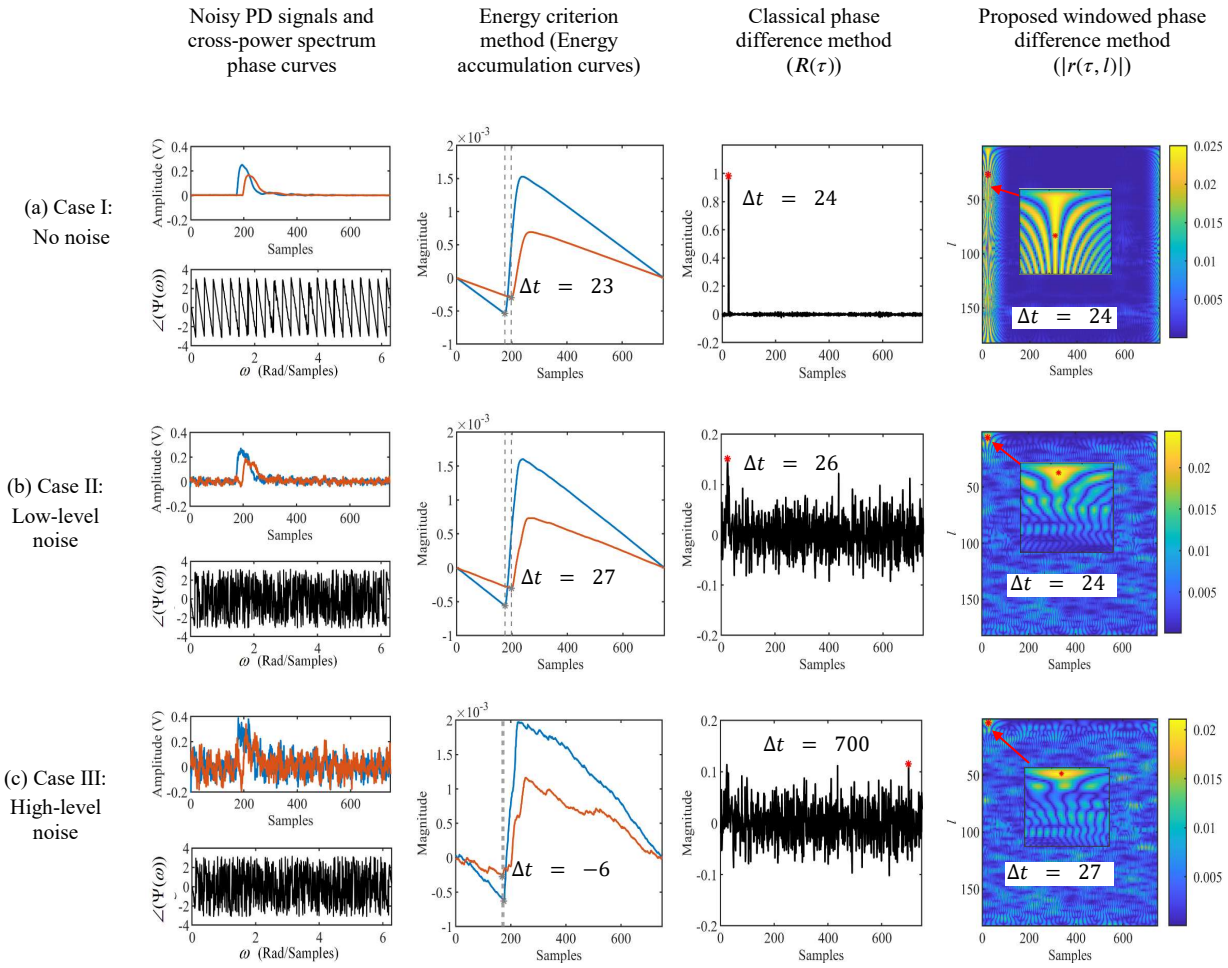

Figure 4-18 Results of the time-of-arrival difference estimation in varying noise levels using the energy criterion, classical phase difference, and the proposed windowed phase difference methods. (The grey star marks denote the minimum values of the energy accumulation curves, and the red star marks denote the maximum values of generalized cross-correlation $R(\tau)$ or the two-dimensional generalized cross-correlation spectrum $|r(\tau,l)|$). (a) Case I: no noise, (b) Case II: low-level noise, (c) Case III: high-level noise.

TOA difference estimation results reveal that the energy criterion, phase difference, and the proposed methods all perform excellently, as shown in the last three columns of the first row in Figure 4-18.

In Case II, low-level noises are added to the synthetic PD signals, and the sawtooth wave characteristic of the cross-power spectrum phase curve becomes unclear, as shown in the second row and the first column in Figure 4-18. Compared with the noiseless signals in Case I, it is pretty challenging to visually identify the onsets of the noisy PD signals. Nevertheless, the energy criterion, phase difference, and the proposed methods are still effective, as shown in the last three columns of the second row in Figure 4-18. Moreover, the results reveal that the errors of the energy criterion and phase difference method are slightly larger than those of the proposed method.

In Case III, high-level noises are added to the synthetic PD signals, and the sawtooth wave characteristic of the cross-power spectrum phase curve is more unclear, as shown in the last row and first column in Figure 4-18. The results reveal that the energy criterion and phase difference methods fail to estimate the TOA difference. In contrast, the proposed method is still effective despite having a small error, as shown in the last three columns of the second row in Figure 4-18.

In conclusion, the proposed TOA difference estimation method performs more robustly than the state-of-the-art energy criterion and phase difference methods in a low signal-to-noise ratio environment, which is inevitable in the online PD measurement of wind farm overhead lines.

4.2.3 Double-Sided Partial Discharge Location Algorithm

Two signals ($\mathbf{x}_A$ and $\mathbf{x}_B$) from a real 5,232-m overhead line with a PD defect (on a grimy insulator 4,691 m along the line) are shown in Figure 4-19. The signals contain not only PD pulses but also a high noise level. In the time domain, this noise is typically composed of continuous interference (CNIs) or impulse noise interferences (INIs). CNIs include white and discrete spectrum noise, and INIs have repeated and random pulse noise [93][95]. From the example waveform of Figure 4-19, the starting part of the PD pulses is cluttered by the CNI, which unavoidably leads to an imprecise estimation of the TOA parameter of the PD pulse. On the other hand, the INI possibly leads to errors in determining the PD location, mainly due to its inherent feature of sharing some waveform similarities with the functional PD pulses. Thus, a specific PD location algorithm is devised to suppress the influence of such interferences. The overall framework of the algorithm is shown in Figure 4-20, and its detailed explanation is described in the following subsections.

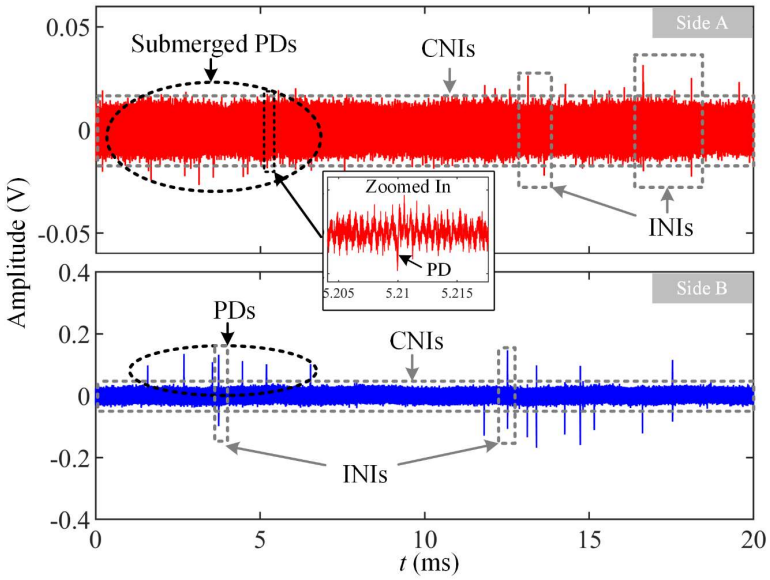

Figure 4-19 Waveforms of two 20-ms noisy signals acquired by two PD detectors mounted on the same phase of a real 5232-m overhead line with a PD defect (on a grimy insulator 4691 m along the line).

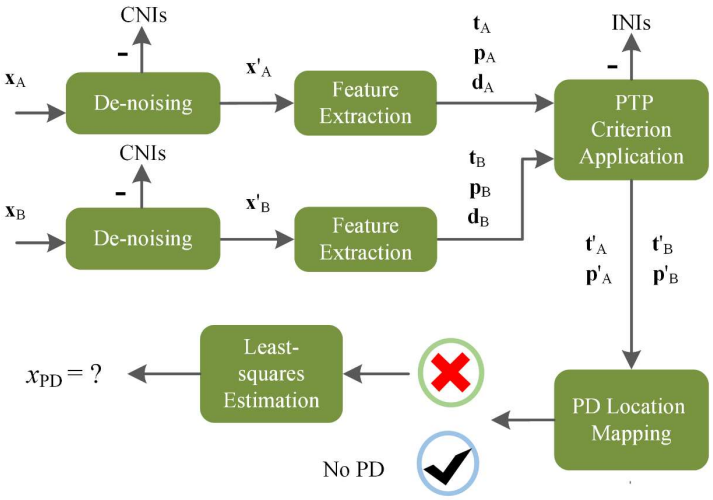

Figure 4-20 Block diagram of the entire PD location algorithm.

1）Suppression of CNIs and Extraction of Pulse TOAs, Peaks, and Polarities

The noisy signals $\mathbf{x}_A$ and $\mathbf{x}_B$ are de-noised via the STFT-SVD algorithm proposed in Chapter 3, and the TOAs of the pulses in $\mathbf{x}_A$ and $\mathbf{x}_B$ are estimated via the improved windowed phase difference method presented in Chapter 4.2.2.2. Then, the peaks and polarities of the pulses are calculated. A peak is defined as the first point over the threshold and after the TOA, where the trend of the first-order difference changes from positive to negative or from negative to positive. If the first-order difference varies from positive to negative, the polarity of the pulse is defined as positive, i.e., 1; if it changes from negative to positive, the polarity is defined as negative, i.e., −1.

Besides PD pulses and INIs, TOAs, peaks, and polarities of their reflections are also

obtained. These reflections are caused by impedance discontinuities at branch joints, which is inevitable in real overhead lines due to their complex branch-type structures. However, these reflections are undesirable because they might lead to incorrect PD locations. Thus, pulses within 20-μs after a higher amplitude pulse are regarded as reflections and removed.

Consequently, the following six feature vectors are obtained: two peak vectors ($\mathbf{p}_A$ and $\mathbf{p}_B$), two TOA vectors ($\mathbf{t}_A$ and $\mathbf{t}_B$), and two PD polarity vectors ($\mathbf{d}_A$ and $\mathbf{d}_B$), as drawn in Figure 4-21.

2）Suppression of INIs using a Pulse TOA-Polarity Criterion

Pulse source location is a distinct physical difference between PDs and INIs. Thus, calculations based on a time-correlation analysis of the TOAs of pulses in the two signals ($\mathbf{x}'_A$ and $\mathbf{x}'_B$) are used to separate PDs and INIs. However, time-correlation analysis alone cannot separate the PDs occurring around terminals from the INIs (e.g., other PDs) generated by different power apparatuses outside the target overhead line range. To solve this problem, the polarity of pulses in the double-sided signals is used, as pulses from the same PD on a target overhead line should have inverse polarities due to their different propagation directions. In contrast, the INIs from other overhead lines or apparatus out of the range of the target overhead line should have the same polarities, as illustrated in Figure 4-22. Thus, the following the pulse TOA-polarity criterion is built:

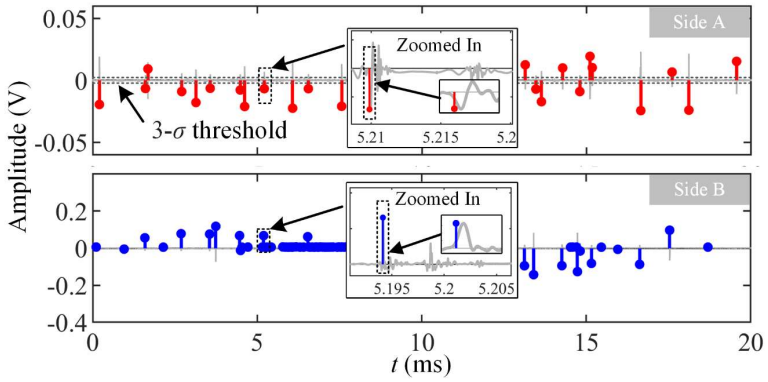

Figure 4-21 TOAs, peaks, and polarities extracted from the pulses in the de-noised signals in Figure 4-19. The zoomed-in inset displays the extracted details, where reflections are removed. The red stems and the blue stems denote the signs of the pulse features, and the gray lines indicate the de-noised signals.

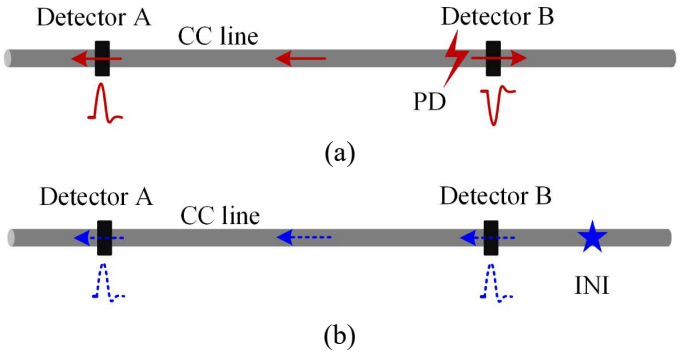

Figure 4-22 Polarities of detected pulses of a PD in the target overhead line (a) and an INI out of the range of the overhead line (b).

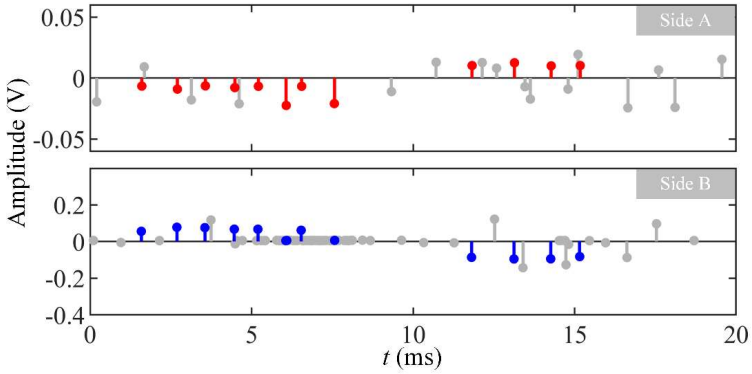

Figure 4-23 Signs of the pulses remaining after applying the pulse TOA-polarity criterion to the feature extraction results in Figure 4-21. The red and blue stems denote the remaining pulses, and the gray stems indicate all pulses before applying the PTP criterion.

$$\begin{cases} |t_{A,i}-t_{B,j}|\le T,\ t_{A,i}\in \mathbf{t}_A,\ t_{B,j}\in \mathbf{t}_B \\ d_{A,i}\cdot d_{B,j}<0\ ,\ d_{A,i}\in \mathbf{d}_A,\ d_{B,j}\in \mathbf{d}_B \end{cases} \tag{4-25}$$

The pulses in $\mathbf{x}'_A$ and $\mathbf{x}'_B$ whose TOAs and polarities satisfy Equation (4-25) are retained, and the remainder are discarded. This process gave the results depicted in Figure 4-23, wherein it can be seen that most INIs, whose amplitudes were slightly larger than those of the PDs, were removed. Consequently, four new feature vectors are obtained: two peak vectors ($\mathbf{p}'_A$ and $\mathbf{p}'_B$) and two TOA vectors ($\mathbf{t}'_A$ and $\mathbf{t}'_B$). The criterion is expected to work effectively because INIs acquired at double sides almost rarely meet it in most cases. Even if few INIs meet the above criterion, their effect can be further reduced by the statistics concentration characteristics analysis on PD location maps described in the following subsection.

3）Estimation of PD Locations Based on Location Mapping and Least-Squares approach

Using $\mathbf{t}'_A$ and $\mathbf{t}'_B$, a location vector $\mathbf{L}_{PD}$ that passes from the smallest to the most significant value can be calculated using Equation (5). Then, $\mathbf{p}_A$ and $\mathbf{p}_B$ can be used to obtain a real PD peak vector, $\mathbf{p}_{PD}$, from the following equation:

$$p_{PD}(i)=p_A(m)\cdot e^{\alpha_{PD}\cdot L_{PD}(i)}+p_B(n)\cdot e^{\alpha_{PD}\cdot (L_{AB}-L_{PD}(i))} \tag{4-26}$$

where $p_A(m)$ and $p_B(n)$ are the PD peaks of the pulses from the same PD, and α_{PD} is the attenuation coefficient of the PD signal propagating on the overhead line. It can be estimated via an approximation formula in [147].

PD location maps are drawn using $L_{PD}(i)$ and $p_{PD}(i)$ as the horizontal and vertical coordinates, respectively, as shown in Figure 4-24. If there is a PD defect on the target overhead line, these maps reveal its statistical concentration characteristics. A mean deviation quantity, *H*, which is used to quantize the concentration characteristics, is defined as follows:

$$H = \frac{\sum_{i=1}^{N}(L_{PD}(i) - \bar{L}_{PD})}{N \cdot L_{\mathrm{AB}}} \quad (L_{PD}(i) \in \mathbf{L}_{PD}) \tag{4-27}$$

where $\bar{L}_{PD}$ is the mean value of $\mathbf{L}_{\mathrm{PD}}$. To automatically identify if a target overhead line has a PD defect, a binary variable (B) is used and is defined as follows

$$B = \begin{cases} 0 & H > k, \text{ there is no PD defect} \\ 1 & H < k, \text{ there is a PD defect} \end{cases} \tag{4-28}$$

where k is a boundary between data concentration and deconcentration, which is empirically set to be 0.05 according to the data from a dozen detected PD defects. Once confirmed that a PD defect is present, the least-squares approach estimates the PD defect's location statistically. An optimal estimate of the PD location x_{PD}, is calculated as follows:

$$\min_{x_{\mathrm{PD}}} \sum_{i \in \mathbf{I}} (L_{PD}(i) - x_{\mathrm{PD}})^2 \tag{4-29}$$

where $\mathbf{I} = \{i \mid \bar{L}_{\mathrm{PD}} - 0.1L_{\mathrm{AB}} \le L_{\mathrm{PD}}(i) \le \bar{L}_{\mathrm{PD}} + 0.1L_{\mathrm{AB}}\}$.

The concentration characteristics analysis and the least-squares estimation could statistically minimize the negative effect of the rest of INIs and TOA errors on PD localization.

In addition, it should be mentioned that a few overhead lines may contain more than one PD source or another corona (collectively referred to as discharge). Then, $\mathbf{L}_{\mathrm{PD}}$ can be cut into multiple segments, one containing only one cluster (i.e., one discharge source). Finally, the locations of the discharge sources are estimated by applying the above-described algorithm to each segment. With the locations of the discharge sources, the technician can further identify the exact types of the discharge sources via the conventional vision- and ultrasonic-based tools, e.g., the widely used ultrasonic camera, which is available in most distribution maintenance teams.

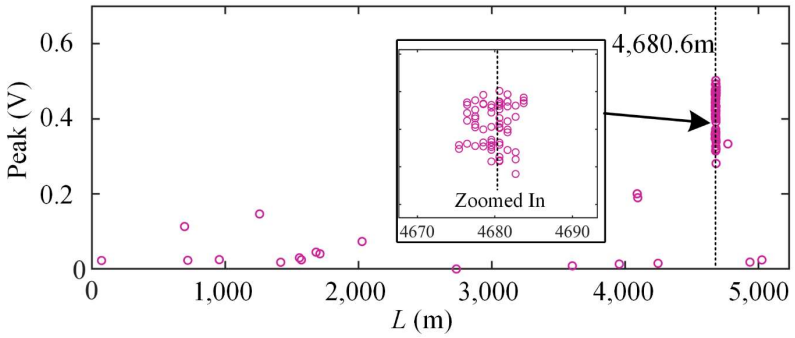

Figure 4-24 PD location maps generated by the remaining pulses from Figure 4-23 and five other measurements on the 5232-m overhead line with a PD defect (on a grimy insulator 4691 m along the line).

4.2.4 Laboratory Validation

A laboratory experiment was carried out on a 50-m single-phase 10-kV overhead line, which was 14 mm in diameter and had a 2-mm layer of insulation to validate the performance of the proposed PD location method and system—the test platform depicted in Figure 4-25. The overhead line was positioned 1.5 m above the ground, and each end of the line was connected to a separate terminal resistor R_g (300 Ω) to simulate a load. A programmable PD simulator, which produces a series of pulses with waveforms similar to PDs, was used to simulate PDs and was mounted on the overhead line 20 m from Side A. The apparent charge magnitude of the pulses produced by the simulator was programmed to vary from approximately 4 to 10 nC. The signals recorded by the two testing units are shown in Figure 4-26. The injected pulses are located at the start of the acquired signals. Calculations of the TOAs of the injected pulses reveal that the pulse traveled from Side A to Side B in 188 ns, which equates to a pulse propagation velocity of 265.9 m/μs.

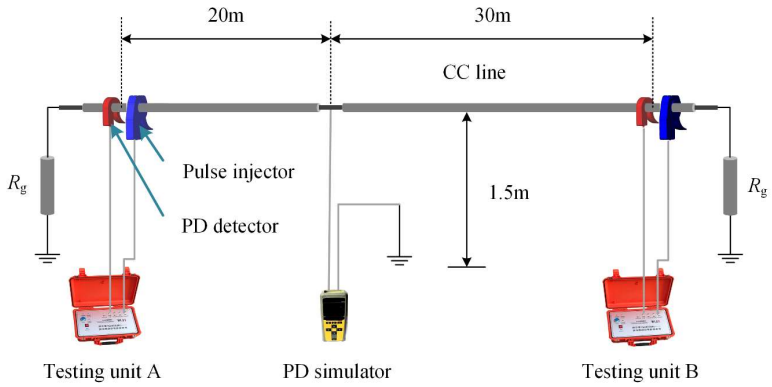

Figure 4-25 Setup of the test platform.

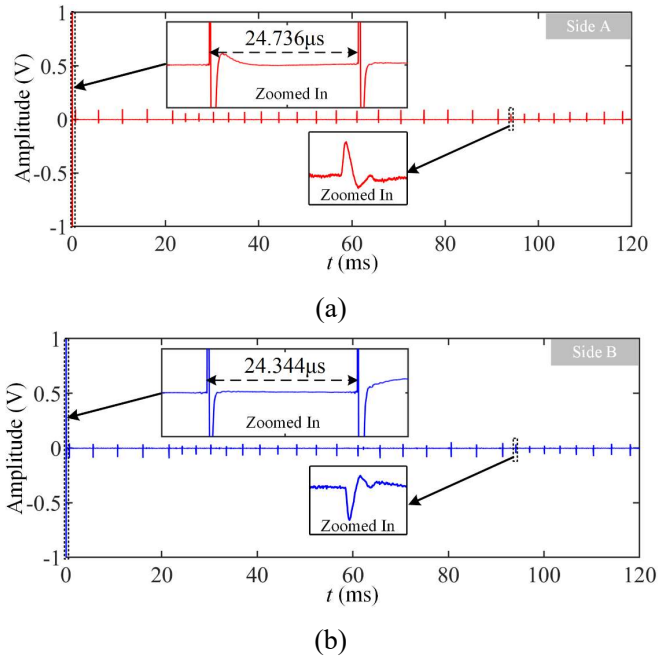

Figure 4-26 Acquired waveforms on Side A (a) and Side B (b) of the measured overhead line. The zoomed-in insets display the waveform details of the injected pulses and simulated PD pulses.

60 PD localizations, driven by GPSM (30 localizations) and GPS (30 localizations), respectively, were calculated, and the statistical results of mapping these locations are given in Figure 4-27. The results show that the maximum and mean errors of the PD localizations driven by the GPS synchronization were 15.94 m and 5.82 m, respectively. In contrast, the PD localizations driven by the GPSM were 2.87 m and 0.79 m. The primary reason why the GPS-based PD localization has more significant errors is that synchronization errors of the PPS outputs of the GPS were always within a range of approximately hundreds of nanoseconds. It is expected that the errors of PD localizations driven by the GPS modules would be even more significant during field testing due to complex environmental factors and propagation velocity errors caused by the unknowing propagation parameters in overhead lines.

Then, the maximum apparent charge magnitude of the outputs of the PD simulator was gradually increased from 10nC to 200nC. The localization results, driven by GPSM and pulse synchronization (PS) (which depends on a threshold triggering mode, referring to [14]), respectively, are listed in Table 4-3. As the apparent charge magnitude of the simulated pulses is more significant than 56nC, the PS-based method with a 500 mV trigger threshold failed to obtain the PD localization results. It demonstrates that the reliability of the PS-based location method is associated with the magnitudes of the injected pulses and PDs and is expected to be lower when used on a long overhead line (e.g., 10km) due to the inevitable high-frequency propagation attenuation. In contrast, the GPSM-based location method is still reliable because it uses GPS to trigger the signal acquisitions. In conclusion, the GPSM-based PD location method locates PDs in overhead lines more accurately and reliably than conventional GPS-based and latest PS-based methods.

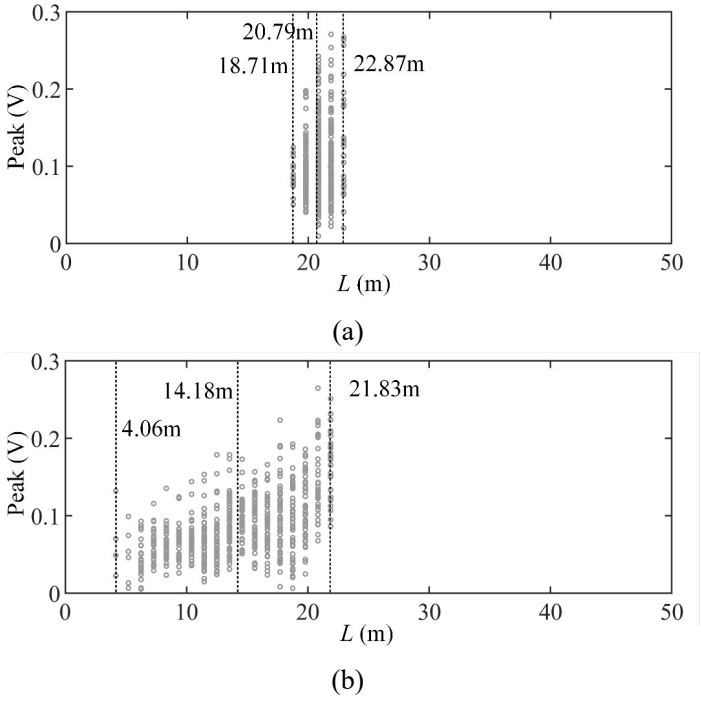

Figure 4-27 PD location mappings are based on the improved PD location method driven by GPSM (a) and the classical PD location method driven by GPS (b), respectively.

Table 4-3 Comparison of the PD localization between GPSM and PS.

The apparent charge magnitude of the pulses produced by the PD simulator	The mean value of PD locations	
	GPSM	PS
<56 nC	20.83 m	20.82 m
≥56 nC	20.74 m	*Error*

In addition, simulated noise disturbances (i.e., CNIs, including white noise and discrete spectrum noise) are added to the measured noiseless PD data to test the accuracy of the proposed algorithm, as shown in Figure 4-28. The frequencies of two harmonics in the discrete spectrum noise are set to 1 and 6 MHz, and their corresponding amplitudes are set to 0.045 and 0.03 V, respectively. White noise is a zero mean Gaussian sequence with 0.03 V standard deviation. The signal-to-noise ratio of the synthetic PD signals can be tuned by proportionally scaling the amplitudes of the noises. Figure 4-29 collects the PD location estimate results under varying signal-to-noise ratios. It can be observed that as the signal-to-noise ratio decreases, the standard deviation of the PD locations becomes unavoidably more prominent. However, the procedure arising from Equation (4-29) is robust and coherently produces the correct estimate of the actual value of the PD location (i.e., 20 m). In other words, that means that although the CNIs can lead to uncertain errors on one PD location estimate, the statistical mean of multiple estimated PD locations is beneficial for very low signal-to-noise ratio scenarios, demonstrating the effectiveness and robustness of the proposed algorithm.

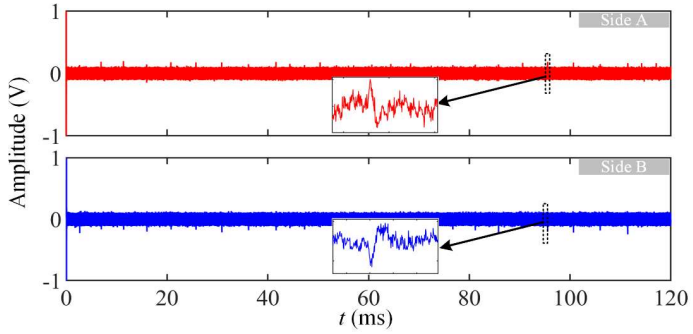

Figure 4-28 Waveforms of synthetic noisy PD signals with a signal-to-noise ratio of -13.3 dB.

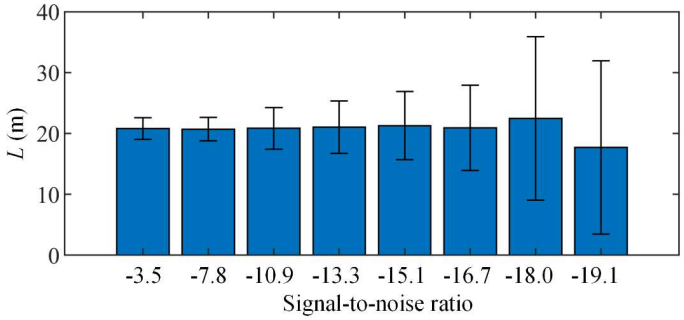

Figure 4-29 Results of PD location estimations under varying signal-to-noise ratios.

4.3 Multiple-Sided Partial Discharge Localization from the Perspective of Optimization

To locate a PD in an overhead distribution network that always contains many branches, the double-sided location method has to be applied to each branch, which requires deploying a mass of PD measurement units (i.e., two units for each branch) or moving the double-sided units repeatedly. This is very expensive and time-consuming. Alternatively, the multiple-sided PD location method is developed for the overhead distribution network. The process is based on the GPSM technique and needs minimal PD measurement units mounted on the branch ends. The PD location formulation of the method is derived based on the TOA measurements of the used PD detectors and the network structure and size information obtained from the distribution network management database. It turns out to be an over-determined set of equations. An optimization algorithm based on the standard vector norm is proposed to solve these equations. Finally, the feasibility and effectiveness of the multiple-sided PD location algorithm are validated via Monte Carlo uncertainty simulation.

4.3.1 Principles

Similar to double-sided PD localization, GPSM can also be used for multiple PD localization. A six-step overview of the working procedure of the GPSM-based PD location method is detailed below (see Figure 4-30 and Figure 4-31).

(1) Multiple PD detectors and pulse injectors are mounted on an overhead distribution network, as shown in Figure 4-30. In this figure, all PD detectors are mounted on the ends of the line system. Nevertheless, it is essential to point out that additional PD detectors and injectors are required to be mounted in the middle of the line system if the internal lines are too long since the PD signal can attenuate along the line.

(2) PD detectors at each side start to acquire data when their respective GPS triggers activate them. PSM is only triggered within a short pre-set time window.

(3) Within the time window, PD injectors are triggered in sequence to inject high-amplitude pulses into the overhead line, as shown in Figure 4-31.

(4) Similar to the GPSM-based double-sided method in the last section, the propagation time T from Side i to Side j ($i, j \in \{1,2,\ldots, M\}$) can be calculated as:

$$T_{ij} = \frac{(t_{ij} - t_{ii}) - (t_{jj} - t_{ji})}{2} \tag{4-30}$$

where t_{ij} denotes the j^{th} synchronization pulse in the data collected by the i^{th} PD detector. Therefore, $\Delta t_{\text{syn},ij}$ can be calculated as:

$$\Delta t_{\text{syn},ij} = t_{ii} - t_{ji} + T_{ij} \tag{4-31}$$

A synchronization vector (using t_{11} as the reference) can be obtained as $\Delta \mathbf{S} = [t_{\text{syn},11}, t_{\text{syn},12}, \ldots, t_{\text{syn},1N}]^{\text{T}}$. Moreover, using the calculated propagation time T_{ij} and

the length L_{ij} of the measured overhead line segment, the signal propagation velocity (v_{ij}) of the overhead line from side i to side j can be calculated as:

$$v_{ij} = \frac{L_{ij}}{T_{ij}} \tag{4-32}$$

The mean of v_{ij} is defined as the propagation velocity $\overline{v}$ of the overhead distribution network, i.e., $\overline{v} = \sum_{j=2}^{j=N} v_{1j}$.

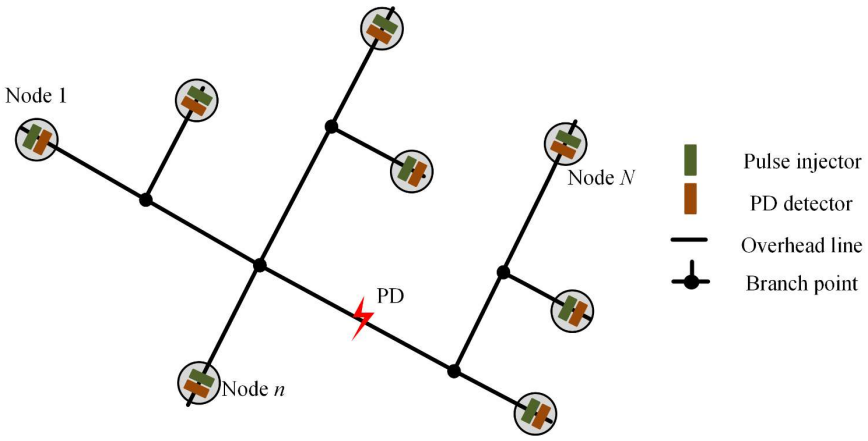

Figure 4-30 Sketch of multiple-sided PD localization.

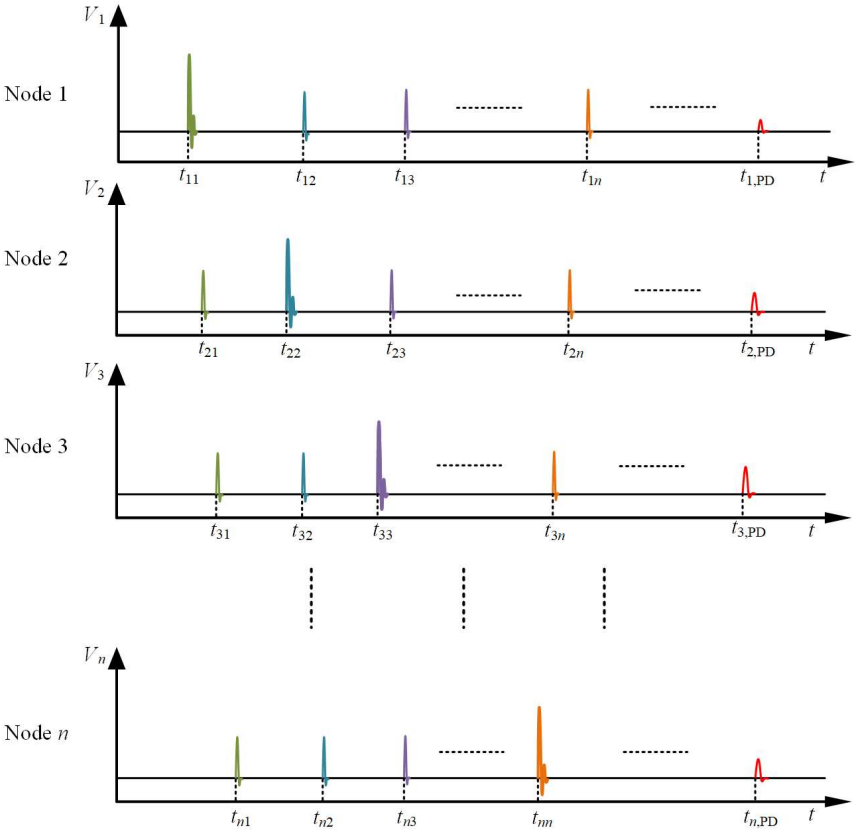

Figure 4-31 Time sequences of injected pulses and the PD pulse collected by n PD detectors.

(5) The PD detectors continue to acquire PD data for more than one power-frequency cycle. Multiple pulses, $V_{1,\mathrm{PD}}$, $V_{2,\mathrm{PD}}$,…, and $V_{M,\mathrm{PD}}$, which originate from the same PD activity, are used to represent the results for all PD detectors, respectively. In addition, $t_{1,\mathrm{PD}}$, $t_{2,\mathrm{PD}}$,…, and $t_{M,\mathrm{PD}}$ are the TOAs of $V_{1,\mathrm{PD}}$, $V_{2,\mathrm{PD}}$,…, and $V_{M,\mathrm{PD}}$, respectively. A TOA difference vector (using $t_{1,\mathrm{PD}}$ as the reference) can be obtained as

$$\Delta\mathbf{T}^{\mathrm{measured}} = \begin{pmatrix} t_{1,\mathrm{PD}} - t_{1,\mathrm{PD}} \\ t_{2,\mathrm{PD}} - t_{1,\mathrm{PD}} \\ \vdots \\ t_{M,\mathrm{PD}} - t_{1,\mathrm{PD}} \end{pmatrix} \tag{4-33}$$

(6) Based on the estimated $\bar{v}$, $\Delta\mathbf{S}$, and $\Delta\mathbf{T}^{\mathrm{measured}}$, the PD location is calculated via the algorithm developed in the following subsection.

4.3.2 Multiple-Sided Partial Discharge Location Algorithm

This subsection describes a multiple-sided PD location algorithm. The PD location formulation is first derived, then an optimization algorithm is developed to solve the formulation. This algorithm assumes that a sufficient number of PD detectors are mounted in the overhead distribution network to guarantee that PD occurring in any location is localizable. The multiple-sided fault location method in [140] inspires the algorithm. Compared to the algorithm in [148], the problems of synchronization error and unknown propagation velocity are addressed. The block diagram of the proposed algorithm is shown in Figure 4-32, and its detailed explanation is described in the following.

Two variables, the line number $m \in \{1,2,\ldots,M\}$ and location coefficient $\alpha\epsilon\{[0,1]\}$, are defined to describe the PD source location. From Figure 4-33, the traveling time to the detector n from a PD source on line m is equal to:

$$T_{m,n} + R_{m,n}\alpha^{(m)}T_m \tag{4-34}$$

where $T_{m,n}$ is the traveling time from the start of line "m" to the detector "n"; $\alpha^{(m)}T_m$ is a propagation delay from the PD location to the origin of line "m." "α" defines the fault location from the line origin as a fraction of the line length; $R_{m,n}$ is equal to −1 if the shortest path to detector "n" includes the line "m" end; otherwise $R_{m,n}$ is +1. It is essential to point out that $T_{m,n}$ and T_m are calculated by multiplying the corresponding line lengths by the propagation velocity $\bar{v}$, which is obtained in the GPSM process.

The TOA difference $\Delta T_{n1,n2}^{(m)}$ between any two PD detectors "n_1" and "n_2" can be calculated as

$$\Delta T_{n1,n2}^{(m)} = \left(T_{m,n2} - T_{m,n1}\right) + (R_{m,n2} - R_{m,n1})\alpha^{(m)}T_m \tag{4-35}$$

Using the detector one as the reference, a TOA difference vector $\Delta\mathbf{T}^{\mathrm{theoretical}}$ can be obtained as

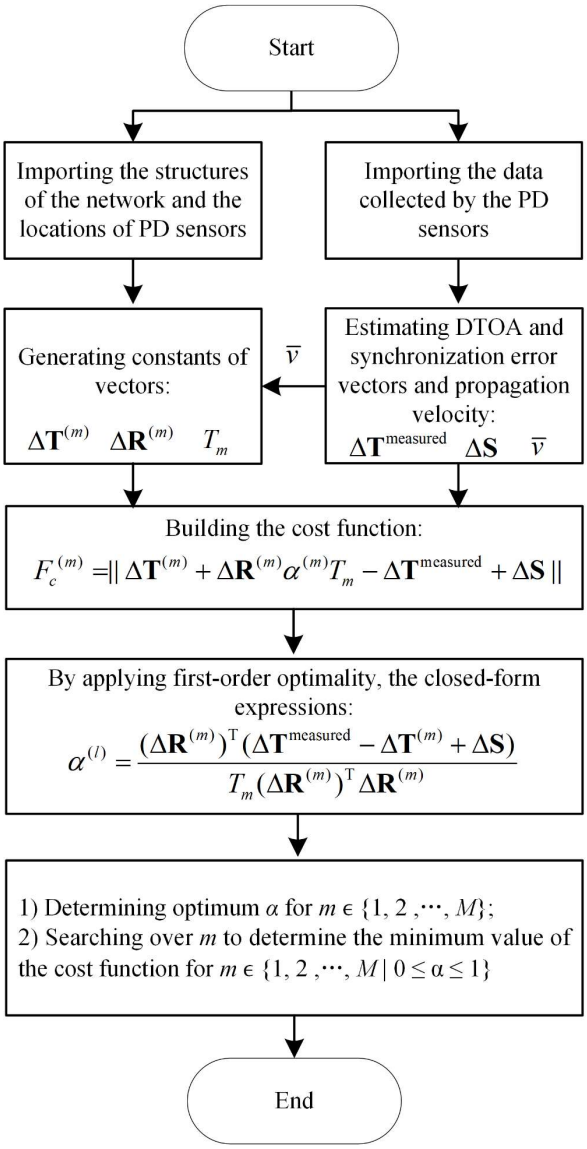

Figure 4-32 Block diagram of the multiple-sided PD location algorithm

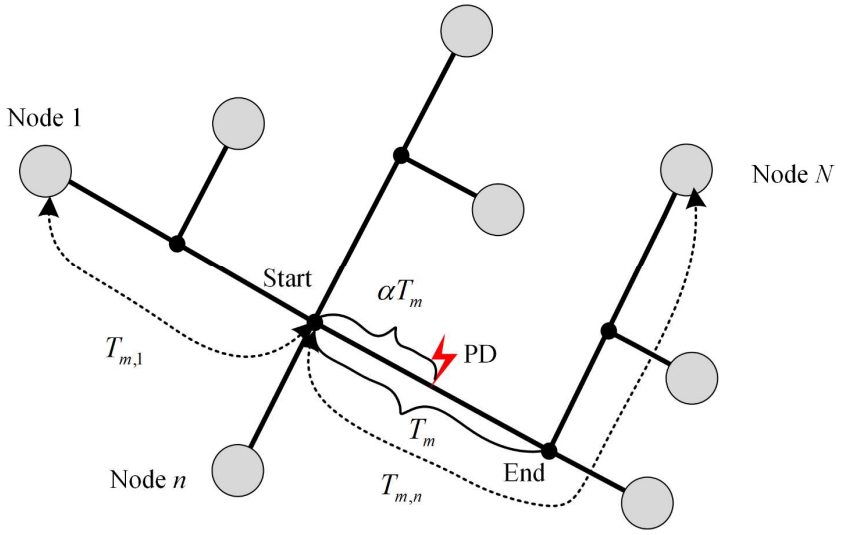

Figure 4-33 Illustration of propagation delays

$$\Delta\mathbf{T}^{\text{theoretical}} = \Delta\mathbf{T}^{(m)} + \Delta\mathbf{R}^{(m)}\alpha^{(m)}T_m \tag{4-36}$$

where

$$\Delta\mathbf{T}^{(m)} = \begin{bmatrix} T_{m,1} - T_{m,1} \\ T_{m,2} - T_{m,1} \\ \vdots \\ T_{m,N} - T_{m,1} \end{bmatrix} \tag{4-37}$$

$$\Delta\mathbf{R}^{(m)} = \begin{bmatrix} R_{m,1} - R_{m,1} \\ R_{m,2} - R_{m,1} \\ \vdots \\ R_{m,N} - R_{m,1} \end{bmatrix} \tag{4-38}$$

A system of equations can be obtained for actual PD location by exchanging the theoretical TOA vector with the measured TOA vector $\Delta\mathbf{T}^{\text{measured}}$, simultaneously taking the synchronization errors $\mathbf{\Delta S}$ obtained in the GPSM process into account. The set of equations is defined as

$$\Delta\mathbf{T}^{(m)} + \Delta\mathbf{R}^{(m)}\alpha^{(m)}T_m - \Delta\mathbf{T}^{\text{measured}} + \Delta\mathbf{S} = 0 \tag{4-39}$$

where

$$\Delta\mathbf{T}^{\text{measured}} = \begin{bmatrix} T_1^{\text{measured}} - T_1^{\text{measured}} \\ T_2^{\text{measured}} - T_1^{\text{measured}} \\ \vdots \\ T_N^{\text{measured}} - T_1^{\text{measured}} \end{bmatrix} \tag{4-40}$$

Since only two variables, m, and α, are unknown, Equations (4-40) is a set of over-determined equations for N>2. $\Delta\mathbf{R}^{(m)}$ is the constant vector that is up to the inherent structure of the overhead distribution network; $\Delta\mathbf{T}^{(m)}$, T_m, and $\mathbf{\Delta S}$ are associated with the transmission line parameters of the line system, and the synchronization of GPSs, and they can be determined after the GPSM process; $\Delta\mathbf{T}^{\text{measured}}$ is measured after a PD occurrence. To solve m and α, these over-determined equations can be redefined as a constrained optimization problem:

$$\begin{aligned} &min_{(m,\alpha)} \ \ ||\Delta\mathbf{T}^{(m)} + \Delta\mathbf{R}^{(m)}\alpha^{(m)}T_m - \Delta\mathbf{T}^{\text{measured}} + \Delta\mathbf{S}|| \\ &\text{S.t. } \alpha\epsilon\{[0,1]\} \text{ and } m \in \{1,2,\dots,M\} \end{aligned} \tag{4-41}$$

where $||\bullet||$ denotes the standard vector norm operator. The cost function can be defined as

$$F_{\text{c}}^{(m)} = ||\Delta\mathbf{T}^{(m)} + \Delta\mathbf{R}^{(m)}\alpha^{(m)}T_m - \Delta\mathbf{T}^{\text{measured}} + \Delta\mathbf{S}|| \tag{4-42}$$

For $\alpha^{(m)}$, equation (4-42) is a quadratic function, which means that $F_{\text{c}}^{(m)}$ has only one minimum point. Therefore, $\alpha^{(m)}$ of the minimum $F_{\text{c}}^{(m)}$ can be calculated by

$$\frac{\partial F_{\text{c}}^{(m)}}{\partial \alpha^{(m)}} = 2\left(\Delta\mathbf{R}^{(m)}\right)^{\text{T}}\left(\Delta\mathbf{T}^{(m)} + \Delta\mathbf{R}^{(m)}\alpha^{(m)}T_m - \Delta\mathbf{T}^{\text{measured}} + \Delta\mathbf{S}\right) = 0 \tag{4-43}$$

Yielding

$$\alpha^{(m)} = \frac{\left(\Delta\mathbf{R}^{(m)}\right)^{\mathrm{T}}(\Delta\mathbf{T}^{\mathrm{measured}} - \Delta\mathbf{T}^{(m)} - \Delta\mathbf{S})}{T_m\left(\Delta\mathbf{R}^{(m)}\right)^{\mathrm{T}}\Delta\mathbf{R}^{(m)}} \tag{4-44}$$

where $(\cdot)^{\mathrm{T}}$ denotes the transposition operator. Since $\alpha^{(m)}$ and m are not coupled to each other, the optimization problem can be solved via a two-step procedure:

(1) Determining optimum α for $m \in \{1,2,\ldots,M\}$;

(2) Searching over m to determine the minimum value of the cost function for $m \in \{1,2,\ldots,M|\alpha\epsilon[0,1]\}$.

4.3.3 Simulation Validation

The proposed algorithm is tested via a simulation experiment on the IEEE 34-bus distribution network. Monte Carlo uncertainty analysis is used to validate the reliability of the proposed algorithm and quantificationally evaluate its sensitivity to the uncertainty of the input and internal parameters. The results validate the feasibility and effectiveness of the proposed algorithm.

1）Simulation Setup

To evaluate the accuracy of the proposed algorithm, an IEEE 34-bus distribution network is used as a test system, as shown in Figure 4-34. Ten PD detectors are mounted on the ends of the network, i.e., buses 1, 5, 12, 14, 18, 22, 24, 30, 32, and 34. The length of the network's line segments is collected in Table 4-4. It is assumed that the propagation parameters of the lines are consistent, and the PD source occurring in any location can be detected by all PD detectors.

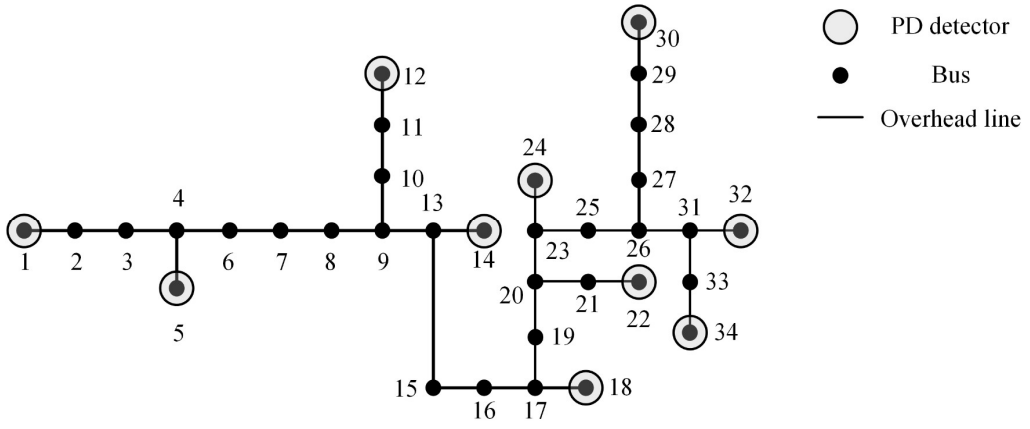

Figure 4-34 Single-line diagram of IEEE 34-bus distribution network.

The output uncertainty of the proposed algorithm can be caused by four input parameters, including the traveling time vector $\Delta\mathbf{T}^{(m)}$, the traveling time T_m in all line segments, the measured TOA difference vector $\Delta\mathbf{T}^{\mathrm{measured}}$, and the synchronization error vector $\Delta\mathbf{S}$. The uncertainty of $\Delta\mathbf{T}^{(m)}$ and T_m can be represented by the uncertainty of the line lengths. Therefore, line length uncertainty, TOA differences estimation uncertainty, and synchronization errors can be regarded as the primary source of the output uncertainty.

Table 4-4 Lengths and connections of the lines in the IEEE 34-bus distribution network (61.678km)

Line number	Start bus	End bus	Length (m)	Line number	Start bus	End bus	Length (m)
1	1	2	516	18	25	30	404
2	2	3	346	19	25	26	56
3	3	4	6446	20	31	34	172
4	4	5	1160.8	21	31	32	56
5	4	6	7500	22	26	27	270
6	6	7	5946	23	27	28	728
7	7	8	20	24	28	29	106
8	9	10	342	25	8	9	62
9	9	13	2042	26	19	20	20
10	10	11	9630	27	17	18	4666
11	11	12	2748	28	17	19	7366
12	13	14	606	29	23	24	324
13	13	15	168	30	23	25	1166
14	15	16	4088	31	30	31	536
15	16	17	104	32	32	33	972
16	20	23	980	33	21	22	2112
17	20	21	20				

The proposed algorithm's accuracy and reliability can be evaluated by adding normal distribution random values to the three input parameters. To achieve the evaluation, Monte Carlo analysis was used in this simulation. Figure 4-35 shows the flowchart of the Monte Carlo simulation experiment. The simulation experiment is completed via an eight-step procedure as follows:

(1) The simulation trial number is initialized, i.e., $i = 0$;

(2) The PD-affected line number m_{PD} and location coefficient α_{PD} are randomly selected in $U(\{1,2,\dots,M\})$ and $U(\{[0,1]\})$, respectively, where $U(\{\cdot\})$ denotes a random value from a uniform distribution in the value range of $\{\cdot\}$. Moreover, i is assigned as $i+1$.

(3) Random values from normal distributions $N(l_j, \mu l_j)$ are added in the line lengths. l_j denotes the length of the j^{th} line, and μl_j denotes its standard deviation. This results in an updated line length vector $\mathbf{L}^e = [l_1^e, l_2^e, \dots, l_M^e]^{\mathrm{T}}$.

(4) Using m_{PD}, α_{PD}, and $\mathbf{L}^e$, the theoretical TOA difference vector can be calculated and assigned to the measured TOA difference vector $\Delta\mathbf{T}^{\mathrm{measured}}$.

(5) Random values from normal distributions $N(\Delta T_n^{\mathrm{measured}}, \delta_T)$ and $N(\Delta t_{\mathrm{syn},1n}, \delta_S)$are added in $\Delta\mathbf{T}^{\mathrm{measured}}$ and $\Delta\mathbf{S}$, respectively. δ_T and δ_S denote the standard deviations. This results in the updated measured TOA difference vector $\Delta\mathbf{T}^{\mathrm{measured},e}$ and synchronization error vector $\Delta\mathbf{S}^e$.

(6) Applying the developed algorithm results in the updated PD-affected line number m_{PD}^{e} and location coefficient α_{PD}^{e}.

(7) The relative PD location error is calculated as

$$E_j = \frac{\Delta L}{\sum_{m=1}^{M} l_m} \bullet 100\% \tag{4-45}$$

where ΔL is the distance between the actual and the estimated PD locations.

(8) Determine whether i exceeds the set simulation trials I. If no, the procedure returns to step 2); otherwise, the process ends.

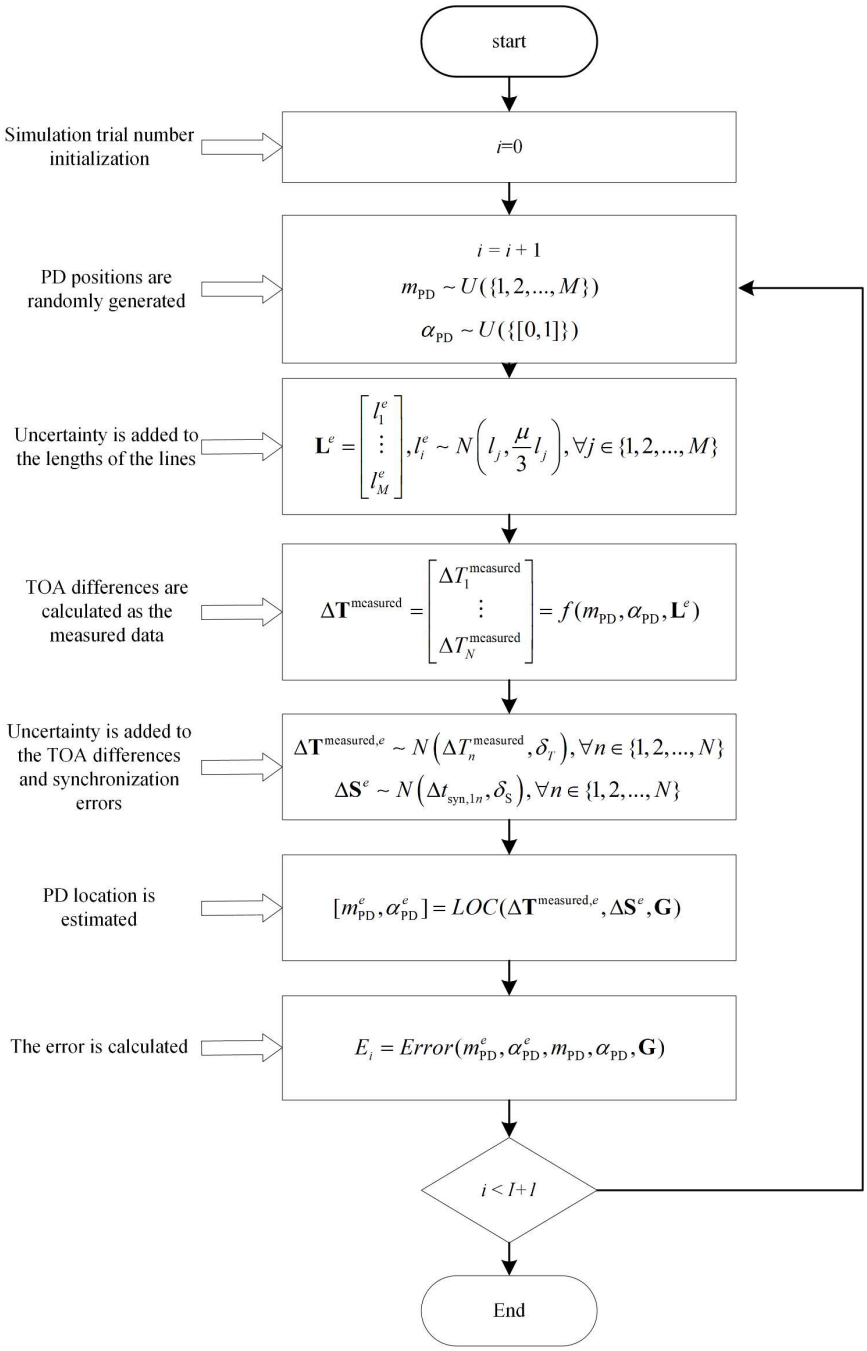

Figure 4-35 Flowchart of the Monte Carlo uncertainty simulation.

2）Result Analysis

Four independent Monte Carlo simulations have been carried out to analyze the output and robustness of the proposed algorithm. Table 4-5 provides the parameter settings for each scenario. Figure 4-36 collects the output error probability of the four Monte Carlo simulations. It can be observed that the means of the error of four scenarios are close to zero, validating the accuracy and robustness of the proposed algorithm to the uncertainties of the input parameters; the standard deviations of the output errors of the four scenarios increase in turn, revealing the output errors are positively correlated with the uncertainties of input parameters.

Table 4-5 Monte Carlo simulation parameters.

Scenario	μ (pu)	δ_T (us)	δ_s (us)	Run trials
1	0.01	0.01	0.05	30000
2	0.02	0.02	0.1	30000
3	0.04	0.05	0.2	30000
4	0.1	0.1	0.5	30000

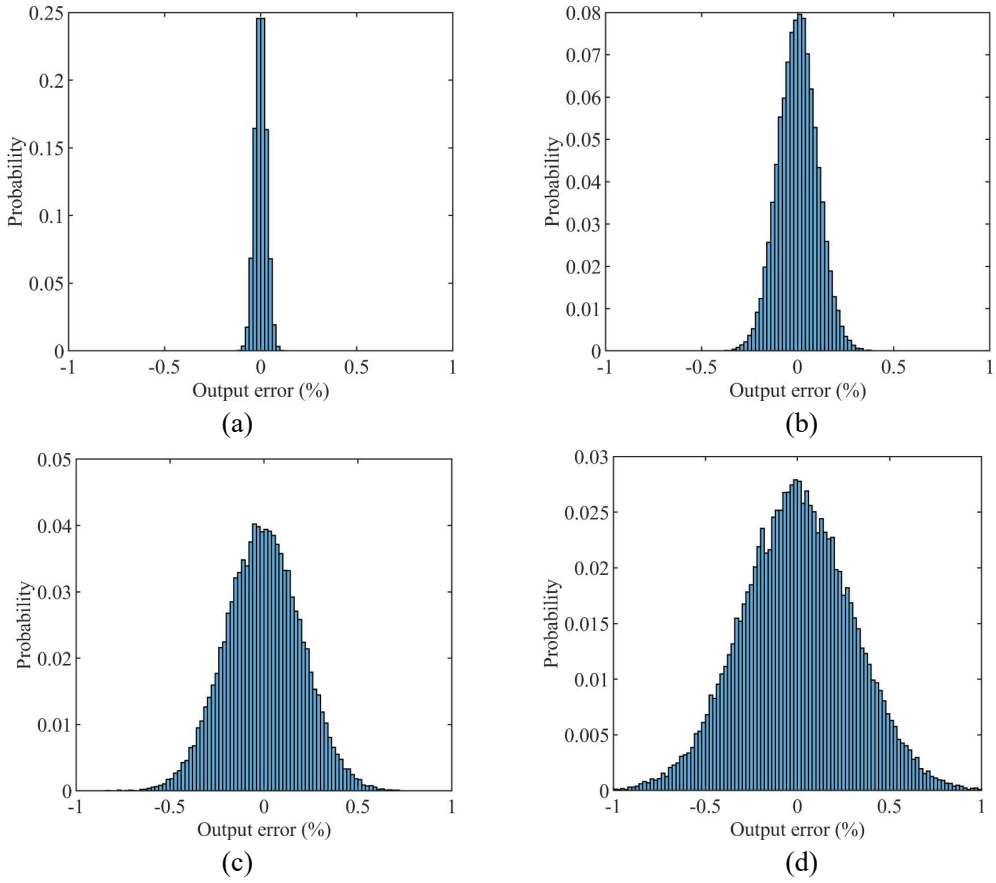

Figure 4-36 Output error probability distributions of the four scenarios: (a) Scenario 1; (b) Scenario 2; (c) Scenario 3; (d) Scenario 4

4.4 Conclusion

This chapter proposes improved PD detection and location methods for MV overhead distribution networks. Three crucial technical benefits are summarized as follows:

(1) To address the issue of magnetic saturation caused by the high-power frequency load current, we have developed a notched high-frequency current transformer. This transformer effectively overcomes the problem without compromising sensitivity of more than 5V/A and frequency bandwidth from 0.1 MHz to 50 MHz. In addition, we propose a digital compensation algorithm to simplify the design and parameter tuning of the high-frequency transformer. This algorithm significantly improves the transfer characteristics of the transformer. As a result, we can more accurately evaluate partial discharge activities, e.g., estimating PD discharge quantity.

(2) An improved double-sided PD location method is proposed. The proposed solution offers three essential benefits: i) The hybrid synchronization approach is developed via the joint application of Global Position Systems and the pulse-based interaction process. The synchronization approach not only can eliminate the inherent random errors of the GPSs but also estimate the average pulse propagation velocity, thus improving on-site PD localization, e.g., location error is significantly reduced from 5.82 m to 0.79 m in the experiment case of a 50-m overhead line; ii) A windowed phase difference method is developed to robustly estimate the time-of-arrival difference between the noisy PD pulses collected by the detectors in low signal-to-noise ratio environment, guaranteeing accurate and reliable PD location identification in the field; iii) The PD location map can automatically separate PD pulses from impulse noise interferences, enabling the easy elimination of their influence.

(3) A multiple-sided PD location algorithm for radial distribution networks is proposed based on the previous double-sided PD location method. The PD location problem of radial distribution networks is transformed into an optimization problem, which can be easily solved from the TOAs of the synchronization and PD pulses. Moreover, the proposed method mathematically identifies an observability factor for each line, which can be used to place the PD detectors optimally. The accuracy and robustness of the algorithm are demonstrated by Monte Carlo uncertainty analysis.

5 System Design and Application Strategy

This chapter combines the methods and techniques from previous chapters into two system prototypes. One is a portable PD detection and location system capable of live-line locating PDs in MV overhead distribution networks; the other is a low-cost PD monitoring system capable of online monitoring PD activities of MV overhead distribution networks in real-time. In-house designs of the two systems, including several hardware and software issues, are presented and thoroughly discussed, along with their applications on real 10-kV overhead distribution networks. Furthermore, a cost-efficient PD diagnosis strategy for MV overhead distribution networks is proposed based on the developed systems.

5.1 Low-Cost On-Line Partial Discharge Monitoring System Based on IoT Sensing Networking and Applications

The availability of accurate and cost-effective solutions for the real-time monitoring of overhead distribution networks is now becoming an essential tool for the reliability and condition assessments of this class of electrical lines. This is even more crucial due to the possibly large number of conductors and the wide geographical spread of the electrical network. This chapter proposes a smart and compact PD detector for monitoring of the MV overhead distribution network, matching the above needs and offering a flexible and cost-effective solution with some essential features, including non-invasive sensing, a field energy harvesting function, and a low-power working operation. The detector has been designed and implemented, proving its effectiveness in two cases involving PD-affected 10 kV CC lines.

5.1.1 Overview of the System

The PD monitoring system for an overhead distribution network comprises a non-invasive and self-powered PD monitor, along with a cloud server, as shown in Figure 5-1. This system is designed to continuously monitor and evaluate the presence of PD activity in the overhead distribution network, ensuring its reliability and safety.

Non-Invasive and Self-Powered PD Monitor: The non-invasive PD monitor is a vital system component installed at strategic locations along the overhead line. It can detect PD signals without direct contact or interruption of the power supply. The monitor utilizes advanced sensing technologies to capture PD signals generated by insulation defects or electrical breakdowns within the system.

Cloud Server: The cloud server performs the central data collection, analysis, and storage in the PD monitoring system. It receives real-time data from multiple non-invasive PD monitors installed across the overhead distribution network. The cloud server analyzes and processes the received data to identify PD characteristics and fault patterns.

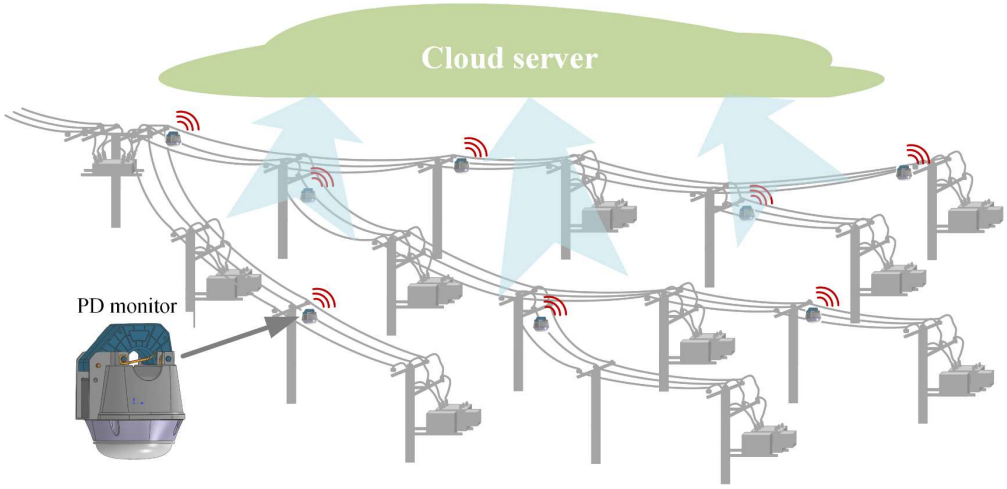

Figure 5-1 Typical application scenario of the online PD monitoring system, including multiple PD monitors and a cloud server.

Benefits of the PD Monitoring System:

(1) Early fault detection: The continuous monitoring provided by the non-invasive PD monitors allows for early detection and identification of insulation defects or failures, facilitating proactive maintenance actions.

(2) Improved reliability and safety: By monitoring PD activity, the system helps utilities identify potential risks and take necessary measures to ensure the reliability and security of the overhead distribution network, minimizing the chances of unplanned outages or accidents.

(3) Cost-effective maintenance: Timely detection of PD activities through the monitoring system enables utilities to focus their maintenance efforts on areas with identified issues, optimizing resource allocation and reducing overall maintenance costs.

(4) Enhanced asset management: The historical PD data stored in the cloud server assists utilities in assessing the condition of the overhead distribution network, identifying areas prone to PD, and making informed decisions regarding asset management and replacement strategies.

The PD monitoring system for overhead distribution networks, consisting of non-invasive and self-powered PD monitors and a cloud server, offers continuous and real-time monitoring of PD activities. This comprehensive system aids in early fault detection, improving reliability, safety, and cost-effective maintenance of the overhead distribution network.

5.1.2 Flexible and Compact Partial Discharge Monitor

This subsection describes the in-house-developed online PD detector for overhead CC lines. Figure 5-2 shows its main components: energy harvesting coils, HFCT, a voltage coupler, and a circuit board. The energy harvesting coils power the circuit board from the CC lines, while the HFCT and voltage coupler are used to non-invasively detect the PD and the power frequency phase, respectively. The circuit board consists of four parts: (i) an energy

harvesting module; (ii) a signal preprocessing module; (iii) a low-power advanced reduced instruction set computer (RISC) machine (ARM) module (STM32L476RG, ST); and iv) a low-power narrowband Internet of things (NB-IOT) module (BC26, Quectel), as shown in Figure 5-3. It is essential to note that the most expensive device among the previously discussed components is the ARM module, which costs around 14 USD. The circuit board manages the energy allocation, processes signals, and communicates with the IoT cloud, which accounts for data collection from all the different detectors spread along the network. Once the data reveals any PD activities, the IOT cloud can issue warnings to the staff via a quick message (e.g., mobile phone messages). The following subsections provide additional information about PD detection, the energy harvesting feature, and power consumption.

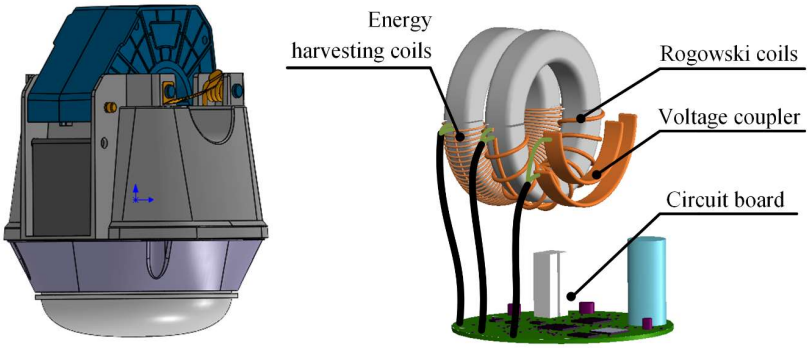

Figure 5-2 Structure and components of the partial discharge monitor.

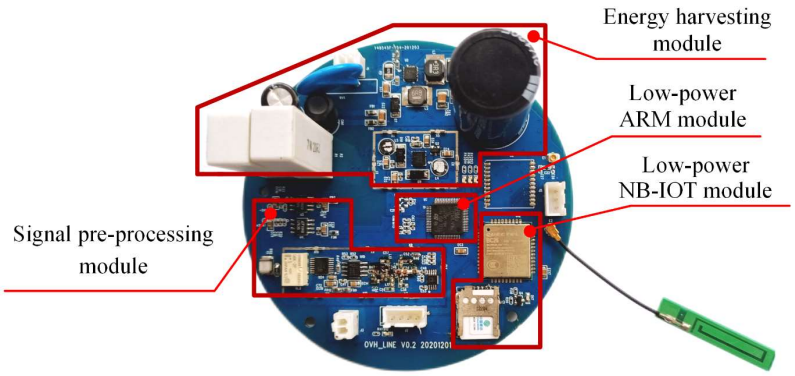

Figure 5-3 Circuit board of the PD monitor.

1）PD Detection

HFCT with a passband frequency from 0.2 to 50 MHz is used to detect PD signals due to their high sensitivity and non-invasive placement superiority. The captured PD signal is preprocessed, as shown in Figure 5-4. First, a band-pass filter and a low-noise amplifier are used to amplify the PD signal. Second, a peak-holding circuit is used to down-convert the high-frequency PD signal to generate a demodulated signal that the low-cost and low-power STM32L476RG ARM can sample with a reduced sampling rate of 5 Msps. Finally, the information about the peak amplitude and the time-of-arrival of the PD pulse are extracted via a simple thresholding method. The threshold is $(m+3\sigma)$, where m and σ are the sampled signal's mean and standard deviation, respectively. The above parameters are computed from

a 50 s long sliding window signal. The estimated time-of-arrival is eventually converted into a phase value, providing information about the exact location of the pulse within a given period of the sinusoidal power signal; the voltage coupler detects this latter signal.

In addition, high-frequency relays (Q-FTR-B3SA003Z, Fujitsu) and gas discharge tubes are placed between the HFCT or the voltage coupler and the signal preprocessing module to protect the circuit board from power system transients. When PD detection is not enabled, the relays short the outputs of the HFCT and voltage coupler.

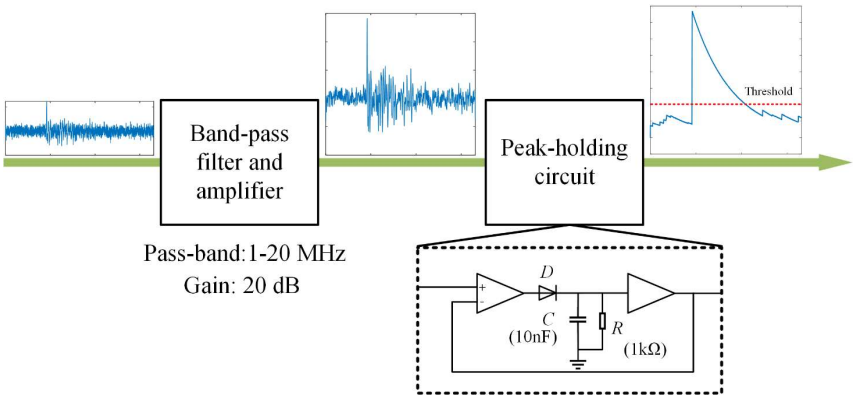

Figure 5-4 Signal preprocessing of the partial discharge signal.

2）Energy Harvesting

This subsection describes the energy-harvesting module, including inductive coils to collect power from CC lines and an energy-harvesting circuit to convert and manage the power. The coils consist of 750-turn coils and a high-permeability permalloy core. The energy-harvesting circuit includes four serial functions: overvoltage protection, rectification, excess energy release, and energy management, as shown in Figure 5-5 and briefly described below. First, overvoltage protection — implemented with an arrester, gas discharge tube, an inductance, and a stabilivolt — is enabled to protect the circuit board from power system transients. Second, the alternating voltage is rectified into direct voltage. Third, an energy release circuit is developed to limit the voltage within 10 V to protect the subsequent circuit, especially when the load current in CC lines is several hundred amperes. When the voltage exceeds 10 V, the metal-oxide semi-conductor field effect transistor M (SQD50N10-8m9L, Vishay Inter technology) is turned on, and the resistance r consumes the excess energy. Finally, the harvested energy is distributed to the subsequent circuits or the 120 F supercapacitor (C_{super}) through an energy management chip (LTC3355, Analog Devices Inc.). The supercapacitor stores power energy and supplies the circuitry when the load current in the CC line is low. It is insufficient for charging the capacitor itself (i.e., this happens when the current is on the order of some Amperes).

3）Low-Power Manager

The measured power consumption of each module in the circuit board is listed in Table 5-1. The energy harvesting module, NB-IOT module, and ARM module with an analog-to-digital converter (ADC) consume very low power. In contrast, the ARM module with the ADC on and the signal processing module consume significantly higher power. A

low-power management strategy is developed to power the PD detector in low-current CC lines, as shown in Figure 5-6, and coded into the ARM module. The ADC and signal processing module are activated only if the voltage of the super-capacitor (Usupercap) exceeds 3.3 V and the interval between two measurements exceeds the set time delay (5 min). The low-power working procedure can activate the developed circuit board under a current as low as 4 A.

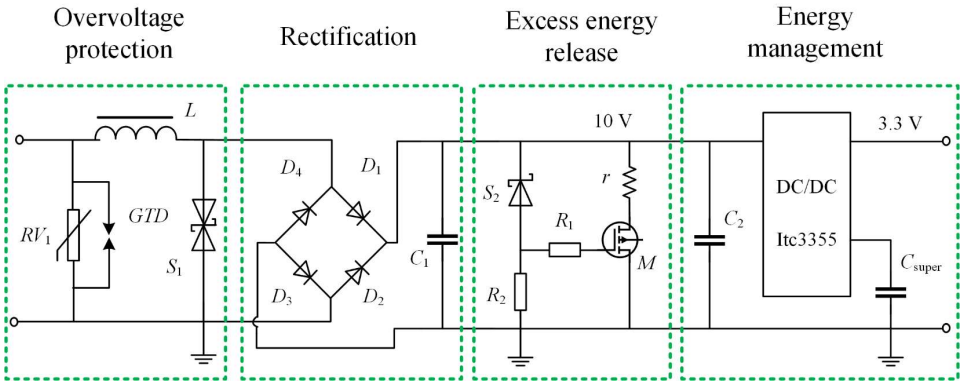

Figure 5-5 Equivalent circuit diagram of the energy harvesting module.

Table 5-1 Measured power consumption of each module in the circuit board

Module name	Energy harvesting	An ARM with ADC on	ARM with ADC off
Power (mW)	9	78	14
Module name	NB-IOT	Signal preprocessing	
Power (mW)	5	232	

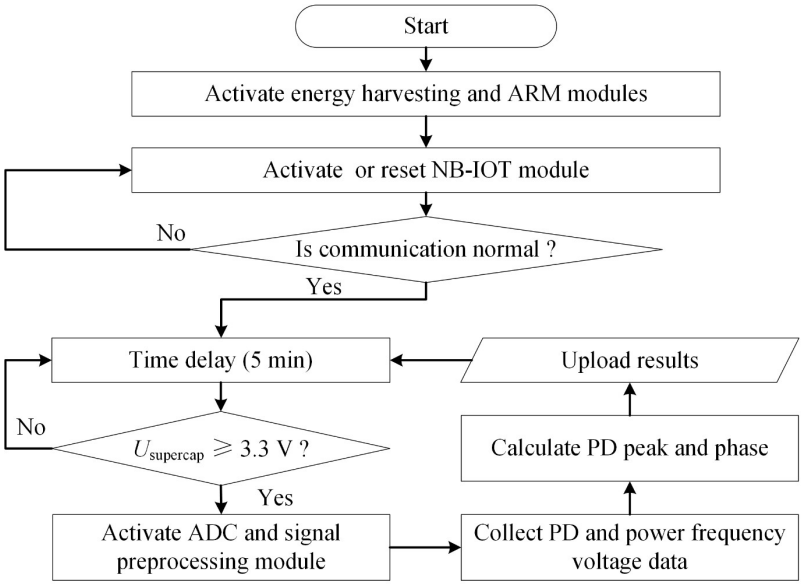

Figure 5-6 Low-power working procedure of the partial discharge (PD) detector.

5.1.3 Networking and Diagnosis via Low-Power Narrowband Internet of Things Technology

This subsection first discusses the overall design of an IoT-based PD sensing network from the perspective of four layers, i.e., the sensing layer, network layer, data layer, and application layer. Then, the benefits of applying the low power wide area (LPWA) communication technique (i.e., NB-IoT) to distributed PD monitoring are described.

1）Design of IoT-Based PD Sensing Network

The Internet of Things (IoT) technology offers a promising solution by enabling the integration of various components and layers within a PD sensing network. A well-designed IoT-based PD sensing network consists of four layers: the sensing layer, network layer, data layer, and application layer [150]. This work will provide a detailed discussion of each layer's design considerations, focusing on scalability and accessibility for an integrated monitoring system.

Sensing Layer: The sensing layer captures PD signals accurately and reliably. It comprises sensors strategically placed in critical areas of the MV overhead distribution network. When designing the sensing layer, the following factors should be considered:

(1) Sensor Selection: Choose sensors suitable for PD detection, such as non-invasive high-frequency current transformers. Consider factors like sensitivity, frequency range, compatibility, and environmental conditions.

(2) Sensor Placement: Identify optimal locations for sensor placement based on the equipment's characteristics and PD occurrence probabilities. Overhead lines, breakers, transformers, and other vulnerable points should be covered.

(3) Calibration and Maintenance: Regular calibration and maintenance routines are essential to ensure accurate and consistent sensor performance. Develop procedures to calibrate sensors and replace faulty ones periodically.

Network Layer: The network layer ensures smooth and reliable communication between the sensing devices and the central monitoring system. Critical considerations for the network layer include:

(1) Communication Protocols: Select appropriate wireless communication protocols, such as LPWA used in this work, based on factors like range, power consumption, data rate, and network coverage.

(2) Connectivity and Scalability: Design a network architecture that allows for easy deployment and expansion of sensing devices. Consider the scalability requirements of the power system, accommodating an increasing number of sensors when necessary.

(3) Reliability and Redundancy: Implement redundancy in the network to ensure continuous data transmission even in device failure or network disruptions. Redundant communication paths, backup power supplies, or mesh network topologies can enhance reliability.

(4) Quality of Service (QoS): Prioritize PD data transmission by defining QoS

parameters like latency, bandwidth, and packet loss. This ensures that critical PD information is delivered promptly and accurately.

Data Layer: The data layer focuses on efficiently processing, storing, and managing the collected PD data. Consider the following factors when designing the data layer:

(1) Data Acquisition and Pre-processing: Employ analog-to-digital converters (ADCs) to convert sensor signals into a digital format. Implement signal conditioning circuits to amplify weak PD signals and filter out noise.

(2) Data Storage and Management: Select appropriate data storage solutions, such as distributed databases or data lakes, to accommodate large volumes of PD data. Ensure data integrity, security, and scalability. Implement compression and deduplication techniques to optimize storage.

(3) Data Processing and Analytics: Utilize cloud-based analytics platforms or edge computing devices for PD data analysis. Develop predictive maintenance models for proactive decision-making.

(4) Data Visualization and Reporting: Design user-friendly visualization interfaces that provide real-time dashboards, graphs, and charts to interpret PD data effectively. Generate comprehensive reports and alerts to notify operators of critical events or deviations from normal behavior.

Application Layer: The application layer utilizes the processed PD data to support various power system monitoring and maintenance applications. Consider the following aspects in the application layer:

(1) Integration with Existing Systems: Integrate the IoT-based PD sensing network with existing Supervisory Control and Data Acquisition (SCADA) systems or other monitoring platforms. Combine PD data with other operational data to comprehensively understand the power system's health.

(2) Proactive Maintenance: Develop predictive maintenance models that utilize historical PD data to anticipate future PD events and generate proactive maintenance plans. Enable automatic fault detection and diagnosis to minimize downtime and optimize maintenance resources.

(3) Decision Support Systems: Design decision support systems that provide operators with actionable insights based on PD data analysis. Implement advanced alarm management techniques to prioritize critical events and facilitate prompt decision-making.

(4) Remote Access and Control: Ensure remote accessibility to the PD sensing network through secure connections. Enable remote monitoring, configuration, and control of the network and connected devices. Implement access control mechanisms to protect system integrity and privacy.

In summary, designing an IoT-based PD sensing network requires careful consideration of each layer: sensing layer, network layer, data layer, and application layer. By focusing on scalability and accessibility, such a network can provide an integrated monitoring system for efficient PD detection in overhead distribution networks. The design considerations

discussed in this subsection will help ensure accurate PD signal capture, reliable communication, efficient data processing, and effective decision support.

2）Data Communication Built on LPWA

To effectively monitor distributed PDs in overhead distribution networks, an IoT-based PD monitoring system is employed. In practical applications, this system requires a reliable low power wide area (LPWA) communication solution that meets specific requirements such as data rate, delay, mobility, and coverage. This subsection will discuss the importance of LPWA communication in IoT-based PD monitoring systems, considering the complex interference environment, the large number of sensor sites, and the wide distribution range. This work will explore NB-IoT as the LPWA technology for data communication.

Importance of LPWA Communication in IoT-based PD Monitoring Systems: In an IoT-based PD monitoring system, many sensors are deployed across a wide area to detect PD signals in real time or at short intervals. These sensors continually collect data and transmit it to a central monitoring system. LPWA communication provides several advantages for such a system, including wide coverage, licensed spectrum bands, low power consumption, etc.

Interference Mitigation: As mentioned earlier, interference is a common challenge in overhead distribution networks. The LPWA communication technology used should be capable of mitigating interference through frequency hopping or other interference avoidance mechanisms. NB-IoT is designed to operate effectively in the presence of interference, ensuring reliable communication.

Security*:* Since PD data is critical and sensitive, the LPWA communication should include robust security measures to protect against unauthorized access, data tampering, and eavesdropping. Secure authentication and encryption protocols should be implemented. NB-IoT incorporates security features to safeguard data integrity and confidentiality.

NB-IoT provides a reliable and efficient LPWA communication solution for IoT-based PD monitoring systems. Its wide coverage, low power consumption, low latency, and interference mitigation capabilities make it suitable for distributed PD monitoring on various apparatus in overhead distribution networks. By leveraging NB-IoT, companies can ensure the reliability and safety of their power distribution networks while optimizing operational efficiency and minimizing maintenance costs.

In summary, choosing NB-IoT for data communication in IoT-based PD monitoring systems brings numerous advantages, including extended battery life, reliable long-range coverage, low latency, mobility support, interference mitigation, and robust security measures. These characteristics make NB-IoT an ideal LPWA technology for effective and efficient PD monitoring in overhead distribution networks.

3）Online Partial Discharge Diagnosis Algorithm

On-line PD monitoring is crucial for identifying sudden and progressive insulation defects in the overhead distribution network. It plays a significant role in evaluating the insulation condition of power apparatuses in this line system. Magnitude, frequency, and phase-resolved statistical analysis of PD provide essential parameters to assess the severity of PD and identify fault patterns. Understanding the correlation between PD events and

phase voltage waveforms aids in recognizing PD patterns during comprehensive status diagnosis. However, this diagnostic process demands high computing power and memory capacity, leading to increased power consumption. Alternatively, a simplified PD assessment algorithm with minimal computing resources is developed. The algorithm is based on multimode data and multi-dimensional analysis, including Quantity Analysis, Parallel Analysis, Pattern Analysis, and Trend Analysis. These are explained in detail as follows (see Figure 5-7):

Quantity Analysis: Quantity Analysis diagnoses whether a PD occurs around a PD monitor by analyzing the pulse magnitudes of the detected PD signal. The PD magnitude P_i detected by the ith PD monitor is given by the mean value of the maximum pulse peaks of 50 power-frequency cycles. Once the PD magnitude of any PD monitor is more significant than 20 mV, an empirical value determined by multiple on-site experiments, A PD may occur. Thus, the subsequent analysis is triggered. Otherwise, the insulation condition of the overhead distribution network is considered normal. Quantity Analysis is performed at the start of the strategy to identify whether there may be a PD or not and at the end to recognize the danger level of the PD.

Parallel Analysis: Parallel Analysis diagnoses whether a PD occurs by analyzing the magnitude difference among all PD monitors. To characterize this difference, the deviation δ_{P_i} is defined as

$$\delta_{P_i} = \frac{(P_i - P_{\text{avg}})}{P_{\text{avg}}} \cdot 100\% \tag{5-1}$$

where P_{avg} is the mean of PD magnitudes of all PD monitors, a threshold criteria can be defined to identify if a PD may occur around the i^{th} PD monitor. The threshold can be set from 20% to 50%. The larger the threshold is, the smaller the area of the PD source is reduced, but the greater the probability of missing a PD is. Parallel Analysis is performed after the initial Quantity Analysis and before Pattern Analysis.

Pattern Analysis: Pattern Analysis diagnoses whether the collected pulses have phase–resolved distribution patterns. Since the PD activities are associated with the power-frequency voltage, and thus the PD pulses always occur around the specific phases of the power-frequency voltage. On the contrary, the impulse interferences (i.e., the switching noise from the power electronic devices) do not have such features. To recognize such features of the collected pulses, they must first be preprocessed. All pulses collected by each PD monitor in 50 power-frequency cycles are transformed into the PRPD spectrum. The phase axis is divided into 100 segmentations. The number of pulses in each phase segmentation is counted. The phase distribution patterns of the pulses are quantized via the standard deviation of the pulse numbers of the 100 segmentations, which is calculated as

$$\sigma_i = \sqrt{\frac{\sum_{j=1}^{100} \left(\frac{N_{i,j} - \bar{N}_i}{N_{i,\max}} \right)^2}{100}} \tag{5-2}$$

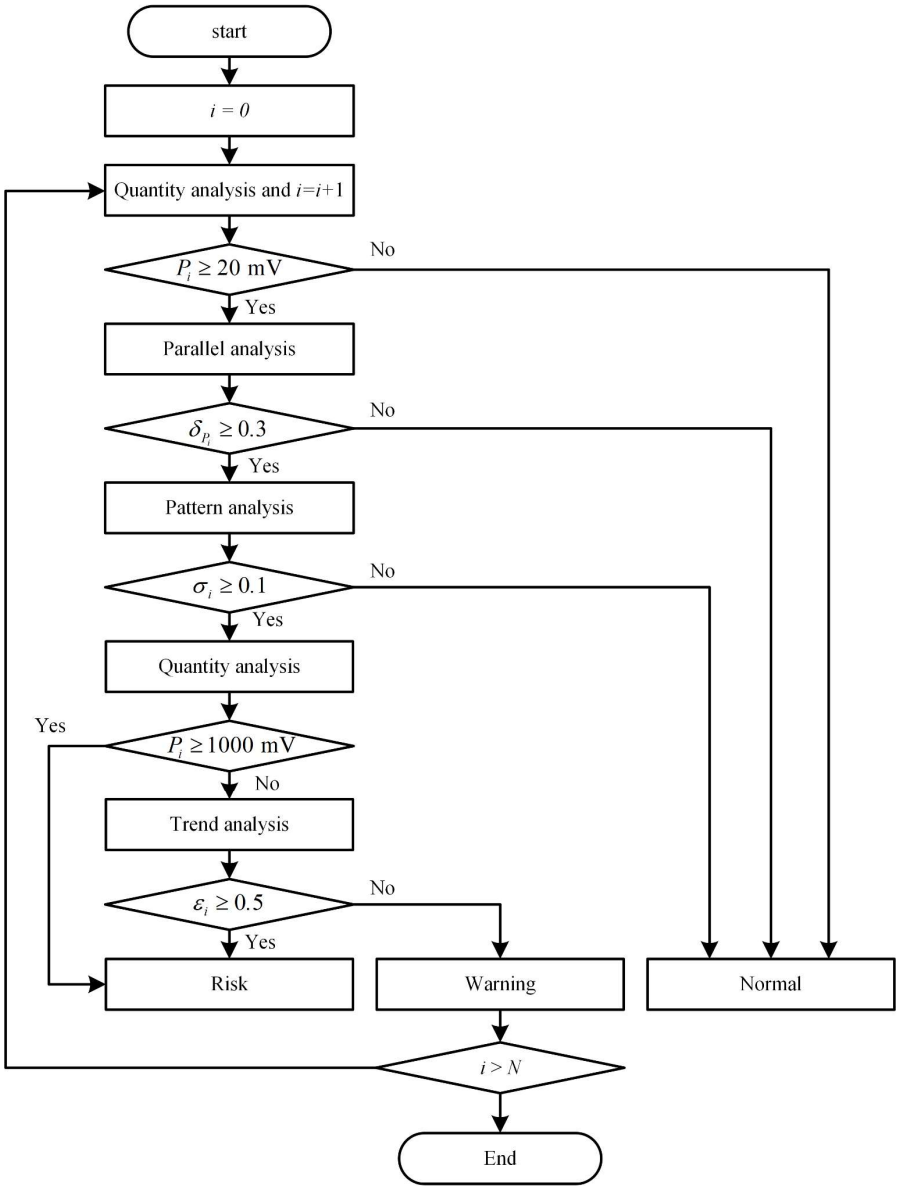

Figure 5-7 Flowchart of the online PD assessment algorithm.

where $N_{i,j}$ is the pulse number of the j^{th} segmentation of the PRPD spectrum obtained by the i^{th} PD monitor, $\bar{N}_i$ is the mean of the pulse numbers of all segmentations, and $N_{i,\max}$ is the maximum of the pulse numbers of the segmentations. If a PD source causes the pulses, the value of σ_i is significantly larger than 0, while if the pulses are caused by noise, the value of σ_i is close to zero. Therefore, a threshold criteria can be used to identify if the collected data includes PD pulses. The threshold value can be set from 0.05 to 0.2, an empirical range determined via the collected data from multiple real PDs. Pattern Analysis is performed after Parallel Analysis and before Trend Analysis.

Trend Analysis: Trend Analysis is performed when PD activities have been confirmed via Pattern Analysis. During Trend Analysis, there is a need to enhance the monitoring density and conduct intensive trend analysis over time. This trend analysis involves utilizing an indirectly derived metric that calculates the relative variation of amplitude information

over time, which is defined as

$$\varepsilon_i = \frac{(P_{i,t_1+\Delta t} - P_{i,t_1})}{P_{i,t_1}\Delta t} \cdot 100\% \tag{5-3}$$

where P_{i,t_1} and $P_{i,t_1+\Delta t}$ are the PD magnitudes of the i^{th} PD monitor at time t_1 and $t_1 + \Delta t$, respectively. The time interval Δt can be automatically adjusted based on the status results or manually set to commence at a specific start time. The trend analysis helps determine if the insulation condition is deteriorating gradually or if there is a sudden fault. If the variation exceeds 50%, the status is considered at a risk level.

Finally, it is essential to point out that the risk or warning PD diagnosis result of a PD monitor means that there is a PD source within a few kilometers of this PD monitor. The PD source's area can be reduced by comparing the PD magnitudes detected by multiple surrounding PD monitors.

5.1.4 Optimal Deployment of IoT-based PD Monitors

The deployment of sensors plays a vital role in achieving cost-effective PD evaluations of MV overhead distribution networks from the perspectives of application effectiveness and economic considerations. Strategic deployment ensures comprehensive coverage while considering network characteristics and optimizing the effectiveness of PD evaluation. Furthermore, efficient sensor deployment contributes to economic efficiency by minimizing resource allocation while maintaining high monitoring effectiveness. The sub-section presents a method to optimally place a given number of IoT-based monitors to maximize the network observability.

1）PD Observability Analysis

In an overhead distribution network, PDs experience attenuations along the line and partial reflections at various points, i.e., alongside the tower, as discussed in Chapter 2. As a result, the energy of PD signals diminishes rapidly as they pass through overhead lines and alongside towers. According to the discussions in Chapter 2.3.3, the refraction coefficients of the towers are different, depending on their type. When there are multiple towers or too long overhead lines between the PD sources and the PD monitor, the energy of the PD signal may become insufficient for detection by the monitor. Therefore, when placing distributed PD monitors, it is crucial to consider the total attenuation coefficient between each line and the PD monitors. In this work, the term "observable" describes a tower that a monitor can detect if a fault occurs in the tower or its adjacent line segments. It is essential to point out that since the distance between two towers in distribution networks is very short, about 50 to 100 meters, which only leads to negligible attenuation, the observability of a tower is almost equivalent to that of its adjacent line segments. Therefore, we only consider the observability of a tower to simplify the subsequent mathematical analysis. In addition, we assume that PD monitors are constantly mounted on the towers for the same purpose.

This detection considers the attenuation coefficient between towers and PD monitors. On the other hand, a tower is considered "unobservable" if the PD on the tower cannot be

detected in that particular segment. The minimum refraction coefficient required for observability can be determined by considering the sensitivity of the PD monitor. This analysis of determining observable and unobservable towers in a radial distribution network is called PD observability analysis in the following discussions.

An attenuation coefficient matrix is defined below for a given network with N towers.

$$\boldsymbol{A}_{N\times N}=\begin{bmatrix} a_{1,1} & \cdots & a_{1,N} \\ \vdots & \ddots & \vdots \\ a_{N,1} & \cdots & a_{N,N} \end{bmatrix} \tag{5-4}$$

where $a_{i,j}$ denotes the total attenuation coefficient for a PD signal to travel from tower "i" to tower "j." $a_{i,j}$ can be defined as:

$$a_{i,j}=a_{\text{line},0}\prod_{m\epsilon\{i\to j\}}\left(a_{\text{line},0}\cdot a_{\text{tower},m}\right) \tag{5-5}$$

where $a_{\text{line},0}$ denotes the attenuation coefficient of the line segment between two adjacent towers, and $a_{\text{tower},m}$ denotes the refraction coefficient of tower "m" in the shortest path from tower "i" to tower "j". The refraction coefficients vector of all the network towers can be defined as $\boldsymbol{A}_{\text{tower},N\times 1}$. $\boldsymbol{A}_{\text{tower},N\times 1}$ and $a_{\text{line},0}$ can be obtained via the physical parameters of the networks according to the models developed in Chapter 2.

Then, a PD observability matrix $\boldsymbol{B}_{N\times N}$ can be defined as:

$$\boldsymbol{B}_{N\times N}=\begin{bmatrix} b_{1,1} & \cdots & b_{1,N} \\ \vdots & \ddots & \vdots \\ b_{N,1} & \cdots & b_{N,N} \end{bmatrix} \tag{5-6}$$

where the non-zero value of $b_{i,j}$ indicates that if the PD monitor is installed at node "i", it can observe PDs within line "j". Otherwise, $b_{i,j}$ is equal to zero. $b_{i,j}$ can be calculated as:

$$b_{i,j}=\begin{cases} 1 & a_{i,j}\geq a_0 \\ 0 & a_{i,j}<a_0 \end{cases} \tag{5-7}$$

where a_0 is a threshold value that depends on the monitor's required sensitivity to detect the PD.

If a binary vector, $\boldsymbol{Z}_N=[z_1,z_2,\dots,z_N]^{\mathrm{T}}$, represents the existence of PD monitors at the corresponding towers. The following observability O_n of tower "n" can be calculated as:

$$O_n=\begin{cases} 1 & \boldsymbol{B}^n_{1\times N}\cdot\boldsymbol{Z}_N>0 \\ 0 & \boldsymbol{B}^n_{1\times N}\cdot\boldsymbol{Z}_N=0 \end{cases} \tag{5-8}$$

where $\boldsymbol{B}^n_{1\times N}=[b_{n,1},b_{n,2},\dots,b_{n,N}]$ is the nth row vector of $\boldsymbol{B}_{N\times N}$. $O_n=0$ denotes that tower "n" is "unobservable", while $O_n=1$ denotes that tower "n" is "observable".

2）Optimization Model for PD Monitors Deployment

In the above discussion, the key is to optimally place a given number of TW detectors to maximize the network observability. The variable is the vector $\boldsymbol{Z}_N$, while the objective function can be defined as:

$$OF\left(\boldsymbol{A}_{N\times N},\boldsymbol{A}_{\text{tower},N\times 1},a_{\text{line},0},a_0,\boldsymbol{Z}_N\right)=\frac{\sum_{n=1}^{N}O_n}{N}\cdot 100\% \tag{5-9}$$

where the output of the OF is equal to the observable ratio of the network, this task is a

typical binary optimization problem.

Binary particle swarm optimization [151] and genetic algorithm [152] are well-known heuristic optimization techniques for handling binary problems. Both binary particle swarm optimization and genetic algorithm are computational optimization methods that iteratively enhance candidate solutions to find the optimal solution. Binary particle swarm optimization is particularly effective for complex optimization problems involving high dimensions, non-convexity, and non-continuity, as it can identify solutions that are close to optimal. Consequently, the proposed optimization problem is solved using the binary particle swarm optimization algorithm. More mathematical details of the algorithm can be found in [153].

The placement of PD monitors involves a constrained optimization problem where the goal is to maximize the observability of towers. However, the solution must also consider the constraint of limited observer resources to ensure economic feasibility. There are various approaches to address constrained binary particle swarm optimization problems. One commonly used technique is the penalty function method, where a penalty term is incorporated into the fitness function to penalize constraint violations [16]. The penalty function, denoted as $PF(\boldsymbol{Z}_N)$, is defined as follows:

$$PF(\boldsymbol{Z}_N)\begin{cases}1 & \sum_{n=1}^{N} z_n = P \\ \left(\sum_{n=1}^{N} z_n - P\right)^2 & \sum_{n=1}^{N} z_n = P\end{cases} \tag{5-10}$$

where P is the desired number of PD monitors. Based on the objective and the penalty functions, the optimization model for maximizing the observable ratio with a given number of available PD monitors is as follows:

$$\begin{aligned}\min CF = &\left(1 - OF\left(\boldsymbol{A}_{N\times N}, \boldsymbol{A}_{\text{tower},N\times 1}, a_{\text{line},0}, a_0, \boldsymbol{Z}_N\right)\right) \\ &+ w \cdot PF(\boldsymbol{Z}_N)\end{aligned} \tag{5-11}$$

where w is the weight of the penalty function.

3）Simulation Results and Analysis

To verify the feasibility, effectiveness, and robustness of the proposed method, a feeder in a real 10-kV radial distribution network, as shown in Figure 5-8, is employed in this analysis. The total number of towers within this network is 101. All overhead line segments between any two adjacent towers are considered to have the same length (i.e., 100 m) and characteristic impedance. According to the results in Chapter 2, the attenuation coefficient of each line segment is set as 0.95; the refraction coefficient of supporting towers is set as 0.9; the refraction coefficient of transformer towers is set as 0.25; the refraction coefficient of branch towers is set as $0.95 \times 2/(N_{\text{branch}} + 2)$, where N_{branch} is the number of branches. The threshold value is set as 0.1, considering the monitor required sensitivity of the developed monitor to detect the PD.

Figure 5-9 collects the results of the optimum placements of PD monitors with different numbers via the binary particle swarm optimization algorithm. It can be observed that: i)

when the number of PD monitors is relatively small, PD monitors should be placed close to the branch towers with more branches, as shown in Figure 5-9(a)-(c); (ii) the total observability ratio increases as the number of PD monitors increases as in Figure 5-9(d)-(h). However, the average observability ratio of each PD monitor decreases as the number increases, as shown in Figure 5-10. This means that the cost performance of PD monitors decreases as the number increases.

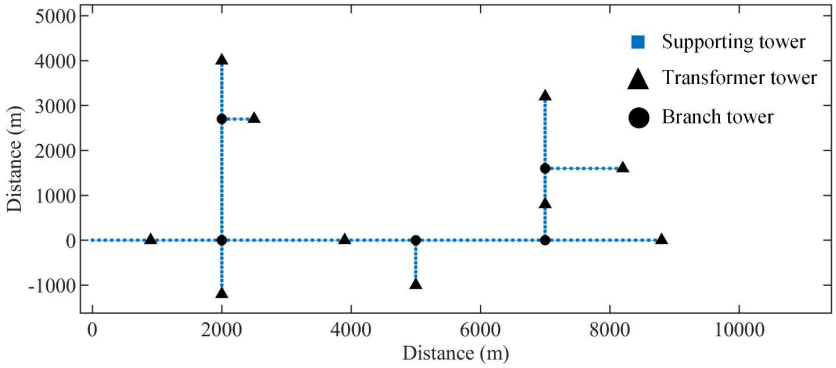

Figure 5-8 Schematic diagram of alongside towers of a feeder in a 10-kV overhead distribution network.

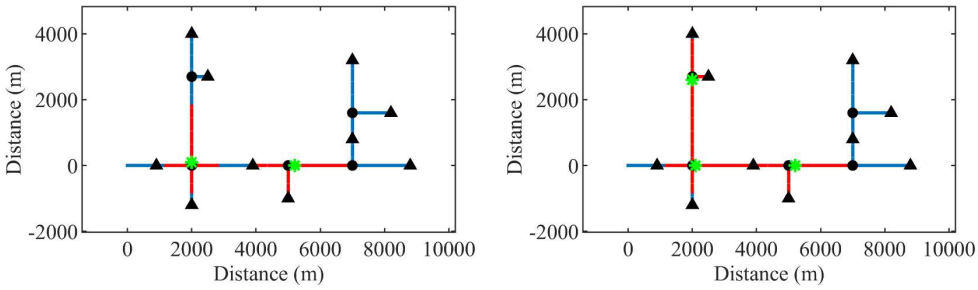

(a) P=2 (b) P=3

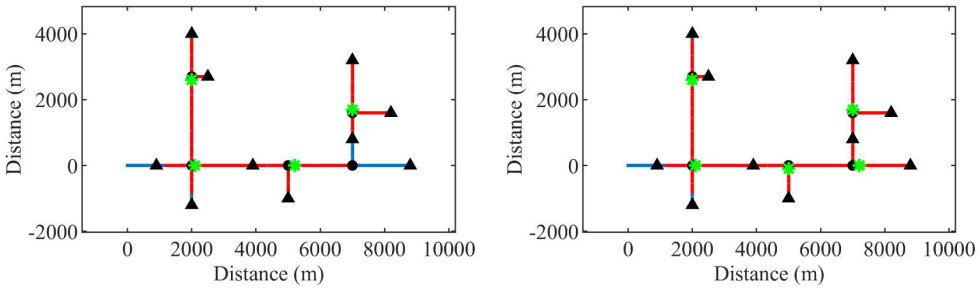

(a) P=4 (b) P=5

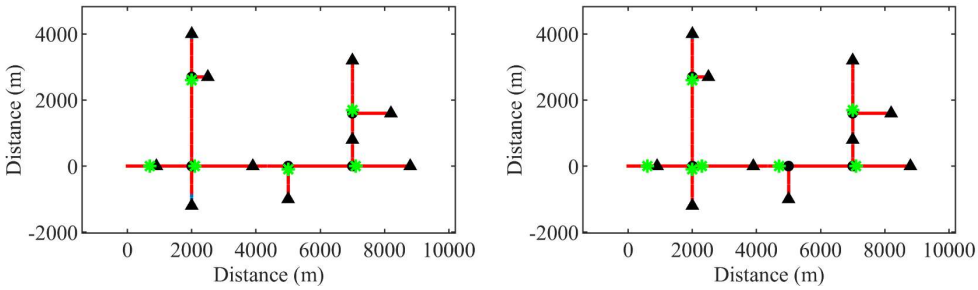

(a) P=6 (b) P=7

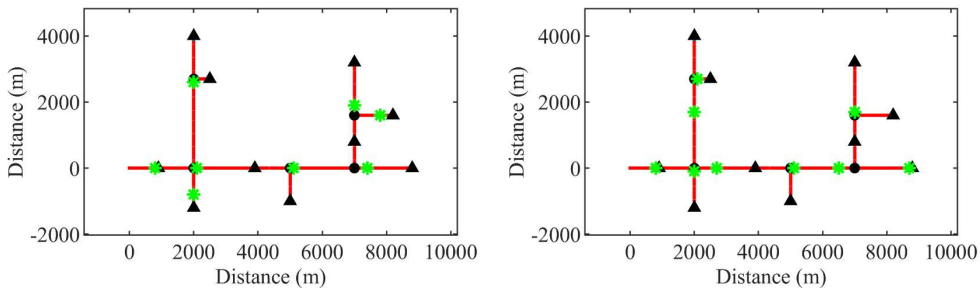

(a) P=8 (b) P=9

Figure 5-9 The optimum placement of PD monitors for a_0=0.1. The red lines are observable. The PD monitors placed at the towers are shown in green stars.

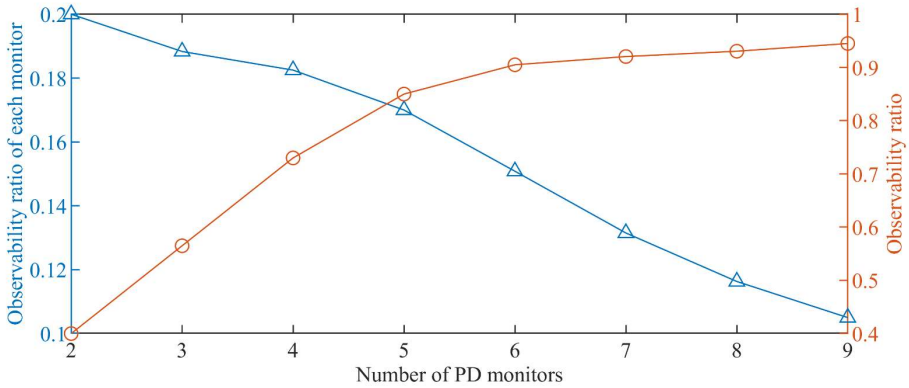

Figure 5-10 Total and average observability ratios of PD monitors with different numbers.

5.1.5 Application Cases

1）Case I: Leaning Tree

An on-site validation experiment was conducted on a PD-affected 10-kV overhead CC line, as shown in Figure 5-11. A leaning tree caused the PD defect, and the insulation of the CC line was visibly damaged, but no relay protection action was recorded. Since simulation research and practice experiments in the last works showed that the signal amplitude detected on the non-faulty phase is close to half of that in the adjacent faulty phase due to their coupling characteristics, a PD detector was mounted on the middle phase of the CC line at a distance of 1,095 m from the PD source. The load current on the CC line was 7.4 A, and the PD detector was successfully powered.

Figure 5-12 collects information about the amplitude and the position of the recorded PD events, which occur in possibly different locations within the period of the sinusoidal power source. Specifically, the solid black signals in the Figure show the wrapped sinusoidal power signal as a function of the phase in the x-axis (i.e., from 0 to 360 degrees). The blue dots, instead, represent the cloud of points associated with the PD events. Each dot is placed in a (x, y) position where x is the phase location and y is the pulse amplitude. The two panels in the Figure correspond to the situation occurring during the PD defect (see the left panel) and after maintenance and replacement of the PD-affected line (see the right panel). Figure 5-12(a) reveals significant PD activities, which disappeared in Figure 5-12(b).

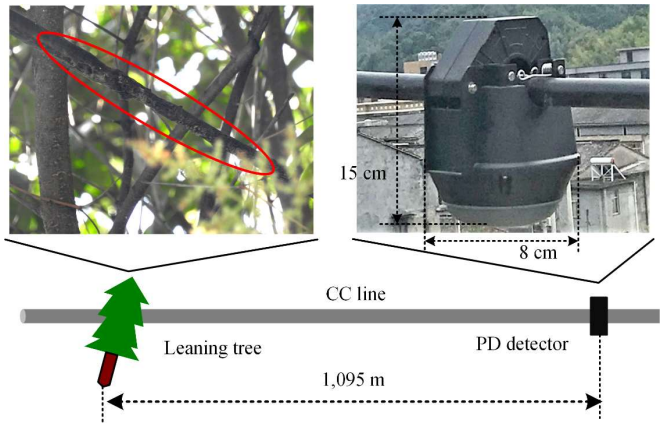

Figure 5-11 Case I: On-site partial discharge (PD) monitoring of a 10-kV covered conductor (CC) line affected by a leaning tree.

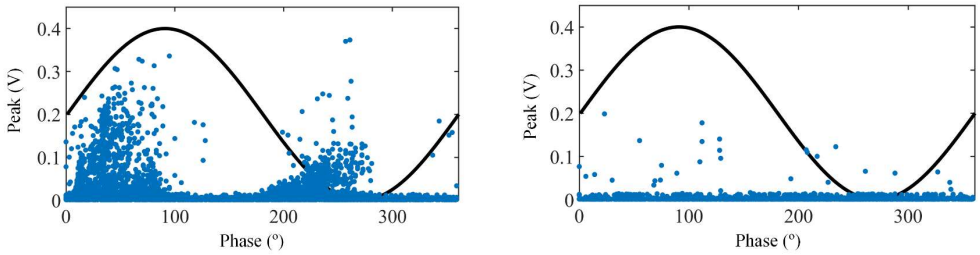

Figure 5-12 Case I: Partial discharge (PD) events before (a) and after (b) replacement of the PD-affected covered conductor line.

2）Case 2: PD Caused by a CC Line Slipping from an Insulator

Dozens of developed PD detectors were deployed in a rural 10-kV overhead CC line distribution network at intervals of about three kilometers. The intervals depend on the high-frequency attenuation characteristics of the CC line and were determined concerning the simulation and experiment results provided in the last works, respectively. After a storm, one of the detectors started to detect significant PD activities, as shown in Figure 5-13. The output of the online PD diagnosis algorithm is a *warning*.

This information was fruitfully used by the developed PD location system in Chapter 5.2 to localize precisely the damaged point, revealing that the PD source was about 675 meters away from the detector and was caused by a CC line slipping from an insulator, as shown in Figure 5-13(c). After the alert, the staff repaired the CC line, and the PD signals disappeared, confirming that the CC line slipping from the insulator had caused the PD.

5.2 Portable Live-line Partial Discharge Detection and Location System and Applications

5.2.1 Overview of the System

This subsection describes developing an online PD location system based on the proposed method. The main components of the system and one of its typical application scenarios are illustrated in Figure 5-14.

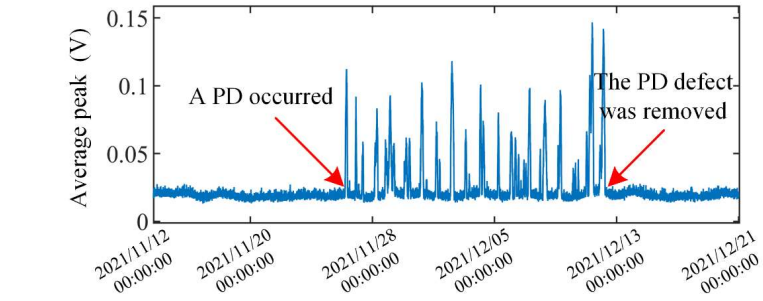

(a)

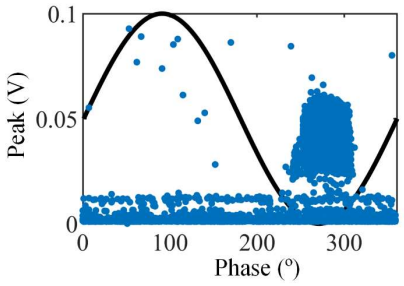

(b) (c)

Figure 5-13 Case II: Historical partial discharge (PD) data (a), phase-resolved PD spectrum (b), and picture (c) of the slipping CC line.

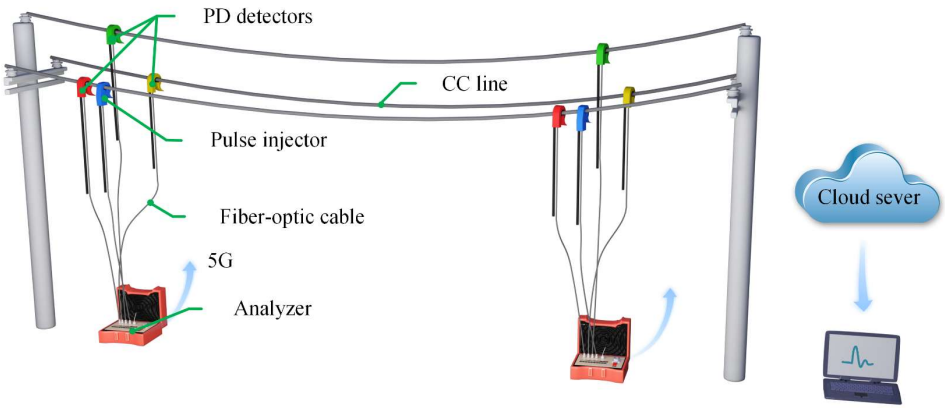

Figure 5-14 Simplified representation of a typical online PD location system application scenario. It comprises two testing units (A and B) and a 5G-based cloud server. Each testing unit contains three PD detectors, a pulse injector, and an analyzer interconnected via fiber-optic cables.

The key part of this system is a cloud server that serves as a centralized hub for data collection, processing, and analysis. The cloud server is connected to two portable testing units mounted on each side of a target line segment or a network. These testing units are designed to be non-invasive, allowing for safe and convenient installation.

Each testing unit comprises three PD detectors, a pulse injector, and an analyzer. The PD detectors are crucial in capturing and analyzing PD signals emitted by insulation defects or breakdowns in the overhead line. With three detectors in each unit, the system ensures comprehensive coverage and accurate detection of PD events. These detectors are

synchronized using the pulse injector, facilitating coordinated testing between the double-sided units.

To ensure safe and reliable operation, all components of the PD location system are interconnected using fiber-optic cables. These cables facilitate the transmission of PD data and provide essential isolation from high voltages.

5.2.2 Non-invasive Partial Discharge Detector

A high-frequency current transformer (HFCT) is used as the sensor in the PD detectors because of its high sensitivity, wide frequency band, and non-invasive installability. In an online testing situation, all measuring instruments must be kept at a sufficient insulation distance from the high-voltage CC lines [149]. This means that conventional HFCT that uses coaxial cable to transmit PD signals must have a specific minimum inner diameter, which hinders their practical installation. To solve this problem, an improved PD detector is developed. The detector uses fiber-optic cables to transmit PD signals. This PD detector consists of a modified HFCT, an instrumentation amplifier, a battery, and an electrical-optical converter, as shown in Figure 5-15. The modified HFCT consists of an incomplete circular ferrite core with a 90-degree gap and 15-turn coils. The incomplete ferrite core aims to avoid magnetic saturation caused by the power current in CC lines. The frequency passband of the instrumentation amplifier is from 0.1 MHz to 82 MHz. The electrical-optical converter (HFBR1412, BROADCOM), which has good linearity and a wide frequency range from DC to 125MHz, keeps reliable electrical isolation between the analyzer and CC lines. The detection sensitivity of the PD detector is approximately 5.6 mV/mA over a dynamic range of −204 to 206 mA, and its −6 dB frequency bandwidth is about 0.2 MHz-50 MHz.

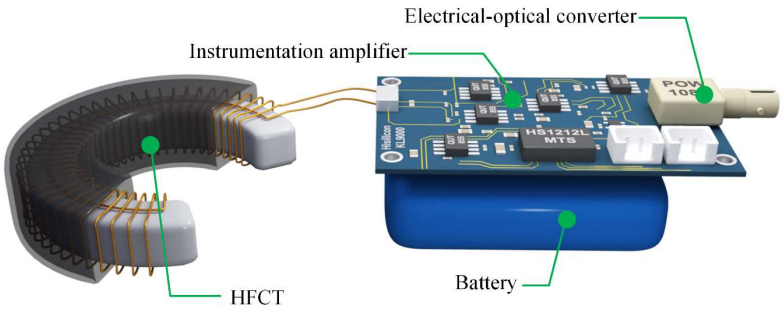

Figure 5-15 Internal structure of a PD detector.

5.2.3 Non-invasive Pulse Injector

Figure 5-16 depicts the internal structure of a pulse injector, showing its pulse-injection coils, an optical-electrical converter (HFBR2416, BROADCOM), a battery, and a simplified high-amplitude pulse generator. Specifically, the mutual inductance between the pulse-injection coils and the CC line is used to couple the high-amplitude pulses produced by the pulse generator into the CC line. An amorphous magnetic core with a high magnetic permittivity of 5000 is used in the pulse-injection coils to increase the mutual inductance. A small gap in the core is also needed to avoid magnetic saturation caused by the power current.

The DE475-102N21A (IXYS) model of the RF power metal-oxide-semiconductor field-effect transistor, G, is selected; it has a fast switching speed of 200V/ns and drain-source breakdown voltage of 1000V. The equivalent circuit of a simplified pulse generator is depicted in Figure 5-17. Here, we briefly describe how a high-amplitude pulse is injected into a CC line. First, G is opened, and the 1,000-V DC supply charges the capacitor C in the presence of the current-limiting resistance R. Next, G is closed. As a result, a high-amplitude pulse is produced on the coils and partly coupled into the CC line via the mutual inductance M0 (formed between the pulse-injection coils and the CC line). Figure 5-18 depicts the voltage waveform of a pulse injected into a 3-m CC line. It can be seen that a high-amplitude pulse, with a voltage peak of 177.3 V, a rising time of 12 ns, and a 50%-peak pulse width of 402 ns, was successfully injected into the CC line. The fast-rising edge of the injected pulse enables an accurate synchronization. The injected pulse's slow-falling edge allows it to travel a long distance while maintaining a high pulse amplitude.

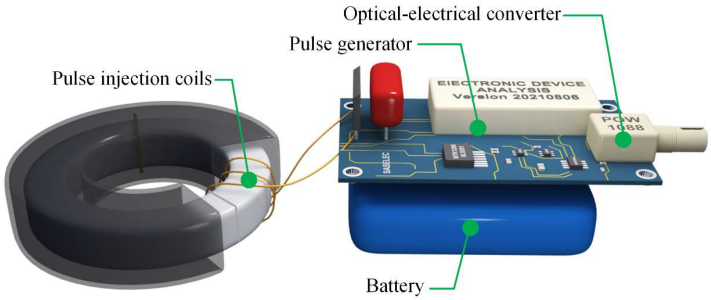

Figure 5-16 Internal structure of a pulse injector.

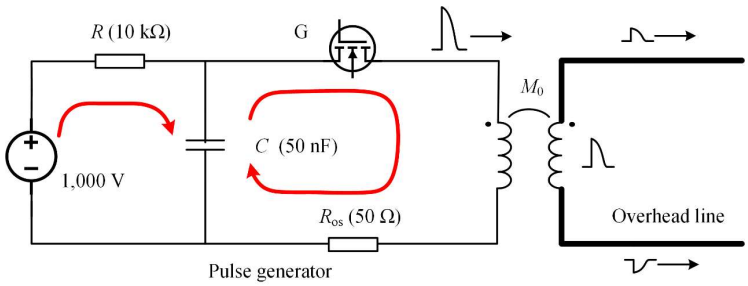

Figure 5-17 Equivalent pulse generator and pulse injection coil circuit.

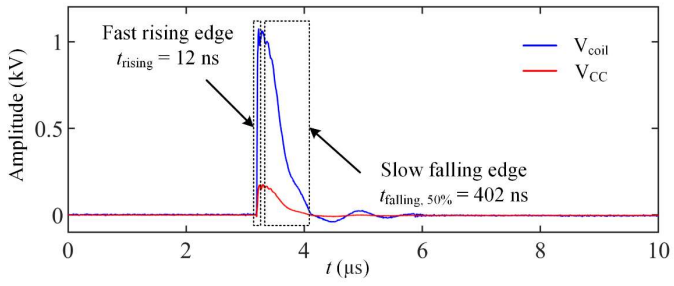

Figure 5-18 Voltage waveforms of the injected pulses on the pulse-injection coils (blue line) and the CC line (red line). This test was conducted on a 3-m CC line, the ends of which were each connected to a separate 300-Ω resistor to provide a model bilateral load on the CC line.

5.2.4 Analyzer

The analyzer consists of four parts: a measurement module, a central processing unit module, a 5G communication module (5G RG200U-CN, QUECTEL), and a commercial GPS module (UM220-III, UNICORECOMM), as shown in Figure 5-19. The measurement module has three optical-electrical converters for PD detection, an electrical-optical converter for pulse injection, and a three-channel analog-to-digital converter (ADC). This is a parallel 12-bit ADC with a sampling rate of 125 MS/s. Time-based errors between the ADCs in the double-sided analyzers can deviate their sampling rate slightly from 125MS/s. The errors depend on the frequency accuracy of the crystal oscillators and gradually accumulate as sampling time increases, which can lead to non-negligible PD location errors. Thus, the conventional voltage-controlled crystal oscillator in the commercial ADC is replaced by the constant temperature crystal oscillator (AOCJY7TQ, ABRACON) in the developed analyzers for PD location application. AOCJY7TQ has less than 0.05 ppm frequency error in the temperature range from -40℃ to 70℃. In other words, time base errors between the two ADCs can be less than 5ns while the sampling time is up to 120ms.

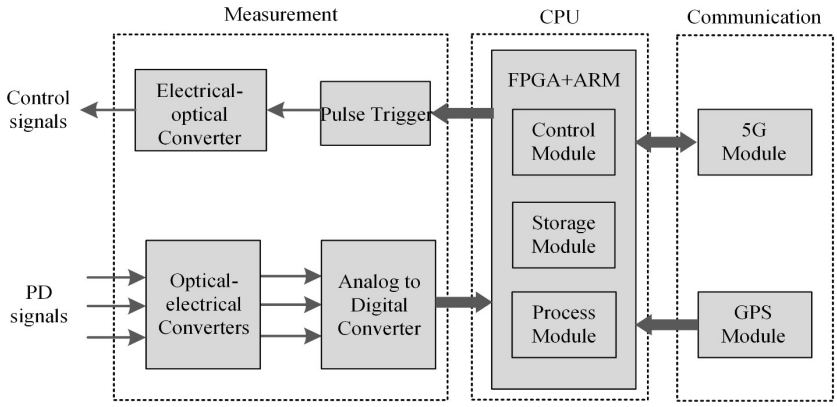

Figure 5-19 Internal components of the analyzer.

5.2.5 Application Cases

1）Case I: PD Caused by a Leaning Tree

On-site testing was conducted on a 2125-m long and approximately 12-m high 10-kV CC line in a town in Jiangsu province, China. The installed test system is shown in Figure 5-20. The length of the CC line was calculated as the sum of the straight-line distances between all towers in the range of the CC line. A PD testing unit was mounted at each end of the CC line. The PD detectors and the pulse injectors were safely and conveniently installed using long insulating rods. The injected pulses, the acquired original signals, the processed signals, and the PD location results are all displayed in Figure 5-21 and are discussed below.

The injected pulses recorded by the testing units are shown in Figure 5-21(a) and (b); it can be seen that a pulse traveled from Side A to Side B in 7.864 μs, which equates to a pulse propagation velocity of 270.2 m/μs. As shown in Figure 5-21(c)-(h), the original signals were acquired by all of the PD detectors on both sides. The original signals contained representative CNIs and INIs that obscured sound PD pulses. These original signals were

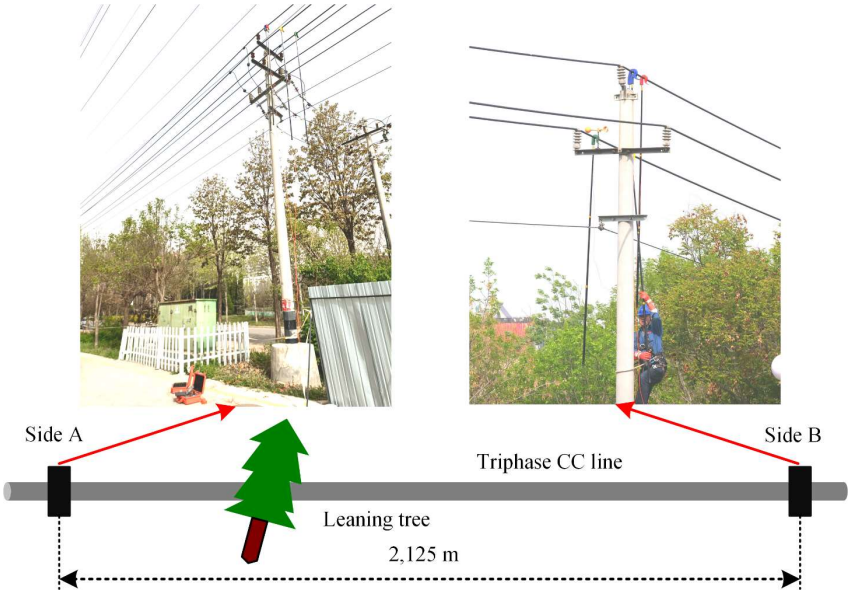

Figure 5-20 Installation of the online PD system on the double sides of a 2125-m CC line. The red, green, and yellow PD detectors are mounted on Phase 1, Phase 2, and Phase 3 of the line, respectively, and the blue PD injector is mounted on Phase 1.

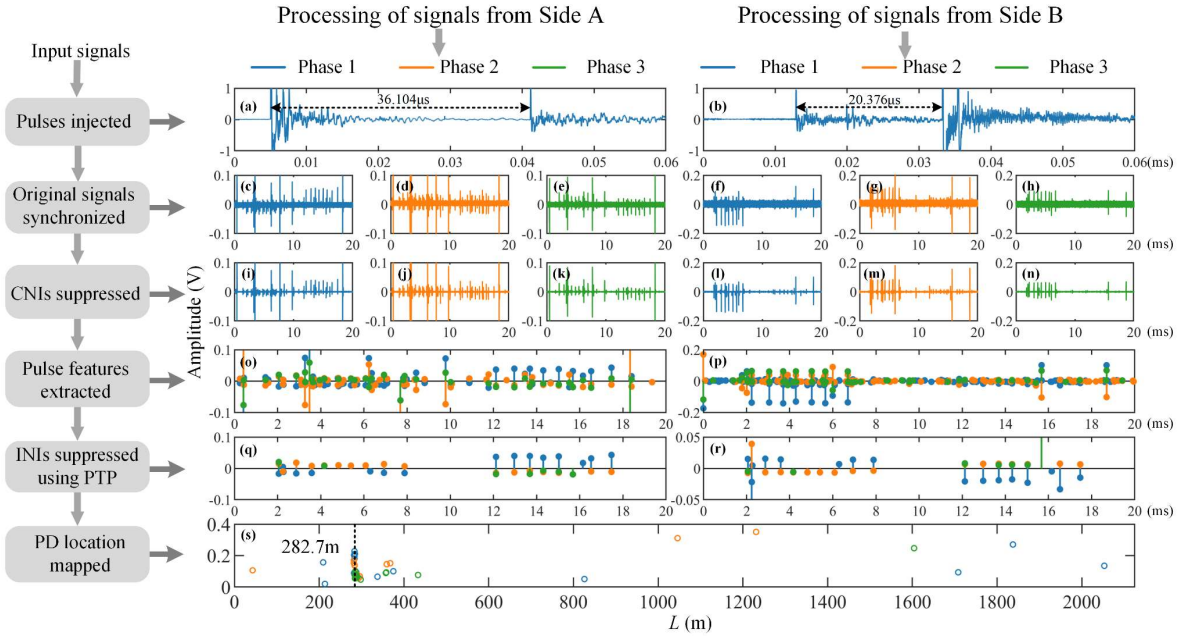

Figure 5-21 Signal processing and location result of the PD measurement on the 2125-m three-phase overhead CC line

de-noised using the DWT, which gave the de-noised signals shown in Figure 5-21(i)-(n). It can be seen that the CNIs were suppressed, such that some pulses with magnitudes less than the CNIs were revealed, as in the rear half of the waveform in Figure 5-21(l). Next, the pulses' TOAs, peaks, and polarities were extracted, as shown in Figure 5-21(o) and (p). Then, the PTP criterion was applied to all extracted pulses. It can be seen that most of the INIs were removed, though their amplitudes were greater than those of the PD pulses (Figure 5-21 (q) and (r)). The remaining pulses had power-frequency correlation patterns that were

typical of PDs. Moreover, as the peaks of the pulses in Phase 1 were higher than those of the pulses in the other two phases, and the pulse polarities of Phase 1 were opposite to those of the different two phases, the PDs were quickly identified as being in Phase 1. Finally, the location map was constructed, as shown in Figure 5-21(s), which indicates that the PD source was located 282.7 m from Side A. To further identify defect types, a commercial ultrasonic PD-detection camera (NL100) was used to determine the exact position of the defect from the location result. This revealed that the PDs were produced by a tree leaning on the CC line 289.6 m from Side A; the ultrasonic imaging result and a picture of part of the tree leaning on the line are shown in Figure 5-22. The location error was calculated to be 6.9 m (0.32% of the length of the CC line). Accordingly, the staff trimmed the tree and conducted a second PD test on the CC line. No PD signals were found, thereby confirming that the tree had been the cause of the PDs. The entire testing process—including the installation of testing units, signal collection, and data analysis—was completed within 15 min, a significantly shorter period than that required for conventional vision and ultrasonic inspections (~60 min), as shown in Table 5-2. Moreover, it is essential to point out that the coverage area of the proposed tool is significantly larger than that of the conventional ultrasonic device.

In summary, the experiment validates the proposed double-sided PD location technique's high accuracy and the developed tool's higher efficiency than the state-of-the-art ultrasonic-based solution.

Figure 5-22 Ultrasonic imaging captured using a commercial ultrasonic camera and an inset showing a picture of the tree leaning on the CC line.

Table 5-2 Comparison of coverage area and measurement time between the classical ultrasonic camera and the proposed system

Tools	Coverage area	Total measurement time
The proposed system	> 2000 m	< 15 min
The state-of-the-art ultrasonic camera (NL100)	< 30 m	> 60 min

2）Case II: Insulator with Cracks

An on-site PD measurement experiment was conducted on a 987-m overhead CC line. The developed PD location system was mounted on the double sides of the line. The PD location result is shown in Figure 5-23. It can be observed that a PD occurred at a distance of 471 m from the reference location (i.e., where one of the PD measurement units was). Meanwhile, the state-of-the-art ultrasonic camera (NL100) was used to assess the overhead line. Its measurement result on the tower located at the distance of 471 m and that of the proposed tool is collected in Table 5-3. It can be observed that the ultrasonic camera did not detect any PD activity in the tower, while the proposed tool detected a PD with a magnitude of about 200 pC. Out of caution, the maintenance department disassembled the three insulators from the tower, as shown in Figure 5-24. It can be observed that a significant crack occurred in one of the insulators. Accordingly, the staff removed the defective insulator and conducted a second PD test on the overhead CC line. No PD signals were found, thereby confirming that the crack had been the cause of the PDs. Moreover, explaining why the ultrasonic tool cannot detect this PD defect is necessary. On the one hand, the PD defect located inside the insulator leads to significant attenuation when the ultrasonic signal caused by the PD propagates out of the insulator. On the other hand, the ultrasonic signal attenuates exponentially as the propagation distance increases, reducing the sensitivity of PD detection when the ultrasonic device is held by a technician staying on the ground ten meters from the insulator.

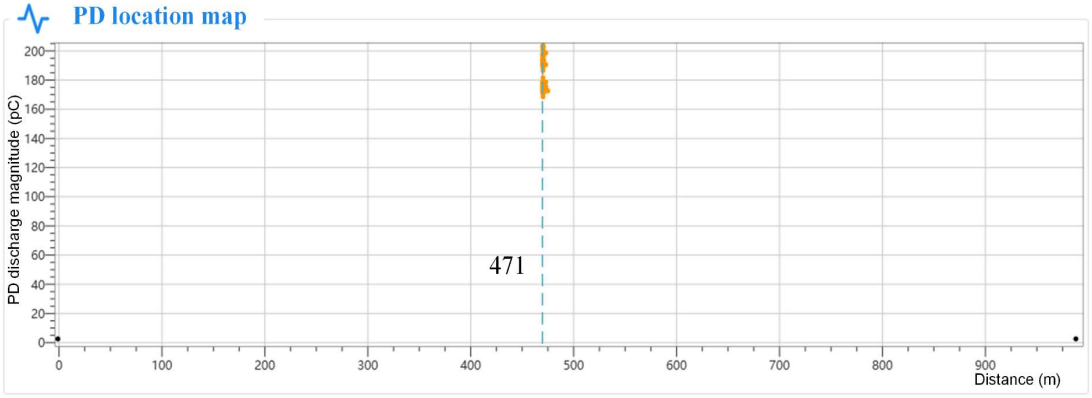

Figure 5-23 PD location result of the defective phase B.

Table 5-3 Comparison of PD measurement results between the classical ultrasonic camera and the proposed system

Tools	PD magnitude	Diagnosis result
The proposed system	≈ 200pC	A significant PD
The state-of-the-art ultrasonic camera (NL100) (sensitivity range: 0-66 dB)	1dB (less than the threshold 8 dB)	No PD

Figure 5-24 Picture of the insulator with a crack.

3）Case 3: Defective Binding Wire

An on-site experiment was carried out on a 448-m overhead CC line. One PD measurement unit was mounted on the outgoing line of the transformer at the end of the overhead line; the other one was directly mounted on the overhead line. The PD location result is shown in Figure 5-25. It can be observed that a PD source occurred at a distance of 0 m from the reference location, i.e., the transformer tower at the end of the overhead line. Figure 5-26 collects the picture of the transformer tower. It can be observed that multiple apparatuses are mounted on the tower, leading to difficulty in identifying the PD-affected apparatus.

An additional PD measurement experiment was carried out on the tower using the developed tool to identify PD-affected apparatus accurately. Two PD detectors connected to the same analyzer were mounted on two of these positions, as shown in Figure 5-26. The PD-affected apparatus is identified via the pulse polarity analysis of the signals collected by the two PD detectors. If the PD source is located between the two PD detectors, the polarities of the pulses detected by one PD detector will be opposite. If not, the polarities will be the same. Figure 5-27 collects the PD polarity maps of multiple measurements. Each blue circle denotes one PD event. These maps display the statistical results of numerous PD events. It can be observed that the pulse polarities detected by the PD detector mounted on position 1 are opposite to that of position 8, as shown in Figure 5-27(a), revealing that the PD source is located between the two PD detectors, i.e., in the tower. Then, the two PD detectors were mounted on each apparatus on the tower. The results are collected in Figure 5-27(b)-(h). It can be observed that the pulse polarities detected by the PD detector mounted on position 1 are opposite to that of position 2, as shown in Figure 5-27(a) and Figure 5-28, while the pulse polarities detected by the PD detector mounted on the other positions are identical, as shown in Figure 5-27(c)-(h). It reveals that the PD source originated from the insulator between positions 1 and 2. Accordingly, careful visual inception was carried out on the insulator. We found that a metal tip occurred on the bonding wire of the insulator. It is supposed that the metal tip was caused by substandard construction. A few days later, the staff replaced the bonding wire and conducted a second PD test on the insulator. No PD signals were found, confirming that the metal tip had been the cause of the PDs.

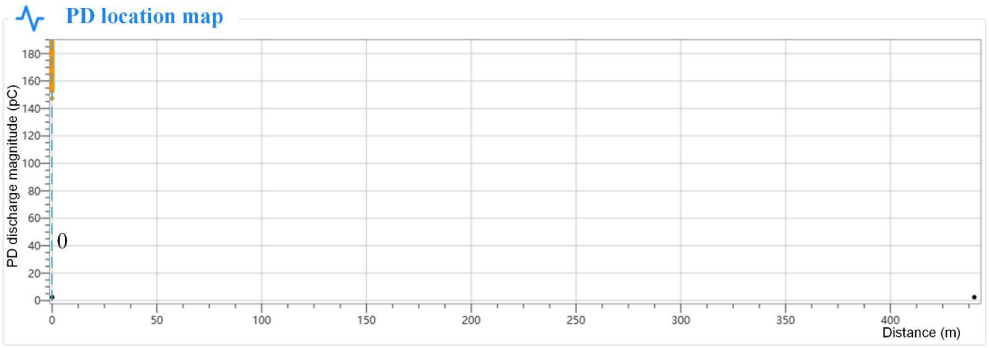

Figure 5-25 PD location result of the defective phase C.

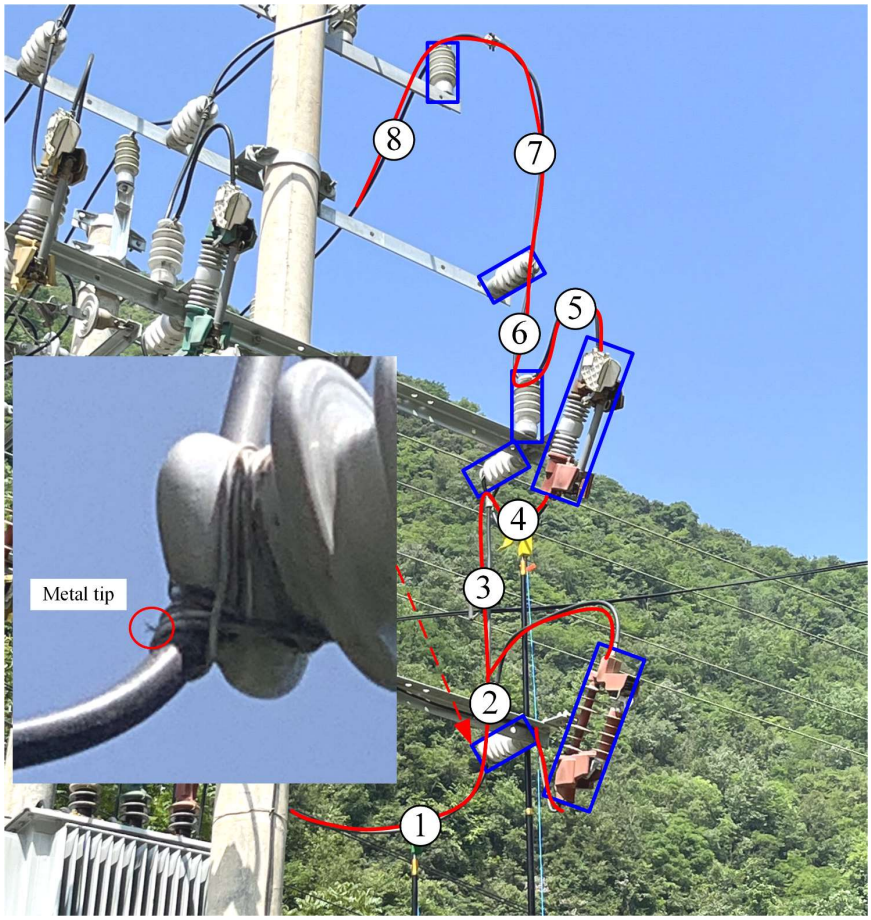

Figure 5-26 Positions of the PD detector.

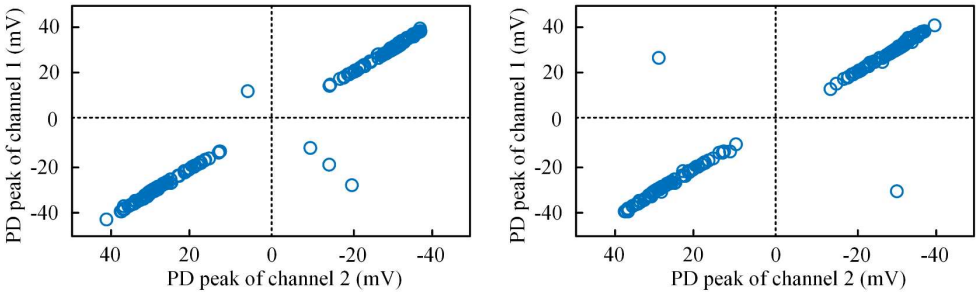

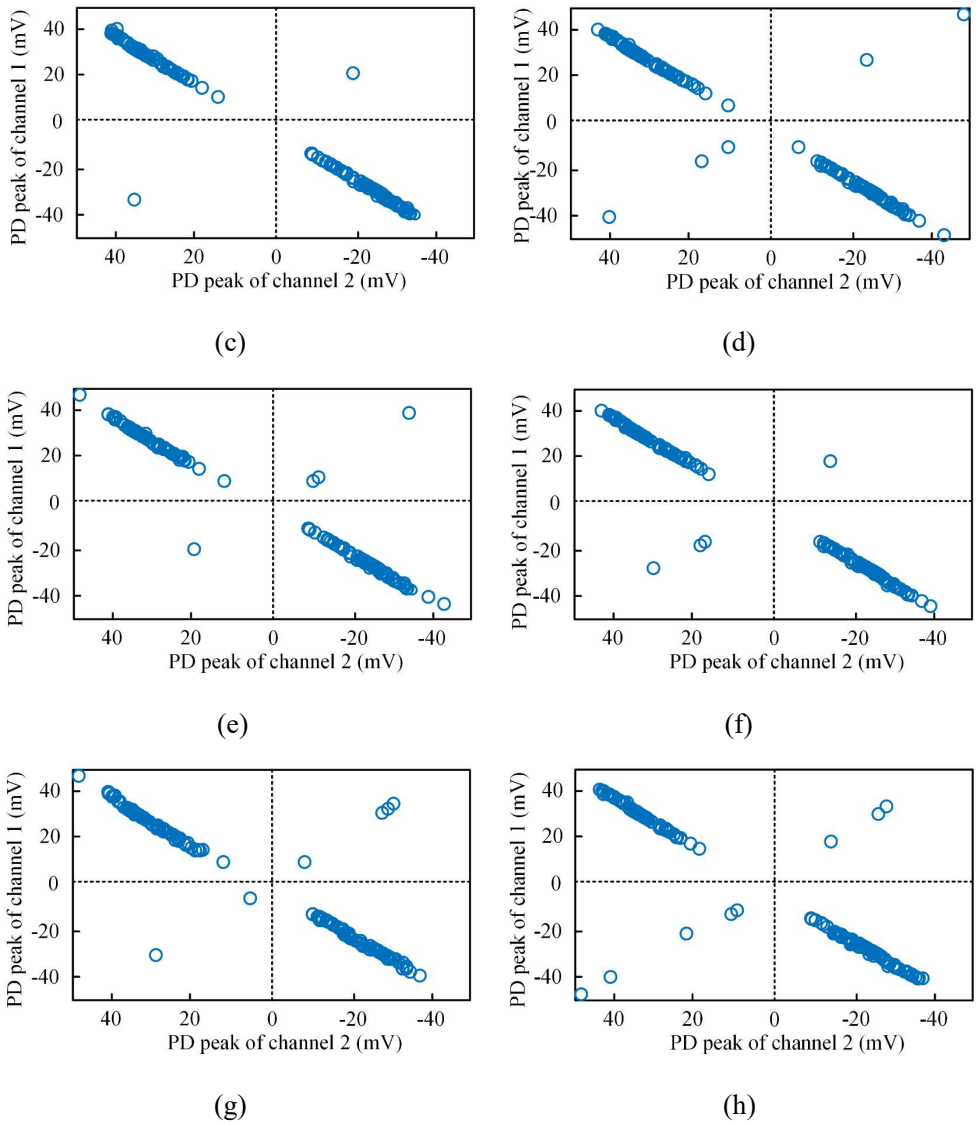

Figure 5-27 PD polarity maps obtained by the two PD detectors mounted on: (a) positions 1 and 8; (b) positions 1 and 2; (c) positions 2 and 3; (d) positions 3 and 4; (e) positions 4 and 5; (f) positions 5 and 6; (g) positions 6 and 7; (h) positions 7 and 8;

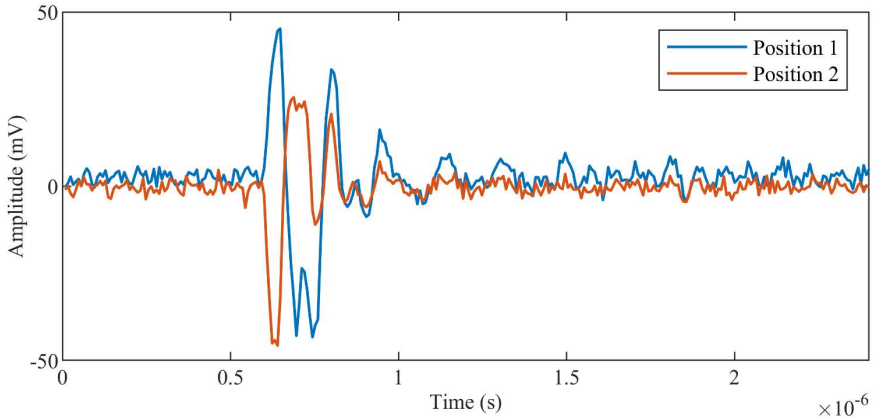

Figure 5-28 PD waveforms collected by the two PD detector mounts on positions 1 and 2.

5.3 Cost-efficient Partial Discharge Diagnosis Strategy for Medium-Voltage Overhead Distribution Networks

A comprehensive strategy involving three stages has been developed to effectively evaluate the presence and characteristics of PD in overhead distribution networks. These stages include distributed PD online monitoring, double-end or multi-end PD localization, and pulse polarity-based PD positioning, as shown in Figure 5-29. We will discuss the benefit of the proposed strategy, and then delve deeper into these stages in this context, highlighting their significance, advantages, and applications in evaluating PD activities in MV overhead distribution networks.

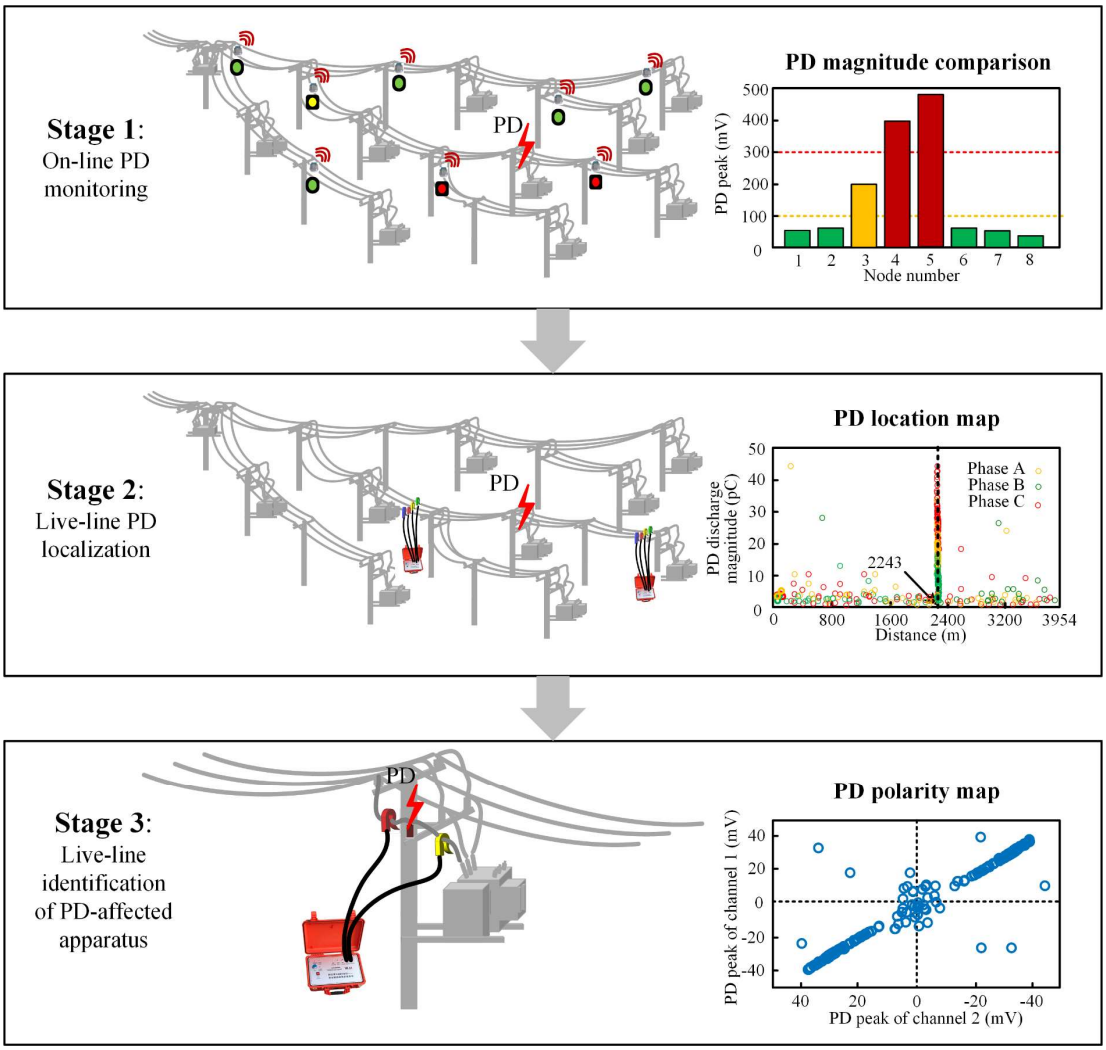

Figure 5-29 Three stages of PD assessment of an MV overhead distribution network.

Stage 1: Distributed Partial Discharge Online Monitoring

Distributed PD online monitoring is a crucial stage in evaluating the PD characteristics of overhead distribution networks in real-time. It involves deploying a network of sensors to monitor PD activity continuously. This stage offers numerous advantages, including real-time performance, low investment costs, and the elimination of human intervention.

The real-time performance of distributed PD online monitoring enables immediate detection of any fluctuations or anomalies in PD activity. By continuously monitoring PD magnitude, frequency, phase-resolved statistics, and fault patterns, this approach provides valuable insights into the health and performance of the overhead distribution network. Any insulation defects or potential failures can be promptly identified, allowing for timely intervention and preventative maintenance actions.

The low investment costs associated with distributed partial discharge online monitoring make it an attractive option for utilities operating within distribution networks. Using sensors and monitoring equipment is relatively affordable compared to traditional inspection methods. This cost-effectiveness allows utilities to implement widespread monitoring across the network, ensuring comprehensive coverage and reducing the risk of undetected PD activity.

Furthermore, eliminating human intervention through automated monitoring systems minimizes the potential for human error and subjectivity. The continuous monitoring provided by these systems removes the need for manual inspections, reducing maintenance costs and improving efficiency. Moreover, automated data collection and analysis ensure accuracy and consistency in evaluating PD characteristics, facilitating more informed decision-making processes.

Stage 2: Double-Sided or Multi-Sided Partial Discharge Localization

The second stage of the evaluation strategy involves accurately localizing PD sources within the overhead distribution network. This stage utilizes double-end or multi-end partial discharge localization techniques to locate the areas experiencing PD activity precisely. It offers high accuracy, sensitivity, and detection efficiency.

Multiple sensors are strategically placed at different ends of the overhead distribution network to achieve accurate localization. These sensors capture PD signals, which are then analyzed to determine the phase difference and magnitude of the discharge. By triangulating this information, the exact location of the partial discharge source can be identified.

This information lets utilities pinpoint the specific areas or equipment experiencing PD activity, facilitating focused maintenance efforts and minimizing downtime. The ability to accurately localize PD sources improves the effectiveness of maintenance actions, leading to optimized resource allocation and reduced repair time. Furthermore, it enables utilities to prioritize critical areas and proactively address insulation defects before they escalate into costly failures.

The advantages of double-sided or multi-sided PD localization lie in its ability to effectively identify and localize PD activity within the overhead distribution network. The high accuracy, sensitivity, and detection efficiency of this technique enhance the overall reliability of the distribution network.

Stage 3: Pulse Polarity-Based PD localization

The evaluation strategy's third stage involves using a pulse polarity-based partial discharge localization technique. This advanced technique confirms the occurrence of PD in specific power equipment. It offers high accuracy and reliability in identifying the exact

sources of PD.

Pulse polarity-based localization relies on analyzing the polarity changes in the PD signals captured from double sides of the apparatus in a tower. Examining the characteristics and patterns of these polarity changes makes it easy to pinpoint the power apparatus associated with the PD activity. This information assists in precise fault diagnosis and targeted maintenance actions.

The advantages of pulse polarity-based partial discharge localization lie in its ability to provide detailed information about the specific power equipment displaying PD activities. This allows maintenance teams to focus on the identified equipment, leading to efficient troubleshooting, faster repairs, and increased overall system performance. By targeting the root causes of PD, utilities can mitigate the risks of insulation degradation and failures, ensuring the longevity and reliability of the overhead distribution network.

Figure 5-30 compares the conventional and the proposed strategies for PD detection of MV overhead distribution network. It can be observed that: the cost of hardware resources for the IoT-based distributed PD monitoring (i.e., Strategy 1) is very small, but the strategy requires plenty of time for PD searching since it cannot provide the information of precise PD locations; the time of PD identification via the online multi-sided PD localization (i.e., Strategy 2) is minimal, but the cost of this strategy is highest since the expensive high-speed analog-to-digital converters and processors are required in each location devices; the cost of hardware resources for the live-line PD localization (i.e., Strategy 3) is minimal, but the strategy requires plenty of time for PD searching since the technician have to move the PD location system to assess the network part by part; in contrast, the proposed strategy (i.e., Strategy 4) combines the advantages of the low cost of IoT-based PD monitors for PD monitoring and the high efficiency of the PD location system for PD localization, yielding a better cost performance than the other strategies.

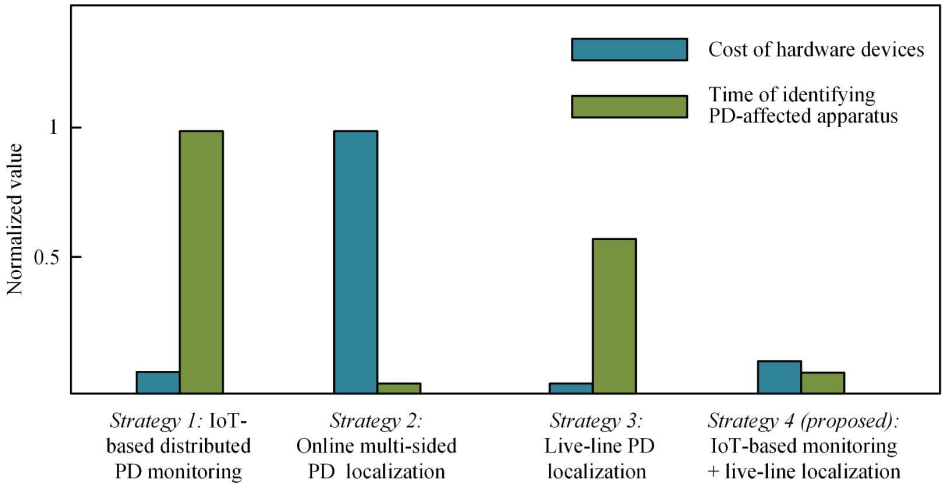

Figure 5-30 Comparison of the conventional and proposed strategies for PD detection of MV overhead distribution network

In summary, evaluating PD in overhead distribution networks within distribution networks involves three essential stages: distributed PD online monitoring, double-sided or

multi-sided PD localization, and pulse polarity-based PD positioning. The strengths of the three stages are listed in Table 5-4. These stages collectively form a comprehensive strategy for assessing and managing the occurrence of PD, ultimately contributing to the reliability, safety, and performance of the overhead distribution networks. By implementing these evaluation techniques, utilities can detect insulation defects, accurately locate partial discharge sources, and perform targeted maintenance actions. This proactive approach reduces the risk of failures, optimizes resource allocation, and enhances the overall efficiency of distribution networks. Ultimately, this results in improved service quality, increased customer satisfaction, and the uninterrupted delivery of electricity to end-users.

Table 5-4 Comparison of the strengths of the proposed techniques used in the three stages

Stages	Techniques	Functions	Strengths
1	IoT-based distributed PD monitoring	Identifying whether a PD occurs, its danger level, and its approximate area.	Real-time monitoring, Low investment, and unsupervised
2	Double-sided or multiple-sided PD localization	Determining the exact location of the PD source.	High sensitivity, accuracy, and efficiency
3	Pulse polarity-based PD localization	Determining the exact PD-affected apparatus	High accuracy and precise information for maintenance

5.4 Conclusion

This chapter develops two systems with different functions for PD diagnosis of MV overhead distribution networks. One is for low-cost online PD monitoring; the other is for advanced PD detection and localization.

The monitoring system addresses the designs of flexible and compact PD monitors and their networking. The three main benefits of using the proposed PD monitor are: i) Frequency down-conversion of the high-frequency PD signal is achieved via a peak-holding circuit, thus eliminating the need for expensive and power-consuming high-speed acquisition and processing chips; ii) An inductive energy harvesting circuit is developed to obtain power on-site from overhead lines to supply the PD monitor, thus increasing the number of sites that can be monitored; iii) The monitor's low-power components and working procedures are developed to be reliably activated by a current value as low as 4 amps in the CC line. In addition, a method based on PD observability analysis and the binary particle swarm optimization algorithm is developed to optimally place a given number of IoT-based monitors.

The portable PD detection and location system addresses the designs of non-invasive PD sensing, non-invasive pulse injections, safe signal transmission, and clock precise

improvement. The benefits of the system are listed as follows: i) A non-invasive pulse injector is designed to synchronize the PD testing units. Beyond that, it can also be used to identify the propagation characteristics of the MV overhead networks online. ii) All parts are connected via fiber-optic cables, ensuring a user is adequately isolated from high voltages. iii) The system can locate PDs from a several-kilometers, such as the on-site experiment shows that the location error of the developed location method and system was less than 10-m when used on a 2125-m long 10-kV overhead line. iii) The system can identify the PD-affected apparatuses from a single tower via the pulse polarity-based PD localization.

Furthermore, a cost-efficient PD detection strategy for MV overhead distribution networks is proposed via the joint application of the two developed systems. The process consists of three comprehensive stages for assessing and managing the occurrence of PD, ultimately contributing to the reliability, safety, and performance of the whole MV overhead distribution networks.

6 Conclusions and Future Work

6.1 Conclusions

Insulation failures in MV overhead distribution networks can cause power outages, disrupting customers' daily activities and harming the economy. The solution to this problem is to conduct online PD diagnosis of the network apparatuses to predict the upcoming insulation failures, enabling electric utilities to repair or remove the defective apparatus promptly. However, a huge amount of apparatuses, complex network structures, and a severe noise environment make it challenging to detect PD in MV overhead distribution networks, causing no quantified solution yet available for accurate, robust, and efficient PD diagnosis. Therefore, improvements in existing techniques are required.

This dissertation focuses on studying PD propagation characteristics, noise reduction, improvement of online PD detection and location methods, and system design, addressing the problems that impede the further application of the traveling wave-based PD detection and location technique in MV overhead distribution networks. The improvements and contributions of this dissertation are summarized as follows.

(1) PD propagation characteristics in MV overhead distribution networks are modeled and thoroughly discussed. The multiple-conductor models of MV overhead distribution networks are developed, considering the effect of alongside towers. Approximation formulas for calculating the frequency-dependent transmission line parameters are derived. The models and formulas allow us to simulate PD signals at any MV overhead distribution network location. Simulations and measurements validate the developed models and formulas. Furthermore, the PD propagation simulations are conducted to analyze the effects of line parameters and network structures. The results reveal several crucial PD propagation characteristics of the MV overhead distribution network: i) PD propagation characteristics in PG and PP channels of MV overhead lines are significantly different, and the sensitivity and accuracy of PD detection and localization based on the signal in the PP channel could be much higher than that in the PG channel. For example, the attenuation coefficient of the PP channel is about 2×10^{-5} at the frequency of 1 MHz for a typical 10-kV overhead CC line, while that of the PG channel is about 3×10^{-4}, resulting in the PD signal in the PP channel can propagate a significantly longer distance than that in PG channel.; ii) The influence of the alongside towers on PD propagation is proven to be non-negligible since they could lead to significant signal attenuation and time delays, such as the time delay caused by the supporting tower can be tens of ns; iii) The apparent discharge quantity of a PD signal is almost immune to the increased propagation distance, but the PD sensor's location significantly influences it. These

crucial conclusions can help develop PD detection and location methods and sensor deployment strategies.

(2) An adaptive and efficient PD de-noising algorithm is proposed. It is based on a well-defined automatic procedure that involves the joint application of the STFT and the SVD tools. The former time-frequency transform enables the separation of the PD signal's functional behavior and the possibly superimposed discrete spectrum noise and the white noise background disturbance. The latter matrix decomposition allows separating all the signal contributions in terms of the dominant terms (or modes) and filtering out all the noisy terms. The algorithm also embeds some additional features, including a soft-masking mechanism and the optimal selection of the terms leading to the accurate estimation of the noiseless PD signal. The SNR of the processed signal was significantly improved, such as from -11.10 dB to 12.97dB in a real measured PD signal. Moreover, the algorithm is further improved to heavily reduce the computational complexity of the proposed algorithm more than 10 times, including PD identification criteria to avoid unnecessary computation, decomposing the spectrogram using a more efficient randomized SVD algorithm, and selecting dominant components via a more straightforward approach. The synthetic test case and the simulation results prove that the proposed de-noising scheme can adaptively reduce, selectively, both the white noise and the discrete spectrum noise in various PD pulses. The proposed algorithm is successfully implemented in three typical embedded systems with various hardware resources, demonstrating the feasibility of applying the proposed algorithm to most PD monitoring devices. A comprehensive comparison of the proposed algorithm and other state-of-the-art alternatives proves its superior de-noising performance and computational efficiency.

(3) Improved PD detection and location methods are developed. A notched high-frequency current transformer is developed, effectively addressing the sensitivity and bandwidth problem. A digital compensation algorithm has been proposed to simplify the design and parameter-tuning process of this high-frequency transformer. This algorithm has significantly improved the transfer characteristics of the transformer, thereby enabling more accurate PD evaluation, such as estimating the magnitude of PD discharges. An improved double-sided PD location method is developed. The technique has three benefits: i) A hybrid synchronization approach has been developed, which combines GPS and pulse-based interaction. This approach eliminates the inherent random errors of GPS and estimates the propagation velocity of pulses, thereby improving location precise, such as location error is significantly reduced from 5.82 m to 0.79 m in the experiment case of a 50-m overhead line; ii) A windowed phase difference method has been developed to accurately estimate the time-of-arrival difference between noisy PD pulses collected by detectors in environments with low signal-to-noise ratio; iii) The PD location map can automatically separate PD pulses from impulse noise interferences. This feature allows for easy elimination of interference's influence. Simulation and laboratory

experiments show that the accuracy and robustness of the proposed location method are significantly higher than the classical GPS-based location method. Furthermore, a multiple-sided PD location algorithm is proposed based on the developed PD detection and location methods. The PD location problem is transformed into an optimization problem, which can be easily solved from the TOAs of the synchronization and PD pulses. Monte Carlo simulations validate the accuracy and robustness of the algorithm. The algorithm can be used to robustly locate the PDs in radial feeders, which is common in MV overhead distribution networks.

(4) Two system prototypes for PD detection and localization for MV overhead distribution networks are developed. Detailed hardware and software designs of the two systems are thoroughly discussed. The first system, i.e., a low-cost online PD monitoring system, addresses the issues of non-invasive and low-cost sensing, a field energy harvesting function, a low-power working operation, reliable networking, and a PD identification algorithm. The system achieves low-cost, flexible online PD monitoring of MV overhead distribution networks, thereby avoiding laborious manual inspections. The second system, i.e., the portable PD detection and location system, addresses the issues of non-invasive PD detection, non-invasive pules injection, safe signal transmission, and clock precise improvement of the analyzer. The on-site experiment shows that the location error of the developed location method and system was less than 10-m when used on a 2125-m long 10-kV overhead line. The system outputs more detailed information on PDs, i.e., the PD apparent quantity, the PD source location, and even the PD-affected apparatuses, thereby enabling more accurate insulation assessment and more efficient condition-based maintenance. Finally, a PD diagnosis strategy is proposed via the joint application of the two developed systems, resulting in a cost-efficient solution for PD-based insulation assessment of MV overhead distribution networks.

6.2 Future Work

To further improve the PD diagnosis of MV overhead distribution networks, follow-up research work can be carried out from the following aspects:

(1) The propagation characteristics research conclusions of this work are only applicable to three-phase (approximately) symmetrical overhead lines and equipment along the lines. However, in real medium-voltage overhead lines, the equipment along the line may not be three-phase symmetrical. For example, for economic reasons, voltage and current transformers are often installed on only two phases. In addition, situations such as multiple lines on the same tower, crossing of lines with different voltage levels, and mixed lines with overhead lines and underground cables are not considered.

(2) Considering the increasingly severe and complex noise issues that may arise with integrating distributed renewable energy sources and intelligent charging stations in MV overhead distribution networks is essential. As more distributed energy sources,

such as solar and wind power, are connected to the grid, their intermittent nature and variable output can introduce fluctuating electrical noise. Similarly, installing intelligent charging stations for electric vehicles can contribute to additional noise sources. To address these future challenges, novel methods should be developed to tackle the more intricate noise problems.

(3) Multi-source partial discharge localization in complex pulse noise environment is still a challenge. In double-sided or multi-sided location method, the pairing of homologous pulse signals by each distributed sensing unit is essential. However, when there are multi-source discharge signals or interference pulses or the sensing unit is far away and the propagation time is long, accurately pairing the pulse sources is difficult. The proposed double-sided or multiple sided location algorithm should be further improved, e.g., via statistical signal processing techniques.

(4) PD pattern recognition and classification are crucial for guiding maintenance. This dissertation mainly focuses on detecting and localizing PDs in MV overhead distribution networks. Interpretation of the results is out of the scope of this study, but it is also crucial for the maintenance departments in the decision-making process. However, this task presents technical challenges. Firstly, various factors influence PD patterns, including equipment types, insulation materials, and environmental conditions, making establishing a universal recognition approach difficult. Secondly, noise often contaminates PD signals, impacting accurate pattern identification. To address these challenges, a possible solution involves using advanced machine learning algorithms.

References

[1] Pihler J, Ticar I. Design of systems of covered overhead conductors by means of electric field calculation[J]. IEEE Transactions on power delivery, 2005, 20(2): 807-814.

[2] Ramirez-Vazquez I, Espino-Cortes F P. Electric-field analysis of spacer cable systems for compact overhead distribution lines[J]. IEEE transactions on power delivery, 2012, 27(4): 2312-2317.

[3] Leskinen T, Kantola K. Lifetime estimation of a covered overhead line conductor[J]. Wind and Structures, 2003, 6(4): 307.

[4] Babuder M, Vizintin S, Toros Z, et al. Assessment of causes and possibilities for preventing frequent conductor damages on 20 kV overhead lines equipped with covered conductors[C]//Proceedings of the XIVth International Symposium on High Voltage Engineering, Tsinghua University, Beijing, China. 2005: 1-6.

[5] Guo Shanghua, Wang Gang. Active distribution network fault location method integrating FTU and distribution transformer alarm information[J]. Power System Protection and Control, 2022, 50 (22): 92-99.

[6] Yang Bin. Research on fault section location and recovery control methods of distribution network containing distributed photovoltaics [D]. North China Electric Power University (Beijing), 2023.

[7] Martinez-Canales J F, Alvarez C, Valero J V. A review of the incidence of medium and high voltage overhead electric power lines in causing forest fires[J]. 1997.

[8] Moutis P, Sriram U. Pmu-driven non-preemptive disconnection of overhead lines at the approach or break-out of forest fires[J]. IEEE Transactions on Power Systems, 2022, 38(1): 168-176.

[9] Yu Y, Yang J, Chen B. The smart grids in China—A review[J]. Energies, 2012, 5(5): 1321-1338.

[10] Chen Shuyong, Song Shufang, Li Lanxin, etc. Overview of smart grid technology [J]. Power Grid Technology, 2009, 33 (08): 1-7.

[11] Sekhar P C, Deshpande R A, Sankar V. Evaluation and improvement of reliability indices of electrical power distribution system[C]//2016 National Power Systems Conference (NPSC). IEEE, 2016: 1-6.

[12] Balakrishna P, Rajagopal K, Swarup K S. Application benefits of Distribution Automation and AMI systems convergence methodology for distribution power restoration analysis[J]. Sustainable Energy, Grids and Networks, 2015, 2: 15-22.

[13] Zidan A, Khairalla M, Abdrabou A M, et al. Fault detection, isolation, and service restoration in distribution systems: State-of-the-art and future trends[J]. IEEE Transactions on Smart Grid, 2016, 8(5): 2170-2185.

[14] Elkadeem M R, Alaam M A, Azmy A M. Improving performance of underground MV distribution networks using distribution automation system: A case study[J]. Ain Shams Engineering Journal, 2018, 9(4): 469-481.

[15] Ferreira V H, Zanghi R, Fortes M Z, et al. A survey on intelligent system application to fault diagnosis in electric power system transmission lines[J]. Electric Power Systems Research, 2016, 136: 135-153.

[16] Raza A, Benrabah A, Alquthami T, et al. A review of fault diagnosing methods in power transmission systems[J]. Applied Sciences, 2020, 10(4): 1312.

[17] Zhao Y, Li T, Zhang X, et al. Artificial intelligence-based fault detection and diagnosis methods for building energy systems: Advantages, challenges and the future[J]. Renewable and Sustainable Energy Reviews, 2019, 109: 85-101.

[18] Prajapati A, Bechtel J, Ganesan S. Condition based maintenance: a survey[J]. Journal of Quality in Maintenance Engineering, 2012, 18(4): 384-400.

[19] Montanari G C, Hebner R, Seri P, et al. Self-assessment of health conditions of electrical assets and grid components: A contribution to smart grids[J]. IEEE Transactions on Smart Grid, 2020, 12(2): 1206-1214.

[20] Standard I E C. High-voltage test techniques: partial discharge measurements[J]. IEC-60270, 2000: 13-31.

[21] Li Junhao, Han Xutao, Liu Zehui, et al. Review of partial discharge detection technology of electrical equipment [J]. High Voltage Technology, 2015, 41 (08): 2583-2601.

[22] Montanari G C, Cavallini A. Partial discharge diagnostics: from apparatus monitoring to smart grid assessment[J]. IEEE Electrical Insulation Magazine, 2013, 29(3): 8-17.

[23] Zhang X, Pang B, Liu Y, et al. Review on detection and analysis of partial discharge along power cables[J]. Energies, 2021, 14(22): 7692.

[24] Fadaeeasrami H, Faghihi F, Mohammadnezhad H. A Review of Partial Discharge Signals Occurrence in Polluted High Voltage Insulator[J]. Signal Processing and Renewable Energy, 2021, 5(1): 51-78.

[25] Spellman C A, Young H M, Haddad A, et al. Survey of polymeric insulator ageing factors[C]//1999 Eleventh International Symposium on High Voltage Engineering. IET, 1999, 4: 160-163.

[26] Bojovschi A, Quoc T V, Trung H N, et al. Environmental effects on HV dielectric materials and related sensing technologies[J]. Applied Sciences, 2019, 9(5): 856.

[27] Venge T, Nyamupangedengu C. A Review of Test Voltages Used in Partial Discharge Measurements[J]. 2021 IEEE AFRICON, 2021: 1-6.

[28] Bartnikas R. Partial discharges. Their mechanism, detection and measurement[J]. IEEE Transactions on dielectrics and electrical insulation, 2002, 9(5): 763-808.

[29] Pakonen P. Characteristics of partial discharges caused by trees in contact with covered conductor lines[J]. IEEE Transactions on Dielectrics and Electrical Insulation, 2008, 15(6): 1626-1633.

[30] Ibrahim M E, Abd-Elhady A M. Calculation of electric field and partial discharge activity reduction for covered conductor/high voltage insulator systems[J]. Electric Power Systems Research, 2017, 144: 72-80.

[31] Hussain M R, Refaat S S, Abu-Rub H. Overview and partial discharge analysis of power transformers: A literature review[J]. IEEE Access, 2021, 9: 64587-64605.

[32] Pan C, Tang J, Tao X, et al. Partial discharge and breakdown characteristics of moving transformer oil contaminated by metallic particles[J]. IEEE Transactions on Dielectrics and Electrical Insulation, 2018, 25(5): 1774-1784.

[33] Korobeynikov S M, Ovsyannikov A G, Ridel A V, et al. Study of partial discharges in bubbles and microsphere in transformer oil[C]//Journal of Physics: Conference Series. IOP Publishing, 2018, 1128(1): 012118.

[34] Murugan R, Ramasamy R. Failure analysis of power transformer for effective maintenance planning in electric utilities[J]. Engineering Failure Analysis, 2015, 55: 182-192.

[35] Yongxiang L, Tianzheng W, Liqiang G, et al. Detection and analysis of high voltage electrical equipment corona discharge based on ultraviolet imaging technology[C]//2017 29th Chinese Control And Decision Conference (CCDC). IEEE, 2017: 6928-6931.

[36] Wu Shiyou, Zheng Shusheng, Zhong Aixu, etc. UHF substation space multi-source partial discharge positioning method based on intelligent clustering algorithm [J]. High Voltage

Technology, 2020, 46 (12): 4309-4318.
[37] Xu Z, Hei G. Rectangular spiral antenna with a Hilbert unit for detecting corona discharge in overhead lines[J]. IEEE Sensors Journal, 2020, 21(2): 930-936.
[38] Shurrab I Y, El-Hag A H, Assaleh K, et al. RF-based monitoring and classification of partial discharge on wet silicone rubber surface[J]. IEEE Transactions on Dielectrics and Electrical Insulation, 2013, 20(6): 2188-2194.
[39] Li T, Song B, Liu Y, et al. Research on Ultrasonic Detection Technology of overhead Distribution Line[C]//2021 IEEE International Conference on Artificial Intelligence and Computer Applications (ICAICA). IEEE, 2021: 938-942.
[40] Suwanasri S, Khetcharoen W, Suwanasri T, et al. Partial discharge investigation and failure analysis on distribution network using acoustic camera[C]//2021 9th International Electrical Engineering Congress (iEECON). IEEE, 2021: 181-184.
[41] Hashmi G M. Partial discharge detection for condition monitoring of covered-conductor overhead distribution networks using Rogowski coil[M]. Teknillinen korkeakoulu, 2008.
[42] Yan Y, Zhao Y, Zhao K, et al. A high-efficiency portable system for insulation condition assessment of wind farm inter-array cables with double-sided partial discharge detection and localisation[J]. IET Generation, Transmission & Distribution, 2023.
[43] Rodrigo A, Llovera P, Fuster V, et al. High performance broadband capacitive coupler for partial discharge cable tests[J]. IEEE Transactions on Dielectrics and Electrical Insulation, 2013, 20(2): 479-487.
[44] Mor A R, Morshuis P H F, Llovera P, et al. Localization techniques of partial discharges at cable ends in off-line single-sided partial discharge cable measurements[J]. IEEE Transactions on Dielectrics and Electrical Insulation, 2016, 23(1): 428-434.
[45] Gulski E, Jongen R, Rakowska A, et al. Offshore wind farms on-site submarine cable testing and diagnosis with damped AC[J]. Energies, 2019, 12(19): 3703.
[46] Zhou K, Li Z, Zhu G, et al. An adaptive pulse separation strategy for PD detection in frequency-tuned resonant tests[J]. IEEE Transactions on Instrumentation and Measurement, 2021, 70: 1-9.
[47] Hu X, Siew W H, Judd M D, et al. Modeling of high-frequency current transformer based partial discharge detection in high-voltage cables[J]. IEEE Transactions on Power Delivery, 2019, 34(4): 1549-1556.
[48] Shafiq M, Kiitam I, Taklaja P, et al. Identification and location of PD defects in medium-voltage underground power cables using high frequency current transformer[J]. IEEE Access, 2019, 7: 103608-103618.
[49] Ohv diagnositic. DAC M30, M40, M60 –ohv diagnostic [OL]. 2014 Oct [cited 2023 February 17]. Available from: http://www.ohv-diagnostic.com/assets/project_components/media/documents
[50] /leaflets/EN/LL_M30M60_en_1.pdf.
[51] Smart cable guard [OL]. 2023 Sep [cited 2023 Sep 17]. Available from: https://www.dnv.com/power-renewables/services/scg/index.html.
[52] PDScope™ Acquisition Unit For PD Monitoring [O/L]. 2023 Sep [cited 2023 Sep 17]. Available from:https://www.altanova-group.com/en/products/partial-discharge-tests/acquisition-units/pd-scope
[53] Hashmi G M, Lehtonen M. Covered-conductor overhead distribution line modeling and experimental verification for determining its line characteristics[C]//2007 IEEE Power Engineering Society Conference and Exposition in Africa-PowerAfrica. IEEE, 2007: 1-7.
[54] Hashmi G M, Papazyan R, Lehtonen M. Comparing wave propagation characteristics of MV XLPE cable and covered-conductor overhead line using time domain reflectometry technique[C]//2007 International Conference on Electrical Engineering. IEEE, 2007: 1-6.

[55] Zhou L, Tian Y. Propagation Characteristics of Partial Discharge Pulse Current on 10kV Covered Conductor[J]. Academic Journal of Engineering and Technology Science, 5(9): 13-23.

[56] de Magalhães Júnior F M, Lopes F V. Mathematical study on traveling waves phenomena on three phase transmission lines–Part I: Fault-Launched Waves[J]. IEEE Transactions on Power Delivery, 2021, 37(2): 1151-1160.

[57] Sriram S, Nitin S, Prabhu K M M, et al. Signal denoising techniques for partial discharge measurements[J]. IEEE Transactions on Dielectrics and Electrical Insulation, 2005, 12(6): 1182-1191.

[58] Long J, Wang X, Zhou W, et al. A comprehensive review of signal processing and machine learning technologies for UHF PD detection and diagnosis (I): Preprocessing and Localization Approaches[J]. IEEE Access, 2021, 9: 69876-69904.

[59] Saha T K, Purkait P. Advanced Signal Processing Techniques for Partial Discharge Measurement[J]. 2017.

[60] Alvarez F, Ortego J, Garnacho F, et al. A clustering technique for partial discharge and noise sources identification in power cables by means of waveform parameters[J]. IEEE Transactions on Dielectrics and Electrical Insulation, 2016, 23(1): 469-481.

[61] Mor A R, Heredia L C C, Muñoz F A. Estimation of charge, energy and polarity of noisy partial discharge pulses[J]. IEEE Transactions on Dielectrics and Electrical Insulation, 2017, 24(4): 2511-2521.

[62] Ma X, Zhou C, Kemp I J. Automated wavelet selection and thresholding for PD detection[J]. IEEE Electrical Insulation Magazine, 2002, 18(2): 37-45.

[63] Hussein R, Shaban K B, El-Hag A H. Wavelet transform with histogram-based threshold estimation for online partial discharge signal denoising[J]. IEEE transactions on instrumentation and measurement, 2015, 64(12): 3601-3614.

[64] Seo J, Ma H, Saha T. Probabilistic wavelet transform for partial discharge measurement of transformer[J]. IEEE Transactions on Dielectrics and Electrical Insulation, 2015, 22(2): 1105-1117.

[65] Ghorat M, Gharehpetian G B, Latifi H, et al. A new partial discharge signal denoising algorithm based on adaptive dual-tree complex wavelet transform[J]. IEEE Transactions on Instrumentation and Measurement, 2018, 67(10): 2262-2272.

[66] Tang J, Zhou S, Pan C. A denoising algorithm for partial discharge measurement based on the combination of wavelet threshold and total variation theory[J]. IEEE Transactions on Instrumentation and Measurement, 2019, 69(6): 3428-3441.

[67] Zhou S, Tang J, Pan C, et al. Partial discharge signal denoising based on wavelet pair and block thresholding[J]. IEEE Access, 2020, 8: 119688-119696.

[68] Zhou Jing, Luo Richeng, Huang Jun. White noise suppression method of transformer partial discharge ultrasonic signal based on improved wavelet threshold-CEEMDAN [J]. High Voltage Electrical Appliances, 2024, 60 (01): 163-171.

[69] Cunha C F F C, Carvalho A T, Petraglia M R, et al. A new wavelet selection method for partial discharge denoising[J]. Electric Power Systems Research, 2015, 125: 184-195.

[70] Altay Ö, Kalenderli Ö. Wavelet base selection for de-noising and extraction of partial discharge pulses in noisy environment[J]. IET Science, Measurement & Technology, 2015, 9(3): 276-284.

[71] Lin M Y, Tai C C, Tang Y W, et al. Partial discharge signal extracting using the empirical mode decomposition with wavelet transform[C]//2011 7th Asia-Pacific International Conference on Lightning. IEEE, 2011: 420-424.

[72] Xie J, Lv F, Li M, et al. Suppressing the discrete spectral interference of the partial discharge signal based on bivariate empirical mode decomposition[J]. International Transactions on Electrical Energy Systems, 2017, 27(10): e2407.

[73] Zhang S, Liu H, Hu M, et al. An adaptive CEEMDAN thresholding denoising method optimized by nonlocal means algorithm[J]. IEEE Transactions on Instrumentation and Measurement, 2020, 69(9): 6891-6903.

[74] Yang Y, Cheng J, Zhang K. An ensemble local means decomposition method and its application to local rub-effect fault diagnosis of the rotor systems[J]. Measurement, 2012, 45(3): 561-570.

[75] Dragomiretskiy K, Zosso D. Variational mode decomposition[J]. IEEE transactions on signal processing, 2013, 62(3): 531-544.

[76] Ni Q, Ji J C, Feng K, et al. A fault information-guided variational mode decomposition (FIVMD) method for rolling element bearings diagnosis[J]. Mechanical Systems and Signal Processing, 2022, 164: 108216.

[77] Zhang J, He J, Long J, et al. A new denoising method for UHF PD signals using adaptive VMD and SSA-based shrinkage method[J]. Sensors, 2019, 19(7): 1594.

[78] Xi Y, Zhou F, Zhang W. Partial Discharge Detection and Recognition in Insulated overhead Conductor Based on Bi-LSTM with Attention Mechanism[J]. Electronics, 2023, 12(11): 2373.

[79] Bin D, Jingwen L, Jianning C, et al. Noise reduction of partial discharge in power cable insulation based on deep learning[C]//2020 IEEE International Conference on High Voltage Engineering and Application (ICHVE). IEEE, 2020: 1-4.

[80] Abdel-Galil T K, El-Hag A H, Gaouda A M, et al. De-noising of partial discharge signal using eigen-decomposition technique[J]. IEEE Transactions on Dielectrics and Electrical Insulation, 2008, 15(6): 1657-1662.

[81] Ashtiani M B, Shahrtash S M. Partial discharge de-noising employing adaptive singular value decomposition[J]. IEEE Transactions on Dielectrics and Electrical Insulation, 2014, 21(2): 775-782.

[82] Zhou K, Li M, Li Y, et al. An improved denoising method for partial discharge signals contaminated by white noise based on adaptive short-time singular value decomposition[J]. Energies, 2019, 12(18): 3465.

[83] Govindarajan S, Subbaiah J, Cavallini A, et al. Partial discharge random noise removal using Hankel matrix-based fast singular value decomposition[J]. IEEE Transactions on Instrumentation and Measurement, 2019, 69(7): 4093-4102.

[84] Li L, Wei X. Suppression method of partial discharge interferences based on singular value decomposition and improved empirical mode decomposition[J]. Energies, 2021, 14(24): 8579.

[85] Zhong J, Bi X, Shu Q, et al. Partial discharge signal denoising based on singular value decomposition and empirical wavelet transform[J]. IEEE transactions on instrumentation and measurement, 2020, 69(11): 8866-8873.

[86] Karami H, Gharehpetian G B. Limitations of partial discharge de-noising of power transformer using adaptive singular value decomposition[C]//2019 International Power System Conference (PSC). IEEE, 2019: 777-781.

[87] Liu Y, Zhou W, Li P, et al. An ultrahigh frequency partial discharge signal de-noising method based on a generalized S-transform and module time-frequency matrix[J]. Sensors, 2016, 16(6): 941.

[88] Hashmi G M, Lehtonen M, Nordman M. Modeling and experimental verification of on-line PD detection in MV covered-conductor overhead networks[J]. IEEE Transactions on Dielectrics and Electrical Insulation, 2010, 17(1): 167-180.

[89] Wang Xiaotang, Wang Yaofei, Song Weichen, etc. New technology for partial discharge charging detection of overhead insulated lines [J]. Electrical Technology, 2015, (01): 33-34+42.

[90] Fernando S C, Rowe W S T, Wong K L. Long wire antenna-like behavior of uninsulated overhead distribution cables[J]. IEEE transactions on power delivery, 2012, 27(3): 1116-1123.

[91] Hamacek S, Misak S. Detector of covered conductor faults[J]. Advances in Electrical and Electronic Engineering, 2012, 10(1): 7-12.

[92] Krátký M, Mišák S, Gajdoš P, et al. A novel method for detection of covered conductor faults in medium-voltage overhead distribution networks[J]. IEEE Transactions on Industrial Electronics, 2017, 65(1): 543-552.

[93] Fulneček J, Mišák S. A simple method for tree fall detection on medium-voltage overhead lines with covered conductors[J]. IEEE Transactions on Power Delivery, 2020, 36(3): 1411-1417.

[94] Zhang W, Hou Z, Li H J, et al. An improved technique for online PD detection on covered conductor lines[J]. IEEE transactions on power delivery, 2014, 29(2): 972-973.

[95] Misák S, Fulnecek J, Vantuch T, et al. A complex classification approach of partial discharges from covered conductors in real environment[J]. IEEE Transactions on Dielectrics and Electrical Insulation, 2017, 24(2): 1097-1104.

[96] VSB power line fault detection [OL], Available from: https://www.kaggle.com/c/vsb-power-line-fault-detection.

[97] Dong M, Sun J. Partial discharge detection on aerial covered conductors using time-series decomposition and long short-term memory network[J]. Electric Power Systems Research, 2020, 184: 106318.

[98] Li Z, Qu N, Li X, et al. Partial discharge detection of insulated conductors based on CNN-LSTM of attention mechanisms[J]. Journal of Power Electronics, 2021, 21: 1030-1040.

[99] Qu N, Li Z, Zuo J, et al. Fault detection on insulated overhead conductors based on DWT-LSTM and partial discharge[J]. IEEE Access, 2020, 8: 87060-87070.

[100] Chen K, Vantuch T, Zhang Y, et al. Fault detection for covered conductors with high-frequency voltage signals: From local patterns to global features[J]. IEEE Transactions on Smart Grid, 2020, 12(2): 1602-1614.

[101] Klein L, Žmij P, Krömer P. Partial Discharge Detection by Edge Computing[J]. IEEE Access, 2023.

[102] Ragusa A, Sasse H G, Duffy A. On-line partial discharge localization in power cables based on electromagnetic time reversal theory-numerical validation[J]. IEEE Transactions on Power Delivery, 2021, 37(4): 2911-2920.

[103] Ragusa A, Sasse H G, Duffy A, et al. Application to real power networks of a method to locate partial discharges based on electromagnetic time reversal[J]. IEEE Transactions on Power Delivery, 2021, 37(4): 2738-2746.

[104] Xie Min, Zhou Kai, He Min, et al. Power cable partial discharge positioning method based on time reversal technology [J]. Chinese Journal of Electrical Engineering, 2018, 38 (11): 3402-3409.

[105] Wang Xianjin, Zhou Kai, Xie Min, et al. Power cable partial discharge positioning based on time reversal phase method [J]. Power Grid Technology, 2020, 44 (02): 783-790.

[106] Lu L, Zhou K, Zhu G, et al. Partial discharge location algorithm based on total least-squares with Matern kernel in cable systems[J]. IEEE Transactions on Industrial Informatics, 2022, 19(3): 2421-2431.

[107] Mohamed F P, Siew W H, Soraghan J J, et al. Partial discharge location in power cables using a double ended method based on time triggering with GPS[J]. IEEE Transactions on Dielectrics and Electrical Insulation, 2013, 20(6): 2212-2221.

[108] Li H, Cui X, Wang H, et al. A novel partial discharge locating system for 10-kV covered conductor lines in distribution network[C]//2020 10th International Conference on Power and Energy Systems (ICPES). IEEE, 2020: 379-383.

[109] He W, Sun H, Li H, et al. A Novel Time Alignment Technique for Online PD Location in Covered Conductors[J]. IEEE Transactions on Power Delivery, 2015, 31(6): 2559-2561.

[110] He W, Li H, Liang D, et al. Implementation of a novel double-side technique for partial discharge detection and location in covered conductor overhead distribution networks[J]. Measurement Science and Technology, 2015, 26(12): 125009.

[111] Van der Wielen P, Wouters P, Veen J, et al. Synchronization of on-line PD detection and localization setups using pulse injection[C]//Proceedings of the 7th International Conference on Properties and Applications of Dielectric Materials (Cat. No. 03CH37417). IEEE, 2003, 1: 327-330.

[112] Isa M, Elkalashy N I, Lehtonen M, et al. Multi-end correlation-based PD location technique for medium-voltage covered-conductor lines[J]. IEEE Transactions on Dielectrics and Electrical Insulation, 2012, 19(3): 936-946.

[113] Wagenaars P, Wouters P, Van Der Wielen P, et al. Accurate estimation of the time-of-arrival of partial discharge pulses in cable systems in service[J]. IEEE Transactions on Dielectrics and Electrical insulation, 2008, 15(4): 1190-1199.

[114] Herold C, Leibfried T. Advanced signal processing and modeling for partial discharge diagnosis on mixed power cable systems[J]. IEEE Transactions on Dielectrics and Electrical Insulation, 2013, 20(3): 791-800.

[115] Mardiana R, Su C Q. Partial discharge location in power cables using a phase difference method[J]. IEEE Transactions on Dielectrics and Electrical Insulation, 2010, 17(6): 1738-1746.

[116] Okamoto T, Kato T, Yokomizu Y, et al. PD characteristics as a stochastic process and its integral equation under sinusoidal voltage[J]. IEEE transactions on Dielectrics and Electrical Insulation, 2001, 8(1): 82-90.

[117] Toader M, Mariana D. Electrical insulation study using partial discharge model[C]//2000 10th Mediterranean Electrotechnical Conference. Information Technology and Electrotechnology for the Mediterranean Countries. Proceedings. MeleCon 2000 (Cat. No. 00CH37099). IEEE, 2000, 3: 1060-1063.

[118] Okubo H, Hayakawa N, Matsushita A. The relationship between partial discharge current pulse waveforms and physical mechanisms[J]. IEEE Electrical Insulation Magazine, 2002, 18(3): 38-45.

[119] Paul C R. Analysis of multiconductor transmission lines[M]. John Wiley & Sons, 2007.

[120] Wang D, Hou M, Guo Y. Travelling wave fault location of HVAC transmission line based on frequency-dependent characteristic[J]. IEEE Transactions on Power Delivery, 2020, 36(6): 3496-3505.

[121] Papadopoulos T A, Papagiannis G K, Labridis D P. A generalized model for the calculation of the impedances and admittances of overhead power lines above stratified earth[J]. Electric Power Systems Research, 2010, 80(9): 1160-1170.

[122] Dommel H W, Dommel I I. Electro–Magnetic Transient Program (EMTP)[J]. Reference Manual (EMTP Theory Book). Portland, OR: Bonneville Power Administration, 1986, 9.

[123] Borghetti A, Bosetti M, Di Silvestro M, et al. Continuous-wavelet transform for fault location in distribution power networks: Definition of mother wavelets inferred from fault originated transients[J]. IEEE Transactions on Power Systems, 2008, 23(2): 380-388.

[124] Mor A R, Heredia L C C, Muñoz F A. Estimation of charge, energy and polarity of noisy partial discharge pulses[J]. IEEE Transactions on Dielectrics and Electrical Insulation, 2017, 24(4): 2511-2521.

[125] Alvarez F, Ortego J, Garnacho F, et al. A clustering technique for partial discharge and noise sources identification in power cables by means of waveform parameters[J]. IEEE Transactions on Dielectrics and Electrical Insulation, 2016, 23(1): 469-481.

[126] Rojas H E, Forero M C, Cortes C A. Application of the local polynomial Fourier transform in the evaluation of electrical signals generated by partial discharges in distribution transformers[J]. IEEE Transactions on Dielectrics and Electrical Insulation, 2017, 24(1): 227-236.

[127] Sawada H, Araki S, Mukai R, et al. Blind extraction of dominant target sources using ICA and time-frequency masking[J]. IEEE Transactions on Audio, Speech, and Language Processing, 2006, 14(6): 2165-2173.

[128] Sharif W, Muma M, Zoubir A M. Robustness analysis of spatial time-frequency distributions based on the influence function[J]. IEEE transactions on signal processing, 2013, 61(8): 1958-1971.
[129] Wax M, Kailath T. Detection of signals by information theoretic criteria[J]. IEEE Transactions on acoustics, speech, and signal processing, 1985, 33(2): 387-392.
[130] Zarowski C J. The MDL criterion for rank determination via effective singular values[J]. IEEE transactions on signal processing, 1998, 46(6): 1741-1744.
[131] DeCarlo L T. On the meaning and use of kurtosis[J]. Psychological methods, 1997, 2(3): 292.
[132] Li H, Kluger Y, Tygert M. Randomized algorithms for distributed computation of principal component analysis and singular value decomposition[J]. Advances in computational mathematics, 2018, 44: 1651-1672.
[133] Halko N, Martinsson P G, Tropp J A. Finding structure with randomness: Probabilistic algorithms for constructing approximate matrix decompositions[J]. SIAM review, 2011, 53(2): 217-288.
[134] Bouchikhi E H, Choqueuse V, Benbouzid M E H, et al. A comparative study of time-frequency representations for fault detection in wind turbine[C]//IECON 2011-37th Annual Conference of the IEEE Industrial Electronics Society. IEEE, 2011: 3584-3589.
[135] Yan Y, Ren S, Lu Y, et al. Efficient and low-cost PD monitoring and locating system for MV switchgears using TEV detectors[J]. IEEE Transactions on Power Delivery, 2021, 36(5): 3266-3269.
[136] Yan Y, Zhao Y, Zhao K, et al. A high-efficiency portable system for insulation condition assessment of wind farm inter-array cables with double-sided partial discharge detection and localisation[J]. IET Generation, Transmission & Distribution, 2023.
[137] Renforth L A, Giussani R, Mendiola M T, et al. Online partial discharge insulation condition monitoring of complete high-voltage networks[J]. IEEE Transactions on Industry Applications, 2018, 55(1): 1021-1029.
[138] Yan Y, Tao J, Trinchero R, et al. A Compact Detector for Flexible Partial Discharge Monitoring of 10-kV overhead Covered Conductor Lines[J]. IEEE Transactions on Power Delivery, 2022, 37(6): 5492-5495.
[139] Zhuang T, Ren M, Gao X, et al. Insulation condition monitoring in distribution power grid via IoT-based sensing network[J]. IEEE Transactions on Power Delivery, 2019, 34(4): 1706-1714.
[140] Can-can L, Shu-qun Z, Zhao-yi L E I. Research and Application of C Code Generated by Matlab Coder[J]. Computer and Modernization, 2013, 1(3): 175.
[141] Shahsavarian T, Pan Y, Zhang Z, et al. A review of knowledge-based defect identification via PRPD patterns in high voltage apparatus[J]. IEEE Access, 2021, 9: 77705-77728.
[142] Fritsch M, Wolter M. High-Frequency current transformer design and construction guide[J]. IEEE Transactions on Instrumentation and Measurement, 2022, 71: 1-9.
[143] Dubickas V, Edin H. High-frequency model of the Rogowski coil with a small number of turns[J]. IEEE Transactions on Instrumentation and Measurement, 2007, 56(6): 2284-2288.
[144] The Vector Fitting Web Site. [OL]. Available: http://www.energy.sintef.no/Produkt/VECTFIT/index.asp.
[145] Benesty J, Chen J, Huang Y. Time-delay estimation via linear interpolation and cross correlation[J]. IEEE Transactions on speech and audio processing, 2004, 12(5): 509-519.
[146] Knapp C, Carter G. The generalized correlation method for estimation of time delay[J]. IEEE transactions on acoustics, speech, and signal processing, 1976, 24(4): 320-327.
[147] Hashmi G M, Lehtonen M, Nordman M. Calibration of on-line partial discharge measuring system using Rogowski coil in covered-conductor overhead distribution networks[J]. IET Science, Measurement & Technology, 2011, 5(1): 5-13.
[148] Tashakkori A, Wolfs P J, Islam S, et al. Fault location on radial distribution networks via distributed synchronized traveling wave detectors[J]. IEEE Transactions on Power Delivery, 2019, 35(3):

1553-1562.

[149] Power-Lines E. IEEE guide for maintenance methods on energized power-lines[J]. Ieee Standard, 2009, 516.

[150] Li J, Liu Y, Xie J, et al. A remote monitoring and diagnosis method based on four-layer IoT frame perception[J]. IEEE Access, 2019, 7: 144324-144338.

[151] Su X, Masoum M A S, Wolfs P J. PSO and improved BSFS based sequential comprehensive placement and real-time multi-objective control of delta-connected switched capacitors in unbalanced radial MV distribution networks[J]. IEEE Transactions on Power Systems, 2015, 31(1): 612-622.

[152] Jin N, Rahmat-Samii Y. Advances in particle swarm optimization for antenna designs: Real-number, binary, single-objective and multiobjective implementations[J]. IEEE transactions on antennas and propagation, 2007, 55(3): 556-567.

[153] Tashakkori A, Abu-Siada A, Wolfs P J, et al. Optimal placement of synchronized voltage traveling wave sensors in a radial distribution network[J]. IEEE Access, 2021, 9: 65380-65387.

Achievements

Papers：

[1] **Yan Y,** Zhao Y, He W, et al. On-line Partial Discharge Localization of 10-kV Covered Conductor Lines[J]. IEEE Transactions on Power Delivery, 2022. (SCI: 000994763100018; EI: 20224613123712).

[2] **Yan Y,** Tao J, Trinchero R, et al. A Compact Detector for Flexible Partial Discharge Monitoring of 10-kV overhead Covered Conductor Lines[J]. IEEE Transactions on Power Delivery, 2022, 37(6): 5492-5495. (SCI: 000891435100098; EI: 20224413035937).

[3] **Yan Y,** Trinchero R, Stievano I S, et al. An automatic tool for partial discharge de-noising via short-time Fourier transform and matrix factorization[J]. IEEE Transactions on Instrumentation and Measurement, 2022, 71: 1-12. (SCI: 000880647100015; EI: 20224513092624).

[4] **Yan Y**, Zhao Y, Zhao K, et al. A high-efficiency portable system for insulation condition assessment of wind farm inter-array cables with double-sided partial discharge detection and localisation[J]. IET Generation, Transmission & Distribution, 2023. (SCI: 000970507800001; EI: 20231613943223).

[5] **Yan Y**, Ren S, Lu Y, et al. Efficient and low-cost PD monitoring and locating system for MV switchgears using TEV detectors[J]. IEEE Transactions on Power Delivery, 2021, 36(5): 3266-3269. (SCI: 000698898900072; EI: 20213310761906).

[6] **Yan Y**, Huo P, Li H. Robust on-line partial discharge measurement of 35-kV cables in wind farms via dual sensors[J]. Energy Reports, 2023, 9: 9-17. (SCI: 000899240300002; EI: 20224513067830).

[7] **Yan Y**, Li H, Wang Y, et al. A portable partial discharge locating tool for 10-kV covered conductor lines[C]. 22nd International Symposium on High Voltage Engineering (ISH 2021), 2021 p. 1954–1958.

[8] **Yan Y**, Zhao Y, Tao J, et al. Efficient condition-based maintenance of overhead distribution lines via partial discharge traveling wave detection[C]. CIRED 2022 Shanghai Workshop, 2022 p. 435–438.

Patents：

[1] **Yan Y**, Li H, Jin L, et al. Device and method for live detection partial discharge of overhead line in distribution network and equipment along line. (Application number: 18/321,888).

[2] Li H, **Yan Y**, Liu L, et al. A partial discharge on-line detection method for distribution network equipment under high-level noises. (Application number: CN202310188766.6).

[3] Li H, **Yan Y**, Tao J, et al. Insulation defect monitoring system and method of overhead power distribution line based on multi-node data fusion. (Application number: CN202310189451.3).

[4] Li H, **Yan Y**, Zhao Y, et al. A partial discharge live detection device and method for overhead line and alongsided equipment. (Application number: CN202210584498.5).

[5] Li H, Zhao Y, **Yan Y**, et al. Method and device for localizing partial discharge of power distribution cable without GPS (Application number: CN202211709192.4).